

R+D 6158-EE-02



AD-A216 134

DTIC
ELECTE
DEC 0 5 1989
S D

DISTRIBUTION STATEMENT A

Approved for public release
Distribution Unlimited

VACUUM
MICROELECTRONICS 89

99

Institute of Physics Conference Series number

6158-EE-02

89 11 28 122

Vacuum Microelectronics 1989

**Proceedings of the Second International Conference on
Vacuum Microelectronics held in Bath, 24–26 July 1989**

Edited by R E Turner

**Institute of Physics Conference Series Number 99
Institute of Physics, Bristol and New York**

Copyright © 1989 by IOP Publishing Ltd and individual contributors. All rights reserved. Multiple copying of the contents or parts thereof without permission is in breach of copyright but permission is hereby given to copy titles and abstracts of papers and names of authors. Permission is usually given upon written application to IOP Publishing Ltd to copy illustrations and short extracts from the text of individual contributions, provided that the source (and, where appropriate, the copyright) is acknowledged. Multiple copying is only permitted under the terms of the agreement between the Committee of Vice-Chancellors and Principals and the Copyright Licensing Agency. Authorisation to photocopy items for internal use, or the internal and personal use of specific clients in the USA, is granted by IOP Publishing Ltd for libraries and other users registered with the Copyright Clearance Center (CCC) Transactional Reporting Service, provided that the base fee of \$2.50 per copy per article is paid direct to CCC, 27 Congress Street, Salem, MA 01970, USA.
0305-2346/89 \$2.50+.00

CODEN IPHSAC 99 1-244 (1989)

British Library Cataloguing in Publication Data

International Conference on Vacuum Microelectronics (2nd:
1989: Bath, England)

Vacuum microelectronics 1989.

I. Microelectronics industries. Applications of vacuum
technology

I. Title II. Turner, Roy E. (Roy Edgar), 1931- III.

Institute of Physics IV. Series

621.5'5

ISBN 0-85498-055-5

Library of Congress Cataloging-in-Publication Data are available

Accession For		
NTIS	CRA&I	<input checked="" type="checkbox"/>
DTIC	TAB	<input type="checkbox"/>
Unanno.		<input type="checkbox"/>
Justification		
By		
Distribution		
Acquisition Notes		
Dist	Acquisition of	
Specialist		
A-1 21		



Published under The Institute of Physics imprint by IOP Publishing Ltd
Techno House, Redcliffe Way, Bristol BS1 6NX, England
335 East 45th Street, New York, NY 10017-3483, USA

Printed in Great Britain by J W Arrowsmith Ltd, Bristol

Contents

ix Preface

Section 1: Fabrication and processing

- 1-4 Self-aligned silicon-strip field emitter array
J P Spallas, S C Arney, C C Cheng and N C MacDonald
- 5-8 Fabrication of sharp field emission structures using ion beam milling
S E Jacobson, N A Cade and R A Lee
- 9-12 Fabrication of densely packed, sharp, silicon field emitters using dry etching
D Stephani and J Eibl

Posters

- 13-16 Fabrication of a fine heating element for microelectronics
S Hoshinouchi, M Kobayashi, N Morita, Y Hashimoto, K Sano and H Nakanishi

Section 2: Fabrication and characterization

- 17-20 Silicon field emitter arrays: fabrication and operation
P C Allen
- 21-24 Fabrication of ultrathin insulator films on n-Si substrate for electron tunnelling emitter arrays
K Yokoo, A Uchimi, T Ogishi, R Nakamura, S Ono and K Usami
- 25-28 Top-layer scandate cathodes by plasma-activated CVD
G Gärtner, P Janiel, J E Crombeen and J Hasker
- 29-32 Lateral cold cathode triode structures fabricated on insulating substrates
H H Busta

Posters

- 33-36 A new 8-inch ECR source for dry etching processes and CVD applications
K Matl, K-H Kretschmer, I Kessler and W Katzschnner
- 37-40 Control of silicon field emitter shape with isotropically etched oxide masks
J B Warren

Section 3: Electron sources

- 41-52 Back-biased junction cold cathodes: history and state of the art
G G P van Gorkom and A M E Hoeberechts (invited paper)

vi *Contents*

- 53–56 Photoemission from back-biased Schottky diodes p-InP-Ag
A L Musatov, S L Filippov and V L Korotkikh
- 57–60 Stimulated cold-cathode emission from metal electrodes coated with
Langmuir–Blodgett multilayers
S Bajic, N A Cade, A D Archer and R V Latham
- 61–64 Miniaturized liquid metal field electron and ion sources
J Mitterauer
- 65–68 Electron emission from GaAs Schottky diodes
T Tsukamoto, N Watanabe and M Okunuki

Posters

- 69–72 Electron emission from GaAsP NEA cold cathodes
P J Hockley and H Thomas
- 73–76 Thin-film metal–insulator–metal systems in the non-heated electron
emitter regime
Yu Yankelevitch, Yu Barengolzs and M Khaskelberg

Section 4: Field emission

- 77–80 Simulation and design of field emitters
R B Marcus, K K Chin, Y Yuan, H J Wang and W N Carr
- 81–84 Electrical characterization of gridded field emission arrays
D F Howell, R D Groves, R A Lee, C Patel and H A Williams
- 85–88 Energetic characterization of field emission cathodes
R Baptist, A Ghis and R Meyer
- 89–93 Fluctuation phenomena in field emission from molybdenum micropoints
I Brodie
- 95–99 A general formula to calculate the field intensity on the field emitter
Luo Enze, Liu Yunpeng and Huang Wenhui

Posters

- 101–104 Low-field ‘cold-cathode’ electron emission from Cu electrodes overlaid
by a resin-particle composite
S Bajic and R V Latham
- 105–108 Construction and performance of field emitting cathodes
R A Lee, A J Miller, C Patel and H A Williams
- 109–112 Modelling of electron trajectories in field emission devices
N A Cade
- 113–116 An experimental study of the physics of field emission by tip arrays
R J Harvey, R A Lee, A J Miller and J K Wigmore

- 117–120 A mathematical model to predict optimum geometry of the elements of a field emitter array cathode
R K Feeney, J K Cochran, D N Hill and A T Chapman

Section 5: Transport in solids

- 121–132 Tunnelling theory and vacuum microelectronics
P H Cutler, T E Feuchtwang, Z Huang and T Sullivan (invited paper)
- 133–136 Monte Carlo calculation and vacuum emission experiments of hot and ballistic electrons from MIS-structures
H-J Fitting
- 137–140 'Particle trajectory' tunnelling: a novel approach to quantum transport
K L Jensen and F A Buot
- 141–144 Silicon cold cathodes based on PIN diodes
P A M van der Heide, G G P van Gorkom, A M E Hoeberechts, A A van Gorkom and G F A van de Walle
- 145–148 Theoretical study of the scanning tunnelling microscope
Th Laloyaux, A A Lucas, J-P Vigneron and Ph Lambin

Poster

- 149–152 Field-enhanced emission
P T Landsberg

Section 6: Diagnostic techniques

- 153–164 Characterization of individual micro-emission centres distributed in planar arrays
R V Latham and A D Archer (invited paper)
- 165–166 An STM controlled field emission microlens electron source
M A McCord, T H P Chang, D P Kern and J L Speidell
- 167–172 The dynamics and stability of solid surfaces of nanostructures
T T Tsong and C Chen
- 173–176 Investigation of field emitting microstructures by scanning electron and scanning tunnelling microscopy
Ph Niedermann, Ch Renner, A D Kent and Ø Fischer

Posters

- 177–180 Lithography on Si by means of STM and SEM
J M Gómez-Rodríguez and A M Baró
- 181–184 Analysis of particle trajectories on an interactive desktop system
C J Edgcombe and D E Roberts

viii *Contents*

- 185–188 **An alternate cathode architecture**
E J Daniszewski

Section 7: Devices

- 189–194 **Comparison of vacuum and semiconductor field effect transistor performance limits**
L F Eastman
- 195–199 **Geometry optimization for a lateral triode**
W N Carr, H J Wang, K K Chin and R B Marcus
- 201–206 **Miniaturization of electrovacuum microwave and radiofrequency low-power devices**
N D Devyatkov, Yu V Gulyaev, A M Alexeenko, M B Golant, J L Grigorishin, A A Negirev and N I Sinitsyn
- 207–210 **Micro-cavity integrable vacuum devices and triodes**
W J Orvis, C F McConaghy, D R Ciarlo, J H Yee, E W Hee, C E Hunt and J Trujillo

Posters

- 211–216 **Electromagnetic properties of a field emission distributed amplifier**
P M Phillips, S T Smith and H F Gray
- 217–221 **Frequency limits of electronic tubes with field emission cathodes**
W A Anderson
- 223–226 **Theoretical study of a vacuum field effect transistor**
Z H Huang, P H Cutler, T E Feuchtwang and H F Gray
- 227–230 **Scaling laws for temporal and spatial dispersions of a short pulse of electrons in a diode in the space-charge regime**
C Girardeau-Montaut, J P Girardeau-Montaut and H Leboutet
- 231–234 **Fabrication and theoretical study of micron-size vertical vacuum triodes**
J Itoh and H Hiroshima
- 235–238 **Ballistic field emission devices**
V I Makhov
- 239 **Papers and posters presented but not included in the proceedings**
- 241–242 **Author Index**
- 243–244 **Subject Index**

Preface

These conference proceedings are the first published 'snapshot' of the current work in the new field of vacuum microelectronics.

The conference provided a lively forum for over one hundred and sixty delegates, from fifteen countries and a wide range of disciplines, to hear a total of fifty-four presentations.

The majority of presenters submitted manuscripts for publication. All of these were refereed and in most cases any changes were agreed during the conference. In cases where both referees felt that clarification was required, and it proved impracticable to contact the author, then changes have been made. Unratified changes are highlighted by a vertical line to the right of the text.

My thanks to the authors, the referees and to the editorial staff of the Institute of Physics without whose cooperation the rapid publication of this text would not have been possible. Thanks also to the conference steering, organizing and programme committees.

As in any new field there were healthy disagreements about, for example, the causes of the deviation from field emission theory or the variations in the actual or projected performance of devices but it is precisely this debate which filled the hall to the end of the last paper. There was general agreement that the conference had been a success and that great strides had been made in the last year in vacuum microelectronics. The next conference in this series will be held in Monterey, California and is currently scheduled for the period 22–25 July 1990.

Rob Turner

Self-aligned silicon-strip field emitter array

J. P. Spallas, S. C. Arney, C. C. Cheng, and N. C. MacDonald

*School of Electrical Engineering and the National Nanofabrication Facility,
Cornell University, Ithaca, NY 14853*

ABSTRACT: We have fabricated vacuum field emission devices based on large arrays of silicon-strip cathodes. The emitter tip radii range from 20 to 25 nm. The self-aligned gate is typically located less than 550 nm from the emitter tip. The collector aperture is 2.45 μm wide and is located 700 nm above the gate. Arrays of thirteen strip emitters, 300 μm and 600 μm long, have been fabricated. Array elements have been modeled and electron trajectories and transit times simulated.

1. INTRODUCTION

Interest in the field of vacuum micro-electronics has been renewed by the successful testing of a planar vacuum field effect transistor (Gray et al 1986). This field emitting structure is a silicon tip with a very small radius of curvature. The device is fabricated on a silicon substrate using standard integrated circuit processing technology. Applying 100 to 200 V to the gate results in field emission of electrons into vacuum. A collector located on the same plane as the gate collects the emitted current.

Devices of this type can be fabricated in large arrays and with the gate electrode located very close to the emitter. Consequently, they are capable of producing large current densities with the application of low potentials. Further, the emitted electrons traverse vacuum instead of a crystal lattice making them ideal structures for very high frequency operation.

Tips are the usual choice for the field emitter structure, but, strips (Spindt et al 1983) and circular edges (Marcus et al 1987) have also been proposed. These structures should produce larger emission currents than tips because they have greater emitting areas. It has been demonstrated that very sharp strips can be fabricated in silicon using a lateral, high temperature thermal oxidation to selectively oxidize beneath isolated silicon islands (Arney and MacDonald 1988). Strips as long as 3.2 mm separated by 2 μm and arrayed in areas as large as 3.2 mm square can be fabricated using this technique. The microstructural properties of these strips have been studied using high voltage transmission electron microscopy (TEM) (Theodore et al 1988).

We have fabricated these structures in arrays of thirteen strips. The strips are either 300 μm or 600 μm long. The gate electrode is self-aligned and is located 550 nm from the emitter tip. The emitter tip radius is less than 25 nm. Here we describe the extension of the isolated silicon island process to produce large arrays of field emitter strips. Array elements have been modeled and the electric fields, electron trajectories, and transit times simulated. These models are used to evaluate the suitability of these arrays for device application.

2. FABRICATION

The fabrication of an array of silicon strips is based on the formation of submicron silicon-on-insulator islands (Arney and MacDonald 1988). The starting material is p-type <100> oriented, 10 ohm-cm boron doped silicon. Using direct write electron-beam lithography, a tri-level resist scheme, and an aluminum lift-off process, arrays consisting of aluminum lines 250 nm wide are generated. Two anisotropic reactive ion etch processes first transfer the pattern to the underlying silicon dioxide/silicon nitride stack, then etch trenches 500 nm deep into the substrate silicon. The sidewalls are masked by a conformal LPCVD silicon nitride deposition and etch back sequence. An isotropic silicon etch followed by a high temperature lateral oxidation results in the formation of linear silicon strips capped by an isolated silicon island. A schematic of this structure after the gate metal has been deposited is shown in Fig. 1.

The emission current from a cathode tip is strongly dependent on the diameter of the gate aperture and on the position of the tip with respect to the lower plane of the gate (Spindt et al 1976). The structure shown in Fig. 1 is ideally suited for the fabrication of self-aligned gates that are very close to the emitter tip. The width and position of the gate aperture are determined by the same silicon nitride layer that determines the emitter position. Because the silicon nitride typically flares during the thermal oxidation, the gate aperture width ranges from 0.8 to 1.2 μm . The emitters are 450 nm tall. The position of the tip with respect to the gate is, therefore, determined by the thickness of the thermal silicon dioxide. By etching the thermal silicon dioxide before the gate metal deposition, we are able to center the strips horizontally in the gate aperture.

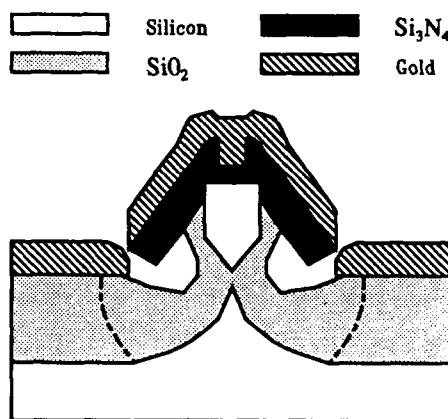


Fig. 1. A strip emitter before the silicon island is removed. The dotted line represents the SiO_2 boundary after the tip is exposed.

The process sequence developed for the fabrication of the gate and collector requires three masking levels. The thermal silicon dioxide is partially etched back using buffered HF, then 150 nm of gold on 10 nm of chrome is thermally evaporated. Because the evaporation is highly directional, the metal film is not continuous at the silicon nitride edge. The over-lying structure can therefore be lifted off by etching the oxide underneath the silicon island using buffered HF. A photoresist mask is used to pattern the gate and the gold and chrome are etched using successive potassium iodide/iodine and ceric ammonium acid solutions. A SEM micrograph showing a cross section of a typical gate and emitter tip is shown in Fig. 2.

A 700 nm silicon dioxide film is next deposited using a PECVD process. This dielectric serves to electrically isolate the collector from the gate. A 200 nm gold on 10 nm chrome film is then thermally evaporated. To achieve smooth sidewalls with a minimum of undercut, the collector is etched using an ion milling process. Photoresist is not a practical mask in this case because the high ion energies needed to etch gold cause severe photoresist reticulation. A 300 nm PECVD silicon dioxide film is deposited to mask the collector. The silicon dioxide is patterned using photoresist and etched using a reactive ion etch process. The gold and chrome are then ion milled to form the collector.

The final masking level utilizes a two step etch to expose the emitters and to make contact to the first and second level metals. First, the contact mask is patterned and the insulating silicon dioxide is etched to 75% completion using a reactive ion etch process. The etch is finished using buffered HF. In this way, damage to the emitters due to ion bombardment is avoided. Also, the insulating silicon dioxide sidewalls are gently sloped without excessive under-cutting. A SEM micrograph of a completed array is shown in Fig. 3.



Fig. 2. A SEM micrograph showing the emitter centered vertically and horizontally in the gate.

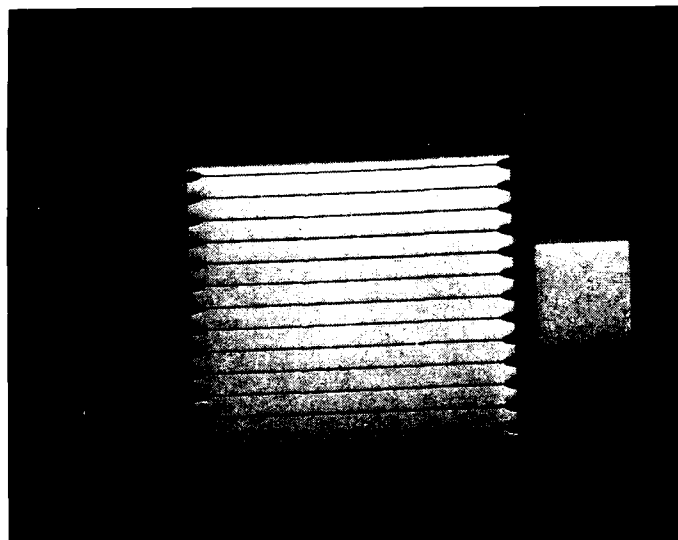


Fig. 3. A SEM micrograph showing a silicon-strip emitter array. This array contains thirteen elements, each 600 μm long.

3. SIMULATIONS

The charge density method is used to solve Poisson's equation in the neighborhood of the emitter, gate, and collector. Electric fields in these regions range from 6×10^6 to 5×10^7 V/cm for applied gate potentials between 50 and 200 V. Electrons emitted from the tip are accelerated along trajectories nearly perpendicular to the gate. Therefore, to achieve picosecond transit times, devices should be designed to intercept the electron trajectories. Figure 4 shows the simulated potential contours and trajectories of a device that has this capability. The collector is located directly above the emitter. The structural dimensions used for modeling the tip and gate match those of our fabricated strips. The calculated transit time for this structure is 0.2 ps for 50 V applied to the gate and 100 V applied to the collector. However, this structure is not optimized to achieve effective control of the emission current by the gate alone.

4. SUMMARY

Arrays of silicon-strip field emitters have been fabricated using silicon integrated circuit processing technology. The tip radii were less than 25 nm. The position of the tip with respect to the gate is controlled by etching. The emitter profile is controlled by a high temperature thermal oxidation. While the emitters fabricated here are separated by $40 \mu\text{m}$, strips separated by $2 \mu\text{m}$ have also been fabricated (Arney and MacDonald 1988). We anticipate that these devices will produce large current densities at low operating voltages. Simulations of array elements suggest that devices utilizing these structures can be designed to operate with picosecond transit times.

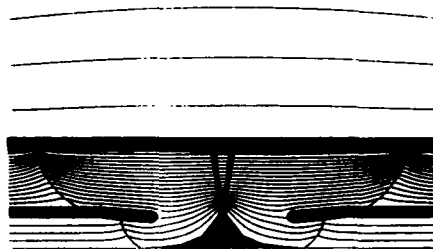


Fig. 4. A model showing the simulated potential contours and electron trajectories. The tip radius is 20 nm. The collector is 700 nm above the gate. The transit time is 0.2 ps for $V_{\text{gate}} = 50$ V and $V_{\text{collector}} = 100$ V.

5. ACKNOWLEDGEMENTS

This work was supported by the Semiconductor Research Corporation via the Cornell Program for Microscience and Technology. Microstructure fabrication, characterization, and simulations were performed at the National Nanofabrication Facility (NNF), which is partially supported by the National Science Foundation, Cornell University, and industrial affiliates. The authors wish to acknowledge Larry Murray, Andres Fernandez, and the staff of NNF for their technical assistance.

6. REFERENCES

- Arney S C and MacDonald N C, *Formation of Submicron Silicon-on-Insulator Structures by Lateral Oxidation of Substrate-Silicon Islands*, J. Vac. Sci. Technol. B:6(1), Jan./Feb. 1988.
- Gray H F, Campisi G J, and Greene R F, *A Vacuum Field Effect Transistor Using Silicon Emitter Arrays*, Proceedings of International Electron Devices Meeting, Los Angeles, Dec. 1986.
- Marcus R B, Soave R, and Gray H F, *A Novel Vacuum Microelectronics Field Emitter*, International Conference on Vacuum Microelectronics, Jul. 1988.
- Spindt C A, Brodie I, Humphrey L, and Westerberg E R, *Physical Properties of Thin-Film Field Emission Cathodes with Molybdenum Cones*, J. Appl. Phys., Vol. 47, No. 12, (1976).
- Spindt C A, Holland C E, and Stowell R D, *Field Emission Cathode Array Development for High-Current-Density Applications*, Applications of Surf. Sci., 16, 268, (1983).
- Theodore N D, Carter C B, Arney S C, and MacDonald N C, *Behavior of Defects Related to Interface-Stresses in Model Submicron SOI Structures*, Materials Research Society Meeting, Boston, MA, Nov. 1988.

Fabrication of sharp field emission structures using ion beam milling

S E Jacobson, N A Cade and R A Lee

GEC Hirst Research Centre, East Lane, Wembley, Middlesex, HA9 7PP, UK

ABSTRACT: The application of argon ion milling to the formation of sharp tip structures for micron scale field emission diodes is investigated using a combined experimental and theoretical approach. The results are discussed with reference to the angle dependence of the etch rate, the differential etch rates of mask and substrate and the initial mask profile. These are illustrated by reference to the milling of sputtered gold.

1. INTRODUCTION

With the recent proliferation of etching techniques for semiconductor device fabrication, there has been renewed interest in the kinematic description of morphological development, particularly for ion milling and plasma etching processes (see Smith (1986), for example). The mechanisms of the chemical and physical processes involved are diverse and not always understood, but the basic mathematical formulation of the kinematics of such etching processes is common to a large number of systems. This mathematical description has been formulated largely by Frank (see Barber et al (1973)), and has been applied to both wet and dry etching processes. In this paper we consider the argon ion beam milling of sputtered gold to produce sharp tips. With the assumption that these films exhibit no crystallographic anisotropy, the etch rates depend only on the angle between the ion beam and the surface normal, allowing a 2D description.

2. ETCH RATE MEASUREMENT

The etch rate determination and tip formation studies were carried out using a Veeco Microetch ion beam miller, providing an 850V argon ion beam with current density of 0.97 mA/cm^2 . A base pressure of $\leq 10^{-6}$ torr was obtained prior to milling. Samples were mounted on a watercooled rotating stage capable of being inclined to give ion beam angles of incidence in the range 0° to -80° . Etch rates were determined by measuring the etch steps of masked samples, using a Tencor Alpha Step. Metal samples were masked with photoresist, while resist material to be used in tip formation trials was masked with silicon in good mechanical contact.

Gold samples were prepared by first coating clean silicon wafers with 500-800 Å of chromium to promote adhesion and then sputtering a $2.4 \mu\text{m}$ layer of gold. For the tip formation, the gold was masked by $1.1 \mu\text{m}$

thick photolithographically defined resist (Hunts 204). Angle dependent etch rates, similar to those of Bollinger (1980) are shown in Figure 1.

3. THEORY

The propagation of the eroding, two dimensional surface of a 3-D solid may be described, with complete generality, by $F(x,y,z) = t$. Differentiating this equation and identifying the velocity components ($\partial x/\partial t$, etc) with normal etch rates

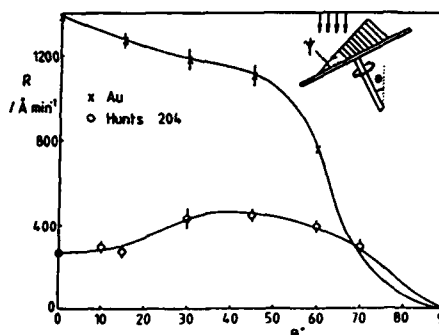


Fig.1 Experimental etch rates

(R), the differential equation describing this propagation may be obtained as (see Cade 1989)

$$H = R(F_x, x_i) (F_x^2 + F_y^2 + F_z^2)^{1/2} = 1 \quad (1)$$

Here the R is assumed to be constant in time but depends on the spatial position and local orientation of the surface, expressed in terms of the spatial derivatives $F_i = \partial F/\partial x_i$ of F . Solutions of such non-linear partial differential equations can be obtained by the method of characteristics (Whitham 1974). Resulting etch trajectories are given by the coupled set of ordinary differential (Hamilton's!) equations:

$$\frac{dF_i}{dt} = - \frac{\partial H}{\partial x_i}, \quad \frac{dx_i}{dt} = \frac{\partial H}{\partial F_i} = V_i \quad (2)$$

For a homogeneous system, H is independent of x_i and the solutions are straight line trajectories of constant surface normal with velocities V_i which are generally not orthogonal to the surface (parallel to F_i) (Cade 1989). For an isotropic sample the etch rates depend only on the angle of incidence, θ , of the ion beam, and the equations of motion are two dimensional. Taking the ion beam in the z direction we have the trajectories given in terms of R and its θ derivative, R' (Cantagrel 1975)

$$\begin{aligned} z &= z_0 + (\cos\theta R(\theta) - \sin\theta R'(\theta))t \\ x &= x_0 + (\sin\theta R(\theta) + \cos\theta R'(\theta))t \end{aligned} \quad (3)$$

For masked systems such a description is not sufficient. The discontinuous change in etch rates at a boundary between two materials produces a simple inhomogeneity. This can be treated as a boundary matching problem and the matching conditions for the straight line trajectories, on the two sides of the boundary, obtained by integrating equation 2 across the boundary. After much algebra, the final result is that the trajectories obey "Snell's Law" at the interface, namely

$$R^{(1)}(\theta^{(1)}) f^{(2).n} = R^{(2)}(\theta^{(2)}) f^{(1).n} \quad (4)$$

$R^{(1,2)}$ are the angle dependent etch rates and $f^{(1,2)}$ are the etching surface normals ($f_1 = F_1 (F_x^2 + F_y^2 + F_z^2)^{-1/2}$) of the two materials with common boundary given by its unit normal \underline{n} .

Although this angle dependent etch rate function is fixed for any material, the effective function may be altered by rotating the sample about an axis inclined to the ion beam. This enables the angle for peak etch rate to be varied. For a substrate inclined at an angle θ with facet angle ψ (see inset to Fig 1), the effective etch rate $r(\theta, \psi)$ is given by:

$$r(\theta, \psi) = \frac{1}{\pi} \int_0^{\phi_0} R(\cos^{-1}(\sin \psi \sin \theta \cos \phi + \cos \psi \cos \theta)) d\phi$$

where $\phi_0 = \cos^{-1}(-\cot \psi \cot \theta)$ or π if $|\cot \psi \cot \theta| > 1$

4. TIP FORMATION

There are two distinct strategies for tip formation based on masking. The first is based on having a resistant mask and allowing the undercutting of the less resistant underlying material to produce a tip when etch fronts meet at the centre of the mask. This is the usual strategy of wet etching (see Cade 1989). This approach is still useful in ion milling, despite its highly directional nature, if the ion beam has a suitably large angle of incidence. The second more conventional method is to use progressive exposure of new substrate as the mask is eroded to provide tip shaping based on the Snell's Law of eqn (4).

The bases of these two methods are shown in Figure 2 where the etch velocities obtained from Figure 1 and Eqn (5) are plotted for gold. A similar set of velocity profiles was obtained for the resist. In the case of normal incidence there can be no undercutting but, for $\psi = 45^\circ$, there is substantial undercutting which would allow a near vertical neck and correspondingly sharp tip.

The tip structures obtained from an application of these approaches are shown below. In all cases non-UV hardened Hunts 204 resist masks were used. Because of the relative thinness

of the gold layer ($2.4 \mu\text{m}$), tip formation should not have been possible without etching into the silicon substrate. However sharp tips were formed without overetching. This can be explained only by resist pad etch rates which were greater by a factor of 1.6 than those for the large area etch rate trials. This increased rate produced a larger tip angle than anticipated (Figure 3a) but use of the undercutting strategy by etching at

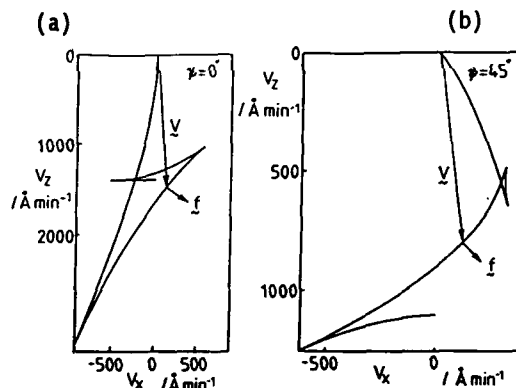


Fig 2: Etch velocity (V_i) contours of gold as a function of orientation (f_i)

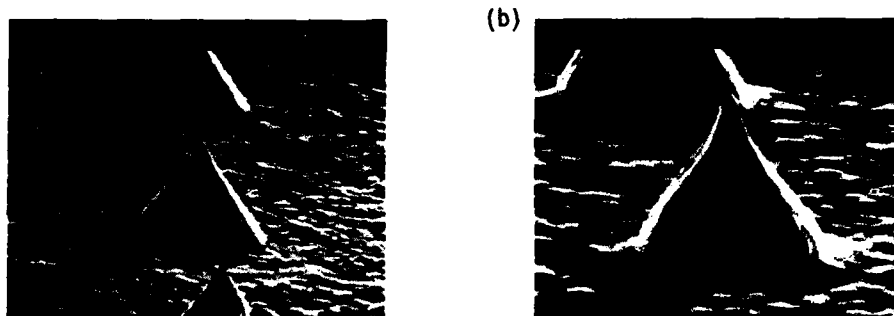


Fig. 3 Experimental gold tip profiles for etch masks $1.5\ \mu\text{m}$ thick and $1.1\ \mu\text{m}$ square tapering to $1.03\ \mu\text{m}$ square at the top.

(a) 14.5 min at $\psi=0$ (b) 10 min at $\psi=0$, then 8 min at $\psi = 45$.

45° allowed the substantial sharpening of Figure 3b. These tip shapes should be compared with the theoretical profiles of Figure 4, obtained using the resist etch rates of Figure 1, multiplied by a factor of 1.6. With this factor the experimental shape is reproduced, including the slope discontinuity at the residual mask edge in Figure 3b. The most significant difference being the narrower base which is sensitive to the very low etch rates of gold near $\theta=90^\circ$.

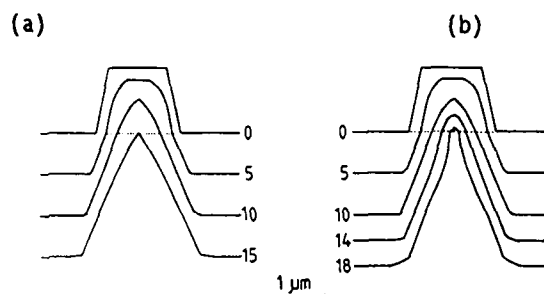


Fig. 4 Theoretical etch profiles corresponding to Fig 3. Successive profiles are shown for the times (min) indicated, starting with the mask profile on the flat gold substrate. Note the slope discontinuity at the (dotted) boundary between them.

5. CONCLUSION

This simple modelling scheme is useful in predicting, understanding and fine tuning ion milling approaches to tip formation. It is also apparent that the successful formation of tips in gold resulted from its relatively fast etch rate. Other slower etching metals will require thicker and possibly narrower resist masks. The apparent sensitivity of mask etch rates to their area requires further investigation.

6. REFERENCES

- Barber DJ, Frank FC, Moss M, Steeds JW & Tsong IST, *J. Mater. Sci.* **8**, 1030 (1973)
- Cade NA, Lee RA & Patel C, sub. *IEEE Trans on Elect. Dev.* (1989)
- Cantagrel M, *IEEE Trans on Elect. Dev.* **IE-22**, 483 (1975)
- Bollinger LD & Fink R, *Solid State Technology* **23**, 79 (1980)
- Whitham GB "Linear and Nonlinear Waves" (John Wiley; NY) (1974)
- Smith R, Tagg MA, Carter F & Nobes MJ, *J. Mater. Sci. Lett* **5**, 115 (1986)

Fabrication of densely packed, sharp, silicon field emitters using dry etching

D. Stephani and J. Eibl

Siemens AG, Corporate Research and Technology, Paul Gossen Strasse 100,
D 8520 Erlangen, Federal Republic of Germany.

ABSTRACT: Two fabrication methods based on dry etching techniques are described with which arrays of sharp silicon field emitters exhibiting a ratio of tip height to tip spacing greater than unity and a density of 20,000,000 tips per square centimeter have been achieved.

1. INTRODUCTION

Wet chemical etching (Thomas 1974) and anisotropic orientation dependent etching of (100)-silicon (Gray 1986) have been used for the fabrication of arrays of silicon field emitters. Using the latter method in (100)-silicon, the tip geometry is determined by the (111) planes of the single silicon crystal. Thus the ratio of tip height to tip spacing is limited to a factor of one over the square root of two. Using isotropic wet chemical etching this ratio is limited to a factor of about 0.5 since the under etching of the mask is very similar to the etched depth into the substrate. To further improve quality and density of field emitter arrays, microfabrication techniques are required which allow control of the shape of field emitting microstructures and their area density independently. Microfabrication techniques such as Ion Beam Etching (IBE), Reactive Ion Beam Etching (RIBE) and Reactive Ion Etching (RIE) can provide the required independent control.

2. FABRICATION METHODS

The first method we have developed to fabricate densely packed silicon field emitters consists basically of only two important steps :

- a) etch silicon columns with vertical walls out of the substrate and
- b) subsequently form sharp tips at the upper end of the columns.

A prerequisite is an etching process with which silicon can be vertically etched. RIE with chlorine or fluorine based chemistry is capable of vertical silicon etching. Many articles may be found in the literature regarding vertical RIE of silicon and here only the work of Jackel et al (1981) and an article by Sellamuthu et al (1987) are cited. The fabrication method we have will now be described. Silicon wafers were steam oxidized at 1050 °C to an oxide thickness of 0.2 µm and afterwards coated with 0.8 µm titanium by magnetron sputtering. AZ 5214 E was spun at 3000 rpm onto the titanium layer and photolithography was used to define a test pattern in which, in addition to other structures an array of 160,000 dots exists. These dots of 1 µm diameter are separated by 2.2 µm. The AZ 5214 E photoresist was used in its image reversal mode to benefit from its superb resolution in this mode (Reuhman 1988). The resist pattern was

transferred into the titanium layer by RIE with chlorine based chemistry as described by Blumenstock and Stephani (1989). The patterned titanium layer now acts as a mask in RIE with pure tetrafluoromethane to etch the silicon columns. The gas pressure chosen was 2 Pa and the power was selected such that a self bias voltage of -500 V developed at the powered electrode of the diode type reactor (Leybold AG, Z 401 S). Under these conditions the wafer, placed onto the graphite covered RF powered (13.56 MHz) electrode, remained nearly at room temperature and underetching is not detectable. A silicon etch rate of 17 nm/min was obtained which is at least four times larger than the corresponding titanium etch rate. The use of a lower pressure e.g. 1.33 Pa decreases the ratio of silicon etch rate to titanium etch rate, the use of a higher pressure e.g. 2.66 Pa results in columns with reduced diameter at their bottom, i.e. shaped like Indian clubs. Having fabricated silicon columns of 3 μm height as described, the remaining titanium and the silicon dioxide layer were removed by wet chemical etching in buffered HF. Here the role of the silicon dioxide layer becomes clear. Because it is used as a sacrificial layer it guarantees a clean silicon surface and complete titanium removal. The subsequent tip forming process consists of IBE with Ar at normal incidence of the argon ion beam to the substrate surface. An acceleration voltage of 1200 V was selected and the argon pressure was set to 0.15 Pa in the IBE apparatus (CSC VIII-C). The faceting of projecting rectangular edges is an inherent attribute in IBE and is here used for tip forming. The angle of faceting is dependent on substrate material, beam energy, beam incidence and mass of the ions used (Carter 1984). Figure 1 shows on its left hand side a high magnification SEM of a tip after forming by IBE. The tip radius measures here approximately 25 nm. To further decrease the tip radius, the wafers were steam oxidized at 900 °C for 25 min. As published by Marcus and Sheng (1982) oxide growth under these conditions is reduced at locations of high curvature compared with locations of low curvature. Therefore a very sharp silicon tip forms under the growing silicon dioxide in the tip region. Removal of the grown silicon dioxide with buffered HF completes the fabrication process and yields tip radii of about 10 nm or less. This is shown on the right hand side in Figure 1. A SEM taken from a cleaved array of sharpened silicon field emitters is shown in Figure 2 and demonstrates the high performance and reproducibility of the fabrication method described here in detail.

The second method for the fabrication of arrays of silicon field emitters is based on RIE with boron trichloride/oxygen chemistry using a slowly erodable mask. Silicon wafers were prepared as follows. After steam oxidation as described before the wafers were coated with 0.2 μm Permalloy and 0.2 μm titanium by sputtering. The photolithography applied and the subsequent titanium etching process were performed as aforementioned. After photoresist removal the etched titanium pattern was transferred into the Permalloy layer by RIBE with a gas mixture of argon and nitrogen. RIE with 40 ml/min boron trichloride and 2 ml/min oxygen at a pressure of 2 Pa was used for silicon etching. Titanium etches at nearly the same rate as silicon in this process but Permalloy is only slightly attacked by the sputter component of the process. In particular the edges of the dot-like Permalloy structures are affected. This leads to shrinking of the Permalloy dots until they vanish. If Permalloy thickness and dot size are properly chosen silicon cones are the result of the etching process. As described before cleaning with buffered HF followed by low temperature oxidation and oxide removal for tip sharpening completes the process. Figure 3 shows a SEM of silicon tips fabricated by this method. The opening angle of the silicon cones can be determined from this figure to



Figure 1: SEM's of silicon tips after forming by IBE with Ar (left) and after sharpening (right), taken at 60° substrate tilt angle.

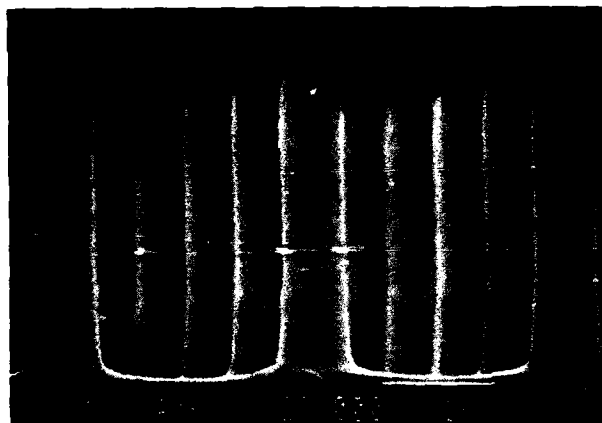


Figure 2: SEM taken from a cleaved array of 160,000 sharpened silicon tips. The SEM was taken at 91° substrate tilt angle.

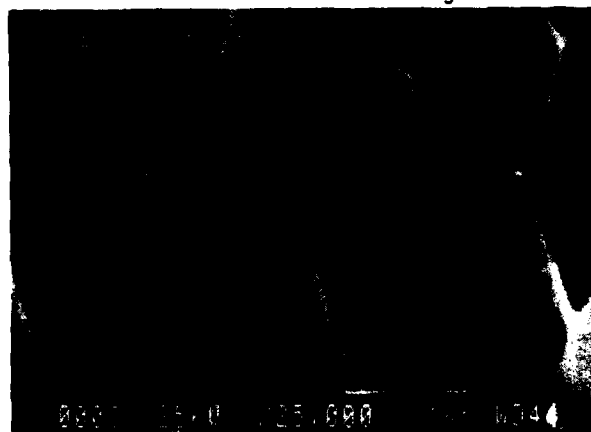


Figure 3: SEM of silicon cones fabricated by RIE with boron trichloride/oxygen chemistry. The SEM was taken at 60° substrate tilt angle.

be approximately 35° , the substrate tilt angle of 60° having been taken into account.

3. DISCUSSION

With the exception of tip sharpening by oxidation, both processes, if properly modified, can also be applied in the fabrication of metallic field emitter arrays. The second fabrication method described here does not allow an independent choice of tip height to tip spacing. It does, however, yield a cone angle of the silicon tips small enough to allow a ratio of tip height to tip spacing greater than unity. The first fabrication method presented here in detail gives the necessary flexibility to produce densely packed microstructures of high aspect ratio for field emission purposes. A detailed discussion of the (high) performance and (high) reproducibility of this method would go beyond the scope of this paper and the space available. However, in conclusion it can be stated that all surfaces of the silicon columns are in the plane of the wafer surface before tip forming starts and the column diameters are all virtually identical since their definition is obtained from the diffraction limited, areal image of a regular array of structures on the photomask. The opening angle of the tips is approximately 60° and therefore variations in column diameter are transferred into variations of the vertical tip position at only a ratio of about unity and without changing the shape of the tip.

4. ACKNOWLEDGEMENTS

The authors wish to express their gratitude to Dr. H. Schindler for his encouragement and support of the project, to Dr. D. Branston for many helpful discussions, to K.H. Jablonski for performing IBE and G. Hartreiter and H. Huebner for performing optical lithography.

5. REFERENCES

- Blumenstock K and Stephani D 1989 accepted for publication in *J. Vac. Sci. Technol.* B, Jul./Aug. 1989
- Carter G and Nobes M J 1984 in *Ion Bombardment Modification of Surfaces* (Elsevier) ISBN 0-444-42365-6 (Vol.1) pp 163-224
- Gray H F, Campisi G J and Greene R F 1986 *IEDM Tech. Dig.* pp 776-779
- Jackel L D, Howard R E, Hu E L, Tennant D M and Grabbe P 1981 *Appl. Phys. Lett.* **39** 268
- Marcus R B and Sheng T T 1982 *J. Electrochem. Soc.* **129** 1278
- Reuhmann M E, Mutsaers C M J, Vollenbroeck F A, Moonen J 1988 *Microcircuit Engineering* **88**, Vienna, Sept. 88, to be published (Amsterdam: Elsevier)
- Sellamathu R, Barkanic J, Jaccodine R 1987 *J. Vac. Sci. Technol. B* **5** 342
- Thomas R N, Wickstrom R A, Schroder D K and Nathanson H C 1974 *Solid-State Electronics* **17** pp 155-163

Fabrication of a fine heating element for microelectronics

S.Hoshinouchi, M.Kobayashi, N.Morita, Y.Hashimoto, K.Sano* and H.Nakanishi*

Manufacturing Development Laboratory, Mitsubishi Electric Corporation,
 8-1-1 Tsukaguchi-Honmachi, Amagasaki, Hyogo, Japan

* Kyoto Works, Mitsubishi Electric Corporation,

1 Zusho Baba, Nagaokakyo, Kyoto, Japan

Abstract: Fabrication of a fine heating element operative at 1300 K is described. The device was constructed of a deposited tungsten film on a sapphire substrate and a welded platinum wire lead. The tungsten film had an interface layer of a deposited titanium layer onto the sapphire substrate. The heating device was operative below 1113 K because of titanium migration to the tungsten film.

1. Introduction

There is a possibility to fabricate a fine heating element by using thin film technology, instead of a conventional heater. Many methods are known for making thin film such as sputtering, ion mixing, chemical vapour deposition and screen printing technique. The screen printing technique has advantages of low cost and ease of implementation, but disadvantages in terms of precision and miniaturization. We have tried to make thin films on sapphire substrates or sintered aluminum nitride (AlN) substrates with the above many kinds of technique. In this paper, we mainly discuss the fabrication and evaluation of a tiny heating device made with the sputtering method, which is constructed of a deposited tungsten film on a sapphire substrate and can be operated at 1300K in vacuum.

2. Production of Heating Element

The heating element is shown in Fig.1. The substrate was made of a single crystal sapphire having a polished mirror-like

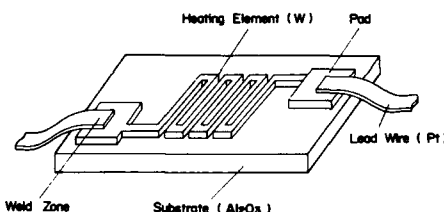


Fig.1 A schematic diagram of the heating element

Table 1 Manufacturing process and operation test sequence

sequence	process step	note
1	cleaning of substrate	neutral agent : CaCO_3
2	metallization	equipment : SBH-3308RDE (trademark, made by ULVAC Corporation : Japan) target : W 99.95 % purity
3	coating of photo resist	KMR-747 (trademark, made by Eastman Kodak Company) containing above 80 per cent xylene
4	exposure	high pressure mercury lamp
5	development	Negative Developer (trademark, made by Eastman Kodak Company)
6	wet etching	$\text{K}[\text{Fe}(\text{CN})_6] + \text{NaOH} + \text{H}_2\text{O}$
7	rinse	QMR-502 (trademark, made by Tokyo Ohka Kogyo CO., Ltd.)
8	welding of lead wires to film	parallel gap resistance welder Pt wire in 80 micron diameter
9	mounting on glass stem and evacuation	degree of 10^{-4} Pa
10	applying power	5V, 0.3A

surface. The dimensions of the substrate were 3mm length, 5mm width and 0.3mm thickness. The heating element on the sapphire substrate was made of a tungsten stripe having 3 micron thickness, 200 micron line width and a meander shape. Tungsten was deposited with a columnar structure of the film in the perpendicular direction to the substrate surface. Pads had a square shape of 0.4 mm X 0.4 mm and were used to connect a lead wire.

Table 2 Sputtering condition

RF POWER	500 W
Ar PRESSURE	0.53 Pa
SUBSTRATE TEMPERATURE	523 K
DEPOSITION RATE	1.4 $\mu\text{m/hr}$

The manufacturing flow chart is shown in Table 1. The substrate was degreased by rubbing with calcium carbonate powder on a wetted cloth before deposition. We used sputtering method to deposit tungsten on a sapphire substrate. This method is advantageous in case of a high refractory metal such as tungsten because a high purity film can be obtained. The sputtering condition is shown in Table 2. The pattern of the heating element was made with photolithography. KMR-747 (Trade mark, made by Kodak) was used for resist material, and the thickness of the coated resist was 1.5 micron. Exposure was done with a high pressure mercury lamp. The Negative developer made by Kodak was used for developing. The etching of the tungsten film was done at 303 K. The etchant was composed of potassium ferrocyanide, sodium hydrate and pure water. The exposed resist on the substrate was removed with OMR 502 (Trade mark, made by Tokyo Ohka) after the etching. A try was done for welding of a platinum wire in 80 micron diameter to the pad with a parallel gap welder, but the film could not hold even a small lead wire. Lift or peeling of the film occurred from the area where the platinum wire was welded, because the adhesive strength of the deposited tungsten film was too weak.

2.1 Improvement in Adhesive Strength

The peel-off phenomenon suggests that the tungsten atom bonds weakly to the oxygen atom of the sapphire. We introduced a titanium layer between the tungsten film and a sapphire substrate. Titanium was at first deposited onto a sapphire substrate, and then tungsten was deposited onto the formerly deposited titanium layer, sequentially.

The titanium layer was 0.05 micron thick, and the tungsten layer was 3 micron thick. The welding of a platinum wire was again tried to the tungsten film with the same method, and it was successfully completed. Fig. 2 shows the improvement in the adhesive strength of the deposited film. The abscissa describes the applied power in the welding operation, and the ordinate describes the tensile strength of the welded platinum lead when the lead is pulled in the direction of 45 degrees from the element. A remarkable improvement in adhesive strength was obtained. However, beyond 4.5 watts

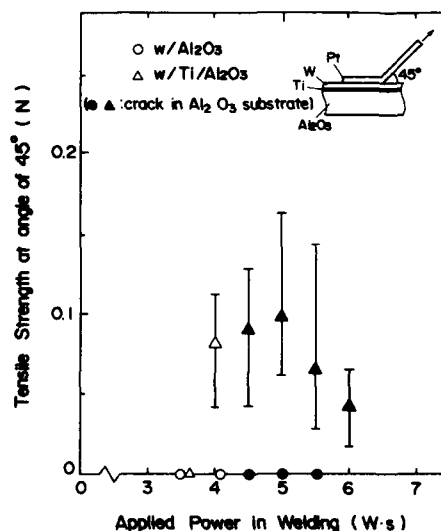


Fig.2 Improvement in the adhesive strength of the deposited film

seconds of the welding power, small cracks were observed in the sapphire substrate. Those cracks make the tensile strength of a connecting lead weak.

2.2 Device Fabrication

The heating element was assembled on a glass stem, and each lead wire was connected to each stem lead in order to apply the operating voltages. The assembly was mounted in a vacuum envelope and evacuated to a pressure of 10^{-4} Pa.

3. Operation Test

The temperature of the heating element could be elevated to 1300 °K by applying a power of 5 volts and 0.3 amperes.



Fig.3 A photograph of the heating element in an operating condition

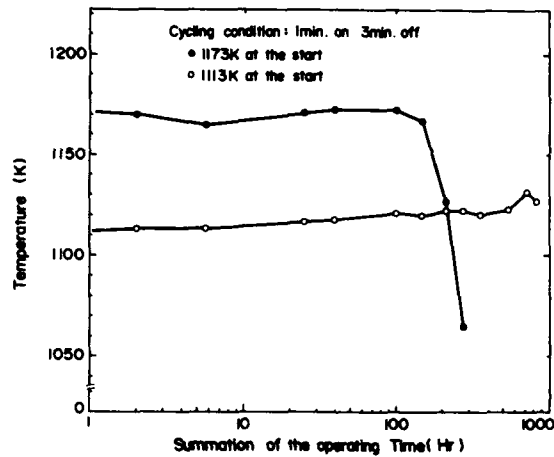
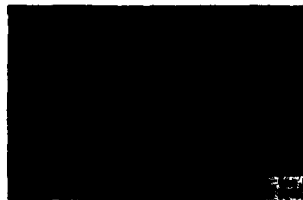


Fig.4 Changes of the heating element temperature in the cycling test



Typical surface of the film



Typical surface of the film



Cross section at an end of the film



Cross section at an end of the film

(a) Before operation

(b) After operation at 1173K

Fig.5 Secondary Electron Image of the W film on the Ti layer

Fig.3 shows the heating element being in an operating condition. Operation tests were implemented in various conditions. Fig.4 shows changes in the element temperature in cycling test of 1 minute on and 3 minutes off. The abscissa shows the summation of "on time", and the ordinate shows the element temperature obtained by applying the given power to each samples at the start point. At 1173 K operating temperature condition, a big change was observed in the tungsten film exceeding 100 hours. Some cracks and lifts appeared in the tungsten stripe, locally, and thus the features of the film changed remarkably, as shown in Fig.5. Also, the film shrank in the edge toward longitudinal direction. The element resistivity increased in accordance with the film state change. The test result teaches us that some phenomena occur in between 1113 K and 1173 K.

4. Discussion

The titanium interface layer increased the adhesive strength of the deposited tungsten film to the sapphire substrate, as described the previous section. Nishiguchi et al(1988) studied on valence electron structure of the metal-ceramics interface with Auger-analysis. They used the evaporated film of chromium, copper, and titanium on a silicon dioxide or single crystal silicon substrates. They reported in the paper that oxygen atom makes strong metal-ceramics bond. However, it is not clear that oxygen atom has same role in case of the deposited titanium or tungsten film by sputtering on a sapphire, single crystal aluminum oxide.

It is known that titanium changes the crystal phase from alpha form to beta form at 1155 K. Our experimental results suggest that beta titanium can easily migrate to tungsten and promotes the recrystallization of tungsten film in the operating condition of 1173 K resulting in cracks, lifts and shrinks.

An aluminum nitride substrate seemed to make the same bond strength of the platinum wire to the deposited film as a sapphire, but the electrical conductivity increased extremely at the aimed operating temperature. The application of the device will be restricted.

5. Conclusion

The deposited titanium interface layer increased the adhesion of deposited tungsten film to a sapphire substrate. The device could be elevated at the operating temperature of 1300 K. However, the layer caused a fatal damage to the tungsten film for >one hundred hours operation in case of the operation temperature of 1155 K. In order to make the fine heating element operative at 1300 K for long hours, we should improve the deposited tungsten film and welding of a lead wire.

Acknowledgement

The authors acknowledge Mr.Y.Kashiba, Mr.Y.Yoshida, Mr.H.Ohnishi, Mr.Y.Maeyama, Mr.T.Shinzyo, Mr.Y.Kusakabe, Mr.T.Kamata, Mr.M.Saito and Dr.Y.Utumi for the contributions in various phases of this study.

Reference

K.Nishiguchi, Y.Takahashi and K.Takahashi, 1988 Preprints of the National Meeting of Japan Welding Society. No. 43 pp106-107

Silicon field emitter arrays: fabrication and operation

P C Allen

Thorn EMI Central Research Labs., Dawley Road, Hayes, Middlesex UB3 1HH

Simple arrays of field emission points have been fabricated on silicon by isotropic etching and also by isotropic plus anisotropic etching. Both methods have produced desirable geometries which are not easily predicted from etch rate data. Electric field modelling has been used to predict the effect of the emitter tip cone angle. Array emission has been observed in a number of experiments. When high voltages are required the individual emitters are susceptible to catastrophic failure. Single emitters have also been successfully fabricated and used as cold cathodes in experimental triode valves.

1. INTRODUCTION

Electronic devices based on field emission of electrons provide at least as much scope for complexity as we see in conventional electronic devices. With this in mind we have resisted the temptation to begin this research with a study of complex structures. We have decided rather to build a base for future work by concentrating our efforts on the fabrication of basic arrays of points in silicon and examining their electrical characteristics and modes of failure. All fabrication methods described here involve the undercutting of square oxide caps (formed by conventional lithography) on silicon. Some effort has been devoted to the modelling of electric field between point arrays and a common anode plane. To further examine the basic behaviour of emitters we have fabricated single points from silicon and also from fine tungsten wires. We have also fabricated a basic triode valve, with overall dimension of less than 3 mm, with a single field emitting cathode formed from silicon.

2. TWO STAGE (ISOTROPIC/ANISOTROPIC) ETCHING OF ARRAYS

This fabrication method relies on the formation of an array of smoothly curved mesas, by isotropic etching which is then followed by a strongly anisotropic etch in order to form sharply pointed geometric shapes and release the original oxide caps. The initial 20 μm pitch array of 15 μm square oxide caps is formed on thermally oxidised <100> cut, n-type, 5 ohm cm., polished silicon. The structure is etched in $\text{HF}:\text{HNO}_3:\text{CH}_3\text{COOH}$ (9:75:30 by volume) at 22 °C with gentle agitation, which gives results than are broadly consistent with the findings of Peterson et al (1982). This process is monitored and terminated when the area of silicon under the oxide caps is at the limit of optical resolution (ie about 1 μm^2). The structure is then transferred to the strongly anisotropic etch $\text{KOH}:\text{H}_2\text{O}$ (44 gm per 100 ml) at 85 °C. After a period of about 1 minute the oxide caps are released and the etch is terminated. The arrays of emitters produced by this method have typical tip radii of about 50 nm and overall height of about 10 μm as shown in micrograph 1. Figure 1 shows the structures produced in terms of the <110> and <211> crystal planes which we believe form this shape. This is consistent with the development of the fast etching planes which are the closest to the surfaces produced by the original isotropic etch. This is in agreement with the data of Weirauch (1975), which is shown in figure 2, where we believe the unidentified fast etching plane is the <211>. In this case our emitters are self sharpening because the <100> apex of our points etches more slowly than the <211> walls.

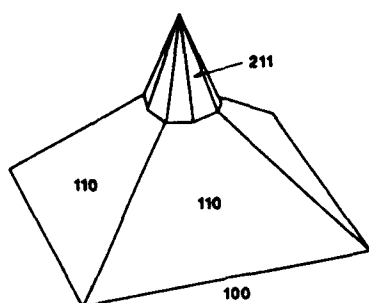


Figure 1: Isotropic / anisotropic emitter

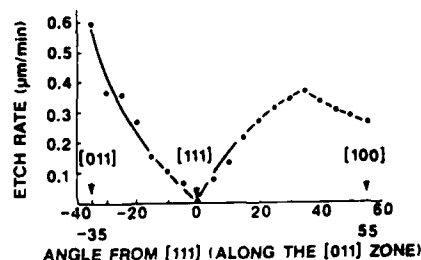


Figure 2: KOH silicon etching (courtesy D.F. Weir, Texas Instruments).

3. ISOTROPIC ETCH FABRICATION

It was originally thought that using only an isotropic etching would lead to large tip radii due to attack of the apex when the oxide caps are lost. This has not occurred in our experiments however. The most favourable results have been obtained using the etch $\text{HF}:\text{HNO}_3:\text{CH}_3\text{COOH}$ (2:95:3 by volume) at 0°C - which in fact does show some degree of anisotropy. Applying this etch to the patterned silicon eventually releases the oxide caps to produce the features shown in micrograph 2. An advantageous feature of this structure is the very acute angled tip which is well differentiated from the smoothly curved main structure. Examination by SEM has revealed tip radii of as little as 15 nm.

4. ELECTRICAL OPERATION EXPERIMENTS

Our earliest experiments were carried out, at a pressure of 10^{-3} to 10^{-4} mbar, using the experimental arrangement shown in figure 3. The planar anode was of identical material to the cathode, which was a silicon array as described in section 2.

The cathode was isolated in the centre of microscope slide and the spacing set at $100\ \mu\text{m}$ with Mylar film. A micrometer was used to carefully reduce the anode to cathode spacing until a short circuit occurred. At this point the micrometer was unscrewed a minute amount to obtain an open circuit and an unstable current was passed in forward bias. After about 10 hours the forward current stabilised and no reverse bias current could be obtained below 135 volts. The structure could be operated in this stable fashion for currents up to $8\ \mu\text{A}$ with voltages of up to 5 volts. For our measured tip radii this result is not consistent with predictions (for metallic or semiconducting emitters) based on the Fowler-Nordheim theory (1928) unless we consider tip-anode spacings of less than 50 nm - which is highly improbable. We have found no satisfactory explanation for this, other than the existence of unresolved features (on an atomic scale) on our emission tips.

Arrays were also tested in pressures of less than 10^{-6} mbar where large spacings and voltages could be employed without causing low pressure gas discharges. With gold evaporated onto the array and emitter anode distances of less than $10\ \mu\text{m}$ appreciable field emission currents flowed at about 1500 volts bias. Numerous Fowler-Nordheim plots for these structures confirm that field emission is occurring (see figure 4). In these experiments typical array areas of $1\ \text{cm}^2$ (some 2.5×10^5 points) were used although comparing the data with predictions indicates that only about 1% of these were active. Attempts to obtain high current by increasing the bias caused visible flashes between anode and cathode. SEM examination of the array indicates that individual operating emitters were failing in a catastrophic manner as shown in micrograph 3.

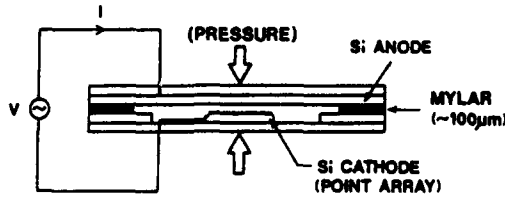


Figure 3: Experimental arrangement

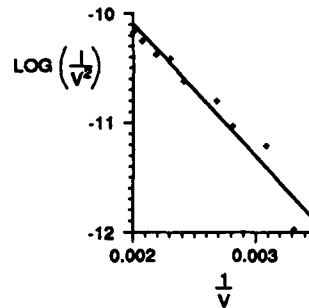


Figure 4: Fowler-Nordheim plot of data

5. PRELIMINARY MODELLING RESULTS

In our investigation of emission from simple arrays we recognize that an important consideration is the angle of the emitter cone. To assess the field at the emitter tip as a function of this angle. We have programmed a micro computer to perform an iterative finite element analysis on a 50 x 50 element array representing the space containing the emitter and anode.

This was tested by solving for electrode geometries with known solutions and was found to be accurate to within 1%. Figure 5 shows a generalised solution for well separated emitters which project half way to the anode from a continuous metallic surface. For parallel sided spikes we predict a maximum value of $0.5V/r$ which should be compared to the theoretical maximum of V/r for a spherical electrode in a Faraday cage and also to the value of $0.36V/r$ obtained by Schroder et. al. (1974). For our array the maximum value of θ is 30 degrees which gives a sufficient field to explain our observations.

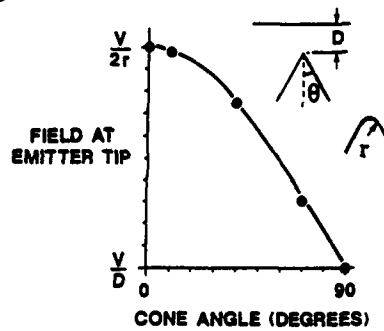


Figure 5: Field vs emitter angle

6. SINGLE EMITTERS IN SILICON AND TUNGSTEN

Single emitters have also been fabricated (i) in silicon and (ii) in fine tungsten wires by the method of Hubner (1983).

Silicon points were fabricated by cleaving silicon wafers at acute angles and etching and these were usually gold coated before use. The silicon structures had typical radii of 100 nm whilst we have produced tungsten points with radii as low as 30 nm. Figure 6 shows a simple triode valve has also been constructed using a single silicon emitter. The 50% transmitting copper grid is used to extract electrons from the point and those not absorbed by it continue on to the phosphor coated anode with sufficient energy to cause emission of light. 1700 volts on the grid and anode produces a cathode current of about 10 μ A. A reduction of the grid bias to 1400 volts results in zero anode current.

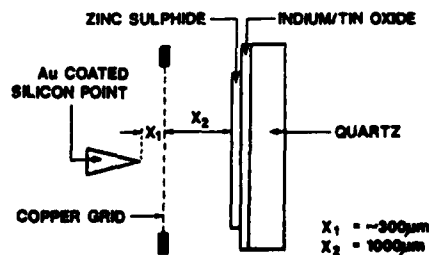
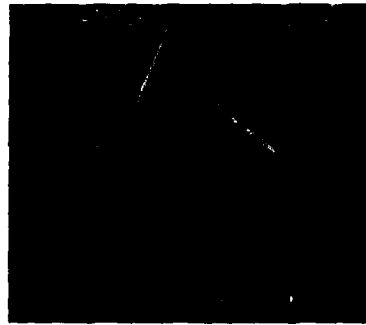


Figure 6: Experimental triode

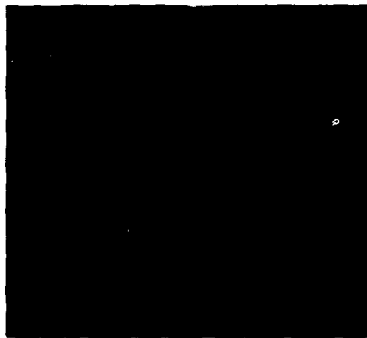
7. CONCLUSION

The fabrication techniques described are capable of producing reasonably uniform emitter arrays over a 3 inch silicon wafer. Due to inhomogenities in the etching there are variations in emitter height although the field emission is insensitive to this for small anode emitter spacings. More of a problem is small variations in tip radius which, we presume, cause the initial emission from only 1% of the array. The subsequent destruction of these individuals at higher voltage is believed to be a consequence of incident energy (associated with 1.5 keV electrons) on the anode. SEM examination has revealed anode and emitter damage following the occurrence of "flashes". This could be explained by plasma arcs formed in material ejected from the anode surface by the incident electrons. If this is so the problem could be solved by using lower work function materials for the emitters. This would result in lower operating voltages which would reduce the incident energy at the anode.

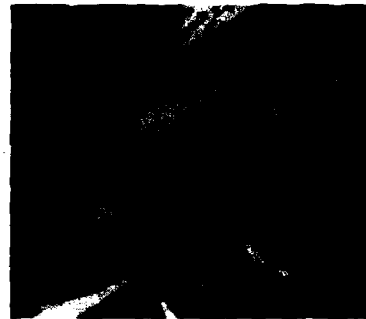
With the one exception described earlier we have been able to explain our results in terms of field emission from point arrays. It should be noted however, that our "rogue" result was obtained in a low, but appreciable, gas pressure which may have affected the operation.



Micrograph 1



Micrograph 2



Micrograph 3

ACKNOWLEDGMENTS

The author wishes to thank Mr. S Birrell and Mr. S D Etienne for SEM operation and Mr. C M Turner and Mr. M Dennis for SEM micrographs and fabrication work.

REFERENCES

- Fowler R H and Nordheim L W 1928 *Proc. R. Soc. London A* **119** pp 173-81
- Hubner H 1983 *Optik* **63** 2 pp 179-83.
- Peterson K E 1982 *Proc. IEEE* **70** 5 pp 420-57
- Schroder D K, Thomas R N, Vine J and Nathanson H C 1974 *IEEE Tr. El. Dev.* **ED21** 12
- Weirauch D F 1975 *J. Appl. Phys.* **46** 4 pp 1478-83

Fabrication of ultrathin insulator films on n-Si substrate for electron tunnelling emitter arrays

K Yokoo, A Uchimi, T Ogishi, R Nakamura, S Ono and K Usami^x

Research Inst. Elect. Commu., Tohoku University, Sendai 980, Japan
University of Electro-Commu., Chofu 182, Japan^x

Abstract: Ultrathin silicon dioxide layers on silicon were formed by chemical oxidation of silicon as an insulator in MIS tunnelling emitter. The honeycomb structure of MIS diodes proved that the dominant charge transport through the insulator layer is tunnelling and good quality ultrathin oxide layer can be formed on silicon by the chemical oxidation.

1. INTRODUCTION

The tunnelling emitter is expected to have very promising characteristics as a cathode of vacuum tubes, because of its higher emission density, lower noise temperature, higher reliability and so on, compared with those of usual thermal cathodes. Although the studies on electron tunnelling emission from MIM structure retroacts to the early 1960's, recently the emitter has become of major interest again in connection with vacuum microelectronics and many other vacuum devices. Tunnelling emitter arrays formed in Metal-Insulator-Semiconductor structure (MIS) have several merits as a fine cathode for such uses, because it is possible to deposit a high quality insulator film on semiconductor by using semiconductor processing technologies and to apply uniform electric field on MIS diode, resulting in higher brightness on tunnelling emission. In this paper, we describe the fabrication of SiO₂ films formed by chemical oxidation of silicon and tunnelling characteristics of the MIS diodes with these films. The results obtained have shown that this method of ultrathin oxide growth can be applied in manufacturing a MIS tunnelling emitter.

2. FABRICATION OF SiO₂ FILM

The tunnelling emitter investigated has a honeycomb structure as is illustrated in Figure 1. n-type silicon wafers with a resistivity of a few Ωcm were used as the substrates. AuSb was evaporated on the back surface of the wafer to provide a good ohmic contact. After depositing silicon dioxide with thickness of around 1 μm by rf sputtering, a film of aluminium was vacuum deposited on the silicon dioxide to provide the positive electrode in MIS tunnelling diode. The top aluminium and the silicon dioxide are etched down to the silicon base to form a honeycomb structure by photolithographic techniques. The silicon base is slightly etched in dilute HF solution. Then the silicon surface is oxidized in boiling HCl-H₂O₂-H₂O solution. The MIS test structure is subsequently formed by vacuum evaporation of aluminium on the oxidized silicon surface.

The thickness of the metal electrode in tunnelling emitter should be thin enough to reduce the scattering of electrons in the metal. Therefore the honeycomb structure is favorable in application of uniform electric field on the ultrathin metal electrode.

Prior to the study of the tunnelling characteristics on MIS diodes, we investigated the thickness and the quality of oxide layer of silicon by the x-ray photoelectron spectroscopy (XPS).

Figure 2 shows the intensity of emitted electrons from Si-2p orbit as a function of the binding energy for a sample oxidized in boiling dilute HCl solution for 10 minutes. The highest peak at near 99eV of binding energy is the emission from the silicon base and the subsholder near the peak corresponds to the emission from Si-H bonds. The second peak near 103eV is the emission from silicon dioxide. A subpeak might appear between these peaks corresponding to the emission from the silicon suboxide, but it should be very small in amount. We also examined the oxide layer deposited on silicon by rf sputtering of silicon dioxide. The emission spectrum was distributed between these main peaks, which suggested that many types of suboxide were grown in the thin oxide layer deposited by sputtering. Thus, it was proved that the properties of chemically oxidized silicon formed a fairly good layer as an ultrathin insulator film for MIS diode. The dotted curves in Figure 2 show the spectrum corresponding to each material such as silicon base, silicon dioxide and so on, which are analyzed by curve fitting on the measured spectrum. We can estimate the thickness of the oxide layer by calculating each area surrounded by the dotted curves and assuming the escape depth of electrons. The thicknesses of the oxides were also measured ellipsometrically and confirmed to be coincident with each other in both measurements. Hence, this method is very effective in determination of the thickness of an

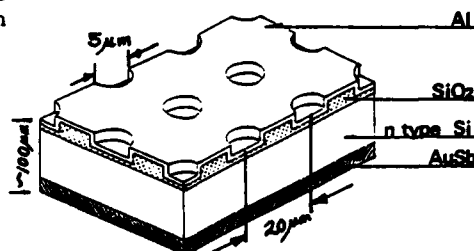


Fig.1 Schematic view of the electron tunnelling emitter with a honeycomb structure.

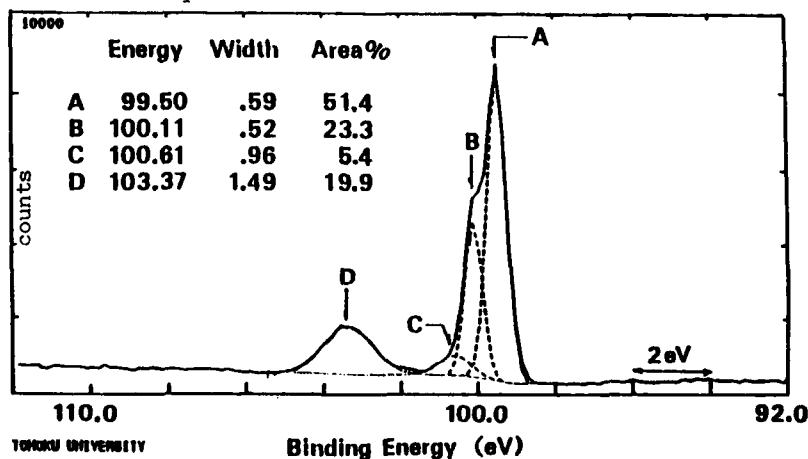


Fig.2 XPS spectrum of a n-type silicon surface oxidized in boiling dilute HCl solution.

ultrathin film.

The thickness of an oxide layer is independent of the oxidation time after dipping in dilute HCl solution for one minute and is around 15\AA . The results obtained have shown that this method of oxide growth is very attractive for fabrication of an insulator layer in MIS tunnelling diode due to the reproducibility of high quality ultrathin insulator films.

3. I-V CHARACTERISTICS AND DISCUSSION

Figure 3 shows the typical I-V characteristics obtained for MIS diode with silicon dioxide of 15\AA in thickness.

The shapes of the curves of both forwardly biased and reversely biased diode can be qualitatively explained as follows. For forward bias conditions majority carriers in the n-type semiconductor tunnel through the oxide layer, play the dominant current flow and result in exponential increase in current with increase in bias voltage. But a different situation appears for reversely biased diodes. Both electrons in the metal electrode and holes in the semiconductor tunnel through the oxide layer and the current flow is similar to that of the forward bias condition at low bias voltage. However, when the tunnelling of holes from the semiconductor to the metal electrode becomes more efficient than the thermal generation of holes, the surface concentration of holes is so small that it does not affect the total charge within the semiconductor. In such a case there is no inversion layer at the semiconductor surface and a depletion layer expands into the semiconductor

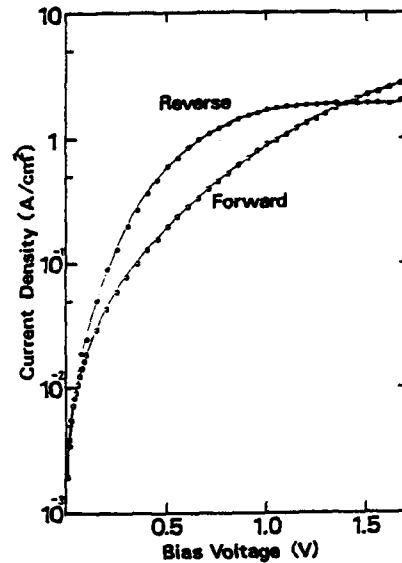


Fig.3 Typical I-V characteristics obtained for MIS diode with silicon dioxide of 15\AA in thickness.

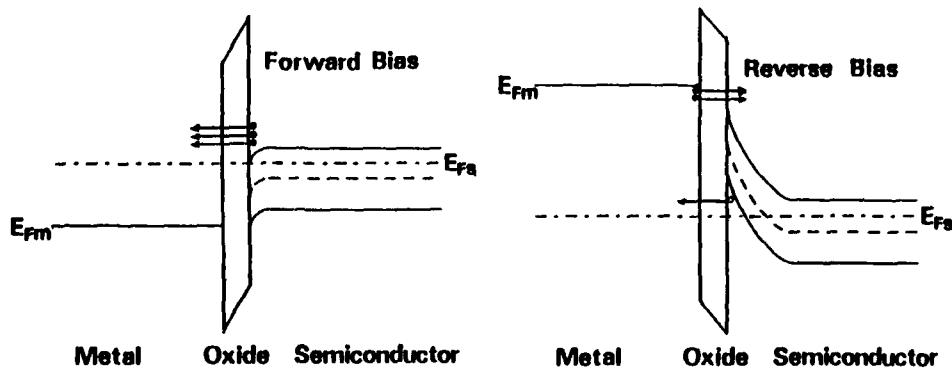


Fig.4 MIS diode energy band diagrams for forward and reverse bias conditions.

with increase of the bias voltage. Hence, the applied voltage drops mainly across the depletion layer in the semiconductor and a limited number of electrons in the metal can tunnel through the oxide layer resulting in the saturation on the current flow.

Figure 4 shows the schematic band diagram under forward and reverse bias conditions. From the figure, the above explanations are easily understood.

As described above, the I-V characteristics examined for the MIS diodes have proved that the dominant current flow is tunnelling through the oxide layer and good quality ultrathin oxide layers are formed on silicon.

4. CONCLUSION

We fabricated MIS tunnelling diodes with a honeycomb structure and measured the I-V characteristics of the diodes. As a results of the studies, it has been proved that the dominant charge transport mechanism through the insulator layer is tunnelling and good quality ultrathin oxide layers can be formed on silicon by the chemical oxidation in dilute HCl solution.

We will soon start to investigate the emission characteristics of the diode.

Top-layer scandate cathodes by plasma-activated CVD

G.Gärtner, P.Janiel

Philips GmbH Forschungslaboratorium Aachen, D 5100 Aachen, West-Germany

J.E.Crombeen, J.Hasker

Philips Natuurkundig Laboratorium Eindhoven, NL 5600JA Eindhoven, The Netherlands

ABSTRACT: Thermionic top-layer scandate cathodes, which are still unexcelled as to their total electron emission capability, have been prepared with the aid of PCVD on conventional impregnated cathode pills. The top-layer of $W + Sc_2O_3$ was deposited by glow-discharge activated CVD from WF_6/H_2 and $Sc(C_3H_7O_2)_3 / O_2$ starting compounds. A characterization of the PCVD layers is given. Emission tests of these PCVD cathodes yielded about the same high electron emission current densities as for the best conventional top-layer scandate cathodes. There is promise that the resistance against ion bombardment can be optimized by suitable top-layer substructure and composition.

1. INTRODUCTION

For most (thermionic) cathode applications in vacuum tubes, e.g. for high resolution displays and projection TV, there is an increasing need for higher cathode loadings and/or longer cathode life. Also a good resistance against ion bombardment during adverse initial processing conditions is needed. The high electron emission of conventionally manufactured scandate cathodes (fig.1), where the top-layer of $W + Sc_2O_3$ is prepared by powder pressing and sintering, has already been demonstrated (Hasker 1986,1989a). The aim of the present project was to realize scandate cathodes, which besides high electron emission should also show improved recovery after ion bombardment. This new type was planned to consist of a porous $4BaO:CaO:Al_2O_3$ impregnated tungsten body and a top-layer of $W + Sc_2O_3$ to be provided by Plasma-activated Chemical Vapour Deposition (PCVD). PCVD allows the realization of new material structures and has the advantage of good processing control. Dc-glow-discharge activated CVD had already been applied to the first successful preparation of thoriated tungsten cathode cylinders (Gärtner et al., 1987a,1987b,1989b,1989c), starting from an initial gas phase consisting of $WF_6/H_2/Ar$ and an organometallic Th-compound. Hence the existing apparatus was adapted for the solution of this new problem.

2. EXPERIMENTAL

WF_6 , H_2 , Ar and/or a Sc- β -diketonate, preferentially $Sc(C_3H_7O_2)_3$ with O_2 and Ar were used as gaseous starting compounds. The organometallic Sc-compound is contained in powder form in a temperature controlled low pressure evaporator device and is transported to the reactor by Ar carrier gas. An improved version of the tubular quartz reactor (fig.2), previously described in (1987a,b), with stainless steel and substrate inserts was additionally externally heated to a constant wall temperature of about 370 °C. Hence for plasma powers between 100 and 300 Watts or more, the contribution of thermal CVD is negligible. The plasma was realized as a normal dc glow discharge between the axial anode head and coaxially stacked substrate cylinders serving as cathode. The substrates used were Cu cylinders for exploratory and test runs or Mo cylinders with cathode pill inlays as shown in fig.3. The anode and hence the plasma were periodically moved up and down with an amplitude of e.g. 19 cm and an anode velocity of 57 cm/min in order to obtain uniform deposits. Depending on the mass flows of the source gases and for a reactor pressure in the region of 6 to 12 mbar, the typical layer growth rates were in the order of 1 $\mu m/min$, which were later reduced to about 0.2 $\mu m/min$.

3. CHARACTERIZATION

The first results of simultaneous PCVD showed that ScF_3 and W_2C were always the dominating phases in the deposit, due to the high F- and C-load of the inevitably organometallic Sc-compounds. This is partly related to the fact, that the Sc/W ratio is an order of magnitude higher than the Th/W ratio of (1987a). After essential modifications of the PCVD process, such as the addition of an oxidizing gas and an intermediate plasma treatment, we now obtain layers which show good adherence, contain W and Sc-oxide as solid phases and have a strongly reduced C- and F- content. An approximately constant axial W- and Sc-concentration in the "plateau"-region of 10 cm width was obtained, which is shown in fig.4. Beside the total growth rate \dot{g} = weight gain rate per cylinder, centered at the axial position numbered with $n = 1, \dots, 12$, also the results of a SEM microprobe analysis for O and C are depicted in fig.4 with respect to the axial position z . The thickness of the single sublayers was reduced from about 200 nm (fig.7) to about 30 nm. An AES depth profile of the different components of a cathode top-layer is depicted in fig.5. The concentration modulation seen here is due to alternate dynamic PCVD, but is usually also obtained with simultaneous PCVD (1989c). After heating to 1000 - 1100 °C in vacuo for cathode activation, carbon, fluorine and also the sublayer-structure disappear and a suitable mixture of Sc-oxide (about 10 % by weight) and tungsten is obtained in the top-layer (compare fig.6). In the case of PCVD covered impregnated cathode pills, Ba was detected at the surface after activation, which means that the desired Ba migration to the surface takes place through the pore ends and the PCVD-layer. Fig 7 shows a part of a cathode cross-section with the porous impregnated cathode body and the PCVD top-layer.

4. EMISSION RESULTS

Due to structural improvements mainly by applying top-layers of about 0.2 μm and an additional heat-treatment in a low pressure O_2 containing atmosphere, thermionic emission tests of PCVD cathodes yielded about the same high emission current densities as for the conventional scandate cathodes of Hasker et al.(1986,1989a). The PCVD top-layer scandate cathodes delivered 2.5 A continuously pulsed peak-emission current from an emitter area of 1.8 mm diameter. For cathode temperatures above 950 °C the electron emission is space-charge limited in the available parameter range. Therefore, instead of trying to determine saturated emission values subject to doubt, PCVD- and conventional cathodes (marked with Nat.Lab, see fig.8) were compared directly in a close-spaced plane diode configuration. The test conditions for pulsed emission were: cathode to anode distance $d = 0.6$ mm, pulse duration $t_p = 100$ μsec , pulse repetition rate 50 Hz. For comparison the conditions of (1986) for the two characteristics marked with scandate and M-cathode are also given: $d = 0.29$ mm, $t_p = 5$ μsec single pulse. Referenced to standard conditions at 950 °C brightness temperature and mean electric field strengths of 1 kV / 0.25 mm, pulsed space charge limited emission of about 100 A/cm² was realized. It can be seen that the top-layer scandate cathodes are very promising compared to one of the previously best and most stable impregnated cathodes, the so-called M-cathode with a sputter-deposited Os-Ru top-layer, which only reaches 20 A/cm². For the PCVD cathodes, the relationship between processing and emission properties, including the recovery after ion bombardment, needs further examination.

5. CONCLUSION

Uniform layer structures of $\text{W} + \text{Sc}_2\text{O}_3$ were obtained by dynamic, dc-glow discharge activated CVD, where the usual difficulties with multicomponent organometallic PCVD have been overcome by major modifications of the process. Impregnated cathode pills with these PCVD top-layers exhibit about the same high emission current density of about 100 A/cm² under standard test conditions at 950 °C as the best conventional top-layer scandate

cathodes. Considering the structure of this new PCVD cathode, there is hope of obtaining good resistance to ion bombardment, which is a subject of future investigation. It should be noted that the possibilities of this new microstructuring approach for thermionic cathode improvement have not yet been fully exploited.

REFERENCES

- Gärtner G., Janiel P. and Lydtin H. (1987a), Proc.6th Europ.Conf.on CVD, Jerusalem 1987, pp. 319-327
 Gärtner G., Janiel P. and Lydtin H. (1987b), Proc.6th Int.Conf.on Ion & Plasma Assisted Techn., Brighton 1987, pp. 17-22
 Gärtner G., Janiel P. and Lydtin H. (1989b), ITG-Fachbericht 108, Vakuumelektronik und Displays, VDE-Verlag Berlin, pp. 297-302
 Gärtner G., Janiel P. and Weling F. (1989c), Proc.7th Europ.Conf.on CVD, Perpignan 1989, Journal de Physique- Colloque C5, 50, pp. 73-82
 Hasker J., Crombeen J.E. and van Dorst P.A.M., (1989a), IEEE Trans. Electron Dev. 36/1, pp.215-219
 Hasker J., van Esdonk J. and Crombeen J.E., (1986), Appl. Surf. Sci. 26, pp.173 - 195

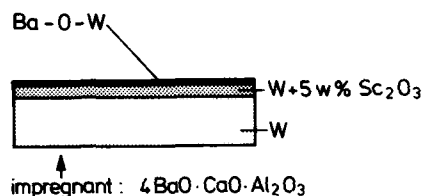


Fig. 1: Schematic representation of a conventional top-layer scan-date cathode. The plug consists of about 0.4 mm porous W with a porous top-layer of about 0.1 mm; its diameter is 1.8 mm.

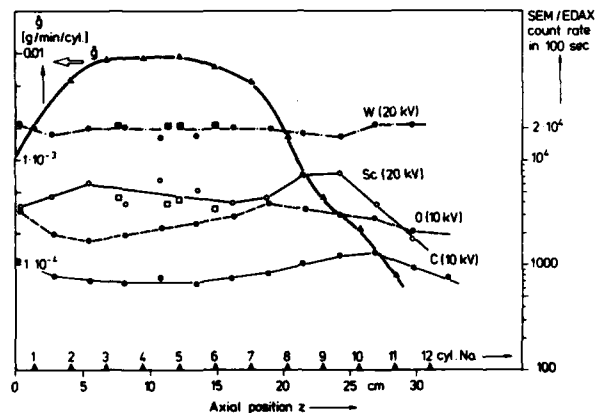


Fig. 4: Axial deposition profiles from SEM microprobe analysis; \bar{g} = total growth rate = weight gain rate per cylinder.

Fig. 2
PCVD-reactor

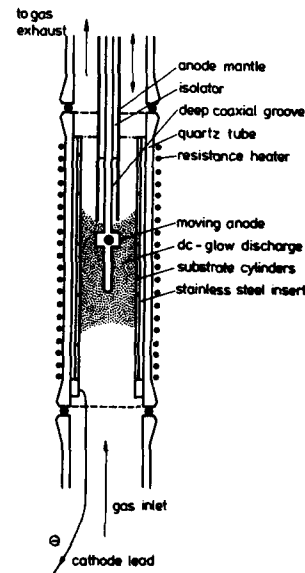




Fig.3: Molybdenum substrate cylinder with cathode pill inlays

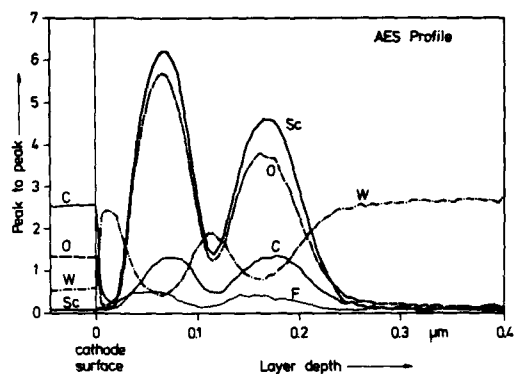


Fig.5: AES depth profile of PCVD top-layer of $W + Sc_2O_3$ before cathode activation

Fig.6: AES depth profile after heating in vacuo for 2 h at 1100 °C (C and F are at the detection level).

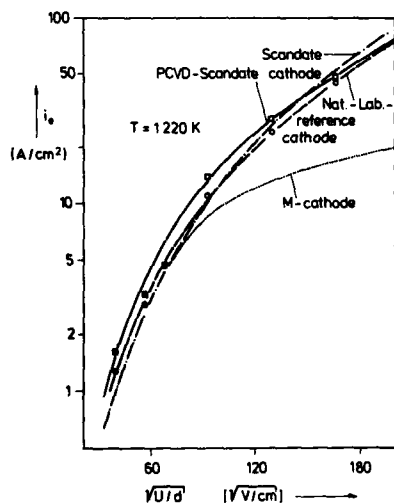


Fig.8: Schottky plot. The pulsed test conditions for the two cathode characteristics marked with PCVD and Nat.Lab. (pulsed test = open symbols, dc-test = solid symbols) were: $d = 0.6$ mm, pulse duration $t_p = 100$ μ sec, $p = 2 \cdot 10^{-8}$ torr. The conditions for the two characteristics from (1986) marked with Scandate and M were: $d = 0.29$ mm, $t_p = 5$ μ sec, $p = 1 \cdot 10^{-10}$ torr.

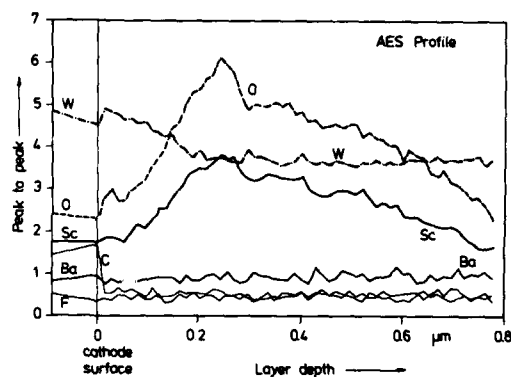


Fig.7: SEM micrograph of PCVD cathode cross section.



Lateral cold cathode triode structures fabricated on insulating substrates

Heinz H Busta

Amoco Technology Company, Amoco Research Center, Naperville, Illinois 60566, USA

ABSTRACT: We have fabricated a lateral vacuum transistor to investigate feasibility for high speed switching. It consists of a metallic, triangular-shaped emitter on a glass substrate which is surrounded by an extraction gate electrode, with a separation between emitter and gate of 300 nm. A metal anode completes the device. We measured a static gain of 3 and a transconductance of 6×10^{-10} Siemens. Several shortcomings exist in the design of this device, especially in the positioning of the gate. To improve performance, several new structures were designed and fabricated and are undergoing performance testing.

1. INTRODUCTION

Interest in vacuum transistor devices is high due to their potential applications in flat panel vacuum fluorescent displays and in high speed radiation hardened circuits. The most mature structure to date is the Spindt emitter array (Spindt 1983) consisting of cone-shaped metal emitters with extraction gate electrodes surrounding the tips of the emitters in an annular, self-aligned fashion. This is a vertical-type structure that is particularly well-suited for display applications. For logic circuit applications, however, some difficulty might exist in reliably interconnecting a large number of devices, due to the relatively large vertical feature size of several micrometers. Lateral-type devices might offer some advantages in this respect.

To prove feasibility of lateral-type structures and also to study the performance of individual emitters rather than arrays, we have designed, fabricated and tested lateral diode, triode and tetrode structures on glass and fused silica substrates. Initial results will be presented in this paper.

2. TRIODE STRUCTURE

The first device fabricated consists of an 80 nm thick triangular-shaped NiCr emitter and a rectangular-shaped collector fabricated on a 2-inch diameter soda lime substrate. The emitter and cathode are fabricated together during the first photolithographical process. The substrate is then coated with a 300 nm thick silicon nitride layer using plasma CVD, and a rectangular-shaped pattern is formed covering the tip of the emitter. The silicon nitride is etched in buffered HF. The substrate is then covered with a 1000 nm thick Al layer by e-beam evaporation, and the extraction

electrode and contacts to the emitter and cathode are formed. The sacrificial nitride layer is then etched in HF to separate the gate from the emitter. Figure 1 shows the SEM micrograph of the device.

The devices are tested in a vacuum chamber at a pressure of 6×10^{-6} torr by mounting the entire substrate on a small platform and inserting it into the chamber. Contacts to the terminals are made with tungsten probes mounted on Alessi XYZ manipulators. These manipulators are part of the assembly that goes into the chamber. After testing a device, the chamber is back-filled to atmospheric pressure. The probes are then repositioned to an adjacent device, and the chamber is evacuated again. This mode of testing avoids time-consuming packaging and wire bonding of individual devices.

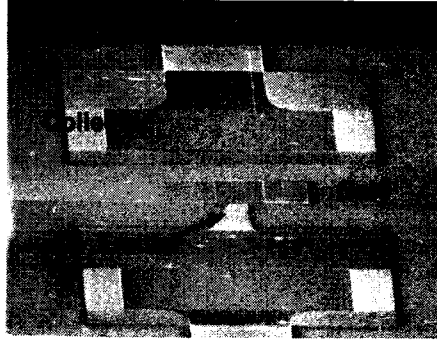


Figure 1 SEM micrograph of a lateral vacuum triode.

Figure 2 shows the collector current as a function of collector voltage for two different gate voltages for the device in Figure 1. At a collector current of 5 nA, the static gain of this device is approximately 3, and the transconductance at $V_c = 350$ V is approximately 6×10^{-10} S. For comparison, we tested a commercial 6AN8A vacuum triode and obtained a gain of approximately 20 and a transconductance of 5×10^{-3} S. Considering that the miniaturized vacuum triode can be encapsulated into a space of $\sim 1 \times 10^{-8}$ cm³ ($50 \times 50 \times 3$ μ m³) using proven micromachining techniques (Guckel, et al 1985) and that the 6AN8A utilizes a space of ~ 10 cm³, the transconductance per unit volume of the microdevice is larger by two orders of magnitude.

The gate current for the 330 V curve in Figure 2 ranged from 15 to 18 nA and that of the 335 V curve from 24 to 30 nA during the measurement. These values, combined with the low collector currents and high operating voltage, are not acceptable for commercial applications.

Several factors can contribute to this poor performance. The high gate current could be caused by the relatively large overlap between emitter and gate, and the high operating voltage by a large barrier height and a small field enhancement factor near the tip.

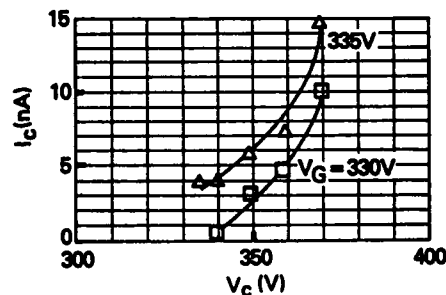


Figure 2 Collector current versus collector voltage of the device in Figure 1 for different gate voltages.

To improve device performance, a new mask set was designed allowing for the fabrication of sharper tips and smaller gate-to-emitter overlaps. To investigate the effect of barrier height, emitters will be fabricated from different materials.

3. IMPROVED DEVICES

To reduce the gate-to-emitter overlap, the gate is positioned at the tip of the emitter and extends away from the emitter and not toward it, as is the case in Figure 1. Figure 3 shows two configurations incorporating this design. In Figure 3a, the gate is interrupted near the tip, whereas in Figure 3b, the gate is raised above the emitter using the sacrificial layer technique employed in Figure 1. Typical dimensions are 2 to 4 μm for the gate line widths and emitter-to-collector distances of 4 to 10 μm . The improved structures are fabricated on fused silica substrates. This eliminates potential ionic currents in the glass substrates under the influence of large electric fields.

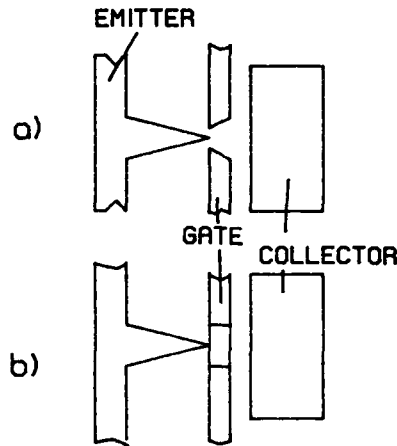


Figure 3 Lateral triode structures with, a) a split gate and, b) a continuous, raised gate.

To form sharp tips with reproducible tip radii, a two-exposure technique is used. A tip similar to Figure 1 is fabricated using standard lithographical techniques. This is shown as "initial exposure" in Figure 4. A second layer of photoresist is applied, and the same mask is used, but slightly offset to define the final shape. The tip is thus formed by two intersecting lines and is independent of the initial radius of the mask and the processes used to transform the image onto the substrate. By using this method, tip radii of less than 30 nm were achieved in NiCr and Mo, with film thicknesses ranging from 40 to 80 nm.

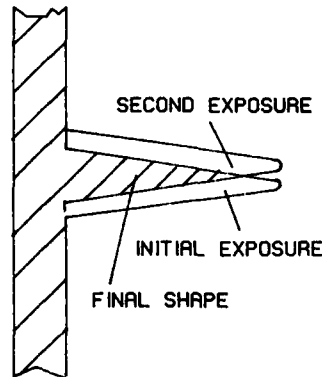


Figure 4 Two-exposure technique for tip formation.

Prior to completing the devices as shown in Figure 3, a 150 nm thick layer is removed from the substrate by isotropic etching (buffered HF for fused silica). This slight underetching results in a free-standing emitter

tip, thus ensuring ballistic transport of the electrons along their journey to the collector.

Devices corresponding to Figure 3a are completed with an additional photolithographic process to form the gate and the collector. Devices corresponding to Figure 3b are completed with two processing steps--one for the sacrificial layer formation and one to define the gate and the collector. Figure 5 shows the SEM micrograph of a finished device according to Figure 3b. The emitter consists of 60 nm of NiCr that is underetched by 150 nm. The gate and the collector are formed of 1000 nm thick Al. The emitter can be contacted by two pads allowing for heating the tip to investigate thermally assisted field emission and/or tip sharpening at elevated temperatures under the influence of an electric field.

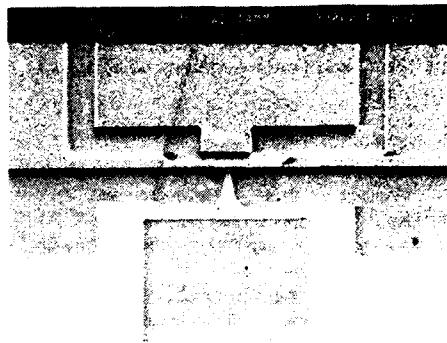


Figure 5 SEM micrograph of an improved triode structure according to Figure 3b.

An improved test apparatus is under construction to test these devices. Initial testing (Figure 2) was performed at a base pressure of $4-9 \times 10^{-6}$ torr on non-baked structures. This can give rise to premature arcing breakdowns prior to the onset of Fowler-Nordheim emission and to noisy currents (Spindt, private communications). With the new apparatus, devices can be UV baked and tested at pressures approaching 1×10^{-9} torr.

ACKNOWLEDGEMENTS

Thanks go to M Roth and J Pogemiller of Amoco for layout, processing and testing of the devices, and for designing the new test apparatus. Valuable discussions with Messrs Spindt (SRI) and Gray (NRL) on specific device aspects and on general issues concerning vacuum microelectronics are highly appreciated.

Guckel H, Burns D W, Busta H H and Detry J F 1985 *Transducers '85*, Digest of Technical Papers, IEEE Catalog Number 85CH2127-9, p 182

Spindt C A 1983 *Applications of Surface Science* 16, p 268

A new 8-inch ECR source for dry etching processes and CVD applications

K. Matl, K.-H. Kretschmer, I. Kessler, W. Katschner
Leibold AG, Siemensstraße 100, 8755 Alzenau, FRG

Abstract:

A new 8-Inch-ECR-source has been designed by LEYBOLD for semiconductor technology. The source operates in the "down-stream" mode for isotropic etching. Anisotropic etch profiles are obtained by ion beam etching with grid extraction of ions or, alternatively, ion extraction by an additionally applied RF-power at the wafer table. The capability of the LH-ECR-source is demonstrated by etching of polysilicon and contact holes in PSG or SiO₂ with fluorine based gases.

General description of the LH-ECR-source

The further development in semiconductor technology toward smaller dimensions and higher integration densities calls for low-energy and high-power plasma sources in etching and deposition as well. A new ECR-plasma-source developed by LEYBOLD may fulfill the necessary requirements for future 200 mm wafer processing.

The LH-ECR-source has been designed for installation in single wafer etching systems. High flexibility and performance data are achieved by the possibility of operation of the source with reactive gases, separation between the regimes where the plasma is induced and where the wafer is treated and by the use of process compatible materials in the plasma chamber (Fig. 1). Attention is also paid in the construction to a compact source design with a source diameter and height of nearly 500 mm for compatibility with semiconductor production lines. Special emphasis has been given to minimize particle generation. Since the source is designed for the etching of up to 200 mm wafers it is necessary to maintain a homogeneous plasma over a large area. This has been achieved through circular symmetry in the construction of the source as well as the microwave transformation via a horn-shaped radiator. The plasma generation is achieved by the resonant heating of electrons with microwave radiation (2.45 GHz) via electron cyclotron resonance.

The magnetic field needed for this purpose (875 G) is created by two rings of Co-Sm permanent magnets. The area, where the resonance condition is fulfilled is located at

the edge of the usable plasma diameter for improvement of plasma homogeneity. Also in this region the coupled E_{01} -wave has a maximum of field strength for optimum energy transfer from the microwave to the plasma. Long term operation of this source shows high mechanical and thermal stability.

The source can be used in several operational modes. In the case of "down-stream" etching the radicals generated in the plasma diffuse to the wafer. The energy of these particles is probably less than 20 eV (Matsuoka et al 1988). For anisotropic etch profiles an additional plasma sheath near the wafer surface is applied by a RF-generator (13,56 MHz) connect to the wafer table. This creates a DC-bias-voltage which accelerates the ions towards the wafer.

Further, one can extract an ion beam from the source with the aid of up to three grids. The usage of three grid extraction optics enables one to get high ion currents at relatively low ion energies due to acceleration - deceleration - operation of the grids and an independent selection of ion beam current and energy (Aston et al 1979).

In comparison to conventional parallel plate etchers, the source based etching has the advantage that the ion energy can be adjusted either by the additionally applied DC-bias or by the grid extraction voltage, independent of the amount of the microwave power, which generates the necessary ions.

Process developments and measurements

Process development to date has concentrated on etching of polysilicon, PSG and SiO_2 using gases of different chemical compositions based on fluorine. Figure 2 shows a SEM-picture from isotropic etching with SF_6 -gas of P-polysilicon on SiO_2 , masked with photoresist. It demonstrates the high selectivity of isotropic etching to photoresist and SiO_2 shown via a 600 % overetching. No damage of the surface of photoresist and SiO_2 during the etch process is visible showing that the energy of the etching particles is low.

Useful etch rates up to 400 nm/min with SF_6 can be obtained with a very low gas flow of only 3 sccm. These described etch characteristics which cannot be obtained by conventional RF-etch systems (Lee et al 1986) are explained by firstly the different fragmentation mechanism in the ECR-microwave plasma and secondly the high fragmentation capability of the LH-ECR-source. This is even supported by etch rates of P-polysilicon of 1 $\mu\text{m}/\text{min}$ with CF_4/O_2 gases.

In the case of contact hole etching of PSG and SiO_2 with CF_4/O_2 -gases the combination of an isotropic and following anisotropic etch step would be advantageous to reach the required different slopes of the contact hole. Figure 3 shows the isotropic etch step of PSG with an aspect ratio

of nearly 1:1, which demonstrates the fully isotropic behaviour of this etch mode. Therefore the LH-ECR-source operates in the "down-stream" mode, where no ions are extracted towards the wafer. Applying additional RF-power at the wafer table fully anisotropic etch profiles are given. Figure 4 demonstrates this anisotropic etch step on PSG. In both cases of isotropic as well as anisotropic etching the etch rates are 40 nm/min. The process pressure for isotropic etching with a relatively small number of ions is 10^{-1} mbar, whereas for anisotropic etching a lower pressure of $5 \cdot 10^{-3}$ mbar is accompanied by a higher ratio of ions to neutral radicals.

Conclusion

The results achieved show that the LH-ECR-source is a powerful tool, designed for 200 mm single wafer processing with superior attributes in comparison to conventional parallel plate etchers. The high performance data were obtained by circularly symmetrical construction of the source and the microwave coupling into the plasma. At the same time compact dimensions allow the application of the source on small footprints in a semiconductor production environment. The process developments show in the case of polysilicon isotropic etch rates in the range of 1 $\mu\text{m}/\text{min}$ with a very high selectivity to underlying SiO_2 . The application potential using the LH-ECR-source was demonstrated by fully isotropic as well as anisotropic etch processes on PSG and SiO_2 , suitable for contact hole processing. Initial results show that the LH-ECR-source may be the base for future etching- and CVD-equipment for sub-micron technology.

References:

- Aston G., Kaufmann H.,
1979, AIAA Journal,
Vol.17, No.1, pp 64-70
Lee Y, Chen M 1986,
J. Vac. Sci. Techn.
B4 (2) p 468
Matsuoka M, Ono K, 1988,
J. Vac. Sci. Techn.
A6 (1) pp 25-29

Acknowledgement:

This work was supported by the BMFT.

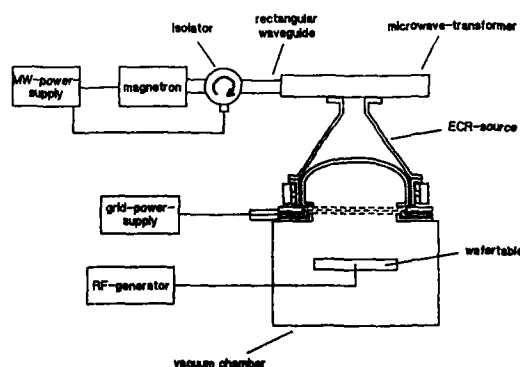


Fig. 1 Basic design of the LH-ECR-etcher



Fig. 2 Isotropic etching of P-polysilicon on SiO₂-substrate with SF₆-gas

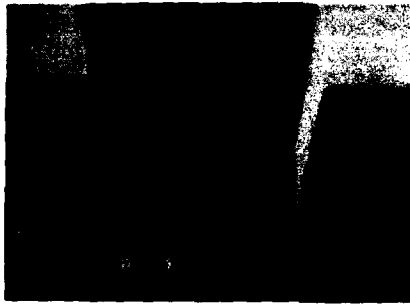


Fig. 3 Isotropic etching of PSG with CF₄/O₂-gas

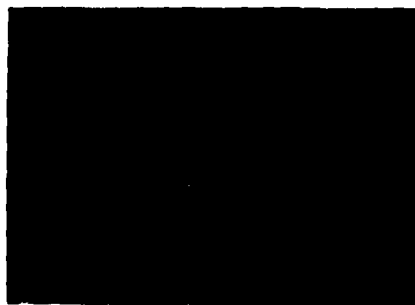


Fig. 4 Anisotropic etching of PSG with CF₄/O₂ gas

Control of silicon field emitter shape with isotropically etched oxide masks

John B. Warren

Brookhaven National Laboratory, Upton, New York 11973, USA

ABSTRACT: Precise control of field emitter diameter and tip radius in silicon was achieved by carefully controlling the shape of the oxide mask used to protect the emitter column during reactive ion etching. By following an anisotropic reactive ion etching step with an isotropic chemical etch, oxide masks with a concave wall curvature and a diameter of 1 to 2 μm can be formed. Controlled attack of the concave oxide mask during reactive ion etching form a silicon emitter column with tapered sides and a tip with a sub-micron radius of curvature.

1. INTRODUCTION

Precise control of emitter tip shape is important for any device using the principle of field emission. The tip radius must be reduced to a sub-micron value to maximize field strength and the uniformity of the tip geometry must be maintained within well defined limits if electron emission is to be held constant from emitters in a multi-element array. Spindt (1976), for example, has shown that changing the field of an individual emitter by 20% may change the electron emission by as much as a factor of ten.

Most recent attempts to construct field emitters that satisfy these dimensional constraints are based on the work of Spindt (1976), that uses electron beam evaporation to deposit a molybdenum emitter cone through an SiO_2 cavity, or Gray (1987), that uses orientation-dependent chemical etching to form a pyramidal emitter from $\langle 001 \rangle$ silicon. Both these approaches require several process steps and form emitter tips from specific materials. Reactive ion etching offers the possibility of fabricating field emitters from a wide range of metals and semiconductors with geometries comparable to these methods. For arrays of emitters with heights greater than 10 μm required for experiments in photo-enhanced field emission (Fisher 1988), this method may be the only possible choice. While this work describes only silicon emitter fabrication, the method can be extended to metals as well.

2. EXPERIMENTAL RESULTS AND DISCUSSION

A Plasma Lab 80 reactive ion etcher manufactured by Plasma Technology Inc., Yatton, England was used for emitter fabrication. The reactive ion etching process uses a 13.56 MHz rf generator to create a plasma in a vacuum of a few mtorr between two parallel electrodes with different diameters. Silicon wafers to be etched are placed on the smaller, powered, electrode that becomes negatively charged with respect to the reactive ions in the plasma. Both fluorine and chlorine-based plasmas have been used extensively for etching silicon, but the chlorine processes generally offer more anisotropy at the expense of a slower etch rate (Herb 1987).

For these experiments, a chlorine process with a Cl_2/BCl_3 etching gas with a ratio of 6:1 was used for reactive ion etching of $\langle 001 \rangle$ 5 ohm cm silicon wafers. The primary reaction product, SiCl_4 , has a reasonably high vapor pressure at ambient temperatures and is easily removed by the pumping system. SiO_2 is not attacked by pure chlorine plasmas and is used as a masking material to protect the underlying silicon substrate. At 15 mtorr, the process is quite anisotropic and trenches 20 μm in depth with almost vertical walls can be etched with a SiO_2 mask of 1 μm in thickness. BCl_3 is used to remove small deposits of SiO_2 present on the unetched silicon surface. Left undisturbed, these sub-micron SiO_2 particles act as *micro-masks* that protect the underlying silicon during the etching process to form a filamentary microstructure that appears black to the unaided eye and grass-like in the scanning electron microscope. Since the BCl_3 attacks the more massive SiO_2 masks as well, the maximum etch depth is determined by the relative rates of attack of Cl_2/BCl_3 of silicon versus that of the protective SiO_2 mask.

The different rates of attack on the protective oxide layers and the silicon by Cl_2/BCl_3 are used to advantage in the fabrication of emitter arrays. A disc-shaped oxide mask of appropriate diameter, thickness, and shape can be used to form a silicon emitter with a relatively broad base that gradually tapers to a sharp tip of sub-micron radius. Such a structure maintains the high electric field in the tip vicinity and is still structurally robust.

The effect of oxide mask geometry on the emitter column shape is shown in Fig. 1. An anisotropically etched oxide mask with nearly vertical walls is attacked at approximately equal rates on its upper face and its walls by the BCl_3 component of the etching gas. For anisotropic conditions during the silicon etch, such a mask will result in a silicon column with a wall angle of constant slope. After the oxide mask is finally destroyed, the top of the silicon column is exposed but is too broad to form a sharp tip required for field emission. An attempt to reduce the tip radius by reducing the emitter column diameter does not produce the desired geometry because the column becomes so slender that it fractures in midsection before the oxide has completely disappeared. In Fig. 2 the oxide mask is isotropically etched to fabricate a tapered concave wall profile. At the beginning of the silicon etching step, the sharply flared portion at the bottom of the mask protects a silicon column of equal diameter. This flared portion of the oxide is destroyed relatively early in the etching process, and a greatly reduced silicon diameter is protected by the remaining oxide. As a result, a silicon emitter column is formed that has a relatively broad base and tapers sharply to a point with the desired sub-micron radius.

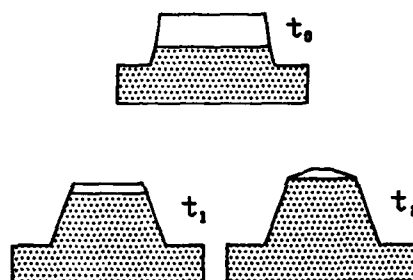


Figure 1. Evolution of silicon column shape with increasing time, t . Oxide mask has walls of constant slope.

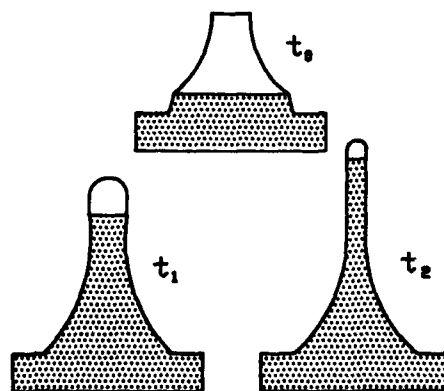


Figure 2. Evolution of silicon column protected by oxide mask with concave wall curvature.

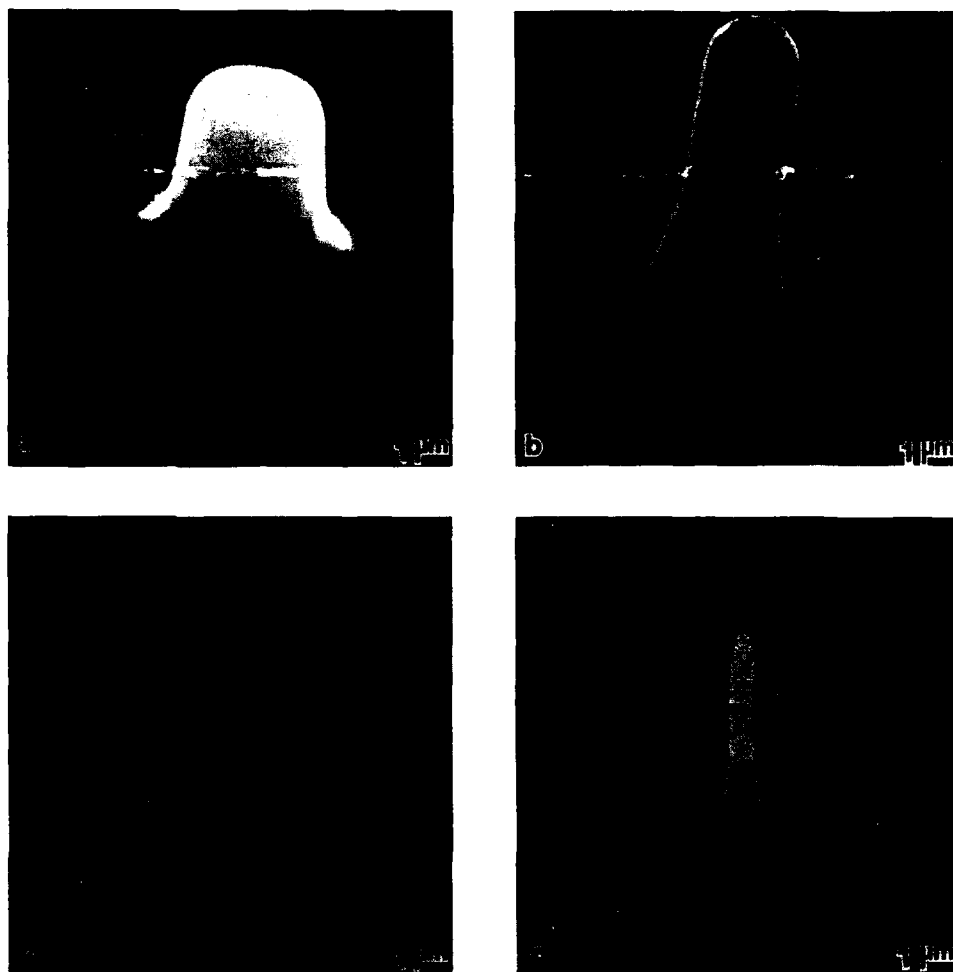


Figure 3. Silicon emitter columns formed from a SiO_2 masks with concave sidewalls. Figure 3a shows the original $2.0 \mu\text{m}$ diameter SiO_2 mask; Fig. 3b, 3c, and 3d show the silicon emitter columns that result after etching with the conditions tabulated below. The SiO_2 masks are still in place in Figs. 3b, 3c, and 3d.

Process Parameters				
Material	Etchant	Time (min)	Power (W/cm^2)	Pressure (mtorr)
SiO_2	CHF_3	30	0.82	15
	BHF	4	--	--
Si	6:1 Cl_2/BCl_3	80	0.33	15

A scanning electron micrograph of an oxide mask with the required profile and physical dimensions is shown in Fig. 3a. For mask diameters of 1 to 2 μm , a one-step etch using buffered hydrofluoric acid (BHF) forms the correct sidewall profile only for oxides less than 0.5 μm in thickness. Masks of this thickness can be used to form emitter columns of not more than 4 to 5 μm in height before the oxide is consumed. For oxide masks with a thickness of 1.0 μm or greater, it was necessary to use a two-step etching procedure for oxide patterning. First, a reactive ion etch step in CHF_3 at 15 mtorr is used to remove 0.5 μm of SiO_2 with an almost vertical sidewall. A second etch in BHF for 4 min removes the remaining 0.5 μm of oxide to form the correct concave wall profile.

Scanning electron micrographs of the silicon emitter columns formed using concave oxide masks are shown in Fig. 3b, 3c, and 3d. All three emitters were etched for 80 min but were formed from oxide masks with diameters of 2.0, 1.5, and 1.0 μm , respectively. The 1.0 μm diameter mask has almost been completely destroyed after this etch but the 1.5 and 2.0 μm masks are still intact. The height of the tapered column is controlled by both the mask thickness and the diameter of the flared portion of the mask. Emitter columns much higher than the one shown in Fig. 3b or 3c could be etched using the 1.5 or 2.0 μm diameter masks by extending the etching period. Once the oxide mask has been destroyed, etching should be terminated immediately to avoid attacking the sharp silicon tip and increasing its radius of curvature.

Further shaping of the emitter can be accomplished with the thermal oxidation methods of Marcus (1982). Oxidation of the silicon at temperatures from 900 to 1100 $^{\circ}\text{C}$ is used to form a conformal SiO_2 layer over the emitter surface. By stoichiometry, it can be seen that the formation of an SiO_2 layer consumes a silicon layer only a third the thickness of the oxide coating so very thin layers of silicon can be removed under well controlled conditions. Kao (1987) has shown that the thickness of the oxide layer is a function of the radius of curvature of the underlying silicon surface. Sharply curved regions such as the emitter tip will tend to grow a thinner oxide layer than the base of the column and lose less silicon. Thus, a controlled oxidation step, followed by removal of the oxide in BHF, offers a means of reducing the column diameter while effecting only minimal changes in the emitter tip.

3. REFERENCES

- Fisher J, Srinivasan-Rao T and Tsang T (to be published in *Proc. Switched Power Workshop, Shelter Island, NY, October 16-21, 1988*).
Gray H F and Campisi G R 1987 *Mat. Res. Symp. Proc.* 76 25
Herb G K, Rieger D G and Shields K 1987 *Sol. St. Tech.* 30 109
Kao D B, McVittie J P, Nix W D, and Saraswat K C 1987 *Trans. Elec. Dev.* ED-34 1008
Marcus R B and Sheng T T 1982 *J. Elec. Chem. Soc.* 6 1278
Spindt C A, Brodie I, Humphrey L, and Westerberg E R 1976 *J. Appl. Phys.* 47 5248

This research was supported by the U. S. Department of Energy under Contract No. DE-AC02-76CH00016.

Back-biased junction cold cathodes: history and state of the art

G.G.P. van Gorkom and A.M.E. Hoeberechts

Philips Research Laboratories
P.O. Box 80000
5600 JA Eindhoven
The Netherlands

Abstract: The history of back-biased junction cold cathodes goes back to 1957 with the invention by Burton of an electron emitting p-n junction in silicon. Thereafter a lot of research was done in this area in the hope of developing a useful cold cathode. In the 1970's electron injection into SiO₂ layers was investigated extensively. This has led to a revival of the reverse biased cold cathodes but now manufactured using modern Si technology. Efficient emitters have been demonstrated capable of delivering current densities of up to about 8000 A/cm² into a vacuum.

1. INTRODUCTION

In the first part of this paper a review of the history of back-biased junction cold cathodes will be given. We do not aim at completeness but merely at describing some of the more important papers that have appeared in this research area. Hereafter, the closely related phenomenon of electron injection into SiO₂ layers will be discussed briefly.

The second part deals with the present state of the art, including a description of advantages and disadvantages and of prospects for reverse biased cold cathodes.

2. HISTORY

2.1 The invention of the back-biased cold cathode

The first paper describing electron emission from avalanche breakdown in p-n junctions was by Burton (1957). He made a p-n junction in silicon that intersected the surface. At first no emission was detected while biasing the diode in the reverse direction, but after cesiating the surface electron emission was observed for the first time. The maximum pulsed emission current was 50 μ A, the emission efficiency η

$$\eta = \frac{i_{vac}}{i_d + i_{vac}} \quad (1)$$

was found to be $5 \cdot 10^{-3}$ at maximum.

Burton also observed white light emission from the line where the junction intersected the surface. Assuming that the electron emission came from the same area as where the light originated, he estimated that the emission current density was greater than 0.05 A/cm^2 . Emission instabilities were observed. This was thought to be due to Cs drift over the surface.

2.2 The early work until 1963

Following the discovery by Burton, a lot of work was done to look into the characteristics of this new phenomenon, see the paper by Hodgkinson (1962) and references cited there. Besides silicon also SiC (e.g. Patrick and Choyke 1959) and germanium (e.g. Simon and Spicer 1960, Pozhela and Shilal'nikas 1962) were investigated. The interest was in straightforward electron emission as well as in field assisted photo-emission.

Most of the work done was on p-n junctions intersecting the surface. There are, however, several problems associated with this configuration as will be discussed later. The paper to be discussed next avoids these difficulties.

2.3 The paper by D.J.Bartelink, J.L.Moll and N.I.Meyer

A very important paper by Bartelink et.al. (1963) dealt with hot electron transport in Si and with electron emission from p-n junctions parallel to the surface. They produced a shallow n++ layer by diffusing phosphorus into $0.02 \text{ } \Omega\text{cm}$ p-type silicon such that the junction was at a depth of 130 nm. The thickness L of this n++ layer was subsequently reduced step by step using the boiling water-HF method. Underway the electron emission was repeatedly measured. It was found that the emitted current (at constant diode current) depended exponentially on L :

$$i_{\text{vac}} = A \exp(-L/L_0) \quad (2)$$

where A is a constant, and L_0 was found to be $L_0 = 4.5 \text{ nm}$. Also energy distributions were measured both in avalanche breakdown and using photo excitation. In the former case an electron temperature of 0.5 eV was observed.

Bartelink et.al.(1963) analyzed their results in terms of the Boltzmann transport equation. The result was:

$$\begin{aligned} l_r &= 6.0 \text{ nm} \\ l_i &= 19.0 \text{ nm} \end{aligned} \quad (3)$$

where l_r is the mean free path of the hot electrons due to phonon scattering and l_i that due to impact ionization. This is an important result because it showed that the ionization rate descriptions by both Wolff (1954) and Shockley (1961) were incorrect, the truth being somewhere in the middle. Hence this paper contributed much to the understanding of avalanche breakdown in silicon and of the phenomenon of hot electron emission from Si into vacuum.

2.4 The period 1963-1970 and the work at GEC

Not much happened during the second half of the 1960's in the area of back-biased cold cathodes. Noteworthy is a communication by Meyer and Palmgren Jensen (1966). They produced the shallow n⁺ layer using ion implantation. The efficiencies found were very low, however.

Starting in 1969, researchers at the Hirst Research Centre of GEC investigated SiC reverse biased cold cathodes (Brander and Todkill, 1969). In the following years several papers on this subject were published (Bellau et.al. 1971, Chamberlain and Lamb 1972, Widdowson and Rose 1973). In all cases p-n junctions intersecting the surface were produced by ultrasonically cutting through the top n layer. Such mesa structures showed peripheral emission.

As was discussed extensively by the GEC group, SiC cold cathodes of this type need an activation procedure before sufficient emission current can be drawn. This procedure involves heating the emitter to 600 - 700 C, by passing current through the diode either in the forward or in the reverse direction. The raise in efficiency to about $1 \cdot 10^{-4}$ is accompanied by a distinct softening of the I-V characteristic of the device. Widdowson and Rose (1973) have developed the following interpretation for this. The electrons are not emitted directly out of the SiC into the vacuum but instead into the thin 'natural' oxide layer, heavily doped with carbon, on top of it. In this oxide-layer the electrons are accelerated by the strong electric field (due to the voltage applied to the diode) and as the oxide has an electron-affinity of only 0.9 eV, rather efficient electron emission into the vacuum occurs. The heating during the activation is believed to produce structural changes in the oxide so that the carbon impurities become active as donors, leading to an increased conductivity of the oxide layer. However, we have observed activation in pure Si junctions intersecting the surface too, see sect.4.3. Hence in our opinion the role of C in this process is questionable. The whole activation process is similar to the forming process of MIM devices (see e.g. Yankelevitch 1979) where increased conductivity is also enforced by heating, with no carbon being present. It seems likely that the activation procedure of the cold cathodes is identical to the, not yet fully understood, MIM forming process.

The SiC cathodes have been used in experimental CRTs and mass-spectrometers (Bellau et.al. 1971), but as far as we know no such devices have become commercially available.

3. INJECTION OF HOT ELECTRONS INTO SiO₂

Since the early 1970's (Nicollian et.al. 1971) an enormous amount of work has been done all over the world on the subject of hot electron injection into SiO₂ layers. Apart from being an interesting phenomenon there are two main reasons for this:

- 1) injection of charge carriers (both electrons and holes) into SiO₂ is detrimental for normal device operation, e.g. causes threshold voltage shifts in MOSFET transistors, hence it constitutes a reliability problem

- 2) it can be used for non-volatile memories, such as EPROM (FAMOS) devices, where a floating gate is charged by the injected current.

Upon scaling down transistors to sub-micron sizes, the reliability problem becomes ever greater. Hence, even at present many investigations are going on to study this phenomenon. It is clearly outside the scope of this paper to present a review of this vast area of research. Let us confine ourselves to discussing a few papers which are relevant to the cold cathode application.

3.1 Injection into SiO₂ with high current densities

The paper of Verwey and de Maagt (1974) describes a p-n junction intersecting the Si - SiO₂ interface. An oxide layer and a gate are present above this interface. By applying a positive voltage to the gate the depletion layer is narrowed at the interface, hence avalanche breakdown occurs first at that position. Electrons and holes are created in the avalanche breakdown and gain energy from the electric field. Some of the electrons become hot enough to be injected into the SiO₂ layer. Most of these travel in the conduction band of SiO₂ towards the gate and are measured as a gate current. The remaining ones are trapped in the oxide, resulting in threshold voltage shifts. An important result of this paper was the fact that the injected current density was considerable: up to about 10 A/cm² was measured.

3.2 The work at IBM by Ning, Osburn and Yu

Not surprisingly, a lot of work in this area has been done at the IBM Thomas J. Watson Research Centre. An important paper by Ning et.al. (1977) describes a quantitative determination of electron injection probabilities from Si into SiO₂. The devices used were n-channel field effect transistors with a special reentrant geometry such that absolute emission efficiencies were measured. Electron-hole pairs were generated in the substrate by incident light using a suitable light source. The electrons gained energy from the electric field in the depletion layer such that some of them were injected into the SiO₂ and collected by the gate.

It was found that the experimental results could be very well described by

$$P = A \exp(-d/l_e) \quad (4)$$

where P is the probability of injection, which is identical to the efficiency as defined in eq.(1), $A = 2.9$ is a constant and l_e is a fitting parameter found to be $l_e = 9.1$ nm at room temperature. The lucky electron model (Verwey et.al. 1975) leads to eq.(4) with l_e then being the effective mean free path. Although l_e is only indirectly connected to the true mean free paths, hence has no real physical significance, eq.(4) is very useful for modeling. With proper adjustments, it can also be used in the case of electron emission into vacuum (van Gorkom and Hoeberechts, 1986b).

4. THE REVIVAL OF THE AVALANCHE COLD CATHODE

4.1 Introduction

The 'success' of the injection of hot electrons into SiO_2 led to a reinvestigation of the possibilities and properties of back-biased p-n junction cold cathodes (p-n emitters for short) at the Philips Research Laboratories by the authors and by others. The idea was that using modern technology the performance of reverse biased cold cathodes could be improved such that practical application would become possible.

One of the advantages of the better technology is that microplasma free avalanche breakdown is rather easily obtained. Almost all earlier p-n junction cold cathodes suffered from poor reproducibility due to the occurrence of micro-plasmas, which are rather unpredictable and noisy by nature. Indeed, all our diodes proved to be free of microplasmas as was checked by verifying that homogeneous white light was emitted during breakdown.

Another important improvement is the following. In the early days a very thin n^+ top layer could not be made easily. Hence mostly p-n junctions intersecting the surface were used, produced e.g. by ultrasonically cutting through the n^+ layer. There are, however, several problems associated with this structure:

- 1) one has to assure somehow that the breakdown occurs (mainly) at the surface
- 2) the average emitted current density is low
- 3) there is a strong electric field parallel to the surface, leading to drift of adsorbates like cesium in this field and hence to emission instabilities (Burton 1957, van Gorkom et.al. 1986c)
- 4) the potential varies from the p to the n area, thus some broadening of the emitted energy distribution will result, which has indeed been observed (van Gorkom and Hoeberechts 1980)
- 5) the quantitative interpretation of the results of the measurements in terms of hot electron transport in the semiconductor is extremely difficult, if not impossible
- 6) the mesa shape of the cathode is unfortunate from an electron-optical point of view, i.e. it is difficult to form a good quality electron beam starting from such a cathode.

Using low energy ion implantation it is now straightforward to produce thin n^+ layers and hence very shallow p-n junctions parallel to the surface. As these can be made micron-sized, large emission current densities are possible as will be discussed later on. Most of our experiments were done using emitters with the junction parallel to the surface.

During the last 10 years or so we have published several papers on the subject (van Gorkom and Hoeberechts 1980, 1984, 1986a, 1986b, 1987a, 1987b, 1988; Hoeberechts and van Gorkom 1986). In the following we will give a brief review of this work.

4.2 Device geometry

A schematic drawing of our p-n emitters is given in Figure 1.

The substrate is heavily doped p type. On top of that we have a lightly doped p type epitaxial layer in which the active area is defined by implanting boron using a suitable masking technique. This produces a p⁺ area where avalanche breakdown occurs first. The very thin n⁺ channel is made by implanting 5 or 10 kV arsenic ions followed by a low temperature anneal. On top of the diode an oxide layer is present covered by a conducting layer (gate), with a hole above the active area.

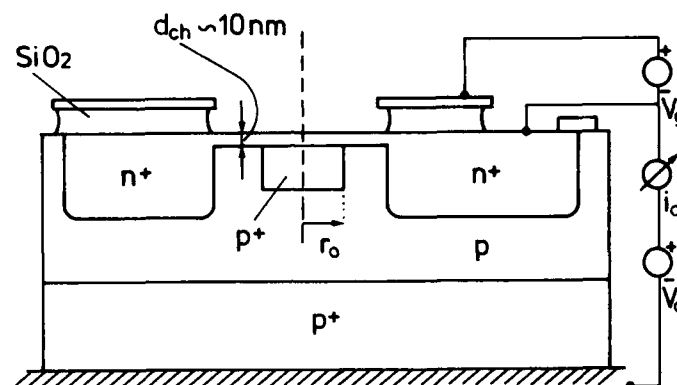


Figure 1. Geometry of the reverse biased cold cathode.

One of the big advantages of silicon cold cathodes is the fact that the shape of the active electron emitting area can be chosen more or less at will. We already made several shapes: circular emitters with diameters between 1 and 8 μm , line emitters with lengths of 200 μm and annular emitters with diameters ranging from 30 to 600 μm . In the latter two cases, the width of the active area was about 3 μm .

Also the shape of the gate electrode can be chosen to suit particular wishes. For instance, we made circular segmented gates, which served as integrated beam shapers. Interestingly, integrated electron lenses are possible too.

Finally, multi-emitter cathodes have been produced with up to 100 emitters on a single chip, the pitch being 10 μm .

4.3 Emission efficiency and electron temperature

These two properties are not dependent upon the (lateral) geometry of the diodes but they do depend on the doping concentrations and doping profiles. Furthermore the efficiency depends strongly on the work function of the surface.

Qualitatively, this dependence is easily understood. Doping levels

and profiles determine the electric field within the depletion layer and hence the rate at which the electrons are created and pick up energy from this field. The combined effect of this energy gain and of energy losses due to e.g. phonon creation together with momentum scattering determine an energy and an angular distribution of the hot electrons. The part of the distribution that is emitted into the vacuum has been measured. The angular distribution was found to be nearly a cosine distribution. Energy distributions were measured using a spherical retarding field analyzer (van Gorkom and Hoeberechts 1980). For bare Si emitters a near Maxwellian distribution was found, enabling the determination of an electron temperature. This temperature was dependent upon the maximum electric field within the diode, as expected, see Figure 2.

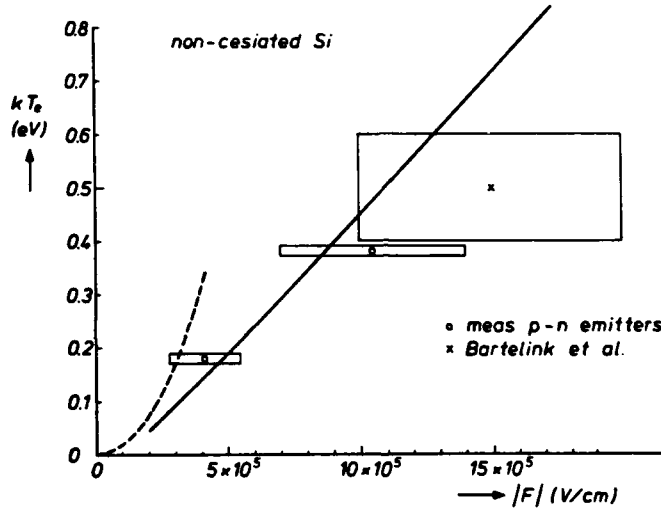


Figure 2. Electron temperature as a function of the electric field in the depletion layer. See the paper by van Gorkom and Hoeberechts (1986b) for more details.

Upon lowering the work function by adsorption of cesium onto the surface, the energy distributions change. The overall shape is still not far from a Maxwell distribution (with an effective electron temperature of 0.49 eV) but with structure present, see Figure 3. This structure is ascribed to the presence of peaks in the density of states of Si.

It has been shown (v.Gorkom and Hoeberechts, 1986b) that for a Maxwellian distribution it is to be expected that the efficiency will depend on the work function ϕ as:

$$\eta = C \exp(-\phi/kT_e) \quad (5)$$

where C is a constant (still depending on doping profiles and the exact state of the surface). Indeed, experimentally the following relationship was measured:

$$\eta = 0.6 \exp(-\phi/0.41) \quad (6)$$

in accordance with expectations. The pre-exponential factor was found to be very dependent on the presence of contaminants on the surface. For clean surfaces, i.e. no elements other than cesium present, this factor can be up to 10 times higher (van der Heide 1989). Hence surface cleaning is very important. The efficiency of a clean surface on which a monolayer of pure Cs is adsorbed is as high as $8 \cdot 10^{-2}$.

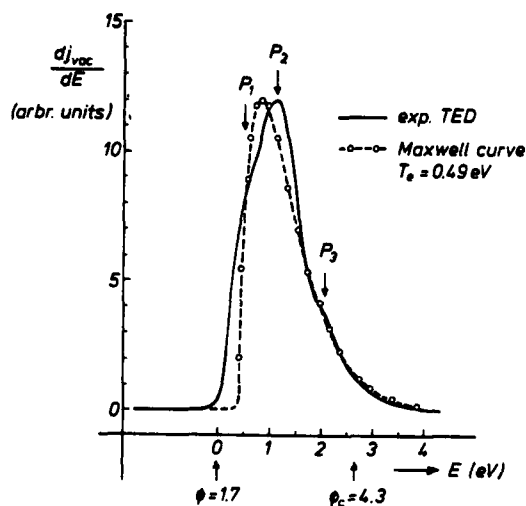


Figure 3. Energy distribution of a cesiated p-n emitter.

We would like to end this subsection with a remark concerning activation procedures. As was mentioned in sect. 2.4, mesa type SiC cold cathodes need a certain activation procedure. In the beginning of our investigations, we also made mesa structures in Si with the junction intersecting the surface. For such emitters an activation procedure similar to the one used for SiC (Bellau et al. 1971) could be applied, which resulted—as in the case of SiC—in a large increase in emission efficiency for bare Si cathodes: up to about $5 \cdot 10^{-5}$ was obtained. As for SiC, this was accompanied by a softening of the I-V characteristic of the device. Emitters with the junction parallel to the surface showed no response to this activation procedure.

4.4 Current density

The emitted current density j_{vac} follows from

$$j_{vac} = \eta j_{dd} \quad (7)$$

where j_{dd} is the current density in the avalanche breakdown, normal to the surface. Given a certain value of η , j_{vac} can be increased by increasing j_{dd} . But of course there are limits to

this, as was discussed before (van Gorkom and Hoeberechts 1986a). An important limit is posed by the occurrence of current crowding, because the non-emitted electrons have to be carried away in the very thin n^+ channel. Hence the smaller the emitter the higher the obtainable current density.

In practice it has been found that we can obtain for 1 μm diameter emitters a $j_{\text{vac}} = 1000 \text{ A/cm}^2$ for each percent efficiency. Up to 8000 A/cm^2 has been obtained. This is a favorable value compared with e.g. LaB_6 cathodes which can deliver up to $j_{\text{vac}} = 50 \text{ A/cm}^2$.

4.5. Switchability

As the size of the active area is usually small (a few microns) the junction capacitance is very small indeed, and as the series resistance of such diodes is of the order of 500 Ω an intrinsic RC time of a few picoseconds is calculated. In the case of larger diodes, e.g. ring shaped, the capacitance is of course larger, but the series resistance is lower. Thus also in the latter case very short RC times result. However, parasitic capacitances limit the fastest switching times to several nanoseconds at present. We expect that this can be reduced considerably.

Another important feature is the fact that for the very small emitters only a few Volts are needed to switch the emitters on/off, and for the large ones less than 1 Volt. These two features, very small RC times and low modulation voltage, mean that very fast devices are possible.

4.6. Lifetime

Because of the needed cesium monolayer coverage, emission stability is not easily obtained. During the course of our investigations we have found 3 major threats to the emission stability:

- 1) oxidizing gases: the pressure of O_2 , H_2O and CO_2 close to the emitter has to be smaller than about $1 \cdot 10^{-11}$ Torr, which is a heavy but not unattainable demand
- 2) ion bombardment: an ion trap is necessary
- 3) Cs desorption by out-going electrons: the surface has to be free of oxygen, hence thorough cleaning (van der Heide et.al. 1989b) is a must.

If the proper precautions are taken then very stable emission is possible. In sealed-off tubes over 20000 hours has been obtained. In UHV systems the lifetime is less usually due to the higher pressure of CO_2 .

4.7. Applications

We have put our p-n emitters in a number of experimental devices, including oscilloscopes, TV picture tubes (van Gorkom and Hoeberechts 1987a) and electron microscopes. Although satisfactory operation was obtained in a number of cases, it has not yet been decided whether such devices will become commercially available.

4.8 Prospects

Having obtained efficiencies of up to about 8 %, we believe that we are close to the maximum possible with p-n emitters made of silicon. Still sticking to Si, better efficiencies and thus higher current densities can perhaps be obtained using p-i-n structures. Such investigations are underway and will be reported on at this conference (van der Heide et.al. 1989c).

Another possibility for improving the cathode is by using other semiconductors. As far as we know only GaAs is being tried (van Zutphen 1988, Miyawaki 1987). Results are awaited.

4.9 Theoretical situation

In addition to having possibilities of practical application, reverse biased junction cold cathodes are important for the understanding of avalanche breakdown and of hot electron transport in semiconductors, especially silicon. This holds true for both the experiments and the theory. Let us look at the theoretical situation and compare with the experimental results.

There are two main relevant theories. The first one to be discussed briefly is the theory of Bartelink et.al. (1963), which is based on the Boltzmann transport equation. This equation is solved under several assumptions in order to simplify the problem such that analytical solutions become possible. Some of these are:

- constant electric field in the depletion layer
- electron mean free paths independent of energy
- free electron gas approximation, i.e. no band structure taken into account

The result of the calculation is that the energy distribution has the Maxwellian shape with an electron temperature dependent a.o. on the electric field. This dependence is shown in Figure 2, the full curve. It can be concluded that this theory describes the experiments rather well: the measured energy distributions of bare emitters have approximately the Maxwellian shape and the calculated electron temperatures do not differ much from the measured ones.

Despite this success there is a need for a better theory with less, preferably no, a priori assumptions at all. Such a theory, or rather calculation method, was developed a number of years ago: the quantum Monte Carlo method, see e.g. Shichijo and Hess (1981), Tang and Hess (1983), Fischetti et.al. (1985). In this theory, the electrons are followed on their way to the surface, their paths being determined by the electric field and by scattering events.

The procedure is roughly as follows. Electrons are started with energy and \mathbf{k} vectors at the bottom of the conduction band. Due to the action of the electric field \mathbf{F} the \mathbf{k} vectors change according to

$$\frac{d\mathbf{k}}{dt} = \frac{e \mathbf{F}}{\hbar} \quad (8)$$

where \hbar is Planck's constant divided by 2π and e is the

elementary charge. After some time, depending on the scattering rate, the electron is scattered by e.g. a phonon resulting in a change in k and possibly in a (small) change in the energy E . The velocity follows from:

$$v = \frac{1}{\hbar} \frac{dE}{dk} \quad (9)$$

The electrons are followed in k space and by integrating the velocity also in the real space. Incorporation of electron-hole pair creation gives some problems. Nevertheless, considerable success was scored in describing avalanche breakdown in silicon and in GaAs (Shichijo and Hess 1981, Tang and Hess, 1983).

The Monte Carlo method can also be applied to back-biased cold cathodes. This involves an additional step in the calculation scheme. At the end of the 'normal' MC calculation the E, k values of all electrons at the surface are known. Emission into the vacuum occurs if $E \geq \phi$ and if (see e.g. van Gorkom and Hoeberechts, 1986b):

$$\hbar |k_t| \leq [2m (E - \phi)]^{1/2} \quad (10)$$

where k_t is the transverse part of k ; umklapp processes are neglected. The electron is emitted with kinetic energy $(E - \phi)$ at an angle α with the normal to the surface, given by (assuming lattice periodicity up to the very surface):

$$\sin \alpha = \frac{\hbar |k_t|}{[2m (E - \phi)]^{1/2}} \quad (11)$$

Hence, both the energy distribution and the angular distribution of the emitted electrons follow.

Higman et.al. (1989) performed MC calculations on back-biased cold cathodes of both Si and GaAs. Results are encouraging.

5. CONCLUSIONS

Reverse biased junction cold cathodes have been known for about 30 years. Early attempts to produce good quality cold cathodes failed, apparently because of problems with material purity and unfortunate geometry. Researchers at GEC came a long way using SiC but also in this case no product appeared on the market. After it was shown that hot electron injection into SiO_2 was possible with high current densities, the authors started a reinvestigation of the feasibility of cold cathodes based on silicon. Using modern technology, a great improvement in performance was possible such that efficient cathodes capable of delivering large current densities were developed. Because of the necessity of having a monolayer of cesium on the surface, it is difficult but not impossible to get good lifetimes. This difficulty has hampered practical application until now. Further developments in this field will be p-i-n structures and other materials like GaAs and AlGaAs.

REFERENCES

- Bartelink D J, Moll J L and Meyer N I 1963 Phys. Rev. 108 972
 Bellau R V, Chanter R A and Dargan C L 1971 J. Phys.D4, 2022
 Brander R W and Todkill A 1969 Mat. Res. Bull. 4 s303
 Burton J A 1957 Phys. Rev. 108 1342
 Chamberlain N G and Lamb D R 1972 Int. J. Electron. 32 565
 Fischetti M V, Di Maria D J, Brorson S D, Theis T N and
 Kirtley J R 1985 Phys. Rev. B31 8124
 Higman J M, Kim K, Hess K, van Zutphen T and Boots H M J
 1989 J. Appl. Phys. 65 1384
 Hodgkinson R J 1962 Sol. St. Electr. 5 269
 Hoeberechts A M E and van Gorkom G G P 1986 J. Vac. Sc.
 Techn. B4 105
 Meyer N I and Palmgren Jensen F 1966 J. Appl. Phys. 37 4296
 Miyawaki M 1987 European Patent Appl. 87111709.9
 Ning T H, Osburn C M and Yu H N 1977 J. Appl. Phys. 48 286
 Patrick L and Choyke W J 1959 Phys. Rev. Lett. 2 48
 Pozhela Yu K and Shilal'nikas V I 1962 Sov. Phys. Sol. St.
 4 1173
 Shichijo H and Hess K 1981 Phys. Rev. B23 4197
 Shockley W 1961 Sol. St. Electr. 2 35
 Simon R E and Spicer W J 1960 Phys. Rev. 119 621
 Tang J Y and Hess K 1983 J. Appl. Phys. 54 5139, 5145
 van der Heide P A M 1989a private communication
 van der Heide P A M, Baan Hofman M J and Ronde J 1989b
 J Vac. Sc. Techn. July / August, in press
 van der Heide P A M, van Gorkom G G P, Hoeberechts A M E
 van Gorkom A A and van de Walle G F A 1989c Proc. 2nd
 Int. Vac. Microelectronics Conf. Bath
 van Gorkom G G P and Hoeberechts A M E 1980 J. Appl. Phys.
 51 3780
 van Gorkom G G P and Hoeberechts A M E 1984 Philips J.
 Res. 39 51
 van Gorkom G G P and Hoeberechts A M E 1986a J. Vac. Sci.
 Technol. B4 108
 van Gorkom G G P and Hoeberechts A M E 1986b Philips J.
 Res. 41 343
 van Gorkom G G P, van Oostrom A, Crombeen J E and
 Hoeberechts A M E 1986c Appl. Phys. Lett. 49 507
 van Gorkom G G P and Hoeberechts A M E 1987a Philips
 Techn. Rev. 43 49
 van Gorkom G G P and Hoeberechts A M E 1987b J. Vac. Sci.
 Technol. A 5 1544
 van Gorkom G G P and Hoeberechts A M E 1988 paper
 presented at the 1st Int. Vac. Microelectronics Conf.
 Williamsburg
 van Zutphen T 1988 paper presented at the 1st Int. Vac.
 Microelectronics Conf. Williamsburg
 Verwey J F and de Maagt B J 1974 Sol. St. Electr. 17 963
 Verwey J F, Kramer R P and de Maagt B J 1975 J. Appl. Phys.
 46 2612
 Widdowson A E and Rose F W G 1973 J. Phys. C6 437
 Wolff P A 1954 Phys. Rev. 95 1415

Photoemission from back-biased Schottky diodes p-InP-Ag

A.L.Musatov, S.L.Filippov, V.L.Korotkikh

Institute of Radioengineering and Electronics Academy of Science, USSR,
 Moscow, 103907

ABSTRACT: The model of hot electron photoemission from back-biased Schottky diodes p-type semiconductor-metal, based on the ballistic transport of photoelectrons in the high electric field is described. The model was confirmed by experiments on the p-InP-Ag Schottky diodes. The mean free path of hot electron in Γ valley of InP conduction band was determined. It was shown, that in the electron energy range 0.9-1.9 eV mean free path does not depend on the energy and is equal to 130 ± 25 Å.

1. INTRODUCTION

Near the surface of back-biased Schottky diodes p-type semiconductor-metal there is the region of high electric field, which accelerates the electrons to the surface. If the metal film is thin enough the part of electrons, accelerated in high electric field, can go out into the vacuum. At the room temperature in the conduction band of p-type semiconductors with large band gap (GaAs, InP etc.) there are practically no electrons. Hence, to attain the emission current from diodes, made from such semiconductors, the electrons must be generated by light with the photon energy, corresponding to the region of fundamental optical adsorption. Thus, the photoemission of hot electrons is observed. The possibility of changing the emission current either by light or by external bias makes such emitters perspective for using in vacuum microelectronics. This report contains the results of theoretical and experimental investigations of hot electrons photoemission from Schottky diodes p-InP-Ag.

2. THEORY

The value of emission current from back-biased Schottky diodes is determined by the distribution function of hot electrons in semiconductor in the high electric field at the electron energy, exceeding the value of electron affinity χ . As was shown by Dmitriev et al (1983) for A³B⁵ semiconductors at not very high electric field, satisfying the condition

$$e \cdot E \cdot l^{\Gamma} < 3\pi\omega \cdot \left[l^{\Gamma} / l^L \right]^2 \quad (1)$$

the asymptotic of energy distribution function of electrons in Γ valley

$f^{\Gamma}(\varepsilon, \theta)$ at $\varepsilon \geq \Delta$ is given by

$$f^{\Gamma}(\varepsilon, \theta) = \Phi(\varepsilon, \theta) \cdot \exp \left\{ - \int_{\Delta}^{\varepsilon} \frac{d\varepsilon'}{e \cdot E \cdot l^{\Gamma}(\varepsilon')} \right\} \quad (2)$$

where $\Phi(\varepsilon, \theta)$ doesn't greatly depend on the energy. Here l^{Γ}, l^L - the mean free paths of hot electrons in Γ and L valley of conduction band, accordingly, $\hbar\omega$ - the intervalley phonon energy, Δ - intervalley separation. It is necessary to note, that the distribution function $f(\varepsilon, \theta)$ corresponds to ballistic transport of electrons in high electric field. In this case almost all electrons with high energy are in the Γ valley in the region of small angle along the direction of electric field. The mean energy of electrons is equal to Δ (Maloney et al., 1980). In such a case, neglecting the dependence of $\Phi(\varepsilon, \theta)$ on the angle, we can write the following expression for the emission current density from back-biased Schottky diodes

$$j = e \cdot (W/h\nu) \cdot T^O \cdot T^e \int_{\chi}^{\infty} N(\varepsilon') \cdot v(\varepsilon') \cdot f^{\Gamma}(\varepsilon') d\varepsilon' \quad (3)$$

where e - the electron charge, W - the density of radiation flux, T^O, T^e - optical and electronic transparency of metal film, accordingly, $N(\varepsilon)$ - the density of states in the conduction band, v - the normal to surface component of photoelectron velocity. The electric field in the Eq.3 is the mean electric field in the region of semiconductor near the surface with thickness d . In this region the electrons accelerate from energy Δ to the energy $\varepsilon \geq \chi$.

$$E^m = \frac{1}{d} \int_0^d E(x) dx \quad (4)$$

where

$$d = D \cdot \left[1 - \sqrt{1 - (\chi - \Delta)/(V + V^D)} \right] \quad (5)$$

and V^D - diffusion potential, D - band bending region. Inserting Eq.2 into (3), we obtain

$$j = e \cdot (W/h\nu) \cdot T^O \cdot T^e \int_{\chi}^{\infty} N(\varepsilon') \cdot v(\varepsilon') \cdot \Phi(\varepsilon') \cdot \exp \left\{ - \int_{\Delta}^{\varepsilon'} \frac{d\varepsilon''}{e \cdot E^m \cdot l^{\Gamma}(\varepsilon'')} \right\} d\varepsilon' \quad (6)$$

When mean free path of hot electron $l^{\Gamma}(\varepsilon) \sim \text{Const}$, or when $l^{\Gamma}(\varepsilon)$ diminishes with the increase of electron energy, in the energy region $\varepsilon > \chi$ the $\exp()$ in Eq.6 has the sharp maximum at the energy $\varepsilon = \chi$. Therefore, the integral in Eq.6 may be approximately calculated by Laplace method. Using this method, we obtain the following expression for j

$$j = j^0 \cdot E^m \cdot \exp \left\{ - \frac{(\chi - \Delta)}{e \cdot E^m} \left[\frac{1}{l^{\Gamma}(\varepsilon)} \right]_{av} \right\} \quad (7)$$

where

$$j^0 = e^2 \cdot (W/h\nu) \cdot T^0 \cdot T^{\theta} \cdot N(\chi) \cdot v(\chi) \cdot \Phi(\chi) \cdot l^{\Gamma}(\chi) \quad (8)$$

$$\left[\frac{1}{l^{\Gamma}} \right]_{av} = \frac{1}{\chi - \Delta} \int_{\Delta}^{\chi} \frac{d\varepsilon}{l^{\Gamma}(\varepsilon)} \quad (9)$$

It is necessary to note, that Eq.7 is correct when the bottom of conduction band in the volume of semiconductor is higher, then the vacuum level, that is if $e(V + V^0) > \chi$. From Eq.7 the conclusion can be made, that $\ln(j/E^m) \sim 1/E^m$. From analysis of these characteristics we may determine the average value of mean free path of hot electron in semiconductors $(1/l^{\Gamma})_{av}$ at electron energy $\varepsilon = \chi$

3. EXPERIMENT

The investigations of hot electron photoemission from Schottky diodes were carried out in ultrahigh vacuum chamber with ultimate pressure 10^{-10} torr at room temperature. Schottky diodes were made by the evaporation of semitransparent Ag films with thickness 50-100 Å on the surfaces of crystals or epitaxial layers p-InP (100) which were heat cleaned in ultrahigh vacuum. The hole concentration was equal to about 10^{18} cm^{-3} . The work function of Ag films was reduced by adsorption of cesium and oxygen and was in the range of 1.2-3.0 eV.

The photoemission quantum yield curves are shown in Figure 1. These characteristics were measured at the work function of Ag film about 1.3 eV. For zero bias (curve 1) only photoemission from Ag film with lowered work function was observed. At 5 V (curve 2) the hot electrons photoemission from InP was arised (Bell et al. 1974, Maloney et al. 1980). The threshold of such photoemission is equal to $0.95 \mu\text{m}$ and corresponds to band gap of InP. At the Figure 2 the bias dependences of photoemission current from p-InP-Ag diodes are shown. These characteristics were measured under illumination at the $0.9 \mu\text{m}$ wavelength at the different work functions of Ag film. As it is seen from Figure 2 the increase of bias causes the sharp growth of

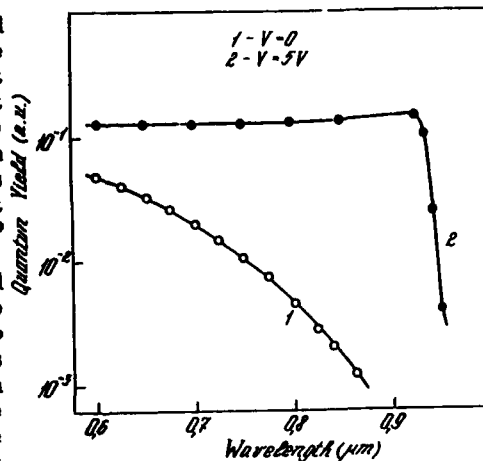


Fig. 1. The photoemission quantum yield from Schottky diodes p-In-Ag

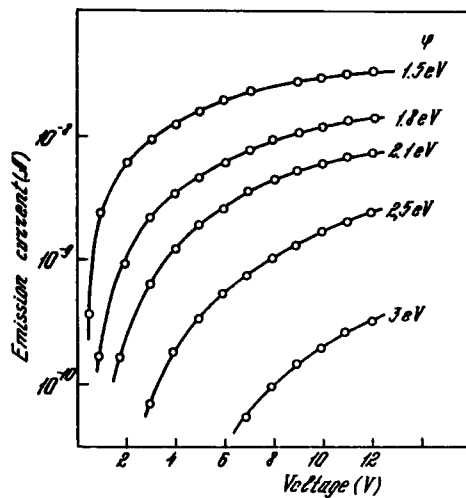


Fig.2. The bias dependences of photoemission current from p-InP-Ag diodes.

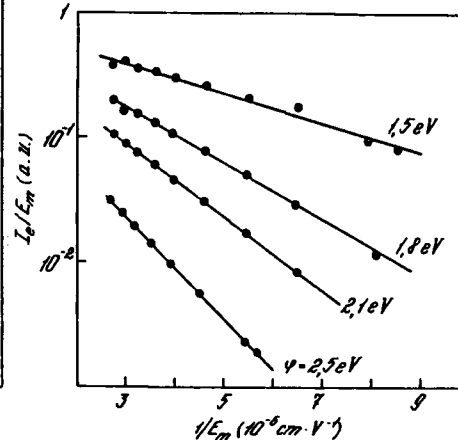


Fig.3. The photoemission current from p-InP-Ag diodes, as a function of inverse electric field.

emission current. The photoemission was observed both at low and at high work functions up to 3 eV. To compare the experimental results with theory, we rebuilt the characteristics $I(V)$ in coordinates $\lg(I/E^m) = f(1/E^m)$. These characteristics are shown at Figure 3. One can see that all characteristics are linear in chosen coordinates, i.e. they correspond to Eq.7. This fact proves our model of hot electrons photoemission, based on the ballistic transport of electrons in high electric field region. Using Eq.7 for analysis of characteristics $\lg(I/E^m) = f(1/E^m)$, measured at the different work functions, and adopting that $\Delta = 0.53$ eV (Maloney et al., 1980) we determined the average values of mean free path $l^{av} = 1/(1/l)^{av}$ for hot electrons with energy $\varepsilon = \chi$. It follows from this analysis, that in the energy range $\varepsilon = 0.9-1.9$ eV mean free path of electron does not depend on the energy and is equal to 130 ± 25 Å. It must be mentioned, that when calculating the distribution function $f(\varepsilon)$ Dmitriev et al (1983) supposed, that the main mechanism of the energy loss is the intervalley scattering. Therefore, we can make the conclusion that the value of mean free path is determined by the intervalley scattering.

Bell R.L., James L.W., Moon R.L., 1974, Appl. Phys. Lett., 25, 645.

Dmitriev A.P., Michailova M.P., Yassievich I.N.,

1983, Fiz.Tech.Polup., 17, 46

Maloney P.E., Burt M.G., Escher J.S., Gregory P.E., Hyder S.B., Antypas G.A., 1980, J. Appl. Phys., 51, 2879.

Stimulated cold-cathode emission from metal electrodes coated with Langmuir-Blodgett multilayers

S. Bajic, N.A. Cade*, A.D. Archer and R.V. Latham
Dept. of Electronic Engineering and Applied Physics
Aston University, Birmingham, B4 7ET, UK.

Abstract An investigation has been undertaken into the field-induced electron emission from various planar metallic electrodes coated with Langmuir-Blodgett (LB) multilayers in the thickness range 90-750Å. Optical imaging and electron spectroscopy techniques have been used to study the populations of emission sites and their spectral characteristics for applied fields of $\leq 20 \text{ MVm}^{-1}$.

1. Introduction

It is well established (Bayliss and Latham 1986) that, under UHV conditions, planar metallic electrodes promote a microscopically-localised cold-cathode electron emission process from typically 1 to 5 sites cm^{-2} at field levels of $15\text{-}20 \text{ MVm}^{-1}$. It is also known that these emission sites are associated with the presence of isolated micron-sized particulate structures that are either loosely adhering to, or partially embedded in an electrode surface. More recently, it has been demonstrated that if such an electrode is coated with a Langmuir-Blodgett dielectric multilayer film (Cade et al 1988, Bajic 1989), an apparently similar emission process is stimulated to occur in the significantly lower field range of $10\text{-}15 \text{ MVm}^{-1}$; furthermore, the number of sites cm^{-2} is greatly increased with this type of cathode.

The present paper reports on two further studies of this latter emission phenomenon. Firstly, an optical imaging technique has been used to determine the current-voltage (I-V) and site distribution characteristics of a range of LB-coated planar cathodes. In the second investigation, a high-resolution electron spectrometer has been used to study the influence of the applied field on the shift and half-width spectral characteristics of individual emission sites.

2. Experimental Systems

This study employed two specialised UHV systems whose operational and design details have been given elsewhere. The first system (Bajic and Latham 1988) consists of a plane-parallel electrode geometry (0.3mm gap) and incorporates a SnO_2 -coated transparent-anode. With this arrangement, the spatial distribution of emission sites can be monitored by photographic or video recording of the associated "anode spots" which are formed due to impinging high-energy electrons. The second system is a purpose-built, high-resolution electron spectrometer (Bayliss and Latham 1985) which electronically locates the positions of emission sites by an anode probe-hole scanning technique. Having located a site, electron energy spectra can be obtained and displayed with respect to the Fermi level of the metallic substrate with a resolution of 25meV.

* GEC Hirst Research Centre, East Lane, Wembley, Middlesex, HA9 7PP

3. Results

Using a Langmuir-Blodgett (LB) film deposition process (Peterson 1984), ten cathodes were produced from various 14mm-diameter substrates, and with ω -tricosenoic acid coatings varying in thickness from 90-750Å (see Table 1). By applying a gradually increasing field to a virgin LB-cathode, it is found that a point is reached, E_{sw} , where a switch-on event is observed. This irreversible process typically occurs at fields of $10\text{-}20\text{MVm}^{-1}$, and results in the establishment of one or more emission sites: subsequently, as the field is further increased, it is typical to observe up to 30 sites for fields $\leq 20\text{MVm}^{-1}$. Thus, Figure 1 compares the resulting I-V characteristics and emission site distribution images obtained for an uncoated Ag cathode and an Ag cathode coated with a 500Å LB-film. This clearly illustrates that thin dielectric coatings dramatically increase the total number of sites and hence emission current from planar metallic cathodes. Table 1 compares the characteristic emission parameters obtained from similar measurements on the ten cathodes used in this study. From these data, it will be seen that, although the LB-cathodes exhibit a high-current and high site density characteristic, there is no correlation between these parameters and the corresponding LB-film thicknesses.

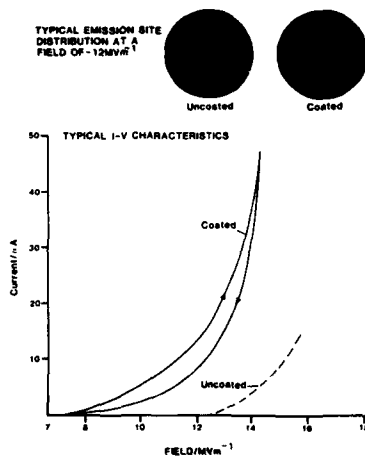


Fig 1: A comparison of the IV and site distribution data typically obtained from uncoated and LB coated Ag cathodes.

Table 1: The emission characteristics of 10 LB coated cathodes.

Substrate	LB-film Thickness (Å)	ESW (MVm^{-1})	I_c (total) at 20MVm^{-1} (μA)	No of sites Cm^{-1}
Ag	uncoated	33.3	0.001	1
Ag	90	23.3	60.0	16
Ag	210	22.3	1.0	8
Ag	270	18.3	110.0	12
w	270	23.3	4.0	23
Au	270	13.3	30.0	1
Ag	510	18.0	120.0	20
w	510	13.3	13.0	16
Au	510	10.0	40.0	2
Ag	750	21.6	0.3	7

The electron spectroscopy system has revealed that individual LB sites are typically composed of a number of sub-sites (Bajic 1989) which each give rise to characteristic single-peaked spectra. These spectra display field-dependent peak shifts (ΔE_s) to energies of $\geq 1\text{eV}$ below the substrate Fermi level, and half-widths ($\Delta E_{1/2}$) of typically $\geq 0.5\text{eV}$, i.e. characteristic of a non-metallic emission mechanism (Bayliss and Latham 1986). Figures 2(i) and (ii) show respectively the field-dependencies of ΔE_s and $\Delta E_{1/2}$ for typical sub-sites on Ag cathodes coated with LB-films of thicknesses of (a) 210Å, (b) 450Å and (c) 330Å. Thus, whilst ΔE_s and $\Delta E_{1/2}$ increase with the applied field, i.e. as observed with sites on uncoated HV

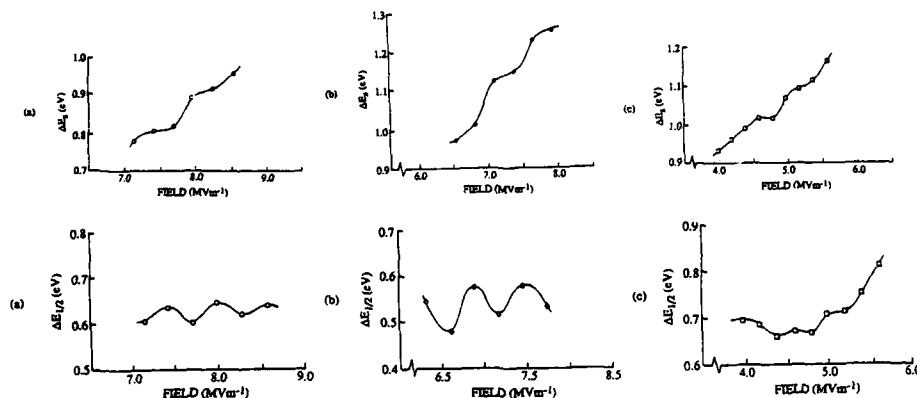


Fig 2: The field dependence of (i) the spectral shift and (ii) the spectral halfwidths for the typical sites on 3 cathodes with different LB film thicknesses.

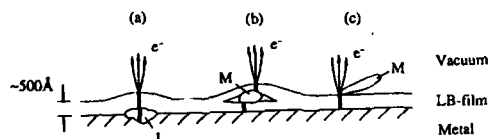


Fig 3: A schematic of three possible forms of film contamination and emission site formation.

electrodes, it is apparent that these parameters also exhibit an anomalous oscillatory behaviour, where the interval between successive maxima and minima is typically 0.6 MVm⁻¹. Finally, further spectral measurements have revealed that there is no correlation between the spectral characteristics of sites and the corresponding LB-film thicknesses.

4. Discussion

The site distribution images and spectral data for these cathodes strongly imply that the emission current derives from a localised "non-metallic" filamentary mechanism, i.e. as is believed to occur on uncoated HV electrodes (Bayliss and Latham 1986). In terms of this mechanism, electrons tunnel into the conduction band of the insulator from a preferential substrate location, where they are subsequently "heated" by the penetrating field and emitted over the surface barrier into vacuum. If it is assumed that the conducting filaments are "formed" in an idealised metal-LB film structure of film thickness d , then, referring to the spectral shift data of Figure 2(i), a comparison of the internal LB field ($E_i = \Delta E_s/d$) with the expected "static" film field (E_g/e_r) would imply that a (possibly non-geometric) field enhancement factor of ≥ 10 exists at these sites. If it is further assumed that ohmic loss along a filament can contribute to the observed spectral shift ΔE_s , then an $i_f R_f$ voltage drop of ~ 0.5 V (i.e. a filament resistance of ~ 0.1 M Ω) is necessary to equate the above internal field values. In fact, similar filament resistances have been obtained from studies on conduction through LB multilayers in MIM sandwich structures (Couch et al 1986), where evidence suggests that metallic filament formation may occur, e.g. due to an electromigration process.

Alternatively, since the experimental data show no correlation with LB-film thickness, there is a strong suspicion that the emission mechanism from these cathodes is associated with film and/or substrate contamination: the role of micron-sized surface contaminants in stimulating emission from uncoated HV electrodes is well known and has been reviewed elsewhere (Latham 1988). Figure 3 shows, schematically, three forms of particulate contamination and the associated filament formation which may occur with the present LB-coated cathodes (Bajic 1989). Considering case (c), it can be shown that the "antenna effect" (Athwal et al 1985) of, for example, a $1\mu\text{m}$ -sized conducting particle will give rise to a field enhancement of ~ 10 times within the LB-film region, i.e. in agreement with the field enhancement factor deduced from the above spectral data. Furthermore, since the field enhancement, and hence emission mechanism, depends on the condition that the particle remains uncharged, the good "blocking contact" provided by the LB-film may account for the formation of more sites with these cathodes when compared with an ambient oxide/contaminated HV electrode regime.

Referring to the oscillatory field-dependencies of ΔE_s and $\Delta E_{1/2}$ shown in Figures 2(i) and (ii) respectively, it is important to note that, although similar non-linear spectral effects have been reported in studies of oxide-coated HV electrodes (Bayliss 1984), no precise explanation of these effects is available at present. According to the non-metallic, hot-electron model (Bayliss and Latham 1986) described above, the spectral half-width ($\Delta E_{1/2}$) will be strongly dependent on the hot electron temperature at the insulator-vacuum interface, which, in turn, will depend on the local interface field and the energy loss mechanisms in this region due to electron-phonon interactions. Considering the latter effect, it is possible that the large, complex molecular structure of the LB-film will provide the characteristic phonon-loss modes for conduction band electrons, i.e. such that the spectral behaviour may be related to the particular frequencies and harmonics of the multilayer structure. Finally, since the "period" of the oscillatory spectral behaviour is apparently independent of the total film thickness, it has been tentatively suggested (Bajic 1989) that the hot electron temperature may be influenced by Bragg diffraction effects at the LB-film planes.

Acknowledgement

The Aston contribution to this work was part of a programme sponsored by SDIO/IST and managed by the Space Power Institute, Auburn University, Alabama, USA.

References

- Athwal CS, Bayliss KH, Calder RS and Latham RV 1985 IEEE Trans. Plasma Sci. PS-13 226-9
- Bajic S 1989 *PhD Thesis* Aston University UK
- Bajic S and Latham RV 1988 J Phys. D: Appl. Phys. **21** 943-50
- Bayliss KH 1984 *PhD Thesis* Aston University UK
- Bayliss KH and Latham RV 1985 Vacuum **35** 211-7
- Bayliss KH and Latham RV 1986 Proc. Roy. Soc. A**403** 285-311
- Cade NA, Cross GH, Lee RA, Bajic S and Latham RV 1988 J Phys. D: Appl. Phys. **21** 148-53
- Couch NR, Montgomery CM and Jones R 1986 Thin Solid Films **135** 173-182
- Latham RV 1988 IEEE Trans. Elect. Insul. EI-23 9-16
- Peterson IR 1984 Thin Solid Films **116** 357

Miniaturized liquid metal field electron and ion sources

J Mitterauer

Institut für Allgemeine Elektrotechnik und Elektronik
Technische Universität Wien, 1040 Wien, Austria

ABSTRACT: The emission site distribution of a slit type liquid metal ion source operating with caesium is investigated, resulting in a micron-sized linear array of emission sites with spacings rather independent of the emission current. Technological methods customary in vacuum microelectronics are suggested for the fabrication of miniaturized linear arrays of liquid metal field effect sources, operating at least at much lower voltages.

1. INTRODUCTION

When the surface of a liquid metal exposed to vacuum is subjected to a high electric field resulting from suitable voltages applied to an emitting electrode geometry, it is distorted into a cone or a series of cones which protrude more and more from the surface with increasing field strength. When the field reaches values of some 10^9Vm^{-1} , according to the polarity of the field generating voltage field emission or field ionization occurs from the apex region of these cones. Because the radius of curvature at the apex of such a cone is of the order of 10^{-7}m or less, applied voltages of some 10^3V are sufficient to obtain the required high electric fields with macroscopic interelectrode distances of about 10^{-3}m . Electron and ion beams can be created from liquid metal wetted needles (or arrays of needles) or from capillaries into which the liquid metal is allowed to flow; field electron emission as well as ion emission from caesium-wetted tungsten needles and stainless steel capillaries has been demonstrated successfully by Mitterauer (1984).

One of the most advanced field ion sources is the slit emitter originally developed at the European Space Agency (ESA) as an ion thruster for electric space propulsion with liquid caesium as propellant (Bartoli et al 1984). In this case, the capillary is elongated to a slit of some 10^{-2}m length with nearly rectangular cross section, allowing therefore the occurrence of a series of equally spaced emitting cones. This type of ion source represents an ultimate development in precision mechanics, demonstrated by actual numerical values of about 10^{-4}m for both the emitter slit width w and the round-off radius r_e of the emitter slit edge (Figure 3).

Besides the original concept as an ion thruster, the slit emitter generally may be employed as a high current liquid metal field effect ion or electron source for terrestrial applications in science and technology.

2. SLIT EMITTER MODULE

The slit emitter module in principle consists of two symmetrical highly polished metal plates of the shape depicted in Figure 1. In one or both of the emitter halves there is milled a recess to be of use as a reservoir of the liquid metal supplied to the emitter module by a feeding capillary tube. On certain regions of one of the inside faces there is sputter deposited a layer of nickel with a thickness of about 10^{-4} m. When the two halves are tightly clamped together they are separated by the thickness of this layer, thus forming a narrow slit of length l , width w and depth d through which the liquid metal can flow and be transported to the edges of the slit by the action of capillary forces. Until now, emitter modules with slit lengths of 15, 30, 50 and 80 mm have been produced. The material used for the emitter fabrication is stainless steel and, more recently, Inconel.

The electrode configuration used to create the proper electric field at the emitter slit edge region is shown in Figure 2. A plane accelerator electrode with an aperture of width $2b$ is mounted in a distance a of the emitter slit edge. Emitter and accelerator are kept at voltages $+U_e$ and $-U_{acc}$ respectively vs. ground potential in order to create the electric field necessary to produce and accelerate the ion beam. Actual data for the emitter-accelerator geometry according Figures 1 and 2 are as follows: $l=1,5 \cdot 10^{-2}$ m; $a=6 \cdot 10^{-4}$ m; $2b=4 \cdot 10^{-3}$ m; $d=1 \cdot 10^{-2}$ m; $w=1,2 \cdot 10^{-4}$ m and $1,5 \cdot 10^{-4}$ m, respectively. Typical voltages for U_e range between 0 and 6 kV at a constant value $U_{acc}=-5$ kV, with a maximum emission current $I_e=5$ mA for $U_e=6$ kV.

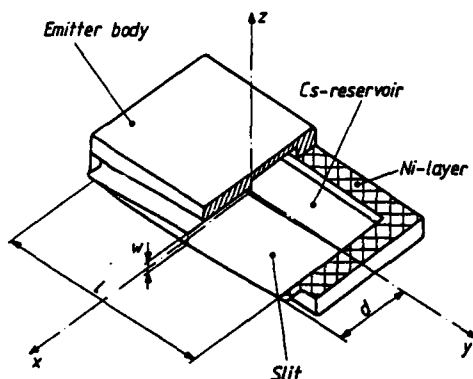


Figure 1. Emitter module and principal dimensions of the emitter slit

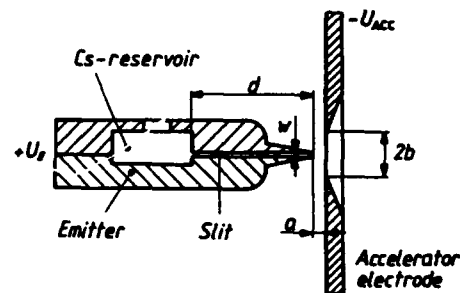


Figure 2. Sectional view of the emitter-accelerator configuration

3. EMISSION SITE DISTRIBUTION

If the emitter is filled with liquid Cs and the surfaces of the slit until the slit edges are uniformly wetted by the liquid metal, a homogeneous linear liquid tip of semicylindrical shape is assumed to exist at the slit edges at onset conditions of emission. The sectional view of this emitter region schematically is outlined in Figure 3, showing also different idealized assumptions on the equilibrium shape of the liquid tip; the tip radius r_0 depends on both the emitter slit width w and the radius of curvature r_e of the emitter slit edges, which are both of the order of 10^{-4} m. Enhancing the electric field, the linear liquid tip is distorted. Due to electrohydrodynamic effects, equidistant spaced emitting sites originate along the extension of the emitter slit. The existence of a matrix arrangement of wavelike instabilities on electrically stressed surfaces of fluids is a well known phenomenon (Melcher 1961). The linear disposition of emitting features observed on slit emitters by Aitken and Prewett (1983) and by Mitterauer (1987) obviously is related to these surface instabilities.

The mathematical treatment of this problem has been discussed in some detail even by Aitken and Prewett (1983), considering also standing wave perturbations with no time variations. For wavelike instabilities occurring on the electrically stressed Cs-surface at the orifice of the emitter slit, a simple relation exists between the wavelength λ of these instabilities, which is identical with the spacing of the emission sites, and the radius of curvature r_0 of the semicylindrical liquid metal tip

$$\lambda = \pi r_0$$

Within the theoretical figures outlined in Figure 3, the case (a) seems to be most unlikely for an emitter slit edge properly wetted with Cs. The equilibrium configurations according (b) and (c) are more realistic as these depend mainly on the actual wetting properties at the emitter slit edge.

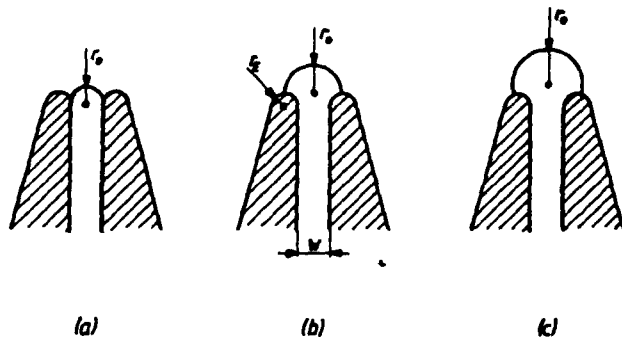


Figure 3. Sectional view of the linear liquid metal tip at the orifice of a slit emitter at onset conditions

With the values of λ measured for two emitter with slit widths of $w=1,2 \cdot 10^{-4}\text{m}$ and $w=1,5 \cdot 10^{-4}\text{m}$, respectively, there result for the radius of curvature r_0

w	λ	r_0
$1,2\mu\text{m}$	$7,5\mu\text{m}$	$2,4\mu\text{m}$
$1,2\mu\text{m}$	$16\mu\text{m}$	$5\mu\text{m}$
$1,5\mu\text{m}$	$10\mu\text{m}$	$3,2\mu\text{m}$

The occurrence of a nearly constant value of λ verified experimentally for a wide range of emission currents obviously may not be explained in terms of a simple standing wave theory neglecting hydrodynamic effects but has rather to be treated by a flow field theory assuming also mutual interactions of adjacent emission sites. As a qualitative approach, one may assume an emission site distribution mainly impressed by the onset conditions which is not changed considerably with increasing emission current due to the concentration of the hydrodynamic flow of Cs to the apices of the emission sites. Considering the instabilities of liquid columns, a similar idea even was proposed by Thomas et al (1980), i.e. in a viscous fluid the positions of the emitting sites are likely to be stabilized by the fluid flow.

4. CONCLUSIONS

Bearing in mind the ultimate stage in precision mechanics involved into the fabrication of the emitter module by grinding and lapping, and considering the micron-sized dimensions at the emitter slit edge outlined in Figure 3 on the one side as well as the macroscopic dimensions of the emitter-accelerator configuration shown in Figure 2 on the other side, a miniaturization of the whole electrode geometry by methods customary in vacuum microelectronics appears to be obvious.

Besides technological advantages resulting in a much more accurate alignment between emitter and accelerator electrode, due to the much smaller interelectrode distance a considerable reduction of the emitter and accelerator voltage is expected.

ACKNOWLEDGEMENTS

This research work was supported by the Austrian Science Foundation (FWF) under Project No.5284.

REFERENCES

- Aitken K L and Prewett P D 1983 *Final Report on ESTEC-Contract No.4462/80*
- Bartoli C, von Rohden H, Thompson S P and Blommers J 1984 *J.Phys.D:Appl.Phys.* **17** 2473
- Melcher J R 1965 *J.Fluid Mech.* **22** 1
- Mitterauer J 1984 *J.Physique* **45** C9/185
- Mitterauer J 1987 *IEEE-Trans.Plasma Sci.* **P-15** 593
- Thomas C Ll, Little P F, Mahony C and Banks C 1980 *Final Report on ESTEC-Contract No.3686/78*

Electron emission from GaAs Schottky diodes

T. Tsukamoto, N. Watanabe and M. Okunuki

Canon Research Center, 5-1, Morinosato-Wakamiya, Atsugi, Kanagawa, 243-01, Japan

ABSTRACT: We have investigated a novel cold cathode based on avalanche breakdown of a Al-GaAs Schottky barrier junction. The magnitude of emission current density (2.6×10^{-5} A/cm²) is consistent with order estimation value.

I. INTRODUCTION

Electron emission cathodes using semiconductors have been investigated for nearly 30 years (Burton 1957). Recently, it has been known that a Si cold cathode with a reverse-biased *pn* junction parallel to its surface has a high current density (compared with that of thermionic cathode) by fabricating a very thin and a heavily doped *n*-type layer (Gorkom et al. 1980). By applying reverse-biased voltage between the junction, avalanche electrons are generated and those electrons with energy higher than the vacuum level will pass through the *n*-type layer into vacuum. It is, however, difficult to make this thin and heavily-doped *n*-type layer with low series resistance because of high fabrication technique and of physical properties (e.g., low carrier density, doping limit) inherent in semiconductors.

Cold cathodes with Schottky barrier junctions would, however, overcome these difficulties since metal resistivity is the order-of-magnitude smaller than highest doped *n*-type layer, and it is relatively easy to fabricate a metal layer on a *p*-type layer. Furthermore, by making a thin metal for the junction, sharp energy distribution of avalanche electrons emitted from the *p*-type layer can ballistically pass through the metal layer if the mean free path of these electrons is longer than the thickness of the metal layer.

Although a cold cathode with Schottky barrier junction could be, in principle, suitable for a high efficient cold cathode, to our knowledge, no investigation has been done for realizing a Schottky barrier cathode. This may be due to the fact that it is difficult to make a heavily doped semiconductor with a good junction characteristics. We have attempted to make a cold cathode with a Schottky-barrier junction using GaAs since GaAs has high Schottky barrier height for novel metal. A good junction has been obtained by using focused-ion-beam (FIB) technique.

In this paper, we shall report cathode design and characteristics of the GaAs Schottky cathode.

II. DESIGN OF SCHOTTKY CATHODE

As shown in Fig.1, the electrons generated by avalanche multiplication in *p*⁺ semiconductor Schottky junction are accelerated by the high field. Electrons that have kinetic energy higher than the work function of the metal surface have a chance of escaping into vacuum.

Schematic cross section of the GaAs cold cathode is shown in Fig.2. This cathode have a small electron emission area which composed Schottky barrier junction and a guard ring consisted of *p-n* junction. The guard ring is formed to prevent a leakage at the edge of the Schottky barrier junction. This device construction is simple and suitable for submicrometer

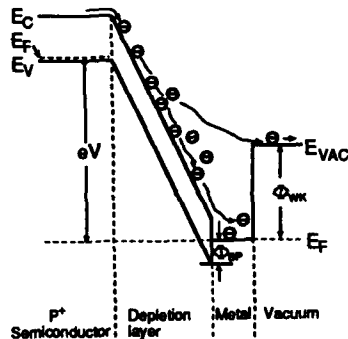


Fig.1. Energy band diagram of a reverse biased Schottky cathode.

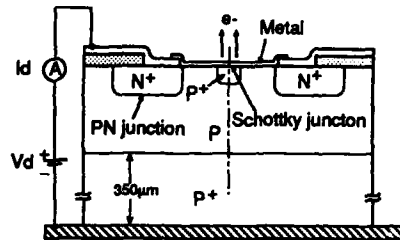


Fig.2. Schematic drawing of the Schottky cathode.

size fabrication. Contact electrode is directly connected to the Schottky-barrier junction to reduce series resistance and to avoid parasitic capacitance.

The high electric field in the depletion layer has to be as large as possible, while avoiding tunnel breakdown, as suggested by Gorkom et al.(1986). Avalanche conditions in the Schottky barrier junction depend on carrier concentration of the semiconductor same as that in *p-n* junction. We have estimated important parameters such as breakdown voltage, maximum electric field, depletion width under the avalanche condition near tunneling condition which by calculating numerically with use of ionization integral equation. We use the value of ionization rates in the high electric field measured by GaAs avalanche photodiode (Ito et al 1978). The field dependence of the ionization rates, α , can be expressed as

$$\alpha_n = 5.6 \times 10^6 \exp(-2.41 \times 10^6/E) \quad 1)$$

$$\alpha_p = 1.5 \times 10^6 \exp(-1.57 \times 10^6/E) \quad 2)$$

where E (V/cm) is electric field of abrupt junction in the space charge region which determined by poisson's equation. From calculation results shown in Fig.3, the impurity concentration is chosen to be $7 \times 10^{17} \text{ cm}^{-3}$. This value can be obtain a threshold field of tunneling breakdown larger than 1×10^6 V/cm. The breakdown voltage and the depletion width in this condition can be evaluated to be 5.0 V and 0.8 μm , respectively.

Metal selection of this type is important to obtain stable electron emission and high efficiency. Total mean free path in the metal is strongly dependent on excess energy (difference of electron energy and Fermi energy). In the energy region of avalanche breakdown, excess energy of the electrons and its total mean free path in the metal is expected to be 2-8 eV and 3-7 nm (Heiblum 1981), respectively. If the thickness is less than a value of the total mean free path, ballistic electron emission could be expected. As the resistivity of a thin metal formed by evaporation method is smaller than $2 \times 10^{-5} \Omega\text{cm}$, surface layer of the Schottky cathode has lower resistance than that of *p-n* cathode.

In this case, aluminum metal was also selected for the material of the property with relatively long mean free path. The Schottky junction was fabricated as parallel to the surface to maintain high field, and to obtain uniform electron emission. The parameters of this diode are summarized in Table I.

III. EXPERIMENT

There are several important processes to fabricate the electron device of the Schottky cathode. The GaAs epitaxial layer was grown by molecular beam epitaxy (MBE) and the diodes were

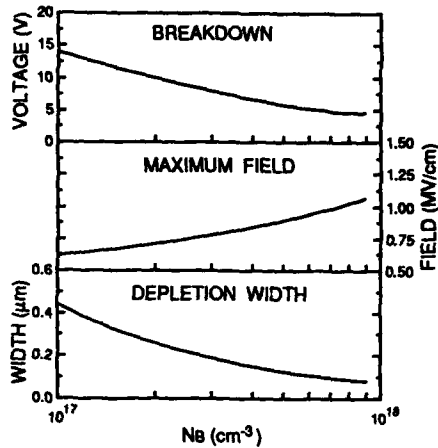


Fig.3. Breakdown voltage, maximum field and depletion-layer width at avalanche condition.

Table I

	Material	Concentration (Dopant)	Thickness (Depth)
Substrate	P-type GaAs (100) ^{7°} off	$5 \times 10^{18} \text{ cm}^{-3}$ (Zn)	350 μm
Epitaxial layer	P-type GaAs	$2 \times 10^{18} \text{ cm}^{-3}$ (Be)	2 μm
Guard ring	N-type GaAs	$5 \times 10^{18} \text{ cm}^{-3}$ (Si)	(500–800nm)
Active area	P-type GaAs	$7 \times 10^{17} \text{ cm}^{-3}$ (Be)	(300–500nm)
Metal	Al	—	9–10nm

fabricated on the surface by the processes using FIB-implantation technique. FIB implantation was carried out in a UHV system with contamination free condition. Two different ions, Be and Si, were implanted to fabricate the active region and guard ring without exposing a sample to the air. In order to fabricate a thin depletion layer of the active region, Be ion having lower energy of 40keV was used. On the other hand, Si ion was used under the condition of higher energy of 160 keV to fabricate a deep *p-n* junction. For the activation of the implanted area, cap anneal with AlN film it was carried out at the temperature of 850 °C. The AlN film encapsulation is most suitable to form the Schottky cathode for a reduction of stress between GaAs and the film and surface smoothness after the anneal process. Cr/Au ohmic-contact metal for back contact and Au-Ge/Au ohmic-contact for guard ring are deposited and alloyed under the condition of 400 °C for 5min. Thin metal for Schottky contact was deposited at the last process after surface cleaning.

IV. RESULT AND DISCUSSION

A typical characteristics of current-voltage and electron emission of the GaAs Schottky cathode are given in Fig. 4. The diode current increases moderately from 5V and linearly at 17V. On the other hand, the shape of the forward I-V curve shows typical characteristics of the Schottky diode. Series resistance, Schottky barrier height, and ideal factor of the diode are 170 Ω , 0.66 V, and 1.25, respectively, which were calculated by using forward characteristics and Nord plots (1979).

Under the reverse bias condition, the luminescence associated with the avalanche break down was observed at the small active region. The characteristics of electron emission measured in a vacuum system (vacuum level is below 10^{-4} Pa), is shown in left-upper side of Fig.4. The maximum emission current is 40 pA (2.6×10^{-5} A/cm²) at the diode current is 9mA (5.9×10^3 A/cm²).

Breakdown voltage is in good agreement with the calculated value. Implanted active region shows good Schottky characteristic and low series resistance value. However the current density of diode is small yet, because the concentration of epitaxial layer is selected as $2 \times 10^{18} \text{ cm}^{-3}$ in order to obtain high breakdown voltage of guard ring. In this investigation,

electron emission from the surface on the Schottky diode is confirmed. The current density of the electron emission is in good agreement with order estimation using the following assumption parameter; electron temperature is 0.3-0.4 eV and work function of Al_2O_3 is 4.7 V.

VI. CONCLUSION

By designing the Schottky cathode and developing the process to fabricate heavily doped P-type layer, it has been confirmed the emission of electrons from Al/GaAs Schottky barrier cathode. The cathode has properties of a ballistic emission, and high speed driving of conventional Schottky diode own. Further, the efficiency and energy distribution of the cathode will be able to improve by using a material of lower work function and thinner metal less than total mean free path of injecting electrons. The process to fabricate the cathode becomes extremely simple by using FIB technique, because two kind of impurities are implanted without exposing a sample to the air. Furthermore this process is suitable for fabricating electron emission cathode in the submicrometer size.

ACKNOWLEDGMENTS

The authors express their spatial thanks to Y. Sekiguchi for preparing epitaxial wafer.

- Burton A B 1957 Phys. Rev. 108, pp1342-3
 Gorkom G G P and Hoeberechts A M E 1980 J. Appl. Phys. 51(7), pp3780-5
 Gorkom G G P and Hoeberechts A M E 1986 J. Vac. Sci. & Technol. B 4, pp108-10
 Heiblum M 1981 Solid-St. Electron. 24, pp343-66
 Ito M, Kagawa S, Kaneda T and Yamaoka 1978 J. Appl. Phys. 49(8), pp4607-8
 Norde H 1979 J. Appl. Phys. 50(7), pp5052-3

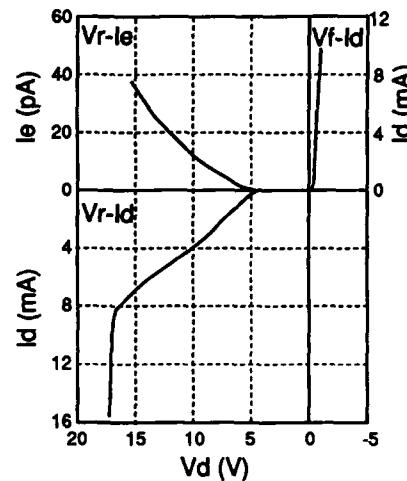


Fig. 4. Electrical characteristics of the Schottky cathode.

Electron emission from GaAsP NEA cold cathodes

P.J. Hockley* and H. Thomas

School of Electrical, Electronic and Systems Engineering, UWCC, Cardiff

ABSTRACT: A model for the p^+-n NEA cold cathode has been derived which accounts for the variation of device efficiency with p-layer removal. Values of 0.5% and 1% were achieved for circular emitting areas of $15\mu\text{m}$ and 1mm diameter respectively and emission current densities up to 2Acm^{-2} . Based on the model a change of p-type doping and a shallower junction depth could give efficiencies up to 30% in GaAsP diodes.

1. INTRODUCTION

The GaAsP NEA cold cathode is an effective means of obtaining electron emission in vacuum without either high cathode temperature or the need of a high electric field. Potential advantages when compared to its thermionic counterpart include a low electron energy spread, emission control with low voltage circuitry, fast direct modulation and the possibility of extended uniform emission sources.

The cold cathodes investigated consisted of a p^+-n junction, the p-surface of which is activated to the negative electron affinity condition using conventional caesium or caesium/oxygen photocathode principles. The electron source is provided by the forward biased p-n junction. Whereas initial efficiency of operation is dependent upon achieving the NEA condition, thereafter optimum efficiency is obtained by tailoring diode parameters through processing. The study therefore presents the results of a phenomenological model and relates cathode efficiency with experimental processing conditions.

2. THEORETICAL MODEL

The model combines the effects of processing conditions, device parameters and subsequent electron escape. The major effects modelled are therefore:

- (a) The potential variation within the emitting window region, which with the p-layer becoming thinner will lead to current crowding effects. Following Kohn (1973) the current dependence for radial geometry is obtained.

*Present address:- B.P. Research Laboratories, Sunbury on Thames, Middlesex

- (b) Changes in diode characteristics with p-layer removal. With decreasing acceptor concentration the electron injection ratio changes and the current path for emission becomes metal-p⁺-p-n.
- (c) The increased probability of injected electrons reaching the surface as the remaining p-layer thickness decreases with sputtering.
- (d) Thermalising of electrons traversing the depleted surface. At the depletion layer edge, electrons are assumed to have a Maxwell-Boltzmann distribution and in the absence of energy losing collisions would obtain an energy $V_{bb} = 0.65\text{eV}$ at the p-surface. However the dominant energy loss is through phonon interactions and the electron energy profiles are therefore computed as a function of acceptor concentration (Escher and Schade (1973)). The proportion of electrons possessing energy greater than the vacuum level yields the emission factor α_{bb} for the bent band region.

The combined effects of the model are shown in Fig.1 for the $15\mu\text{m}$ window diameter diode. Curves (a) and (b) represent the contributions from bulk properties with electron diffusion length, L_e , as the variable. Curve (c) shows the effect of electron thermalisation represented by the emission factor α_{bb} . In addition, the term $\alpha_g = 0.75$ for GaAsP is used to account for surface escape probability (Burt and Inkson 1976). A similar plot was obtained for the 1mm grid diode and an increased d.c. efficiency was predicted, typically 3% for $L_e = 1\mu\text{m}$ and 1% for $= 0.3\mu\text{m}$.

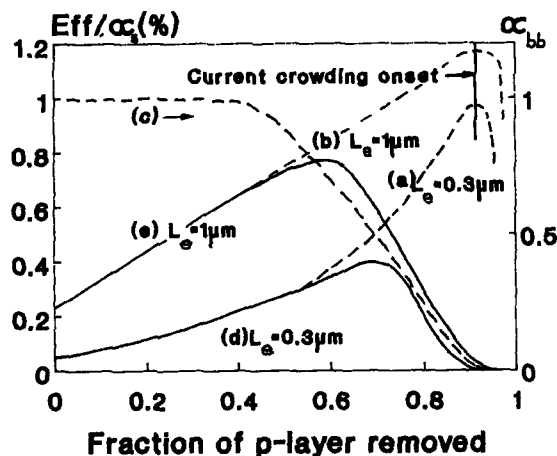


Fig.1 Theoretical cold cathode efficiency calculated for $15\mu\text{m}$ diameter device. (a) and (b), variation due to bulk effects only, (c) emission factor, α_{bb} due to bent band region; (d) and (e), net variation.

The response shows that the effect of current crowding is not important in these devices where the efficiency is seen to decrease at an earlier stage of processing and is due to electrons thermalising.

3. EXPERIMENTATION

The GaAsP diodes were conventional LEDs mounted on To-5 headers in a UHV chamber. The p+ surface of the window region is slowly sputtered by low energy (100-200eV) Argon ion bombardment and the total flux recorded in units of current \times time. Following sputtering, the diode surface was coated with caesium by thermal decomposition of caesium chromate. Cold cathode emission is then monitored and the sputter-caesium cycle repeated sequentially until peak efficiency had been passed.

It was found that few devices achieved the NEA condition immediately after the initial sputtering and caesiumation and they usually displayed superior static I-V characteristics. The techniques of surface photo-emission and diode photo-voltage response were therefore employed to study the activation mechanism wherein the NEA state, photo emission would reveal emissions from band to band excitation and also from caesium induced surface states. Photo voltage, though conceived as a means of quantifying the p-layer removal proved complementary to photo-emission and in all cases the onset of NEA was accompanied by the disappearance of the photo-response. It was thus a simple diagnostic technique to establish the NEA condition. Fig.2 shows the subsequent photoemission response and the threshold at 1.96 eV can be identified as the band to band excitation and the lower thresholds at 1.75 eV and 1.65 eV correspond to surface state emissions. Fig2(b) shows that with the chamber illuminated the lower threshold at 1.65 eV is obtained.

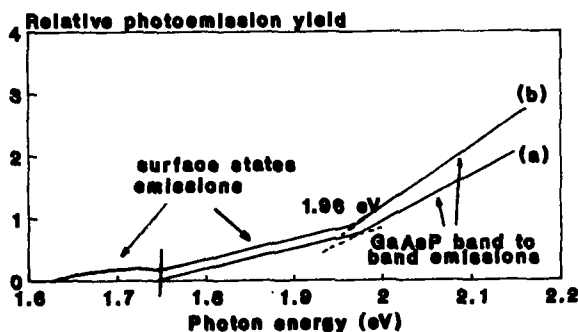


Fig.2 Photoemission response after activation. (a) No illumination; (b) With background illumination.

A model which fits these results is that the Fermi level is pinned at the 1.75 eV state and electrons are available for emission, whereas the 1.65 eV state above the Fermi level is depleted. It is therefore the effect of illumination which permits the state to capture electrons and hence produce emission. The density of the 1.75 eV state therefore limits the NEA condition, but the density decreases with p-layer removal until cold cathode emission occurs. With the attainment of full, theoretically predicted NEA, cold cathode efficiency was measured and compared with theory.

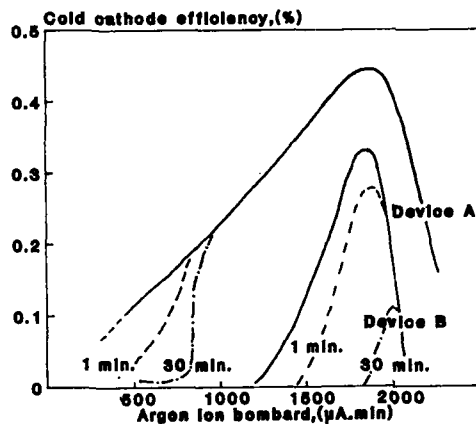


Fig.3 Cold cathode efficiency versus cumulative argon ion sputtering.

Fig.3 shows the cold cathode efficiency as a function of p-layer removal for two 15 μm . devices. The emission stability is also demonstrated at 1 min and 30 min post-caesiation intervals for the early sputtering sequence. The peak efficiency is close to the predicted 0.3 to 0.7% range for these devices. Comparable measurements on the larger grid structure diodes gave values in excess of 1%. Measurements taken after peak efficiency has been reached show no sign of current crowding until further p-layer is removed in agreement with the theoretical model.

Based on the transport parameters of electrons in the p-region accompanied by thermalisation in the depleted surface the model derived predicts efficiencies in the range 25%-30% for a uniform doping density of $1 \times 10^{19} \text{ cm}^{-3}$ and a p-layer thickness of 0.2 μm.

4. CONCLUSIONS

Using UHV facilities and careful preparation techniques, cold cathode efficiencies of typically 0.5% and 1% were achieved for circular emitting diodes of 15 μm and 1 mm diameter respectively and continuous emission current densities up to 2 A cm^{-2} were obtained for the smaller devices. Photoemission studies of the NEA surface showed that full theoretical NEA could be achieved but the presence of surface states reduced band bending and consequent reduction of electron affinity.

The experimental results support the key features of the theoretical model which predicts that a reduction in the p-layer doping and thickness, to $1 \times 10^{19} \text{ cm}^{-3}$ and 0.2 μm respectively, would yield efficiencies in the range 25% to 35% for GaAsP cold cathodes. Further improvements in device structure would necessitate advanced microfabrication/micromachining techniques to decouple the active NEA surface through a recessed cathode.

REFERENCES

1. E.S. Kohn. App. Phys. Lett. 18 p272 (1971)
2. J.S. Escher and H. Schade. J. App. Phys. 44 pp 5309-13 (1973)
3. M.G. Burt and J. N. Inkson. App. Phys. Lett. 28 p5 (1976)

Thin-film metal-insulator-metal systems in the non-heated electron emitter regime

Yu Yankelevitch, Yu Barengolzs, M Khaskelberg.

Pedagogical Institute, pr.Komsomolsky,75,Tomsk,634044, USSR.

ABSTRACT: Analysis of work on the investigation of "formed" metal-insulator-metal (MIM) systems based on oxynitride silicon films (Me-Si_xNyOz-Me) is presented. Research of MIM-system behaviour in extreme conditions: low temperature (up to 4K) short impulses of voltage ($10^6 - 10^7$ V), superstrong field (up to 10^8 V/m) allowed to build a physical model of forming and operating of thin film system, and on the other hand to receive important data for its practical use as non-heated cathodes for the solution to some problems of electrical engineering.

I. INTRODUCTION.

One of the basic problems of vacuum microelectronics is a problem of active elements creation and this is in the first place of problems of effective electron emitters. To solve these tasks the electron emitters must have a number of necessary qualities, such as to be economic, quick activity, be fast in operation, to have radiation stability, low noise, technological creation, possibility of micromidget manufacturing, etc. It's only natural that research of such emitters must be centred on non-heated cathodes. In this respect multipoint field emission systems ("Spindt-cathodes") attract attention of researchers in present time. But from our point of view (and we haven't changed it for almost 20 years) non-heated cathodes on the basis of thin-film forming system metal-insulator-metal present a certain interest for solving a great many tasks of vacuum microelectronics.

1.1 In MIM-systems at $10^2 - 10^4$ Å primarily ultradispersive amorphous insulator thickness and at 100 to 200 Å upper metal electrode thickness one observes the phenomenon of electric formation. As a result of the forming process (that is after treatment of MIM system of voltage 10 to 15 V in vacuum) the system becomes capable of electronic emission into vacuum from the so-called "channels of increased conductivity" (Yankelevitch 1980). Besides, electroluminescence, switching and memory effects are observed. Such effects were observed in metal-insulator-vacuum systems which led to intensification of breakdown development in vacuum (Athwal 1984, Yankelevitch 1988). Channels diameter is about several hundreds angstrom, the upper electrode in these places is missing. Estimations show

that channels number on one square centimeter is 10^6 to 10^8 . Our research showed that the forming process itself, like a growth of channels of increased conductivity, presents explosive emissive primary stage at the metal-insulator border, with following combination of solid endothermic and exothermic chemical reactions in the insulator layer. Such a complex process which depends on many external conditions (thickness and content of layers, environment temperature, surrounding atmosphere, electric field, etc.) makes this systems also sensible to external changes after forming process.

We traditionally do all researches on Me-SixNyOz-Me systems. Thermodynamic analysis showed that substance filling channels body even after the forming process is left non-metallic, but a part of it crystallizes and can be written SixNyOzMe. As a result of forming process insulator resistance in the channel decreases by 7 to 8 orders. At voltage 10 V conduction current density in the channel achieves a fantastic value for insulators 10^4 to 10^5 A/cm². At that the system functions steadily for dozens and hundreds of hours.

1.2 Analysis of I - V characteristics shows, that several processes are responsible for current condition (jump-type conductivity; a current, limited by volume charge; current of liberation carriers from the impurity centres due to thermal and field effects; and etc.), and their importance depends on electric fields, temperature, surrounding atmosphere, etc. Moreover, taking into account that the field is nonuniform, we can say that current character is different in the insulator layer itself.

1.3 Now for us the most interest are the results of the conduction current I_c and emission current I_e measuring up to the low temperature (4K). It must be noted that the value and the physical mechanism of conductivity depends on the operation conditions. For the "high" vacuum (the residual pressure less than 10^{-8} Torr) I - V and temperatures characteristics of the I_c and I_e are monotonic. The initial part of the I_c current I - V characteristic is the Ohm law. At the electric field intensity $E > 10^8$ V/m for I_c and I_e currents I - V characteristics are linear in the Poole-Frenkel coordinates. The fact that the main part of the current is due to that mechanism is confirmed by the temperature dependences of the I_c and I_e which turn out to be linear in the $\ln I - \frac{1}{T}$ coordinates. On the other hand, a part of the electrons injected by the negative electrode arrive at the positive electrode by the jumping over the localized states in the forbidden zone of the insulator accompanied with the photon emission. Under the definite conditions the current may be limited by the negative space-charge of the electrons on the traps, what follows from our results obtained by the investigation of the conductivity in the MIM-system at the medium vacuum (10^{-5} Torr). Fig. 1, 2 show temperature dependences of I_c and I_e . On the interval $T = 80$ to 150 K they have an anomalous character: the conductivity decreases with increase of temperature. I - V characteristic of the conduction current there appears an area of the negative differential resistance (fig. 3). These special features may be probably explained by the sorption effects. The electronegative molecules of the residu-

al gases (in the first place - oxygen) being absorbed on the walls of channels of increased conductivity trap the electrons and form the negative space-charge. The temperature growth leads to their desorption and, consequently, to the current rise. On the contrary, the hydrogen absorption leads to the current rise (Kimura et al 1980) since a localized states area appears in the forbidden zone. This causes the jumping conductivity current growth. The explanation of the N - form of the I - V characteristic for this case is given by Dearnaley et al (1970).

1.4 Measuring of noise characteristics of conduction and emission current within wide range of temperature shows a great lowering of noise level up to high frequency at the decrease of temperature up to 4,2 K. This speaks about suppression of explosive emission processes at metal-insulator border at low temperature and stabilization processes in channels of increased conductivity body.

1.5 Research of MIM-system behaviour with short (10^{-7} Sec.) pulses of operating voltage showed, that I_c and I_e - pulse amplitude depends from amplitude of previously pulse voltage also ("mutual pulse interference effect"). That is every pulse reverse the MIM-structure in a new state ("memory effect"). In "high" vacuum these effects are absent. We can say that we meet with sorbtion effects on the impurity centres in forbidden band of insulator - space charge is accumulate on this centres.

1.6 Investigated non-heated cathodes have the following working parameters; emissive current density $\sim 10 \text{ mA/cm}^2$, effectiveness $\sim 10^{-2}$, durability in impulse regime and in low temperature ~ 2000 hours. We showed (in non-published works) a principal possibility of vacuum microelectronics problems solving with MIM-cathodes

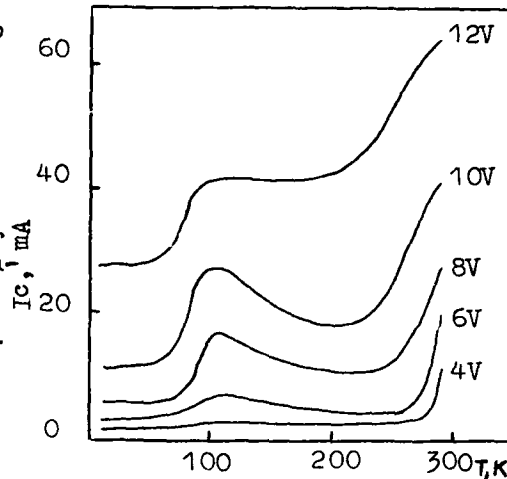


Fig. 1. Temperature dependences I_c at the different voltage

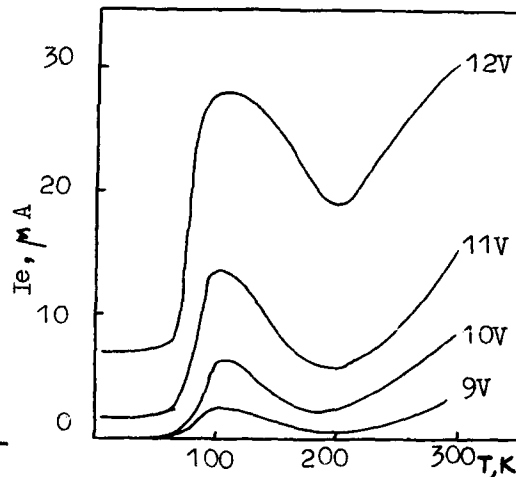


Fig. 2. Temperature dependences I_e at the different voltage

even now by the example of vidicon with cold cathode, thin film vacuum diode, triode and defelectron, ionization non-heated manometer, etc.

In these special apparatuses we used those or other differentiative positive qualities of our cathodes: low operating temperature and possibility of cooling MIM-cathodes for vidicon of infrared range of wave length; low operating temperature and thin film manufacturing for active elements of vacuum integral circuits; low operating temperature and as a result no influence on surrounding atmosphere and impulse control directly on MIM-cathode operating circuits for special measuring non-heated manometer.

Our experiments with switching and memory effects of MIM-systems are expected to be favorable. The first experiments showed, that the electron emission from local areas (the top of the channels of increased conductivity) allows to receive the electron emitter with a light emission area for solving of special electron-beam tasks.

We see commercial use of MIM-cathodes in such unique tasks which can be solved only with their help and with the condition that engineers will meet them halfway.

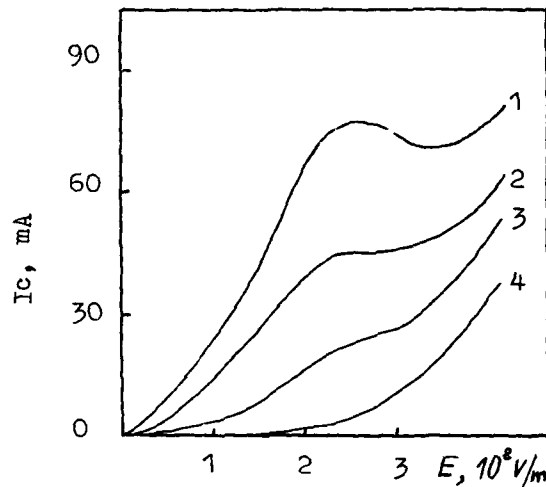


Fig. 3. I - V characteristics of Ic: 1 - $T = 293$ K, 2 - $T = 150$ K, 3 - $T = 40$ K, 4 - $T = 4.2$ K

II References

- Athwal C S, Bayliss K H, Calder R and Latham R V 1984 Proc. XI th. ISDEIV (Berlin) 2 pp 77-82
 Dearnaley G, Stoneham A M and Morgan D V 1970 Rep. Prog. Phys. 33 pp 1129-1191
 Kimura T, Yamamoto K and Shimizu T 1980 Thin Solid Films 70 pp 351-362
 Yankelevitch Yu 1979 Vacuum 30 N 3 pp 97-107
 Yankelevitch Yu, Barenholz Yu, Khaskelberg M and Yankelevitch B 1988 Proc. XIII th. ISDEIV (Paris) 1 pp 19-21

Simulation and design of field emitters

R.B. Marcus^a, K.K. Chin^b, Y. Yuan^c, H. J. Wang^c, and W. N. Carr^d

a) Bellcore, 331 Newman Springs Road, Red Bank, NJ 07701

b) Physics Department, NJIT, Newark, NJ 07102

c) Electrical Engineering Department, NJIT, Newark, NJ 07102

d) Physics and Electrical Engineering Departments, NJIT, Newark, NJ 07102

ABSTRACT

Electron emission and Joule heating are modeled for conical tip and wedge-shaped electron field emitters as a function of changes in emitter shapes.

INTRODUCTION

A surging interest in vacuum microelectronics (Greene, et. al., 1986) has resulted in numerous proposed advanced device structures which utilize the cold cathode or field emitter as electron source. However, a number of fundamental questions remain unanswered which are essential to the design of field emitters and which are guided by limitations imposed by processing methods and capabilities. In this paper we discuss two generic emitter structures, a cone and a wedge, and calculate effects of realistic variations in geometry on emission current, spatial and temporal dispersion of electron emission, and on emitter heating. Calculations are performed analytically and by computer simulation. Simulations are made with SIMION 4.0 simulation software, which was developed by D.A. Dahl and J. E. Delmore of the Idaho National Engineering Laboratory and modified for calculation of electric fields and solution of the Fowler-Nordheim equation (Spindt, et. al., 1976)

$$J = AE^2 \exp \left\{ -B \frac{\Phi^{3/2}}{E} \right\} \quad (1)$$

For purposes of simulation the conical tip is approximated by part of a spherical surface, and the wedge-shaped emitter tip is approximated by part of a cylindrical surface (Fig. 1). In all cases where wedge emission is compared with conical tip emission the basal areas of the two emitters are made the same. Fig. 1 also defines various parameters used in the calculations. The main design parameters considered are the cathode-to-anode spacing (d in Fig. 1), the radius of curvature of the emitter r , the cone or wedge half-angle θ , and the height of the emitter tip from the surface h . These quantities can be controlled during processing to varying extent. In addition the angle ϕ which represents the deviation from the normal at the emitting surface (origin at end of radius r) is an important parameter in calculating temporal and spatial dispersion of emitted electrons. The sheath length L can be controlled by simple lithography.

Simulation results are shown graphically in Figs. 2-7, and values for the essential parameters are given in Table I. The effect of Joule heating on the tip temperature is given in Table II.

DISCUSSION

While conical tips are most commonly used as electron field emitters, wedge-shaped emitter surfaces have been proposed and used in a few cases (Chesnokov, et. al., 1976; Spindt, et. al., 1983; Marcus, et. al., 1988; Spallas, et. al., 1989). In most comparisons of emission current or current density, wedges with the same basal area as cones have significantly reduced emission

TABLE I

Values for various parameters used in the simulations

Fig No	$d(\mu\text{m})$	$r(\text{nm})$	$h(\mu\text{m})$	$\theta(\text{deg})$	$V(\text{volts})$	$L(\mu\text{m})$	$\Phi(\text{eV})$
2	--	50	1	20	500	62.8	4.5
3	.5	--	1	20	500	62.8	4.5
4	.5	50	--	20	500	62.8	4.5
5	.5	50	1	--	500	62.8	4.5
6,7	.5	50	1	20	500	62.8	4.5

Table II

Heating effect in conical and wedge-shaped tips

material	$\kappa(\text{W/cm}^2 \text{ K})$	$\rho(\omega\text{-cm})$	$I = 150\mu\text{m}$			$I = 50\mu\text{m}$		
			$T_{\text{ca}}(^{\circ}\text{C})$	$T_{\text{w}}(^{\circ}\text{C})$	$T_{\text{bw}}(^{\circ}\text{C})$	$T_{\text{ca}}(^{\circ}\text{C})$	$T_{\text{w}}(^{\circ}\text{C})$	$T_{\text{bw}}(^{\circ}\text{C})$
Si	1.5	$6 \times 10^{-3} *$	1.024	0.103	0.0114	0.114	0.0114	1.27×10^{-3}
Ge	0.6	$2 \times 10^{-3} *$	0.85	0.085	9.4×10^{-3}	0.094	9.4×10^{-3}	1.05×10^{-3}
GaAs	0.46	$3.8 \times 10^{-4} *$	0.21	0.021	2.36×10^{-3}	0.023	2.33×10^{-3}	2.62×10^{-4}
Mo	1.38	5.7×10^{-6}	1.05×10^{-3}	1.05×10^{-4}	1.18×10^{-5}	1.17×10^{-4}	1.17×10^{-5}	1.31×10^{-6}
W	1.73	5.6×10^{-6}	8.24×10^{-4}	8.24×10^{-5}	9.23×10^{-6}	9.16×10^{-5}	9.16×10^{-6}	1.03×10^{-6}

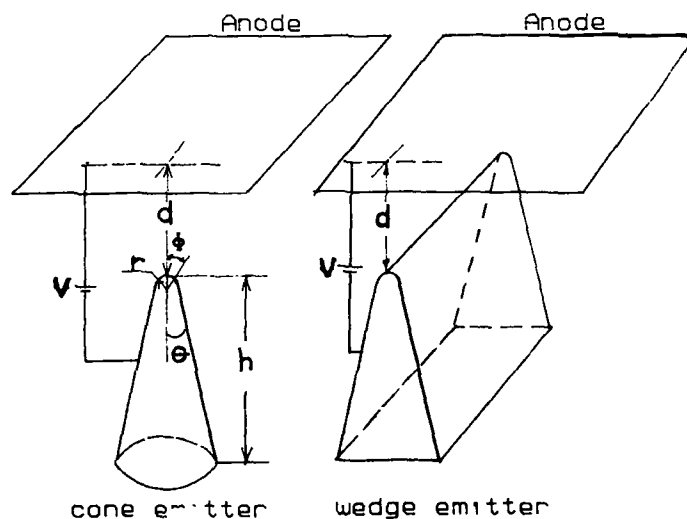
* $N_D = 10^{19} \text{cm}^{-3}$.

Fig. 1 Models of cone and wedge-shaped emitter structures assumed for simulation, defining parameters and showing positions with respect to anode.

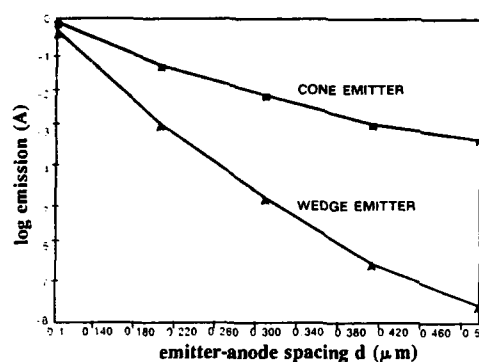


Fig. 2 Effect of emitter-anode spacing d on emission for wedge and cone emitters.

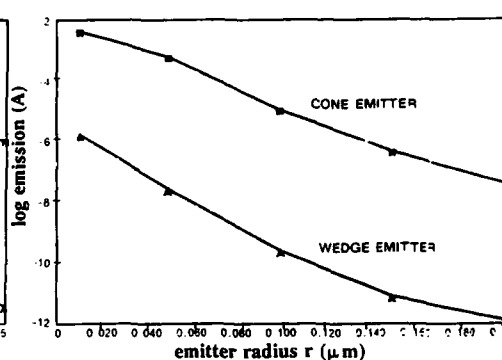


Fig. 3 Effect of tip radius r on emission for wedge and cone emitters.

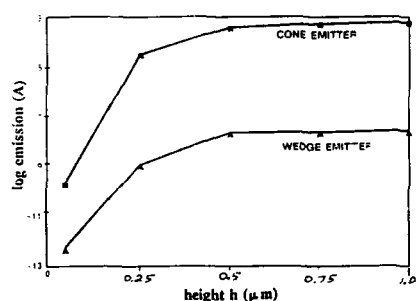


Fig. 4 Effect of tip post support height h on emission for wedge and cone emitters.

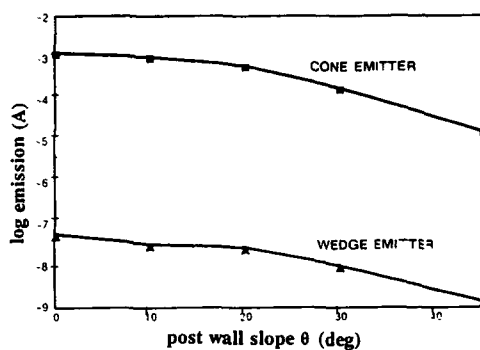


Fig. 5 Effect of wall slope θ of tip post on emission for wedge and cone emitters.

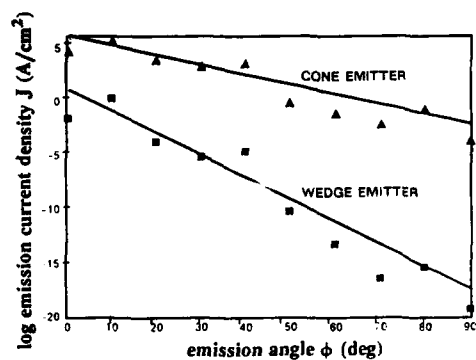


Fig. 6 Effect of emission angle ϕ on emission from wedge and cone emitters.

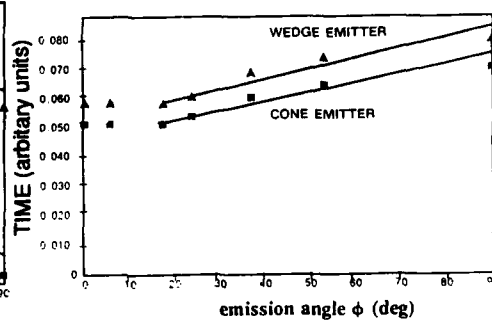


Fig. 7 Temporal dispersion of emission from wedge and cone tips.

(see Figs. 2-6). Cone and wedge performance converge and improve as the emitter-anode spacing becomes smaller for a given radius r and as the systems approximate a parallel plate capacitor (Fig. 2). Both performances also improve without converging as post height increases to a value comparable to the emitter-anode spacing (Fig. 4). The slope of the side-wall support post has a small influence on the performance of both structures; changing from a vertical-wall post to one with a half angle of 20° only reduces emission to about $1/3$ (Fig. 5). Current density fall off in a direction away from the tip normal, and the drop is faster for wedges than for conical tips (Fig. 6). Temporal dispersion resulting from varying electron transit times from a curved emitter (Fig. 7) may therefore be less of a problem from wedges, where most of the emission is concentrated near the tip normal.

It is clear from the calculations shown in Table II that temperature rise due to Joule heating is very small for all materials considered under the boundary conditions given. This result is consistent with the analyses of McCord and Pease (1985), Dolan, et. al., (1953), and Gray and Moglestue (1987).

Three arguments support the use of wedge emitters, although the strength of these arguments depend on the application: 1) Sneaky processing tricks may permit wedge tips to be made with very high curvature, significantly higher than might be attainable with conical tips. Two examples of such tricks have been described (Spallas, et. al., 1989; Marcus, et. al., 1988). As shown in Fig. 3 a small wedge tip radius may offset some or all of the loss incurred in moving away from a conical tip. 2) Wedges offer an advantage where point sources are not necessary, and a greater fraction of the available substrate surface area can be utilized for support of emitting elements. 3) Heat is dissipated more readily through wedges and temperature rises are much smaller (Table II). This may be a decisive factor in protecting against thermal runaway during tip "disruption" (Spindt, et. al., 1976) or against Nottingham heating, should that prove to be significant.

REFERENCES

- [1] V.V. Chesnokov, V.M. Gaiies, A.M. Domakhina, L.S. Simenshtein, Sh. Sh. Sattarov, V.A. Ugarov, and B.K. Bogomolov, *Izvestiya Akad. Nauk SSSR*, **40**, 1585 (1976).
- [2] W.W. Dolan, W.P. Dyke and J.K. Trolan, *Phys. Rev.* **91**, 1054 (1953)
- [3] H. Gray and C. Moglestue, 34th Int. Field Emission Symposium, Osaka, July 1987.
- [4] R. Greene, H. Gray and G. Campisi, *Proceed. IEDM* **85**, 172 (1986).
- [5] R.B. Marcus, R. Soave and H.F. Gray, *Proc. 1st Intern. Conf. Vac. Microelec.*, Williamsburg, June 13-15, 1988, paper 8-4.
- [6] J.P. Spallas, C. Chen, S.C. Amey and N.C. McDonald, *Proc. 2nd Intern. Conf. Vac. Microelec.*, Bath, July 24-26, 1989.
- [7] C.A. Spindt, I. Brodie, L. Humphrey and E.R. Westerberg, *J. Appl. Phys.*, **47**, 5248 (1976).
- [8] C.A. Spindt, C.E. Holland, R.D. Stowell, *Appl. Surf. Sci.*, **16**, 268 (1983).
- [9] M.A. McCord and R.F.W. Pease, *J. Vac. Sci. Tech.*, **B3**(1), 198 (1985).

Electrical characterization of gridded field emission arrays

D.F. Howell, R.D. Groves, R.A. Lee, C. Patel and H.A. Williams

GEC Hirst Research Centre, East Lane, Wembley Middlesex, HA9 7PP, UK.

We report the results of experiments on gridded arrays of wet-etched silicon field emission tips. Both I-V measurements and angle resolved electron emission spectra are presented. We found that emission occurred from a small fraction of the available surface area with an anomalously small radius of curvature. The spectroscopic measurements revealed that the emission originated from several eV below the Fermi energy in the silicon and that the linewidth was narrow with $\Delta E = 0.28\text{eV}$ (FWHM).

In this paper we present the results of experimental measurements on gridded arrays of silicon field emission tips, which have recently excited considerable interest as potential electron sources for vacuum electronic applications, both as direct replacements for thermionic cathodes and as a basis for very small novel devices. Such a gridded structure is illustrated schematically in Figure 1. In addition to discussing the basic electrical characterisation of these structures, we present some preliminary angle resolved measurements of the electron energy distribution. These results provide information on the basic electronic processes at the surface of the emitters and enable the performance of these structures to be assessed for potential device applications.

The structures took the form of 10×8 rectangular arrays with a spacing of $10\mu\text{m}$ between adjacent tips. They were fabricated from n-type silicon ($N_d \approx 10^{18}\text{cm}^{-3}$) by wet-etching in KOH solution using a photolithographically defined silicon dioxide mask consisting of an array of $2\mu\text{m}$ square pads. After mask removal the tips were sharpened by a differential oxidation process. The final height of the tips was approximately $2\mu\text{m}$. Before depositing the dielectric layer the tips were diffusion doped to $N_d = 10^{20}\text{cm}^{-3}$. The dielectric was 6% phosphorus doped silica glass (PSG) grown by the dissociation of silane at 350°C . This layer was then planarised by the repeated deposition and sacrificial etch back of spin on glass. The grid metal was Al doped with 1.5% Si, sputter deposited to a thickness of $0.5\mu\text{m}$. The grid holes, nominally $1\mu\text{m}$ in diameter, were defined by UV photolithography and wet etched in a proprietary aluminium etch. Finally the dielectric surrounding the tips was removed by wet etching in an acetic acid and ammonium fluoride solution.

Basic electrical measurements were made with the aid of a plate anode mounted parallel to and about 1mm above the grid. In addition, angle resolved measurements of the energy distribution were performed with a VG CLAM 100 concentric hemispherical electron energy analyser which has an ultimate resolution approaching 20meV and an acceptance angle of order 1° (measured at the sample position).

Figure 2 depicts an I-V curve and a Fowler-Nordheim (FN) plot [Fowler and Nordheim (1928)], with the latter being a reasonable approximation to a straight line. The error bars ($\pm 10\%$) represent the approximate mean value of the observed fluctuations in current. If we assume a value for the work function Φ , the FN plot allows us to calculate

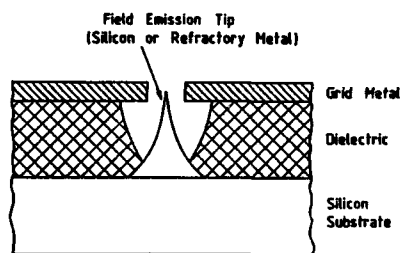
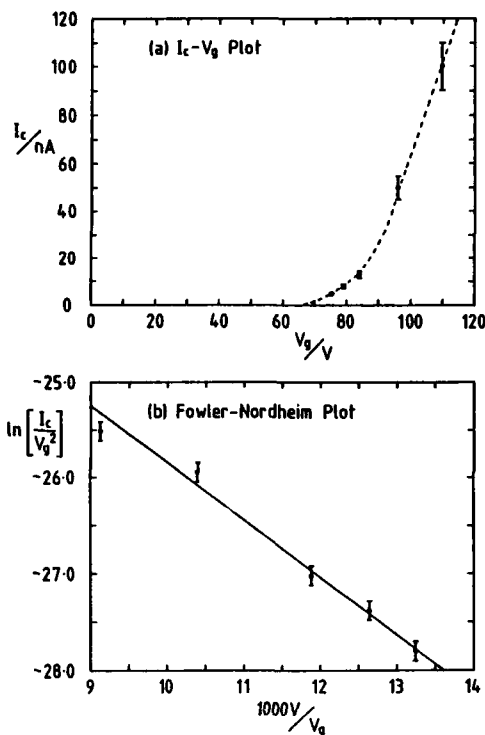


Figure 1: A schematic cross-sectional view through a gridded field emission tip.

Figure 2: (a) An I-V curve and (b) a Fowler-Nordheim plot for a typical 10×8 array of gridded silicon field emitters.



F_0 , the electric field at the surface and S , the total area from which emission originates. A value of $\Phi = 4.5\text{eV}$ [Thanailakis (1974)] gives $F_0 = 0.8 \rightarrow 1.2\text{V}/\text{\AA}$, (corresponding to a field enhancement factor of around 200) and $S = 57\text{\AA}^2$. This value for the total emission area is extremely small, corresponding to a fraction of the surface area of a single tip. Even allowing for the error in the gradient of the FN plot, the maximum reasonable value for S is of order 200\AA^2 .

Using the field enhancement approximation [Cade (1989)], an enhancement factor of 200 corresponds to a tip radius $R \approx 45\text{\AA}$, which is considerably smaller than suggested by scanning electron micrographs of this sample. These values are not very sensitive to the choice of work function since even a value as small as $\Phi = 3.0\text{eV}$ gives $S \approx 130\text{\AA}^2$. A current of 100nA emitted from an area of 100\AA^2 corresponds to a very high current density of 10^{11}Am^{-2} . The small values for S and R deduced above are consistent with previous measurements on other similar systems [Spindt *et al.* (1976) and Brenac *et al.* (1987)]. The most likely explanation for these low values is that the emission originates from sharply pointed features which protrude above, and possibly also have a lower workfunction than, the surrounding tip material. It is possible that these features are centred around dopant atoms since we have found that the etch rate is affected by the dopant concentration.

By biasing the anode close to cathode potential we create a crude retarding plate energy analyser. Figure 3 shows a typical plot of normalised anode current I_a/I_c against anode voltage V_a for two different grid voltages V_g . The derivative $\partial I_a/\partial V_a$ of these curves is effectively a measure of the axial energy distribution of the electrons at the plane of

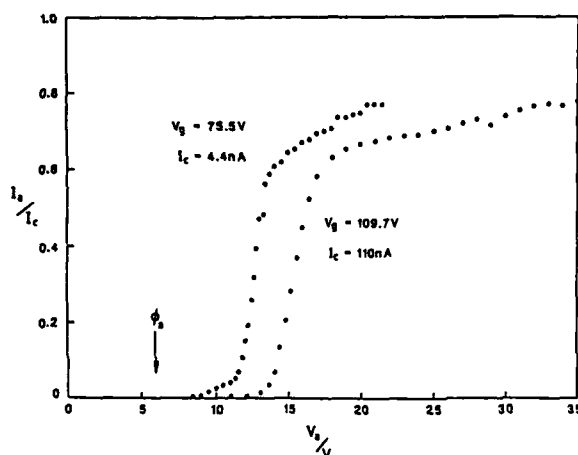


Figure 3: Two typical plots of the normalised anode current against anode voltage for the retarding plate mode. Notice that no anode current flows until V_a is substantially greater than Φ_a , the anode work function. This implies that the axial energy of the electrons leaving the grid is less than $V_g - V_c$.

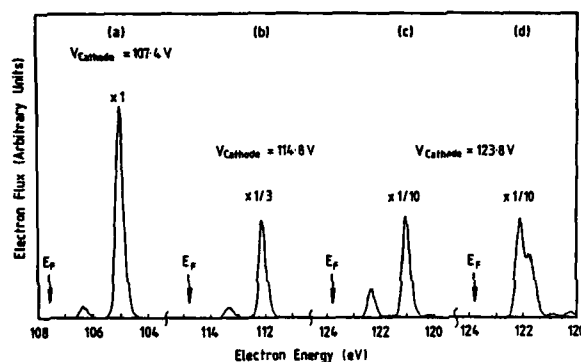


Figure 4: Typical electron energy spectra recorded with the sample orientation adjusted so as to maximise the electron flux collected by the spectrometer. The arrows indicate the estimated positions of the cathode Fermi energy in each case.

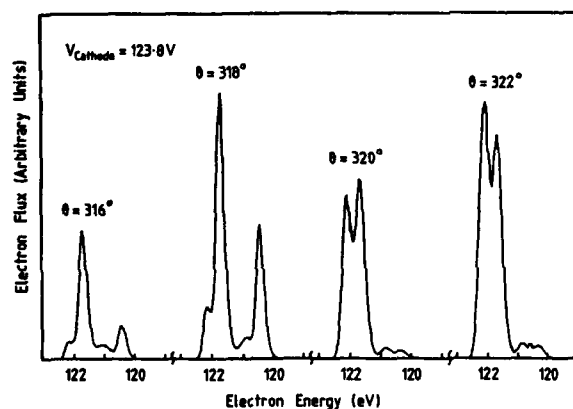


Figure 5: A typical series of spectra recorded in 2° steps close to the direction along which the emission was a maximum

the grid. Unfortunately, due to the small size of the grid, the analysis is complicated by the presence of fringing fields. However, it is clear that the axial energy distribution is strongly peaked with the maximum occurring some way below the Fermi energy in the cathode. This suggests either that the electrons have a substantial transverse component to their velocity or that emission is taking place from below the Fermi edge in the silicon.

Note that the effect of the fringing field is to reduce any radial velocity that the electrons may have.

Turning to the experiments performed with the CLAM energy analyser (in which a different sample was used), Figure 4 depicts a typical series of spectra recorded with the sample orientation adjusted so as to maximise the total electron flux collected by the spectrometer. Figures 4(a)–(c) show the effect of varying the cathode-grid voltage (for these measurements the cathode was negative and the grid grounded to ensure that there were no electric fields in the vacuum chamber). The most obvious features are that emission occurred at several energies and that, significantly, all of them lie below the Fermi energy in the cathode. A subsequent check of the spectrometer calibration against the electrometer used to measure the cathode bias revealed agreement to within $\pm 0.03\%$. Although a simple ohmic resistance would be insufficient to account for the entire shift to below the Fermi energy, some dissipative process is implied by the small shift down in the energy of the main peak with increasing cathode bias. It is clear from Figure 4(d), recorded under identical conditions to Figure 4(c) the following day, that we cannot yet attach any fundamental significance to the detailed structure in these spectra.

High resolution measurements of the main peak in Figure 4(a) clearly demonstrated the narrow linewidths attainable from field emission cathodes with $\Delta E = 0.28\text{eV}$ (FWHM). This value is consistent with a simple model based on FN theory [Bell and Swanson (1979)], although the emission in the model occurs close to the Fermi energy.

Figure 5 shows some typical spectra in which the angle was varied in 2° steps close to the direction along which maximum emission occurred. It is clear that the angular distribution was very complex with given spectral features changing rapidly as the angle was varied. The overall angular distribution was also very narrow with the total electron flux falling to 10% of its maximum value at $\pm 6^\circ$, although several weak maxima ($\leq 3\%$) could be observed at angles up to $\pm 20^\circ$ away from the direction of the main peak.

In conclusion, we have demonstrated reliable field emission from several gridded arrays of wet-etched silicon tips. The results of I-V measurements indicate that emission took place from a small area of order 100\AA^2 , and that, although the current observed was quite small, the current density was extremely large ($\sim 10^{11}\text{Am}^{-2}$). We have also shown that field emission from these structures has a very narrow energy distribution and occurs over a small range of angles. Both of these are desirable features for potential device applications. The detailed structure of the angle and energy distributions is complex and suggests that the surface electronic structure may be important, at least for a semiconductor.

We wish to acknowledge valuable discussions with Drs N.A. Cade and R. Johnston.

References:

- Bell AE and Swanson LW (1979) *Phys. Rev. B* **19** 3353
- Brenac A, Baptist R, Chauvet G and Meyer R (1987) *Revue Phys. Appl.* **22** 1819
- Cade N (1989) *2nd Int. Conf. on Vacuum Microelectronics (Bath, 1989)* (in press)
- Fowler RH and Nordheim LW (1928) *Proc. Roy. Soc. London A* **119** 173
- Spindt CA, Brodie I, Humphrey L and Westerberg ER (1976) *J. Appl. Phys.* **47** 5248
- Thanailakis A (1974) *Inst. of Phys. Conf. Ser. No. 22* p59

Energetic characterization of field emission cathodes

R. Baptist, A. Ghis and R. Meyer

CEA/IRDI - Division LETI - D.OPT - 85X - 38041 GRENOBLE Cédex FRANCE

ABSTRACT : The energetic characteristics of field emission cathodes consisting of 10 000 micron sized tips are presented. Typical energy distribution curves show an energy resolution ΔE (full-width-at-half-maximum (FWHM)) of the order of 0.3 eV for electrons emitted with a kinetic energy of 55 eV and a beam current of 10 μA .

1. INTRODUCTION

Recently Brenac et al (1987) have published the measurements of the energy distribution curves (EDC) as a function of the kinetic energy for electrons emitted from field emission cathodes. These cathodes consisted of a large number of micron sized tips arranged at the surface of a component and realized using thin film technology. *Emphasis was also placed* on the difficulties of measuring such EDCs for beam currents which either saturate the electron spectrometer power supplies (and detectors) or produce strong parasitic phenomena due to space-charge effects and reflections on the walls of the spectrometer or its elements (slits, einzel lens, etc). However, by using different techniques we were able to show that the measured ΔE values (for example $\Delta E = 0.9$ eV for electrons emitted at ≈ 60 eV with a beam current of ≈ 100 μA) were essentially due to voltage drops occurring at the interface between the tips and the substrate.

In the present work, we describe the performance of two types of cathodes. We conclude that when the electrical contact between the tips and the metallic substrate is conductive, then the energy spread is of the same order than the one observed from a thermionic electron beam.

2. ENERGY DISTRIBUTION OF THE FIELD EMITTED ELECTRONS

Cathodes of two different types were observed. The type I cathode similar to those described by Brenac et al (1987) consisted of 10 000 molybdenum tips deposited on a "resistive" silicon substrate ; the type II cathodes consisted of 10 000 tips of a Fe/Ni alloy deposited on a thin metallic sodium oxide film.

For emission currents below 1 μA we have measured the EDC's using the previous deflecting spectrometer (Brenac 1987). For higher currents (up to 10 μA), these measurements were done using another spectrometer described by Drouhin and Eminyan (1986). This spectrometer associates a cylindrical electrostatic deflection analyzer and a Faraday cup

collecting the electron beam. This analyzer provides the possibility of suppressing the "unwanted" electrons by collecting them on plates surrounding thin highly transparent grids. The role of these grids is to fix the values of the various electrode potentials in order to determine the electron pass energy value. For both analyzers, the resolution was approximately 50 meV.

Fig.1 presents two EDC's for electrons emitted at an energy of 31 eV (the $E = 0$ eV energy value refers to the Fermi level of the spectrometer). The energy at which electrons are detected is then equal to the voltage difference applied between the tips and the gate times the electron charge. The cathode is a type I cathode. As observed, the EDC's for both acquisition times are similar.

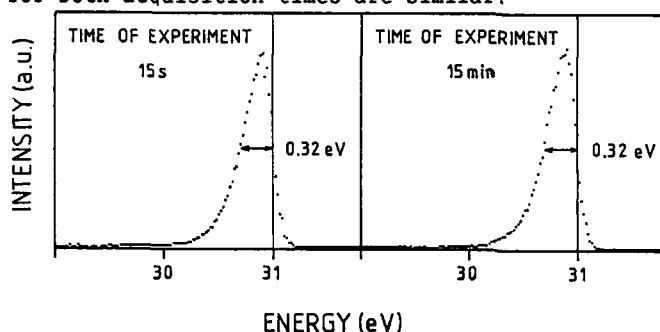


Fig.1 : EDC's recorded during two different acquisition times (15 sec. or 15 min) for electrons having an energy of 31 eV.

These EDC's are asymmetric at around 31 eV with a smooth decrease towards lower energy. The FWHM (ΔE) is of 0.32 eV for an emission current in the nanoampere range. When going to higher energies, 35 eV or 38 eV (fig.2) we observe first a change of the curve shape concomitant with an increase of the energy spread and secondly a shift towards lower kinetic energies. This shift is attributed to the voltage drop at the interface resistance which naturally increases in the same way as the emission current.

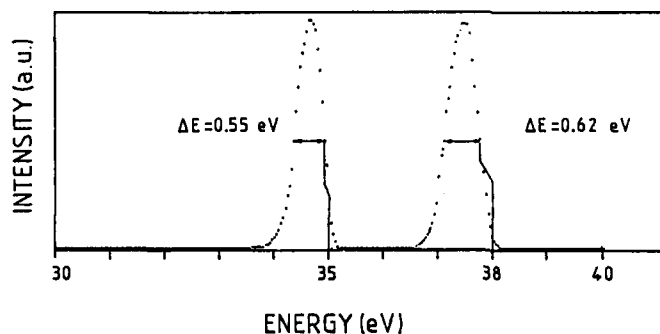


Fig.2 : EDC's recorded for electrons having an energy of 35 eV or 38 eV.

Fig.3 presents an expanded view of fig.2 (35 eV) which enhances the signal corresponding to all secondary electrons generated at energies below 35 eV. As observed, the magnitude of this background is completely negligible in comparison with the intensity of the principal peak.

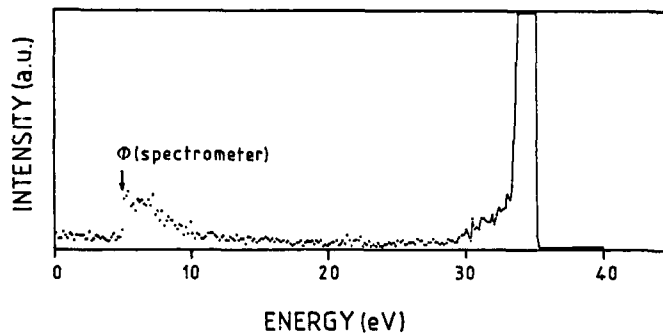


Fig.3 : Expanded spectrum of electrons having an energy of 35 eV.

When operating at low energy (< 40 eV) with type II cathodes, we observe similar curves except that the EDC's are narrower and do not show any shift. At higher energy it is necessary to use the second spectrometer. Fig.4 presents a spectrum recorded at high energy (55 eV) for a $10 \mu\text{A}$ emission current. We can see that the shape is totally asymmetric and that no shift occurs : the interface resistance is so small that no shift is detectable at this emission current. If we neglect the spectrometer resolution, we can easily derive upper values for the two parameters d and kT involved in the formulation of the theoretical total energy distribution dJ/dE (Young 1959, Swanson and Crouser 1967, Bell and Swanson 1979). This equation is :

$$\frac{dJ}{dE} \propto \frac{\exp(E - E_F)/d}{d(1 + \exp(E - E_F)/kT)}$$

where : $E - E_F$ is the electron energy relative to the Fermi level E_F of the tip material,

kT is the temperature of the emitting tip area,

and d is a parameter given by the following formula :

$$d(\text{eV}) = 0.93 \times 10^{-10} |\vec{E}| / \phi^{1/2} (\text{eV}),$$

\vec{E} being the applied electric field at the extremity of the tip and ϕ the work function of the tip material.

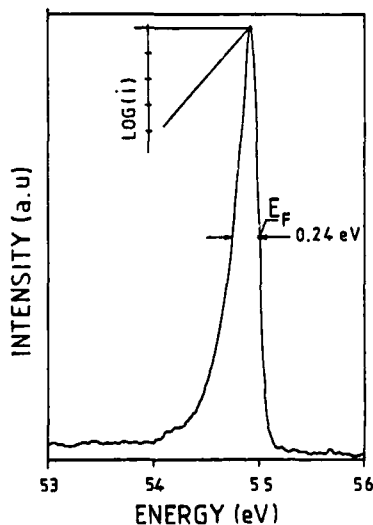


Fig.4 : EDC recorded for electrons having an energy of 55 eV (Inset : log (intensity) versus energy).

The values found for kT and d are $kT \approx 0.030$ eV and $d \approx 0.3$ eV. The experimental shape is interpreted as follows : at around E_F , the decrease is due to the cut-off (over a width $2 kT$) of the Fermi distribution function calculated at ambient temperature ; below the curve maximum, the decrease is purely exponential ($\exp (E - E_F)/d$). It reflects the gradual difficulty encountered by the electrons whose energies are more and more inferior to E_F and then cannot tunnel through the triangular potential barrier present at the surface.

For this type of cathode the total width ΔE , which normally depends on both d and kT , is then of the order of ΔE ($d, kT = 0^\circ K$). Its value (0.23 eV) is lower than the energy spread that is found for thermoionic cathodes and even for alkali oxides cathodes. Furthermore, as the cut-off value (E_F) does not depend on the temperature (which is low), these cathodes can be used for the calibration of electron spectrometers with an incertitude of ± 50 meV.

3. CONCLUSION

The experimental results presented in this paper demonstrate that regarding the energy spread of the emitted electron beam current, highly performant field emission cathodes can be achieved. Moreover the emission currents are more stable than those previously observed. These improvements are connected with better quality control of the different steps of the fabrication process and better cleaning procedures for the tips.

In any case progress in these directions has to be made before using such cathodes in common electron guns.

Acknowledgements : We thank the Department de Recherche Fondamentale (CEN/G) at which these measurements were performed. We would like also to thank Dr Drouhin and Prof. G. Lampel (Ecole Polytechnique Paris) for their fructuous collaboration.

- Bell A E and Swanson L W 1979, Phys. Rev. B 19, 3353
Brenac A, Baptist R, Chauvet G and Meyer R, 1987, Revue Phys. Appl. 22, 1819
Drouhin H and Eminyan M, 1986, Rev. Sci. Instrum. 57, 1052
Swanson L W and Crouser L C, 1967, Phys. Rev. 163, 622
Young R D 1959, Phys. Rev. 113, 110

Fluctuation phenomena in field emission from molybdenum micropoints

I. Brodie
SRI International, Menlo Park, California 94025 USA

Abstract: The field emission of electrons from untreated molybdenum tips with radii in the range of 300Å - 1200Å appears to come from one or a few atomic sites. Modulation of the emission from these sites gives rise to bursts of current pulses quantitatively similar to those observed in p-n junction devices of germanium and silicon.

1. Introduction

Field emission tips for vacuum microelectronic devices may be formed by a variety of techniques (First International Conference on Vacuum Microelectronics, Williamsburg, Virginia, USA, 1988) including etching and deposition from the vapor phase. However, since the tip radii are in the range of 200Å to 500Å the emitting area cannot be unambiguously defined even in the case where the original tip material is a single crystal. This is because irregularities in the tip forming process combined with strongly adsorbed surface impurity molecules prevent a simple form being given to the tip surface. In the classical Muller technique (Good and Muller, 1956) a single crystal is formed at the tip and the adsorbed molecules removed from the surface by heating it to very high temperatures (greater than 2500 K). Due to the thermodynamics of crystal growth however, this process usually leads to the development of a single crystal at the tip with a radius between 2000Å and 10,000Å, even if the original tip radius was much smaller (Dyke and Dolan, 1956). For vacuum microelectronic devices tip radii in the range of 200 to 500Å are necessary in order to obtain field emission at low operating voltages, in the 10-100V range. This means that the field emitting tip is necessarily imperfect in the classical sense.

2 The Emitting Area

The area from which field emission originates can be estimated from the Fowler-Nordheim theory to better than 10% accuracy without a knowledge of the work function (assuming it to be in a range of 3.4 eV to 11.6 eV) (Van Oostrom, 1962). This is done by simply measuring I , V , and dI/dV at various points along the current-voltage characteristic (Spindt, et al. 1976).

Table I shows results for several untreated molybdenum tips with radii in the range of 300Å to 1200Å. It will be seen that the areas correspond to one or few atomic sites at each tip. There is obviously some question as to whether the Fowler-Nordheim theory is valid for this case, however the linearity of the Fowler Nordheim plots combined with the nature of emission micrographs from such points and metal whiskers seems to corroborate the hypothesis that the emission comes from single atomic sites (Brodie, 1978).

Table I
Field Emitting Area for Different Cathodes
Estimated from Fowler-Nordheim Plots

Cathode Type	Tip Radius (Measured on SEM)	Emitting Area (Square Å)	No. of Lattice sites (assuming for Mo, 1 lattice site occupies 13 Å squared)
1. Spindt single tip	300Å	13	1
2. Spindt Multiple tips	300Å	13 per tip	1
3. Etched Wire	500Å	50	4
4. Etched Wire	1200Å	710	27

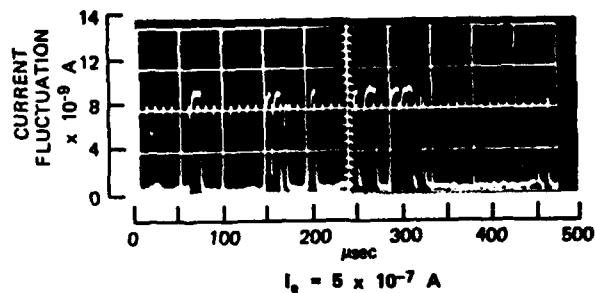
3. Burst Noise

If the current at a fixed voltage is measured in ultra-high vacuum (less than 10^{-9} torr), as a function of time for these small tips the phenomenon of burst (or popcorn) noise is seen. Burst noise, which is also commonly observed in semiconductor devices (Wolf and Holler, 1967, and Hsu et al. 1970), consists of sequences of bi-stable current pulses of certain specific amplitudes but of random pulse lengths and random intervals between pulses. These sequences of current pulses are separated by quiescent periods which may be of the order of tens to hundreds of seconds. The burst noise sequences themselves may last from hours to milliseconds. As the time resolution is increased, a given burst current pulse can itself be seen to consist of pulses of similar character, with a limiting pulse length being of the order of microseconds for field emission and milliseconds for semiconductor devices.

Figure 1(a) shows a noise burst from a single tip Spindt cathode delivering a base emission current of 0.5 mA, and Figure 1(b) shows a noise burst from an etched molybdenum point radius $\sim 500\text{Å}$ delivering a base emission current of 1.0 mA. In the first case the pulse height is 10^{-8} A and in the second case 2×10^{-8} A, giving the same ratio of pulse height to base current of 10^{-2} (1%). For the etched molybdenum tip the current pulse height ΔI was measured as a function of the base emission current I_e as shown in Fig. 2(c). It will be seen that ΔI appears to saturate at a value of $2 - 3 \times 10^{-8}$ A as I_e is increased above 10^{-6} A. This behavior is remarkably similar to that occurring in p-n junction devices of germanium (Wolf and Holler, 1967) (Fig. 2(a)) and silicon (Fig. 2(b)).

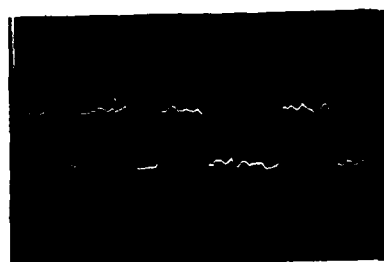
Note that pulse height saturation results occurs in all three cases in a device current range from 10^{-6} to 10^{-5} A. The similarity of behavior argues for a closely related mechanism causing the burst noise in both the solid state and the vacuum devices.

Noting that the current pulses in the solid state devices contained only about 10^8 electrons, Hsu, Whittier and Mead (1970) argued that the effect was due to modulation of the current flow by the change in occupancy of a single recombination-regeneration center created by a defect in the p-n junction. In field emission we have seen current pulses containing as few as 10^3 electrons arguing that the pulses are due to modulation of the emission from a single atomic site. Such modulation could occur due to changes in the work function or electric field at the site generated, for example, by changes in the vibrational state of an adsorbed impurity atom.



NUMBER OF ELECTRONS PER PULSE $\sim 5 \times 10^5$

Fig. 1(a) Burst noise pulses from a single tip Spindt cathode (short time scale)



10^{-8} A/div

50 $\mu\text{sec/div}$

$I_0 = 1 \times 10^{-6}$ A

$V = 850$ V

Number of electrons per pulse $\sim 10^7$



5×10^{-9} A/div

50 $\mu\text{sec/div}$

$I_0 = 1.3 \times 10^{-7}$ A

$V = 700$ V

Number of electrons per pulse $\sim 5 \times 10^5$

Fig. 1(b) Burst noise waveform from untreated etched molybdenum point. Tip radius $\sim 500 \text{ \AA}$

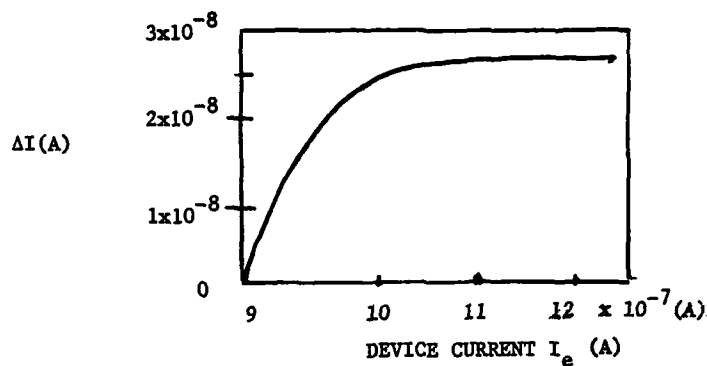


Fig. 2(a) Reverse Bias p-n Junction of Germanium (data from Wolf & Holler, 1967)

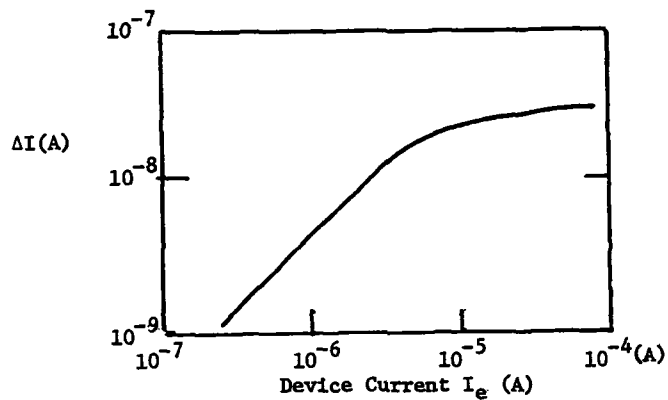


Fig. 2(b) Forward biased p-n junction of silicon (data from Hsu et al. 1970)

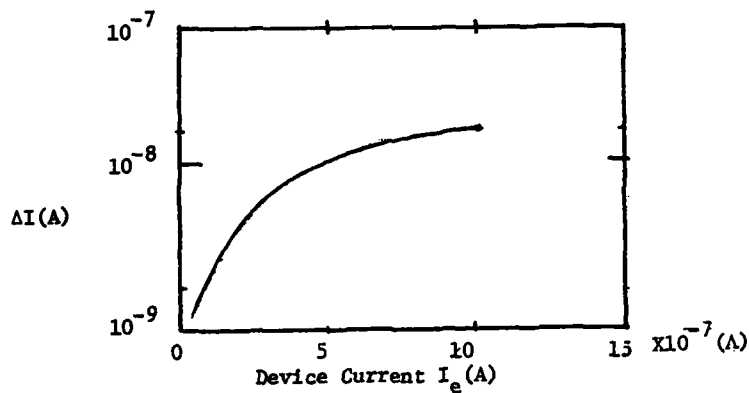


Fig. 2(c) Etched molybdenum field emission point, radius $\sim 500\text{\AA}$

4. Discussion

The nature of the emitting sites of untreated molybdenum tips used in vacuum microelectronics with radii in the range of 300Å - 1000Å remains obscure. However, the evidence points to the emission arising from one or a few atomic sites. Random current fluctuations of remarkably constant amplitude are superimposed on the emission and are apparently due to modulation of the work function or field at the emitting site.

The amplitude of the current pulses increases with increasing total emission but saturates at about 2×10^{-8} A when the total emission current exceeds about 10^{-6} A. The reason for this saturation is not understood. Current pulses may be as short as a few microseconds and contain as few as 10^5 electrons. The burst noise behavior of semiconducting p-n devices is quantitatively similar to field emission burst noise in all respects except that of the limiting pulse length which is 1000 times greater than that for field emission, and thus the smallest pulses contain 10^8 electrons in solid state devices rather than 10^5 as observed in field emission.

Acknowledgments

The author wishes to acknowledge the contributions made to this study by C.A. Spindt, L. Humphrey, E.R. Westerberg and N. Couch.

References:

- Brodie, I. 1978 *Surface Science* 70, pp 286-196
- Dyke, W.P. and Dolan, W.W., 1956, *Advances in Electronics and Electron Physics* 8, pp 90-182
- Good, R.H., Jr. and Muller, E.W. 1956 *Handbuch der Physik* (Berlin, Springer-Verlag) pp 176-231
- Hsu, S.T., Whittier, R.J. and Mead, C.A., 1970 *Solid State Electronics* 13 pp 1055-1071
- Spindt, C.A., Brodie, I., Humphrey, L. and Westerberg, E.R. 1976 *J. Appl. Phys.* 47 pp 5248-5262
- Van Oostrom, A. 1962, *J. Appl. Phys.* 33 pp 2917-2922
- Wolf, D. and Holler, E. 1967 *J. Appl. Phys.* 38 pp 189-192.

A general formula to calculate the field intensity on the field emitter

Luo Enze, Liu Yunpeng and Huang Wenhui
Xidian University, Xian, China

ABSTRACT: A general formula of field intensity with respect to the average curvature of equipotential surfaces in the electrostatic field is derived. This formula when supplemented by data measured from experiment using an analogue technique can be used to calculate the field intensity on the tip of field emitter with any configuration accurately.

It lacks a general and accurate formula to calculate the field intensity at a point on the equipotential surface with high curvature in the electrostatics. Here we try to derive such a formula and apply it to calculate the field intensity on the tip of the field emitter.

1. Derivation of the formula

The derivation of such a formula was given in previous papers [1] and [2]. Here we give a simpler derivation.

It is known that the Laplace equation can be written as

$$dE/dn + 2kE = 0 \quad (1)$$

where E is the field intensity at a point in the field and the differentiation dE/dn is with respect to the outward normal of the equipotential surface with average curvature k at that point. (1) was established by George Green in 1828 [3]. As it is one of the more important equations in electrostatics, we will henceforth refer to it as Green's equation. We can express it as

$$dE/E + 2k(n)dn = 0 \quad (2)$$

or

$$dE - 2k(V)dV = 0 \quad (3)$$

Integrate (2) and (3) along the force line from a point with field intensity E_0 to a point with field intensity E , where the path increment is Δn and the potential increment is ΔV . Hence we have

$$E = E_0 \exp \left[- \int_0^{\Delta n} 2k(n)dn \right] \quad (4)$$

or

$$E = E_0 + \int_0^{\Delta V} 2k(V)dV \quad (5)$$

Substituting (4) into (5). We get

$$E_o = \frac{\int_0^{\Delta V} 2k(V)dV}{\exp\left(-\int_0^{\Delta n} 2k(n)dn\right) - 1} \quad (6)$$

let

$$\bar{k} = \frac{1}{\Delta V} \int_0^{\Delta V} k(V)dV, \quad \bar{k} = \frac{1}{\Delta n} \int_0^{\Delta n} k(n)dn \quad (7)$$

be the main value of the function $k(V)$ from 0 to ΔV and that of the function $k(n)$ from 0 to Δn respectively, then (6) can be written as

$$E_o = \frac{2\bar{k}\Delta V}{\exp(-2\bar{k}\Delta n) - 1} \quad (8)$$

(6) or (8) is the general formula which we want to find.

2. Application of the formula

The general formula (6) or (8) when supplemented by data measured from experiment using an analogue technique can be used to calculate the field intensity at any point in the field accurately.

The fabrication of a field emission cathode is a very interesting problem in modern electronics technology. In order to make the surface of the conductor produce a field electron emission, the field intensity on the surface of the conductor must be over 10^7 V cm^{-1} . According to formula (6) or (8) we know that in order to attain such high intensities, the potential difference ΔV between the electrodes should be enhanced. However, in order to enhance the stability of emission and the life of the cathode, the lower the ΔV the better. For the sake of getting high intensity at a lower potential difference, we must fabricate the tip of the cathode to a high curvature (i.e., increase k) and fabricate the gate electrode as near to the tip as possible (i.e. decrease Δn). We can fabricate such low potential difference field emission cathodes by thin film technology (now known as the Spindt device). However, to calculate the field intensity on the tip and in the field is a very complex electrostatic boundary value problem. By applying the general formula (6) or (8) to solve this problem, however, we can get the result in an easy way.

One of the emission cones of the thin film field emission cathode array is shown in figure 4. The curvature radius of the tip is $r=540\text{\AA}$, the height of the cone is $1.53\mu\text{m}$, the diameter of the base of the cone is $1.2\mu\text{m}$, the diameter of the aperture on the gate electrode is $1.5\mu\text{m}$, and the distance between gate electrode and base is $1.5\mu\text{m}$.

The field intensity at the tip of the cone can be calculated by considering a three-dimensional revolving symmetric field. At the top of the cone, $k=k_x=k_y$. A deep water trough method is used to find the field distribution. The size of the model electrodes is on a scale of 35,000:1 to the actual electrodes (the size of figure 1 is the same as the model). Apply a voltage between two electrodes and draw the distribution map of the equipotential surfaces between the electrodes.

Through the top of the cone, draw an electric displacement line orthogonal to the equipotential surfaces. Suppose we take a path difference from the top of the cone along the displacement line $\Delta n = 11 \text{ mm}$ (according to the scale of the model). Measure the curvature radius of the equipotential surface along the electric displacement line at the following points.

At point o, where $r = 1.9 \text{ mm}$, $k = 370 \text{ m}^{-1}$, $n = 0$, $V = 0$

At point a, where $r = 4.9 \text{ mm}$, $k = 143 \text{ m}^{-1}$, $n = 2.1 \text{ mm}$, $V = 6 \text{ V}$

At point b, where $r = 9.2 \text{ mm}$, $k = 77.0 \text{ m}^{-1}$, $n = 5.7 \text{ mm}$, $V = 9.8 \text{ V}$

At point m, where $r = 13.3 \text{ mm}$, $k = 53.0 \text{ m}^{-1}$, $n = 11.3 \text{ mm}$, $V = 12 \text{ V}$

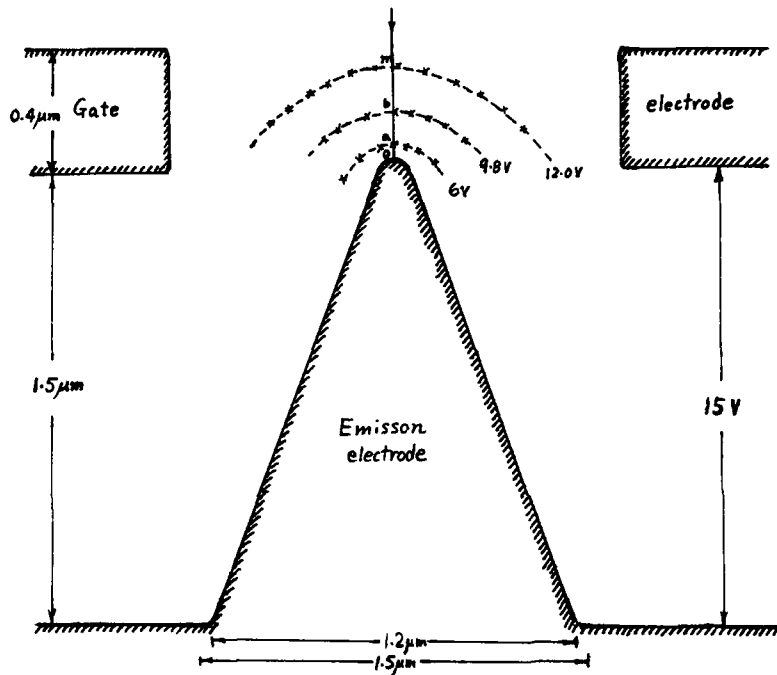


Figure 1: The model of geometric construction of the thin film field emission cathode (35,000:1 scale). Figure 2 (below) shows these data used to produce k - n and k - V curves.

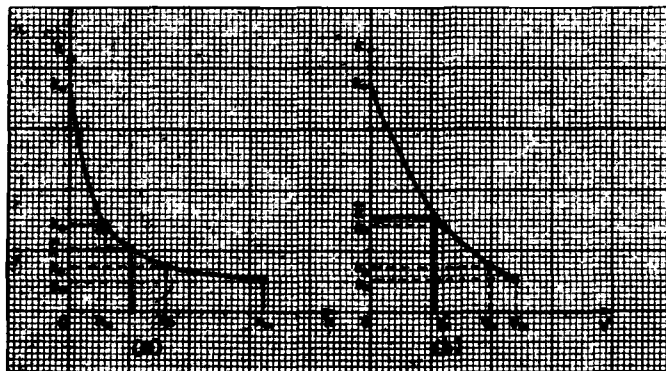


Figure 2. (a) The k - n curve and (b) the k - V curve for example 1.

The mean value of k for the k - n curve, \bar{k} , can be calculated by the k - n curve using formula (7):-

$$\bar{k} = \frac{566}{11.3} = 50.1 \text{ m}^{-1}$$

The mean value of k for the k - V curve, \bar{k} , can be calculated from the k - V curve:-

$$\bar{k} = \frac{1880}{12.0} = 156.6 \text{ m}^{-1}$$

Thus the geometric factor at the top of the cone is

$$\beta' = \frac{2\bar{k}}{\exp(-2\bar{k}\Delta n) - 1} = -\frac{313.2}{0.678} = -462 \text{ m}^{-1}$$

As the actual size of the model is magnified 35,000 times, the geometric factor, β , of the actual cathode is 35000 times the geometric factor, β' , of the model, ie.

$$\beta = 35000\beta' = -1.62 \times 10^7 \text{ m}^{-1}$$

If the voltage between the gate electrode and cathode is 200V, then the field intensity at the top of the cone is

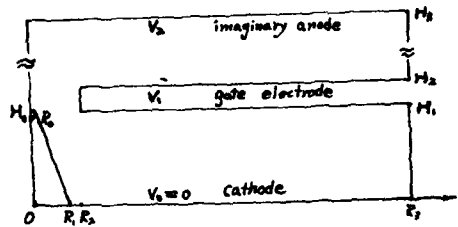
$$E_0 = \beta \Delta V = -1.62 \times 10^7 \left(200 \times \frac{12}{15} \right) \text{ Vm}^{-1} = -2.59 \times 10^7 \text{ Vcm}^{-1}$$

The negative sign indicates that the direction of E points to the top.

In principle, formulae (6) or (8) are exact solutions of Laplace's equation. The inaccuracies in this method arise from the technique of deducing the field plot and measuring the curvature of equipotential surfaces.

3. Comparison with the boundary element numerical method

Let us applying the boundary element numerical method to calculate the field intensity on the tip of the field emitter and compare with the result which we got by the general formula (8). Figure (3) shows the boundary of a Spindt device.



$R_0 = 0.054$	$R_1 = 0.6$	$R_2 = 0.75$	$R_3 = 6.25 \text{ (}\mu\text{m)}$
$H_0 = 1.53$	$H_1 = 1.5$	$H_2 = 1.9$	$H_3 = 15.9 \text{ (}\mu\text{m)}$
$V_0 = 0$	$V_1 = 200$	$V_2 = 209$	(V)

Figure 3. The boundary of a Spindt device'

The boundary element equation corresponding to the Laplace equation of a revolving symmetric field is

$$C_i V_i = \sum_{j=1}^N (H_{ij} V_j - G_{ij} q_j)$$

where i, j are the order numbers and N is the total number of boundary elements. V_j is the potential of j th element. $q_j = \partial V_j / \partial n$ is with respect to the outward normal of the boundary.

The formulas of the matrix elements G_{ij} and H_{ij} are:

$$G_{ij} = \int_0^{2\pi} \left[P(R_1 - R_2) + (PB - r_1) \ln \frac{R_2 + B + S}{R_1 + B} \right] d\phi$$

$$H_{ij} = \int_0^{2\pi} \frac{R_n}{R_1^2 - B^2} \left[\frac{PA^2 - Br_1}{R_1} - \frac{(PA^2 - Br_1) + S(PB - r_1)}{R_2} \right] d\phi$$

where

$$R_1 = [r_1^2 + r_i^2 - 2r_1 r_i \cos \phi + (Z_1 - Z_i)^2]^{\frac{1}{2}}$$

$$R_2 = [r_2^2 + r_i^2 - 2r_2 r_i \cos \phi + (Z_2 - Z_i)^2]^{\frac{1}{2}}$$

$$R_n = Q(r_1 - r_i \cos \phi) - P(Z_1 - Z_i)$$

$$B = P(r_1 - r_i \cos \phi) - Q(Z_1 - Z_i)$$

$$P = (r_2 - r_1)/S, \quad Q = (Z_2 - Z_1)/S_1$$

where S is the length of j th element; (r_1, Z_1) and (r_2, Z_2) are the coordinates of the terminal points, and (r_i, Z_i) is the coordinate of i th boundary element.

The field intensity on the tip of this field emitter which we calculated by boundary element numerical method is:

$$E = 2.58 \times 10^7 \text{ Vcm}^{-1}$$

It coincide with the result calculated by our general formula (8).

It is remarked that the numerical method can only be used to calculate specific problems with specific calculation. But this is not true for calculation by the general formula (8) which can often provide physical understanding and be used for technical design.

References:

- [1] Luo Enze 1986 J.Phys. D:Appl.Phys. **19** 1-6.
- [2] Luo Enze 1987 J.Phys. D:Appl. Phys. **20** 1609-1615
- [3] IW McAllister and A Pedersen 1988 J.Phys D:Appl. Phys **21** 1823-1825

Low-field 'cold-cathode' electron emission from Cu electrodes overlaid by a resin-particle composite

S. Bajic and R. V. Latham

Department of Electronic Engineering and Applied Physics
Aston University, Birmingham, B4 7ET, UK.

Abstract An optical imaging technique has been used to characterize the emission capabilities of resin-particle composite cathodes fabricated from a range of materials. These cold-cathodes have been shown to exhibit a high-current characteristic, and offer some potential for use in both extended-area and array-cathode applications.

1. Introduction

From detailed studies of the physical origin of the prebreakdown currents that flow between vacuum-insulated, high-voltage electrodes (Latham 1981), it has been established that the presence of "naturally occurring" micron-sized surface particles can promote a highly localised cold-cathode electron emission mechanism in the field range $15\text{--}20\text{MVm}^{-1}$. Subsequently, it was demonstrated that a similar process can be stimulated at even lower fields ($10\text{--}15\text{MVm}^{-1}$) by "artificially introduced" particles, notably graphite (Xu and Latham 1986), or alternatively, by coating a metallic cathode with a thin layer of dielectric material (Cade et al 1988, Bajic 1989). More recently, we reported on a hybrid emission regime in which a planar copper cathode was coated with a dielectric epoxy resin medium that was "loaded" with a suspension of graphite particles (Bajic and Latham 1988). This latter system proved to be particularly interesting, since it yielded a dense population of copiously emitting sites at fields as low as $5\text{--}10\text{MVm}^{-1}$.

The present paper reports on a further study of the composite-coated cathodes, composed of a range of particle sizes and species. As will be discussed, these findings are of considerable significance to the development of new types of broad-area and point-array cold-cathodes.

2. Experimental System

The present UHV cold-cathode testing facility consists of a plane-parallel electrode geometry with a variable gap spacing, d , and incorporates a SnO_2 -coated transparent-anode for imaging the spatial distribution of the electron emission sites. In operation, emitted electrons are accelerated across the gap to impinge on the transparent-anode with energies of typically $\geq 2\text{keV}$. Under these conditions, "anode spots" are formed, which, in turn, effectively mark the position and intensity etc of the sites. Video or photographic techniques can then be used to obtain a permanent record of the site populations over an extended test period. Full details of the construction and operational characteristics of this system can be found elsewhere (Bajic and Latham 1988).

3. Experimental Findings

The total I-V characteristics and site distribution images of the composite-coated cathodes were

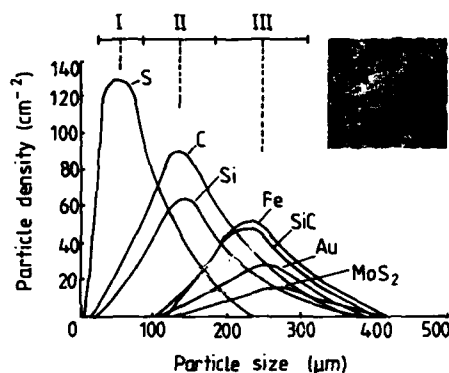


Fig1: The particle size distribution for the seven composite cathode types.

Composite cathode	ESW (MVm ⁻¹)	I_e (μA) (at 20 MVm ⁻¹)	β	i_s (μA) (at $I_e = 10^{-4}$ A)	P_{sw} (%)
C	6	500	2571	14.0	5.1
MoS ₂	6	400	1552	2.0	22.3
Au	7	80	753	5.0	3.3
Si	10	30	1705	7.7	2.2
SiC	7.5	15	595	2.2	2.6
S	12	10	572	2.5	2.4
Fe	10	1	623	2.9	2.5

Table 1: Typical emission data for the seven composite cathode types

obtained at a base pressure of $\sim 10^{-8}$ mbar and an interelectrode gap spacing of 0.5 mm. The cathodes were fabricated by a spinning process (Bajic and Latham 1988), in which 14 mm-diameter Cu-cathodes are coated with a composite overlayer consisting of conducting or semiconducting particles encapsulated in an epoxylite resin medium. To illustrate the type of coatings used in this study, Figure 1 shows both an optical micrograph taken at normal incidence to the surface of a Si-composite cathode and the particle size distributions for the seven cathode types.

In order to illustrate the switch-on process for these cathodes, Figures 2(a) and 3 show respectively the initial I-V behaviour and evolution of emission sites on a virgin C-composite emitter as the gap field is increased. Table 1 compares the typical values of the switch-on gap field (E_{sw}) obtained from measurements on the seven composite-cathode types. This shows that all the cathodes exhibit a low-field switch-on characteristic, although a considerable difference is observed between the respective values of E_{sw} for the C and S-composite emitters.

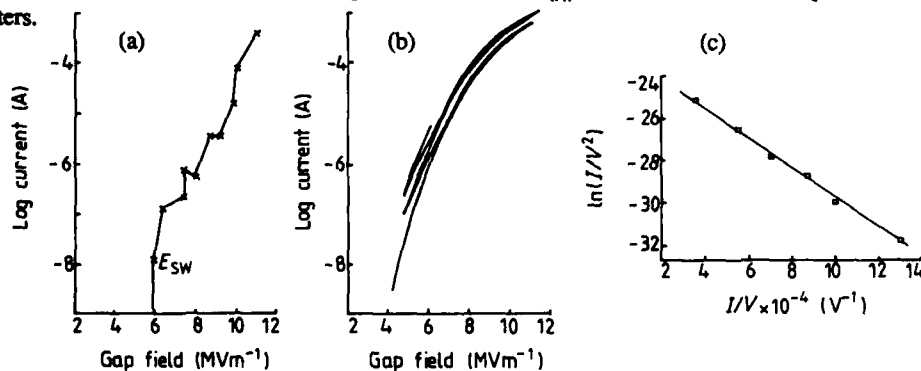


Fig 2: Typical (a) switch-on (b) I-V and (c) Fowler - Nordheim characteristics of a C-composite cathode.

Figure 2(b) shows the effect of the initial field cycling following the switch-on process, and clearly demonstrates that the cathode emissivity progressively increases for increasing-field half-cycles, until a reversible I-V characteristic (dotted line) is obtained after typically 2 or 3 cycles; here, the C-composite cathode is capable of delivering a current of ~ 1 mA at fields as low as 10 MVm^{-1} . The high emissivity of the C-composite cathode is further illustrated by the linear Fowler-Nordheim (F-N) characteristic shown in Figure 2(c), which yields a

characteristic field-enhancement, or β -factor, of ~ 2600 . The emission current data and β -factors of the seven composite cathode types are given in Table 1, and illustrate the considerable difference between the highly emissive C- and MoS_2 - composites and the lower emission levels obtained from the Fe-composites.

The site distribution images, shown for example in Figure 3, can be used to compare the average site currents, i_s , for each cathode type. Thus, Table 1 collates the values of i_s , and also the switch-on probability of sites, P_{sw} , which is defined as the percentage of the total number of particles that are found to emit for gap fields of $\leq 20 \text{ MVm}^{-1}$. It will be seen that the C- and MoS_2 -composites convincingly give rise to the highest values of i_s and P_{sw} , e.g. $14 \mu\text{A}$ and 22.3% respectively.

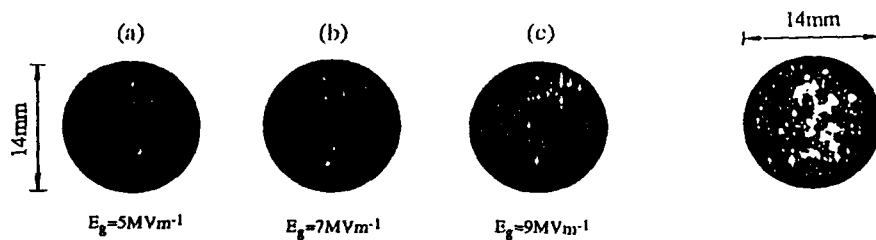


Fig 3: The evolution of emission sites on a virgin C-composite cathode. Fig 4: The emission site image resulting from a "dense" composite coating.

The transparent-anode imaging facility has also been used to evaluate the performance of two modified prototype cathodes based on the same composite sub-structure (Bajic 1989). Thus, referring to Figure 4, it is evident that high site densities of $n_s \geq 130 \text{ cm}^{-2}$ can be obtained using "heavily loaded" composite coatings, although it is generally difficult to increase n_s further due to limitations in the spinning process. Figure 5 shows a time sequence of constant-field site images obtained during a 5 minute video recording of a 3×3 SiC-composite array cathode produced from $400 \mu\text{m}$ -sized particles. Although these images illustrate the inherent site instability associated with the composite emitters (Bajic 1989), it is clear that the location of individual sites can be controlled to a considerable degree using this fabrication process.

4. Discussion

As discussed elsewhere (Bajic and Latham 1988), it is presently believed that field-induced electron emission (FIEE) from the composite-coated cathodes is associated with an MIMIV microregime (shown schematically in Figure 6), and involves a two-stage switch-on process in which "conducting" channels are "formed" within the thin dielectric regions above and below the encapsulated particle. The dielectric switching processes in regions 1 and 2 will depend on the field enhancement factors (β) in these regions, i.e. $\beta_1 \sim h/d$ and $\beta_2 \sim h/r$ respectively. The factor β_1 , which represents the "antenna", or field-probing effect (Athwal et al 1985) of an isolated conducting particle, suggests that the larger particles would undergo a primary switch-on in region 1 for relatively low fields, i.e. indicating that a size effect may exist. Referring to the E_{sw} , P_{sw} and size distribution data of Table 1 and Figure 1(b), it will be seen that there is indeed evidence to suggest a size effect, i.e. where the large-particle composites (e.g. MoS_2)

exhibit low E_{sw} and high P_{sw} values, and *vice versa*. However, although a particle size effect may influence the general emissivity of these cathodes (column 2 in Table 1), it is important to note that this cannot account for the anomalously high levels of emission obtained from the C-composites.

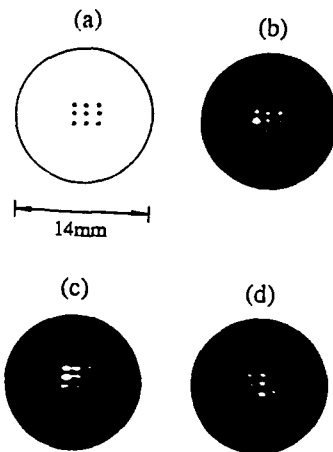


Fig 5: Constant - yield emission image from a 3x3 composite array cathode $E_g=10\text{Mvm}^{-1}$.

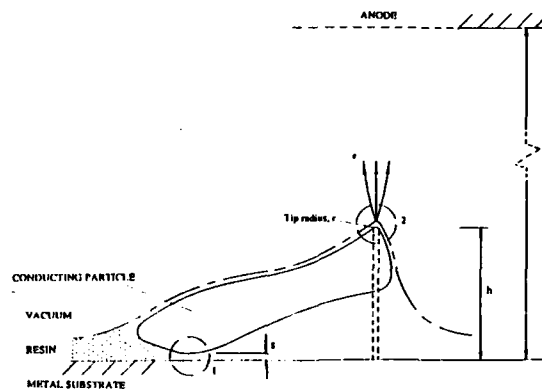


Fig 6: A schematic of FEE from an MIMIV microregime.

From a technological viewpoint, it is clear that the present cathodes exhibit exciting emission characteristics, with the possibility of broad-area current densities of $\geq 0.1\text{Acm}^{-2}$ being achieved by optimising the choice of materials and using a modified fabrication process which increases the particle density of the coatings (Bajic 1989). At this stage, however, it appears that the inherent instability of the individual sites (Figure 5) would limit the use of these emitters in array cathode applications.

Acknowledgement

This work forms part of a programme sponsored by SDIO/IST and managed by the Space Power Institute, Auburn University, Alabama, USA.

References

- Athwal C S, Bayliss K H, Calder R S and Latham R V 1985 IEEE Trans. Plasma Sci. PS-13 226-9
- Bajic S 1989 *PhD Thesis* University of Aston UK
- Bajic and Latham 1988 J. Phys. D: Appl. Phys. **21** 200-4
- Cade N A, Cross G H, Lee R A, Bajic S and Latham R V 1988 J. Phys. D: Appl. Phys. **21** 148-53
- Latham R V 1981 *High Voltage Vacuum Insulation: The Physical Basis* (New York: Academic)
- Xu N S and Latham R V 1986 J. Phys. D: Appl. Phys. **19** 477-82

Construction and performance of field emitting cathodes

R A Lee, A J Miller, C Patel, H A Williams

GEC Hirst Research Centre, East Lane, Wembley, Middlesex, HA9 7PP, UK

ABSTRACT: Field emitting structures have been fabricated using both wet and dry etching techniques, with final tip radii below 300 Å. The materials have included n-type silicon, by itself or coated with metal, and all-metal tips. Emission characteristics have been measured. A new experimental apparatus is described, with the versatility not only to perform electrical characterisation under UHV, but also to treat the surfaces of the device structures by heating or atom bombardment, and apply surface analysis techniques. Issues affecting exploitation of the technology are discussed.

1. INTRODUCTION

Field emitting cathodes fabricated by silicon microlithography and related techniques are becoming a competitive means for delivering electrons into a vacuum, and could form the basis of a future environmentally robust electronics technology, with applications in microwave devices and displays, for example. The successful application of vacuum microelectronics devices requires a number of related development stages to be fully researched and understood, and choices made so as to optimise performance. Firstly, processing the geometrical structures required must be perfected in the chosen materials: this is discussed in the first part of this paper. Secondly, controlling and understanding the vitally important physical processes at the emitting surface must be carried out with suitable apparatus and techniques. This is described, together with representative results. Thirdly, data relevant to practical aspects of real devices such as noise, lifetime, priming, and packing needs, must be collected and analysed.

2. PROCESSING

The silicon tips are produced by standard microlithographic techniques, using mask dots of $2\ \mu\text{m} \times 2\ \mu\text{m}$. Wet etching produces pyramids, and has the disadvantage that the etching time is critical, so that over-etching results in a rounding effect. A dry plasma etch process has also been developed. This enables tip with radii of less than 300 Å to be obtained (Figure 1). In this case, over-etching merely reduces the height of the tip.

Although some experimental work has been done on arrays of bare silicon tips, most work has involved diode structures. These were formed by

deposition of phosphosilicate glass (PSG) on the tips, followed by a sacrificial etch-back process to planarise this layer. Carefully controlled wet etching is then used to uncover the tips by 3000 Å, following which a layer of grid metal is deposited and the grid structure defined lithographically. The metal grid is then used as the etch mask for creating cavities around each tip by further wet etching. The final emitting tip and grid structure is shown in Figure 2. As these micron valve structures are, in contrast to ordinary silicon devices, unpassivated, it is often necessary to protect them with photoresist during wafer cutting operations.

The alternative of all-metal emitters, formed by sputtering on to a silicon wafer, has also met with success. Niobium and molybdenum emitters, shaped by reactive ion etching, have been obtained in this way (Figure 3) and they have been incorporated into diode structures. Gold emitting tips have also been fabricated and shaped by ion beam milling. The relationship between observed etch rates and tip shape have been discussed by Jacobson (1989).

Further optimisation and development is in progress, for the testing and operation of devices at higher temperatures by using molybdenum instead of aluminium as a metallisation layer. The progress of processing development has been such that silicon tips can be produced routinely and research on surface treatments to enhance emission are being pursued without processing variations entering into the experiments.

3. MICRON VALVE CHARACTERISATION EQUIPMENT

A new UHV chamber, adapted from a standard surface analysis system, has been commissioned for all aspects of research and testing on micron valve structures. The micron valve specimen is mounted horizontally on a five axis manipulator arm modified to incorporate a number of electrical feedthroughs. The temperature of the specimen stage can be controlled and varied between -100°C and 900°C. The UHV system incorporates a cold trapped diffusion pump and titanium

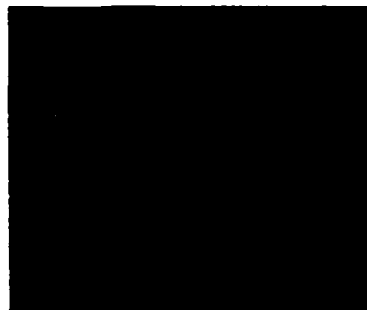


Fig 1: Array of dry etched silicon tips

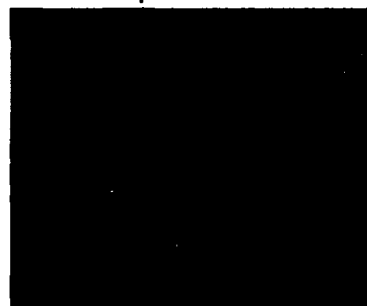


Fig 2: Final gridded structure

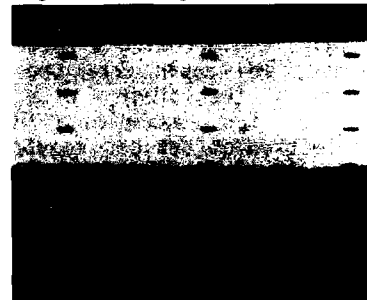


Fig 3: Niobium tips and molybdenum grid

sublimation pump capable of achieving chamber better than 6×10^{-11} mbar. In all experiments, pressures better than 5×10^{-9} mbar were used. The structure under investigation can be observed using an electron gun and scintillator/photomultiplier, forming a scanning electron microscope with 2000 Å resolution. An electron spectrometer is used for Auger analysis of surface layers under electron beam irradiation, and thus can determine the condition of specimen surfaces before and after treatment. The spectrometer has also been used to examine spatial and energy distribution of field emitted electrons (Howell et al 1989). Residual gas analysis is provided by a quadrupole mass spectrometer. This is also used for detecting atoms emitted from specimens during outgassing and during atom bombardment. The atom or ion bombardment, using argon or other inert gases, is carried out to remove surface layers from emitting structures and so expose fresh surfaces for exploration of the ideal characteristics of field emitting materials. An example of Auger data before and after fast atom bombardment is given in Figure 4, showing removal of organic contamination from the titanium layer but suggesting that oxygen was present throughout the layer.

A fine needle probe has been installed in the UHV system on its own manipulator so that it can be positioned over an individual emitting tip in an array. The probe can be replaced with a flat plate which acts as an electron collector or simple retarding plate energy analyser for gridded samples.

4. RESULTS AND DISCUSSION

The goal of increased field emission at lower applied voltage is being pursued by the processing already described, and by subsequent treatment of the field emitting structures, with a basic assessment by I-V and Fowler-Nordheim plots. Differences in observed emission behaviour can be related to a combination of tip radius, grid metal geometry and work function of the emitting areas.

Figure 5 shows a diode characteristic for a gridded 40 tip silicon array, demonstrating very low (<1 nA) reverse leakage. Figure 6 shows two IV plots, one for titanium covered silicon and the other for gold, which indicate quite different properties. The currents have arisen from arrays of different sizes, and have been normalised. The anode, used both to impose the field on the ungridded tip arrays and to collect the current, was

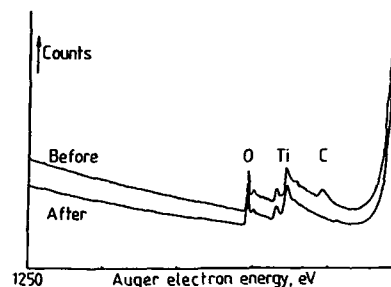


Fig 4: Auger data before and after fast atom bombardment of titanium coated silicon surface, showing removal of surface contaminant.

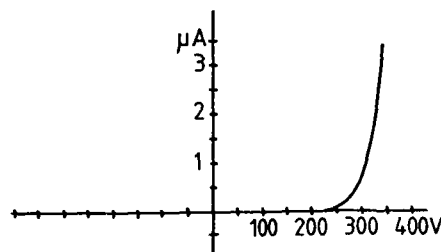


Fig 5: IV characteristic for gridded 40 tip silicon array

fixed at $10\text{ }\mu\text{m}$ away in each case. Another example of results, this time from one single tip in an array of dry-etched n-type silicon tips, with field imposed and current taken by the probe, is shown in Figure 7. Here the Fowler Nordheim plots cover four orders of magnitude of emission, and clearly show a difference due to work function alteration, as a result of heat treatment, in this case at 250°C for three hours. A single tip has so far produced $1\text{ }\mu\text{A}$ without damage, a considerable improvement on previous results (Lee et al 1989).

At the current state of development, the remaining pure research needed in this technology centres on understanding the nature of the field emission and its dependence on surface conditions, and on finding surface treatments that both enhance emission and stabilise it, both in the short term (noise reduction) and in the long term (lifetime). The further development needs are the investigation of array phenomena, since arrays of various sizes are bound to be used. Scaling of the emission with array size, current sharing between emission tips, and field limiting of very closely spaced arrays will have to be addressed. The measurements reported here have not involved spatial resolution of the emission. However emission uniformity can be improved by suitable priming (Harvey et al 1989).

Finally, we have the problem of a practical packaging. Although, as in the present case, research is carried out under UHV conditions, this is essentially impractical in packages of commercially useful dimension, and the characteristics of emitting tips in pressures of 10^{-6} mbar, possibly with a selected gas forming most of the residual atmosphere inside the package, will have to be studied.

REFERENCES

- Harvey RJ, Lee RA, Miller AJ & Wigmore JK 1989, this conference.
 Howell DF, Groves RD, Lee RA, Patel C & Williams HA 1989, this conference.
 Jacobson SE, Cade NA & Lee RA, 1989, this conference.
 Lee RA, Patel C, Williams HA & Cade NA 1989, IEEE Trans. Elect. Dev., in press

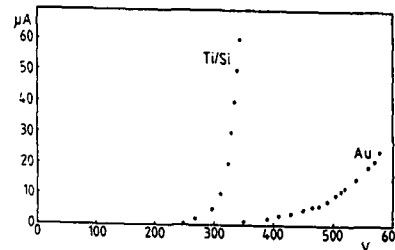


Fig 6: Comparison of IV characteristics for titanium coated silicon and gold arrays. The gold results have been normalised.

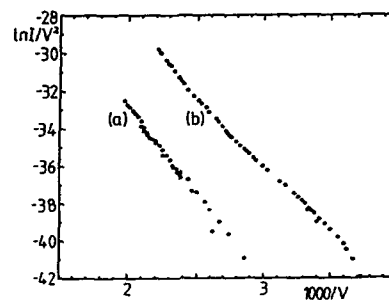


Fig 7: Effect of heat treatment on emission characteristics of a single silicon tip (a) before and (b) after treatment.

Modelling of electron trajectories in field emission devices

N A Cade

GEC Hirst Research Centre, East Lane, Wembley, Middlesex, HA9 7PP, UK

ABSTRACT: The modelling of micron scale field emission devices is complicated by the wide range of length scales involved. A substantially analytic method has been developed which allows field emission devices to be modelled accurately, allowing the effects of changes in geometry to be determined. The method involves the integration of Poisson's Equation for carefully chosen forms of pseudo-charge distribution. Results are presented for simple triode devices.

1. INTRODUCTION

Because of the high fields close to the surface of a field emitter, electrons are rapidly accelerated away from the cathode surface. Thus the space-charge effects, characteristic of thermionic cathodes are greatly reduced. It is therefore a reasonable approximation to model the emission characteristics of a field emitter in terms of single particle trajectories in the static electric field obtained as a solution of Laplace's equation for the emitter geometry. Both analytic and numerical approaches have previously been used (see Gipson et al (1979) and references therein). However, it has been generally recognised that the sensitivity of the electrostatic fields to geometric details makes analytic methods at best only an indication of trends while the use of numerical techniques is complicated by length scales ranging from the few hundred Å tip radius to the several micron electrode spacings of the field emission triode (Spindt et al 1976).

In this paper we consider an intermediate approach in which the electric fields in gridded sharp tip structures are modelled by a near analytic method while retaining a realistic geometry. This method is based on replacing the boundary conditions of the metal emitter and grid surfaces by a charge distribution within their surfaces. A similar method has previously been used by Tagawa et al (1987) for fields at a thermionic emitter surface.

2. THE METHOD

The basic problem of obtaining electrostatic fields and potentials is that of finding the inverse of the Laplacian operator having the boundary conditions appropriate to the electrode geometry. In conventional numerical methods this is done by discretising the Laplacian on some finite element mesh and inverting the resulting Laplacian matrix. This

approach does not easily yield accurate solutions for field emitter structures. For these, very fine, non uniform meshes are essential for accurate evaluation of the fields at the sharp emitters.

Rather than obtain such an inverse we take the inverse embodied in Coulomb's law and evaluate the field resulting from a given charge distribution within the actual electrode surfaces. This distribution is chosen to provide the correct long distance behaviour and is defined by a few parameters allowing fine tuning of the potential contours in the tip region. Given such a distribution, each electrode surface is chosen as one of the resulting equipotential contours.

In the case of an isolated, cylindrically symmetric tip on a flat metal electrode, an analytic solution for its potential contours may be obtained using a line charge density $\lambda(h) = \lambda_0 F_0 h$ for $|h| < d$ at $r=0$, where F_0 is the external field applied by a distant electrode. With this charge density and applied field, the potential is given by

$$V(h, r)/F_0 = h + \lambda_0 \{ [(d-h)^2 + r^2]^{1/2} - [(d+h)^2 + r^2]^{1/2} \} \\ + \lambda_0 h \ln \{ ([(d-h)^2 + r^2]^{1/2} + d - h) / ([(d+h)^2 + r^2]^{1/2} - d - h) \} \quad (1)$$

with the corresponding electric field obtained by differentiation. By choosing a potential contour close to $V=0$ as the contour of the sharp tip, a tip shape of arbitrary small tip radius may be obtained. The parameters d giving the tip height and λ_0 giving the tip width allow a range of tip shapes to be modelled. Because of the analytic form of Eqn. 1 correspondingly analytic expressions for field properties may be obtained. For example, the field at the tip is $F/F_0 = 2\lambda_0 d^3 R(h^2 - d^2)^{-2} \approx 2\lambda_0 R/d$ where R is the tip radius and the vertical coordinate at the tip is $h \approx d + \frac{1}{2}R$. For small tip radius d is approximately the tip height.

Although such isolated tips have been the subject of many calculations (Gipson et al 1979), gridded tips have not. The method is easily generalised to them by including an axially symmetric charge distribution mimicing the fields of the close grid. This charge distribution is based on the sum of the surface charge densities induced by the distance anode field F_v above the grid and the grid-cathode field F_0 far from the tip, augmented by a dipole distribution corresponding to the finite separation of these surface charges across the thickness of the grid. The full pseudo-charge distribution is then obtained by removing this charge from the grid hole region and redistributing it partly as an image below the cathode and partly on the edges of the grid hole. The dipole distribution is also removed from the grid hole region. The resulting potential contours are obtained by adding charge and dipole contributions of the forms

$$V_c = \int_a^b 4x\sigma(x)dx [h^2 + (r+x)^2]^{-1/2} \kappa(4rx/[h^2 + (r+x)^2]) \quad (2)$$

$$V_d = \int_0^a 4xhdx\mu(x)[(r-x)^2 + h^2]^{-1} [(r+x)^2 + h^2]^{-1/2} \epsilon(4rx/[h^2 + (r+x)^2])$$

onto the tip potential of equation 1. κ and ϵ are complete elliptic integrals of 1st and 2nd kinds. σ and μ are uniform sheet charge and dipole densities. Radial limits a and b chosen to optimise the grid shape. These distributions allow analytic integration on the axis of symmetry giving a precise, but implicit relationship between tip field and radius. Typical electrode contours are shown in Figure 1 for grid hole radius $a = 0.5 \mu\text{m}$ with charge redistributed out to a radius of $b = 1.3 \mu\text{m}$.

3. RESULTS AND DISCUSSION

The axially symmetric electrode contours of Figure 1 allow an analytically tractable form at the price of requiring a smoothed version of the flat and square edged grids obtained experimentally. The two extremes shown, with large accelerating and retarding anode fields above the grid, provide electric fields at the tip which, for the same tip radius, differ by 10%. Thus, although non-quantitative, the implication is that the tip field is relatively insensitive to both grid shape and anode field.

The effects of other geometric features on device performance are quantitatively assessed by evaluating the field F over the tip surface and evaluating the current density J using the field enhancement approximation, i.e. the Fowler-Nordheim equation with this geometry enhanced field.

$$J = AF^2/\phi \exp[-B\phi^{3/2}F^{-1}] \quad (3)$$

where ϕ is the work function. For J in units of Am^{-2} , ϕ in eV and F in VA^{-1} , $B = 0.683$ and $A = 1.54 \times 10^{14}$. The total emission current was evaluated and electron trajectories were obtained using Newtonian mechanics, so that both the angular spread of the emission and the current intercepted by the grid were determined. A typical result is shown in Figure 2. Substantial emission occurs only over an angular range of 70° and the grid interception is minimal provided the tip does not lie below the grid.

This angular range of emission is insensitive to geometry for a wide range of grid heights. However, the field at the tip is not. The tip field enhancement is plotted in Figure 3 as a function of radius for a range of grid heights. For large tip radii these curves show a

Fig 1:
Electrode
contours.

(a) $5 \times 10^6 \text{Vm}^{-1}$
accelerating
anode field

(b) 10^7Vm^{-1}
retarding
anode field.

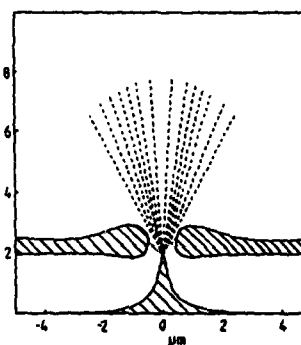
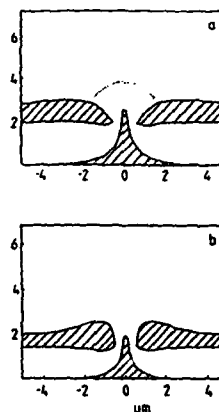


Fig 2: Electron
trajectories. Line
density proportional
to current density.

tendency for the tip field to become independent of radius. For all of the curves plotted the radial dependence is approximately $F \propto (R^{-1} + B^{-1})$ with $B = 630 \text{ \AA}$. This is in agreement with the experimental curves of Spindt et al (1976) but the results obtained here do not show the stronger saturation of the R dependence suggested by Enze (1988). As the tip protrudes through the grid, the potential contour at grid voltage, occurring only for an accelerating anode field (Figure 1), projects further out into the grid anode gap and Enze's argument that the tip gets substantially closer to this contour is incorrect for these grid shapes.

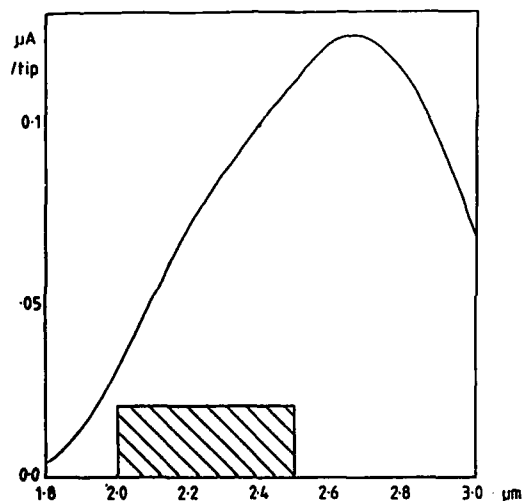


Fig 4: Field emission current per tip as a function of tip height H , for a $2 \text{ }\mu\text{m}$ grid-cathode gap, 300 \AA tip radius and $0.5 \text{ }\mu\text{m}$ grid hole radius. The work function was 4.5 eV and the grid (position shaded) bias 200V .

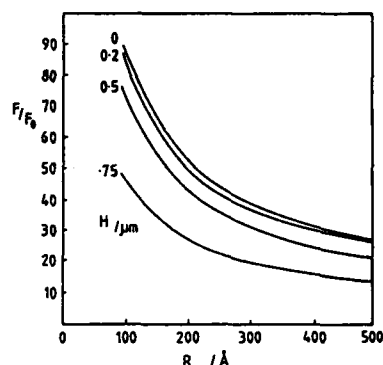


Fig.3: Field enhancement vs tip radius (R) and grid height H relative to the top of $2 \text{ }\mu\text{m}$ high tip.

Perhaps more significant than this saturation is the tip height dependence of the field enhancement for fixed tip radius and grid structure. In Figure 4 this dependence is plotted showing that maximum current and minimum sensitivity to height are obtained for the tip just above the top of the grid.

The main conclusion is that with fixed dielectric thickness, maximum field enhancement is obtained for the tip lying just above the grid. For such positioning the emission is also least sensitive to geometry and gives minimal grid current. Although this positioning does give a slightly larger angular spread, this minor effect will be dominated by work function anisotropy.

REFERENCES

- Enze L J Phys D **20**, 1609 (1987)
- Gipson GS, Yannitell DW & Eaton HC J Phys D **12**, 987 (1979)
- Spindt CA, Brodie I, Humphrey L & Westerberg E R J Appl Phys **47**, 5248 (1976)
- Tagawa M, Takenobu S, Ohmae N & Umeno M Appl Phys Lett **50**, 545 (1987)

An experimental study of the physics of field emission by tip arrays

R J Harvey⁺, R A Lee^{*}, A J Miller^{*} and J K Wigmore⁺

⁺ Physics Department, University of Lancaster, UK.

^{*} GEC Hirst Research Centre, Wembley, UK.

Abstract: We have studied the characteristics of silicon emitter arrays as a function of temperature both directly and with a field emission microscope. The highly unstable emission observed at room temperature became much more uniform above about 100° C, indicating the presence of water vapour. Results suggested that emission took place only from a small number of tips out of a large array, and from very small areas. Possible space charge effects were also indicated.

Introduction

Some of the most promising prospects in the area of micron field emission electronics are those based on the application of VLSI silicon processing. A particular advantage of device fabrication by this method is that the wafers are single crystals. Much field emission work on tips (as opposed to plane surfaces) has been carried out on etched wires of polycrystalline metals (see, for example, Dyke and Dolan, 1956). For such samples, stable emission from crystalline facets is achieved only after high electric field and high temperature (>1500K) cleaning, annealing, and surface reconstruction. In addition, continuous operation at high temperature is recommended in order to minimise sputtering and adsorption. It has been proposed that lithographically produced silicon emitter tips, since they are inherently both clean and monocrystalline, may display stable and reproducible behaviour under much less extreme conditions.

In this paper, we report experiments in which the characteristics of field emission from bare ungridded arrays of conical silicon tips produced by dry etching were studied at temperatures up to several hundred K, in order to explore the practicality of this suggestion.

Experimental Details

Details of emitter fabrication are given by Lee et al. (1989). The form of the arrays is shown in figure 1, taken by scanning electron microscope. Samples had spacings between the tips of either 10 μm or 3 μm . From the photographs the average tip radius was determined to be 30 ± 5 nm. The overall area of an array was 2×2 mm² and the material was n-silicon doped to approximately 10^{18} cm⁻³.

Investigations were carried out in a liquid nitrogen-trapped, diffusion-pumped UHV system, with a titanium sublimation pump final stage, capable of operation down to 10^{-9} torr. The anode was a flat glass screen coated with tin oxide and phosphor

forming a simple field emission microscope which allowed observation of the spatial distribution of emission. The emitter array was mounted parallel to the anode. Its distance from the latter was less than 1 mm and could be varied by a micrometer z-motion with a precision of $\sim 10 \mu\text{m}$. Temperature was varied by a flat nichrome heater clamped to the sample wafer, and measured by a contiguous thermocouple. Before measurements were taken, the system was baked at 420 K for 24 hours for each sample.

Results

The emitters were not formed or trained in any way. Consequently the current observed immediately after switch-on at room temperature was extremely noisy, being subject to wild fluctuations on a time scale of seconds or shorter. Simultaneous observation with the field emission microscope revealed that the current was also spatially inhomogeneous, consisting of a small number of intense beams which switched on and off sporadically and varied in direction over an area of a few mm^2 on the FEM screen. A typical FEM display of emission at room temperature is shown in Figure 2. Close correlation was observed between the switching of these beams and the temporal fluctuations in current. There was no qualitative difference between the 3 and 10 micron samples.

Raising the temperature even by as little as 130 K changed the picture dramatically. The current fell by a factor of 2 or 3, whilst the amplitude of the fluctuations decreased by orders of magnitude. In addition, the FEM display revealed a shift to an approximately uniform spatial distribution of current. Figure 3 illustrates the changes in current observed as a 3 micron sample was thermally cycled between 290 K and 420 K. The high-temperature stable phase appeared to break up on cooling through $\sim 370 \text{ K}$, suggesting that a major factor was the adsorption of water vapour. Such cooling traces also depended on chamber pressure, presumably through surface coverage and accommodation. Mass spectrometer analysis is planned to identify the adsorbates.

Heating the emitter arrays to much higher temperatures, around 1000 K, had relatively little effect. Figure 4 shows sections of a cooling curve which began at this temperature. Two features should be noted. First, the overall current remained approximately constant over the whole temperature range, suggesting that the silicon was sufficiently heavily doped for it to be regarded as metallic, with no surface band-bending. Second, the current remained relatively smooth over most of the temperature range, confirming that most degradation occurs relatively close to room temperature.

The likely involvement of adsorption was supported by a comparison of Fowler-Nordheim plots of the data taken in the two phases (Figure 5). The slope of the plot for the stable phase was found consistently to be 10 to 20% higher than that obtained in the low temperature, noisy, phase. In order to infer a value of the work function, ϕ , from these data, it is necessary to have a value for β , the geometric factor which relates cathode potential to tip electric field. This point will be discussed below.

Discussion

Emission appears to be taking place only from a small number of discrete areas. The clearest evidence for this is the large magnitude of the current fluctuations, and

their direct correlation with the appearance and extinction of the individual electron beams observed by the FEM. If a significant fraction of the 40,000 tips present were emitting, then statistical effects, both in space and time, would be proportionately much smaller. In addition, inspection of arrays that have been cycled as described above confirms that only very few tips show any distortion from their original shape.

Whilst recognising that Fowler-Nordheim theory is good only to an order of magnitude, and noting that even highly doped n-silicon is not a true metal, we nevertheless used this model to estimate from our data the approximate area necessary to supply the current observed in the stable phase. We used the simple expression (Dyke and Dolan, 1956) relating current i with anode-cathode potential difference V ,

$$\frac{i}{A} = (1.54 \times 10^{-6}) \frac{\beta^2 V^2}{\phi} \exp \left\{ -\frac{6.83 \times 10^7 \phi^{3/2}}{\beta V} \right\}$$

For all runs, the answer obtained for the emitting area, A , was in the range 2-20 (lattice spacing)², that is, much smaller than the area of a tip. We also attempted to estimate the emission area from the observed FEM spot size via the magnification factor of the FEM (approximately 10^5). This method gave an answer approximately 100 times larger. A possible explanation of this discrepancy is that space charge effects are causing beam divergence. If the emitting areas are really as small as estimated above, then the current densities are considerably greater than the space charge threshold (Barbour et al. 1953).

It is not clear why only such small regions of so few, supposedly identical, tips should be emitting. Presumably, once in the stable emission phase and free from significant adsorbates, all tips have the same work function. Therefore the only possible variable is β , the field enhancement factor, which depends critically on emitter radius and height, and more weakly on tip separation and anode distance. Our best estimate of β for these experiments is $1.8 \times 10^6 \text{ cm}^{-1}$, leading to a value for ϕ of $5.1 \pm .2 \text{ eV}$. We are continuing investigations into the dependence of β on the various parameters. Preliminary results (Figure 6) indicated that the current falls off more rapidly with increasing anode distance for the 3 micron array than for the 10 micron device. It will be possible to work back from such measurements to more accurately determined values of β and ϕ .

We are indebted to Helen Williams for her careful preparation of the samples, and to SERC for support for RJH through a CASE award.

References

- Barbour J P, Dolan W W, Trolan J K, Martin E E and Dyke W P. 1953. *Phys. Rev.* **92** 45.
- Dyke W P and Dolan W W. 1956 *Advances in Electronics and Electron Physics*, ed. L Marton (Academic Press, New York) **8** 89.
- Lee R A, Miller A J, Patel C and Williams H A. 1989. (this conference).
- Spindt C A, Brodie I, Humphrey L and Westerberg E R. 1976. *J Appl Phys.* **47** 1.

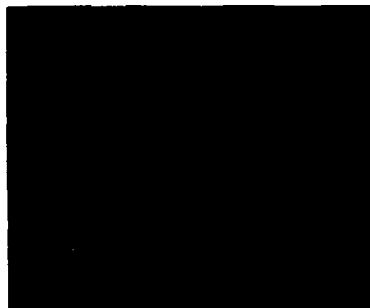


Figure 1 : Scanning electron micrograph of part of an array before use.

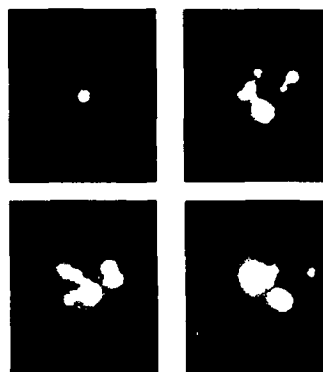


Figure 2 : Succession of FEM pictures over a few seconds.

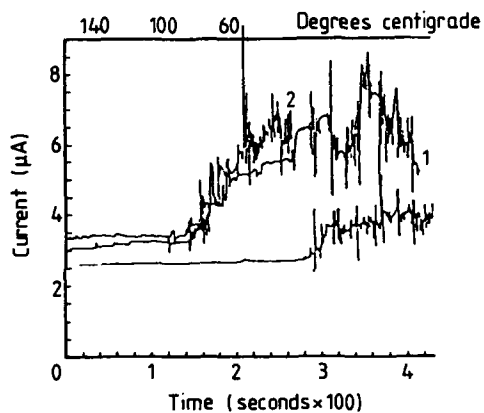


Figure 3 : Successive (1 → 2 → 3) cooling curves of a 3 micron array.

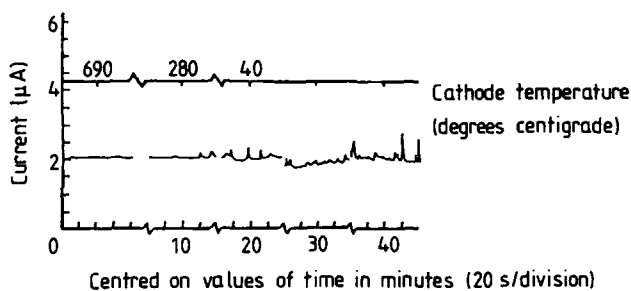


Figure 4 : Cooling curve of a 10 micron array from a temperature of ~ 1000 K.

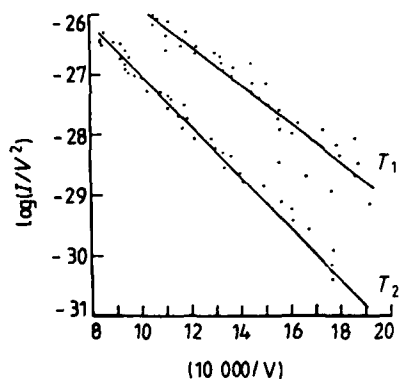


Figure 5 : Fowler-Nordheim plots of the sample above: T_1 unstable, T_2 stable.

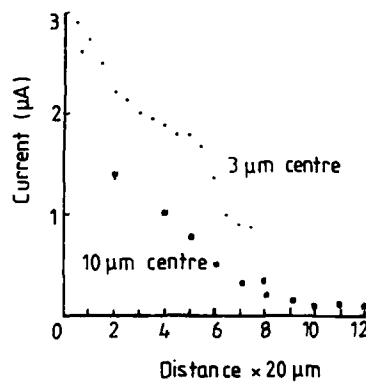


Figure 6 : Dependence of array current at constant voltage on anode distance.

A mathematical model to predict optimum geometry of the elements of a field emitter array cathode

R K Feeney, J K Cochran, D N Hill, and A T Chapman

Georgia Institute of Technology, Atlanta, Georgia USA 30332-0245

ABSTRACT: Calculations have been made that simulate the effects of device geometry on the electron emission performance of a family of composite-based field emitter array cathodes. These emitters, made by thin-film techniques from unidirectionally-solidified oxide-metal composites, contain arrays of pointed fibers centered in the apertures of a gate film. The effects on emission and electron trajectories of variables such as emitter pin tip radius, pin cone angle, gate film thickness, and pin position relative to the gate film were modeled.

1. INTRODUCTION

A field emitter array cathode, based on a unidirectionally-solidified, oxide-metal, eutectic composite was developed and studied at Georgia Tech (Cochran et al, 1980,1984). The composites, developed by Chapman and Clark (1970), contain arrays of single-crystal tungsten fibers (500 nm dia.) in an oxide matrix, with fiber packing densities ranging from $1-10 \times 10^5 \text{ cm}^{-2}$. The cathodes were fabricated by first etching the composite to expose and point the tungsten fibers, then depositing the insulator and gate films by electron-beam evaporation. A micrograph of an element of one of these composite-based field emitter arrays (CFEA) is shown in Figure 1. As part of the cathode development effort, an extensive program of calculations was undertaken to provide guidance for the adjustment of the controllable parameters of the fabrication process. The effects on electron emission and electron trajectories of variables such as emitter pin-tip radius, pin-cone angle, gate film thickness, and pin position relative to the gate film electrode were examined.

2. ANALYSIS PROCEDURE

The theory of field emission, originally developed by Fowler and Nordheim (1926), describes electron emission from cold metals into a high electric field. The theory relates current density, J , in A/cm^2 , field strength E , in V/cm , and the work function ϕ according to the expression:

$$J = \frac{1.54 \times 10^{-6} E^2}{\phi t^2(y)} \exp \frac{-6.83 \times 10^7 \phi^{3/2} f(y)}{E} \quad (1)$$

where $f(y)$ and $t(y)$ are slowly varying elliptic functions of the variable y defined by the equation,

$$y = \frac{(e^3 E)^{1/4}}{\phi} = \frac{3.79 \times 10^{-4} E^{1/4}}{\phi} \quad (2)$$

The substitution of typical numbers for ϕ shows that negligible field emission results until the electric field strength exceeds about 10^7 V/cm. This high value of electric field precludes the existence of a significant space-charge region in the vicinity of the emitter-tip until the current density approaches 10^6 A/cm². Most FEA operation occurs at current densities below this value. Hence, a space-charge-free analysis of the FEA is capable of giving considerable insight into the operation of the device.



Figure 1. Micrograph of CFEA Emitter Element.

Most of the emitter simulations were done with a space-charge-free model. For this case, a procedure involving the numerical solution of Laplace's equation and integration of the equation of electron motion was developed. Laplace's equation was solved for a single emitter element placed below a biased collector. In order to obtain adequate spatial resolution, the portion of the potential mesh including the emitter tip was expanded several times to provide a resolution of 0.67 nm. The electric field over the surface of the emitter pin was numerically determined and the electron emission and trajectories were calculated.

The electrostatic potential within the interelectrode space was calculated using a difference equation approximation to Laplace's equation (Hildebrand, 1968). Specific forms of the difference equation were required depending upon whether the applicable region was in the inter-electrode space, on the z-axis of the emitter or on a boundary. These equations, together with the boundary conditions, were solved to obtain the potential matrix. Boundaries that were not $r = \text{constant}$ or $z = \text{constant}$ surfaces were represented by adjusting the potential of neighboring mesh points so that they properly reflected the actual position of the potential boundary. The numerical solution was accomplished by repeatedly applying the potential equations to the potential matrix until the desired degree of convergence was obtained. The calculation was terminated when the values of successive iterations were less than some convergence value, typically 1 mV.

The electric field was obtained from the potential by a difference equation approximation including a second-order correction. The second order correction was necessary because the trajectories did not necessarily pass through mesh points. Equation (1) was used to calculate the emission current density at points on the surface of the emitter pin. The electron emission current was then obtained by numerically integrating the electric current density over the spherical and conical surfaces of the emitter.

The trajectory starting points were assigned to correspond to the emission of specified fractions of the total current. This was done by comparing the total current, calculated as described above, with the cumulative current starting from the emitter tip. A polynomial was fitted to the calculated current with the cumulative current as the independent variable and the position on the emitter as the dependent variable. The polynomial coefficients were then used to determine the starting location of each trajectory for the specified fraction of emitted current. Usually, a new trajectory was initiated for every five percent increase in the cumulative current. Once the electric field and the starting points of the trajectories were determined, the equations of motion could be integrated to determine the complete trajectories of the electrons.

3. DISCUSSION OF RESULTS

The techniques outlined in the previous sections were utilized to perform a parametric study of the Georgia Tech CFEA cathode, the nominal or reference

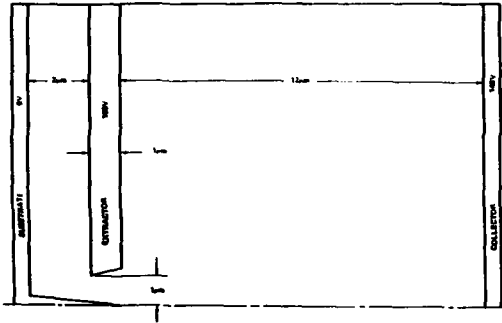


Figure 2. Reference Geometry of CFEA Cathode.

geometry of which is shown in Figure 2. The collector potential of 148 V was selected to provide the same electric field that would be obtained from a collector biased 1000 V above the gate film and located 0.25 mm away. The effects of geometry variations were examined by changing one or more of the nominal dimensions of the CFEA while leaving the remaining device parameters constant. The emitted current was calculated from Eq. (1) using a work function of 8.0 eV, corresponding to oxygenated tungsten.

3.1 Variation of Electric Field on Emitter Surface

Figure 3 shows the variation of the electric field as a function of pin tip polar angle. These results indicate that the electric field is slowly varying near the pin tip, but falls off rapidly along the shank. Results for other pin radii and cone angles show a similar variation. It should be noted that these data are qualitatively similar to those for other FEA devices, but the Georgia Tech CFEA cathodes often exhibited a significantly larger electric field.

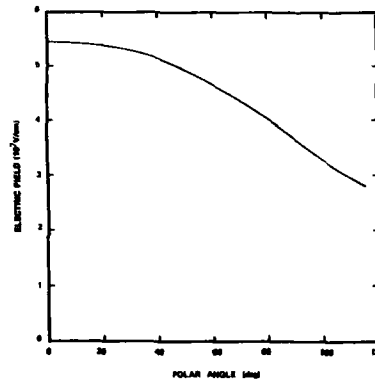


Figure 3. Variation of Electric Field with Pin Tip Polar Angle.

3.2 Effect of Pin-Tip Radius on Peak Electric Field

One potential advantage of the CFEA devices over other types of emitter arrays is the very small pin tip radius obtainable by chemical etching. Pin tip radii of

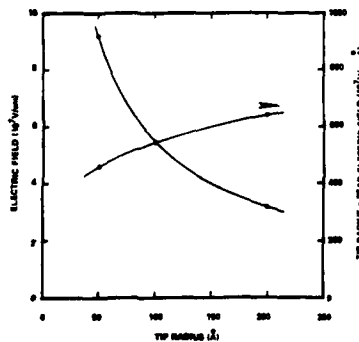


Figure 4. Effect of Tip Radius on Peak Electric Field.

less than 5 nm can be produced. It was important to ascertain if such small tips could lead to the significant improvements in device performance and to evaluate the sensitivity of electron emission to small variations of pin radii. The results of the electric field calculation are given in Figure 4. These data show the expected strong dependence of the electric field on the tip radius. From these results it can be concluded that the small radii of the CFEA device pins result in a significantly larger electric field than that obtainable with the usual 25-75 nm radii of vapor-deposited emitters. A second conclusion is

size distribution of the pin-tip radii must be carefully controlled if spatially uniform emission is to be achieved.

3.3 Effect of Pin Cone-Angle on Peak Electric Field

The CFEA fabrication process yields emitter pins significantly sharper than those obtained by other methods. Calculations were made to assess the effect of the pin cone-angle on the peak electric field and hence on electron emission. The results of this study are shown in Figure 5. It is apparent that a small cone half-angle (30°) results in a significant increase in electric field when compared to the larger angle (60°) characteristic of other FEA devices. Thus, the etched metal-oxide composites appear to yield an emitter pin that is reasonably optimized with respect to pin cone-angle.

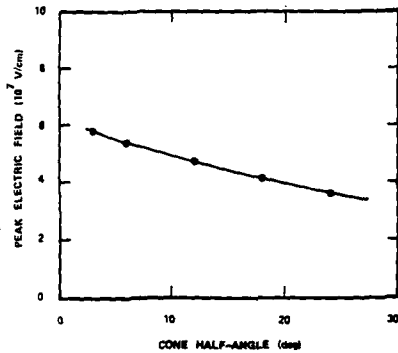


Figure 5. Effect of Cone Half-Angle on Peak Electric Field.

3.4 Effect of Pin Position Relative to Gate Film

Because of variations in effective etching rates, the precision with which emitter pin length can be controlled was somewhat limited. It was thus very important to assess the effect of variations in placing the pin relative to the gate film. Figure 6 shows the peak electric field as a function of the

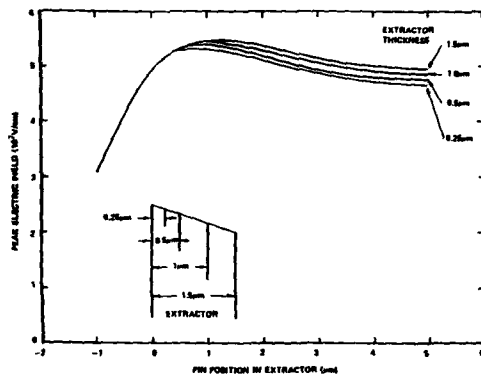


Figure 6. Effect of Pin Position Relative to Gate Film on Peak Electric Field.

position of the emitter pin relative to the base of the gate film with gate film thickness as the parameter. The calculations lead to the important conclusion that the peak electric field, and hence emission, is insensitive to the position of the pin tip, provided that the tip is positioned at least midway within the gate film. It is also apparent that there is negligible effect on the electric field from reasonable variations in gate film thickness. This allows other considerations, such as the current capacity of the gate film to determine the actual thickness of the film.

4. REFERENCES

- Chapman A T and Clark G W 1970 *J. Am. Ceram. Soc.* 53 112
- Cochran J K, Chapman A T, Feeney R K, Hill D N 1980 *Technical Digest IEEE International Electron Devices Meeting* p 462
- Cochran J K, Chapman A T, Feeney R K, Hill D N, Lee K J, Jones R D, Kolarik R V, Moh K H, and Price J P 1982 *Final Report, USAF Systems Command, AFWAL-TR-82-1089*
- Hildebrand F B (1968) *Finite-Difference Equations and Simulations* (New York: Prentice-Hall) pp 284-90

Tunnelling theory and vacuum microelectronics

P. H. Cutler, T. E. Feuchtwang, Z. Huang and T. Sullivan*
Pennsylvania State University, 104 Davey Lab, University Park, PA 16802,
USA, and *Temple University, Department of Electrical Engineering,
Philadelphia, PA 19122 USA.

We review first one dimensional tunneling theory, beginning with the kinetic method of field emission by Fowler and Nordheim. Current theories, including many-body effects, will then be discussed. The role of the electron-surface interaction and the models for the resulting effective potential barrier will be considered. For nanometer scale devices, a variety of size and geometry effects manifest themselves. In this context, recent theories of multi-dimensional tunneling will be discussed. Application of tunneling theories to vacuum microelectronics will be illustrated by the calculation of the I-V characteristics for a fully three dimensional model of the scanning tunneling microscope.

1. INTRODUCTION

Electron tunneling has been an intriguing subject every since the advent of quantum mechanics[Fowler and Nordheim, 1928; Oppenheimer, 1928]. This phenomenon has been the subject of extensive theoretical analysis, and experimental observation, some of it dramatic, such as field emission[Good and Müller, 1956 and Gadzuk and Plummer, 1973], field ion microscopy[Müller and Tsong, 1969], scanning tunneling microscopy[Hansma and Tersoff, 1987], and superconductive tunneling[Solymar, 1972]. However, there still remain unresolved fundamental issues in tunneling theory. For example, there is no unique theory of the characteristic time for electron tunneling through a quantum barrier[Lucas, et al, 1988; and Huang, et al., 1989]. Another problem of current interest is the formulation of a multidimensional theory of tunneling, in non-separable potentials[Berry and Mount, 1972]. These topics and others are not of exclusive interest to the description and application of solid state tunneling devices[Dalvern, 1980], and are also relevant to such diverse fields as chemical reaction dynamics[Pollak and Miller, 1984, 1985], field theory[Banks, et al., 1973], and study of the cosmological evolution from the initial 'big-bang'[Banks, 1985; Brout, 1987].

Our understanding of both the operation of electron tunneling devices, such as pn-junctions, FET's and Schottky barriers, and their practical development are based on a simple one dimensional model of quantum barrier penetration. This approach is justified by invoking translational invariance of the tunneling barrier in the transverse directions normal to the "plane" of the junction. In addition, the model is taken to be

separable into one dimensional tunneling and "free electron" motion in the transverse directions. Devices with close-spaced electrodes (i.e., 1-2 nm's) are sensitive to the anisotropies of the barrier, which are due to geometric asymmetries of the electrodes and enhanced by the multiple image interactions.

In a recent study of STM, using an exact three dimensional Green function, Lucas, et al.[1988], found pronounced anisotropies of the tunneling current density. They suggested that the barrier anisotropies lead to the observed focusing of the tunneling current and hence, ultimately to the atomic resolution of the STM. Lang[1985], using a transfer Hamiltonian formulation, also found a tunneling current density which is highly concentrated along the cylindrical axis of symmetry of his model. Here also the current density distribution reflects the underlying anisotropy of the barrier. Both calculations clearly demonstrate the essential role of the multidimensionality of the barrier, which obviously cannot be accounted for in the one dimensional models.

In this paper we will review the current status of tunneling theory. It is understood that by tunneling theory we mean the determination of the transmission coefficient and the tunneling current density. By contrast, in multidimensional tunneling the transmission coefficient is replaced by a differential scattering probability. We shall emphasize the physical interpretation of the formal theory. The details of the mathematical analysis will be kept to a minimum. There are several excellent monographs[Burstein, 1969; Duke, 1969; Wolf, 1985] and reviews[Gadzuk and Plummer, 1973; Feuchtwang, et al, 1983; Feuchtwang and Cutler, 1988] which include the mathematical details of elementary tunneling. The theories of tunneling in multidimensional potential barriers with and without dissipation are the subject of much current activity. Some recent work on this topic will be discussed in the paper.

In section 2, we give a brief review of one dimensional normal electron tunneling into vacuum. We begin with the Fowler Nordheim theory, and then discuss the classical WKB method and the transfer Hamiltonian formalism. In Section 3, we consider the electron-surface interaction and the surface-vacuum tunneling barrier. The problem posed by the possible multidimensionality of a tunneling barrier is also briefly considered. In this context, we describe, in Section 4, recent theoretical work using semi-classical and Green function techniques to calculate tunneling through nonseparable three dimensional barriers. We then apply these concepts and results to tunneling problems in vacuum microelectronics (i.e., the STM). Conclusions are presented in Section 5.

2. REVIEW OF ONE DIMENSIONAL NORMAL ELECTRON TUNNELING THEORY.

Electron tunneling is a non-classical transport mechanism involving transitions of electrons between classically allowed regions separated by a forbidden region, that is, a potential barrier. In the forbidden region the kinetic energy is negative because the total energy of the electron is less than the (local) potential energy. Whether a region is forbidden or not is determined by the energy of the electron involved in the transition. The definition can be extended to include electron tunneling in solids. In crystalline and disordered solids, whether a region is allowed or forbidden at a given energy depends on the one-electron band structure for that region. The potential barrier or forbidden region is, in this case, determined by the band structure modulated by non-periodic fields such as the surface field, or the external bias field. Within the

barrier the electron wave functions cannot be represented by plane waves, but instead are linear combinations of real exponentials. Thus tunneling may be visualized as the coupling of the plane waves in the solid to those in the vacuum due to the overlap within the vacuum barrier region of their respective exponentially decreasing tails.

Finally, a brief comment concerning tunneling in MVM junctions (e.g., the STM). It is customary to distinguish two regimes of operation for these junctions. The field emission or Fowler-Nordheim regime occurs for relatively large interelectrode spacings, and is distinguished by the fact that the tunneling distance is a small fraction of the interelectrode spacing. The so-called "tunneling regime" occurs when the interelectrode separation is of the order of the width of the tunneling barrier, i.e., $\lesssim 30\text{\AA}$. The main distinction between the two regimes is that, in principle, the electrons in the Fowler-Nordheim regime could be described in terms of a classical or ballistic trajectory in the interelectrode space beginning about 30\AA beyond the "surface" of the field emission tip. Nevertheless, there is no essential difference in the electron transport mechanism in field emission and metal-vacuum-metal junctions since physically both are tunneling phenomena.

One of the earliest theories of vacuum tunneling was developed by Fowler and Nordheim [1928] to explain electron emission from solids in a high electric field. These authors use a kinetic model to calculate the tunneling current density given by $j = nev$. Here n is the number of electrons per unit volume, e is the electronic charge, and v is the electron's group velocity in the state $|\vec{k}\rangle$.

In the kinetic model the tunneling current density is calculated from the product of the incident flux, the transmission probability per electronic state and the occupation probability of this state, given by the Fermi factor. For a one dimensional potential barrier denoted by $V = V(x)$, this leads to the following expression for the field emitted current,

$$j = \frac{(2s+1)e}{(2\pi)^3 \hbar} \int dk_x d^2\vec{k}_t f(E) D(E_x) \left(\frac{\partial E}{\partial k_x} \right) \quad (1)$$

Here s is the electron spin, $f(E)$ is the Fermi factor, E is the total energy, $D(E_x)$ is the transmission probability at normal energy E_x , and $\partial E / \partial k_x$ is the normal or x -directed group velocity. The normal energy is $E - (\hbar^2 \vec{k}_t^2) / 2m$ and \vec{k}_t is the wave vector parallel to the plane of the junction, and normal to the x -direction. Equation (1) can be rewritten,

$$e \int_0^\infty D(E_x) N(E_x) dE_x,$$

where $N(E_x)$, the supply function, is given by

$$N(E_x) = (2s+1) 2\pi m (k_B T / \hbar^3) \ln(1 + \exp((E_F - E_x) / k_B T)).$$

The product $P_n(E_x) = D(E_x)N(E_x)$ is referred to as the normal energy distribution of the emitted electrons. To calculate j , one requires the solution of the Schrödinger equation for the transmission coefficient $D(E_x)$ [Duke, C. B., 1969]. For any reasonably realistic barrier, this cannot be done in closed form. Therefore, it is necessary to resort to approximate methods for the calculation of the transmission coefficient. One of the most commonly used is the so-called WKB method, which, for a one dimensional model, gives

$$D_{\text{WKB}}(E_x) = e^{-2 \int_{x_1}^{x_2} \kappa(x) dx}$$

where

$$\kappa(x) = \sqrt{\frac{2m}{\hbar} (V(x) - E)}$$

$V(x)$ is the potential barrier and $x_{1,2}$ are the classical turning points at which $\kappa(x_1)$ and $\kappa(x_2)$ vanish. The advantage of this method is that it does not require an explicit calculation of the Schrödinger equation. Although widely used for its simplicity and convenience, it should be recognized that D_{WKB} is derived assuming a thick barrier and therefore it becomes less accurate for energies near peaks of the barrier, and for all energies above the barrier [Gadzuk and Plummer, 1973; Modinos, 1984].

For the Fowler-Nordheim model with an applied electric field F , but no image interaction, $V(x) = \phi + E_F - eFx$, where ϕ is the work function. The turning points are $x_1 = 0$ and $x_2 = (eF)^{-1} (\phi + E_F - E_x)$. The integral for D_{WKB} can be done exactly, yielding

$$D_{\text{WKB}}(E_x) = \exp \left\{ - \left[\frac{4}{3} eF \right] \left(2m/\hbar^2 \right)^{1/2} \left[\phi - (E_x - E_F) \right]^{3/2} \right\} \quad (2)$$

The exponential dependence in Eq. (2) characteristic of tunneling has been well verified in field emission [Gadzuk and Plummer, 1973] for fields $\gtrsim 10^8$ volts/cm. [Cutler and Nagy, 1965]. It is remarkable that this simple one dimensional model fits so well to much of the experimental data. Gadzuk [1969], and Politzer and Cutler [1970, 1972] have demonstrated that tunneling from the free-electron-like states is about two orders of magnitude more probable than tunneling from the "d" and other higher angular momentum states.

Two final comments concerning the accuracy of the WKB method. It can be shown that the variation in the potential energy $V(x)$ has to be a slowly varying function of position and that the kinetic energy of the particle must be large compared to $V(x)$ for the approximation to be applicable.

That is, $\frac{\lambda |dV/dx|}{2(E-V)} \ll 1$, where λ is the de Broglie wavelength of the tunneling electron. [Bohm, 1955]

Before the advent of computers several analytic approximations of D_{WKB} were introduced to simplify the evaluation of the tunneling integral. These were often of limited applicability and, more important, they were frequently inadequate [Duke, 1969]. One of the widely used approximations was developed by Simmons [1964]. Recently, Simmons' 'mean barrier approximation' for the trapezoidal barrier (including all classical multiple-image-potential corrections), has been critically examined [Miskovsky, et al., 1982]. It was found that the current calculated using just the WKB approximation differs significantly from that obtained using any of several widely used versions of the Simmons 'mean-barrier approximation' confirming that commonly used alternatives to the WKB approximation are less reliable than the WKB itself. [Miskovsky, et al., 1982].

The conventional formulations of electron tunneling are mostly effective

single-electron theories. That is, the electrons are treated as non-interacting particles subject to Fermi-Dirac statistics. In contrast, modern formulations of electron tunneling are basically many-body theories including electron-electron and/or electron-phonon interactions. These many-body tunneling analyses reduce in the limit of non-interacting electrons to the conventional theories.

The most commonly applied formulation of many-body tunneling invokes the so-called transfer Hamiltonian [Duke, 1969; Gadzuk and Plummer, 1973]. Interpretation of this pseudo-Hamiltonian follows from the observation that this formalism was developed as an extension of Fermi's golden-rule for the calculation of a transition or tunneling probability per unit time. It is given by $(2\pi/\hbar)|M|^2$, where M is the effective matrix element coupling the wave functions in the solid and vacuum. For vacuum tunneling, in the independent particle model, tunneling current in the transfer Hamiltonian formalism can be written in the form [Feuchtwang and Cutler, 1976],

$$j = \frac{2e}{h} \int_{-\infty}^{\infty} |M|^2 F(E) dE, \quad (3)$$

where E is now the total energy. Equation (3) is usually derived by kinetic arguments and corresponds to the Fowler-Nordheim result in Eq. (2).

In the presence of interactions, or many-body effects, the expression for the current tunneling into vacuum is now given by

$$j = \frac{2e}{h} \int_{-\infty}^{\infty} |\Lambda^{(0)}(E)|^2 \rho_m(E) \rho_v(E + eV) f(E) dE \quad (4)$$

Here $\rho_{m,v}$ are the local densities of states for the metal (vacuum) evaluated at the metal (vacuum) sides of the interface. Explicitly the local density is reduced to a one dimensional quantity by averaging over the interface,

$$\rho_{m(v)} = \int_{z=m(v)} \rho_L(\vec{r}, E) dx dy.$$

The local density of states is a generalization of the ordinary density of states $\rho(E) = \sum_i \delta(E - E_i)$ for non-uniform systems. [Feuchtwang and Cutler 1978]. For non-interacting electrons described by the single particle wave function $\psi(\vec{r}; E)$,

$$\rho(\vec{r}, E) = \int_{-\infty}^{\infty} |\psi(\vec{r}; E')|^2 \delta(E - E') dE' \quad (5)$$

The ordinary density of states is just the volume integral of the local density of states,

$$\rho(E) = \int \rho(\vec{r}, E) d^3r.$$

We interpret the energy integral of the local density of states as the probability of finding an electron at the position \vec{r} ,

$$\rho(\vec{r}) = \int_{-\infty}^{\infty} \rho(\vec{r}, E) dE = \int_{-\infty}^{\infty} |\psi(\vec{r}; E')|^2 dE'.$$

We interpret $\rho(\vec{r}, E)$ as the probability that an electron is at the position \vec{r} and has an energy E , and hence its usefulness. The delta function $\delta(E-E')$ in Eq. (5) signifies that the electronic energy is conserved so that j is the elastic tunneling current.

The quantity $|\Lambda|$ is often called a matrix element, although it has the dimensions of energy per unit length. It can best be thought of as the matrix element of a pseudo-operator which induces the tunneling "transition". The several different formulations of many-body tunneling theory differ essentially in their definition of $|\Lambda|$. We shall not dwell on this point since it requires analysis beyond the scope of this article. However, in elastic tunneling and for the case of non-interacting electrons, these 'matrix elements' are related by

$$|M(E, eV)|^2 = |\Lambda^{(0)}(E)|^2 \rho_m(m, E) \rho_v(v, E+eV) = D(E, eV). \quad (6)$$

We note that the expression for the transmission coefficient in Eq. (6) in terms of the local densities of states is primarily of conceptual importance, and has little computational advantage compared to, say, DWKB. This is not the case when interactions have to be considered. Then, the tunneling experiment can, for instance, be used to probe the effect of interactions on the single particle densities of states. Physically, these quantities are affected by the modification of the dispersion relation $E(\vec{k})$ due to the interactions. These "modifications" are called self-energy effects and are important, for example, in superconducting tunneling junctions and in the many-body formulation of inelastic tunneling. The application of the many-body formalism to study metal-vacuum tunneling in the Fowler-Nordheim regime (i.e., field emission) is discussed by Gadzuk and Plummer[1973] and Feuchtwang and Cutler[1976].

As an example of the use of the transfer Hamiltonian in an independent particle problem, we consider field emission into a vacuum. Then, the matrix element $\Lambda^{(0)} = M_{m,v}$ has the form

$$M_{m,v} = \frac{\hbar^2}{2m} \int_S \left[\phi_v^* \nabla \phi_m - (\nabla \phi_v^*) \phi_m \right] \cdot d\vec{S}$$

where ϕ_m and ϕ_v are eigenfunctions of the decoupled Hamiltonians for the metal and vacuum, respectively, and S denoted the surface of separation between metal and vacuum. An evaluation of the current proceeds directly from the substitution of $M_{m,v}$ into Eq. (4). A second important example of the application of the transfer Hamiltonian formalism is the calculation of the tunneling current in the spherical tip model of STM by Tersoff and Hamann[1983] and Chung, et al.[1983]. Although approximate in its treatment, it nevertheless represented the only practical way (i.e., computationally simple) of calculating the three-dimensional tunneling currents.

Finally, a distinct advantage of this formalism is that it stresses the importance of the local densities of states in tunneling currents which can be deduced from measured tunneling currents[Tersoff and Hamann, 1983, and Feuchtwang, et al., 1983].

Lang[1984] has introduced a useful modification of the Bardeen[1961] transfer Hamiltonian tunneling theory. Lang's formalism permits him to calculate current density rather than integrated total currents. This enabled Lang[1985] to present an analysis of the lateral resolution.

A detailed discussion of the many-body theory of tunneling is beyond the scope of this article because of both the mathematical and conceptual complexities. However, we wish to briefly indicate the reasons for interest in this topic. Most important in a many-body formulation of tunneling is the need to take account of inelastic processes such as electron-electron and electron-phonon interactions in order to study them experimentally. A first successful application of this approach was the study of the phonon density of states in superconductive tunneling [Schrieffer, J. R., et al., 1963 and Feuchtwang, et al., 1983]. Formal many-body theories of tunneling based on the Keldysh[1965] transport theory have been developed by Caroli, et al.[1972] and Feuchtwang[1976]. However, because of mathematical difficulties, these theories have not been applied to any realistic problems. An interesting many-body effect relevant to vacuum tunneling is the dynamical image interaction which is the time and velocity dependent potential experienced by a charge in the vacuum moving relative to the surface. This is to be contrasted with the ordinary image interaction which is calculated for a static charge outside a solid surface. To determine the dynamical image charge, it is necessary to account for the collective or many-body response of the electron gas in the metal. Recent experiments on the image-potential bound states by inverse photoemission[Riehl, et al., 1984; Straub and Himpel, 1986] and STM[Binnig, et al., 1985] have prompted renewed theoretical interest in this subject[Garcia, et al. 1985; see also Jonson, 1980 and Echenique, et al. 1987]. This will be discussed further in the next section.

III. ELECTRON-SURFACE INTERACTION AND THE POTENTIAL BARRIER.

For a free electron metal the simplest model of a potential barrier at the metal-vacuum interface is a step function whose height is equal to the sum of Fermi energy and the work function. The discrete ion cores are assumed smeared out into a uniform density of positive charge which is referred to as the jellium model. Stability of this system in the presence of the conduction electron gas requires a spreading of electron charge density beyond the step in the positive jellium. The resulting electric dipole is the source of the surface contribution to the work function of the metal and the barrier that confines the electron to the solid. Such a model does not exhibit tunneling out of the solid because the surface barrier is of infinite width.

To induce tunneling one has to reduce the effective width to less than 30Å. The simplest way to achieve this is to apply an external electric field. For the jellium model without image interaction, this leads to a triangular barrier first introduced by Fowler and Nordheim. This model of a field dependent barrier was extended to a metal-insulator (vacuum)-metal (MIM/MVM) junction in which case it becomes the well-known trapezoidal barrier[Simons, 1964]. Both models were refined by inclusion of the image interaction. In the field emission case, the simple image interaction suffices to describe the dominant effect which leads to a maximum in the potential barrier. This effect is readily confirmed[Good and Müller, 1956]. Because of the close spacing of the electrodes in the MVM junction, it is necessary to include the multiple image interactions. The importance of this has been demonstrated by the calculations of Miskovsky, et al.[1982] and in the construction of the three-dimensional tunneling barrier for a model STM by Lucas, et al.[1988]. The multiple-image theory just discussed is completely classical and is probably not valid for distances less than about 2-3Å from the surface[Lang and Kohn, 1973]. Lang and Kohn[1973] calculated the quantum correction to the simple image

interaction at a metal-vacuum interface. This correction takes the form of a shift into the metal of the classical image plane. Lucas, et al. [1988] used a similar but phenomenological quantum correction of the multiple image potential first proposed by Seitz[1940]. Other schemes have been used to approximate the multiple image interactions [Simmons, 1964; Garcia, et al. 1985]. These are essentially phenomenological fits to a combination of Kohn-Lang quantum corrections and the classical interactions. We note that, except for the model used by Lucas, et al. [1988], the image interactions described above are effectively one-dimensional. This follows from the use of the WKB transmission coefficient, whereas Lucas, et al. [1988] use a three-dimensional scattering formalism to calculate the effective tunneling probability. Finally, there have been numerous calculations of the surface potential barrier using the density functional formalism and other techniques. This is beyond the scope of this review and a detailed discussion of this subject can be found in the book by Lundquist and March [1983].

IV. MULTIDIMENSIONAL TUNNELING - WHY AND HOW?

We have previously alluded to the fact that the multidimensionality of the tunneling barrier becomes important when the barrier exhibits either strong spatial anisotropies or inhomogenities. This means that the potential function describing the barrier is nonseparable in any coordinate system and hence, the problem cannot be reduced to decoupled one-dimensional tunneling. The multi-dimensionality will manifest itself, especially in devices with closely spaced conducting electrodes, exemplified by point-contact diodes [Feuchtwang, et al., 1983] STM-like junctions [Binnig, et al., 1987], vacuum field-effect transistors [Huang, et al., 1989], as well as other vacuum microelectronic structures. Ultimately, the multidimensionality is a consequence of the close spacing and the architecture of the constituent electrodes.

In addition to the transfer-Hamiltonian, which is both a many-body and multidimensional tunneling theory, there is the Green function scattering approach of Lucas, et al. [1988], mentioned earlier and a quasi-classical WKB method for multidimensional tunneling [Huang, et al., 1989]. In the former, tunneling is treated as the scattering of an incident plane wave state $|\vec{k}\rangle$ into scattered states $|\psi_{\vec{k}}\rangle$. The current density $\vec{j}(\vec{r})$ is obtained from

$$\vec{j}(\vec{r}) = \int_{E_k - V_b}^{E_F} dE \int_{k_z > 0} d\hat{k} \cdot \vec{j}_{\vec{k}}(\vec{r})$$

where V_b is the forward bias and \hat{k} is a unit vector of the incident plane wave, energy E .

$$\vec{j}_{\vec{k}}(\vec{r}) = \frac{\hbar}{2mi} \left[\psi_{\vec{k}}^*(\vec{r}) \nabla \psi_{\vec{k}}(\vec{r}) - \psi_{\vec{k}}(\vec{r}) \nabla \psi_{\vec{k}}^*(\vec{r}) \right]$$

is the current density carried by the scattered state. The current density is determined by calculating the scattering of the plane wave incident on the barrier. In this calculation the STM is modeled by two parallel conducting plates with a hemispherical boss on one of them representing the effective tip. The total barrier is decomposed into a planar MVM junction and the boss is treated as a perturbation localized in a small region where most of the tunneling current occurs. The unperturbed part (i.e., planar MVM barrier) is exactly solvable. The unperturbed wave

function plus the known localized perturbation of the barrier due to the boss is used to construct the full Green function, G , of the total tunneling Hamiltonian via the Dyson equation. With G known the exact scattered wave functions $|\psi_k\rangle$ can be obtained from the Lippmann-Schwinger equation. What makes the scheme feasible is the localized nature of the perturbation. Because of this, both the Dyson and the Lippmann-Schwinger integral equations can be discretized on a finite grid covering the spatial region where the perturbation does not vanish. Thus, the integral equation for the tunneling wave functions are transformed into matrix equations easily handled on a computer.

Before discussing the results reported by Lucas, et al. [1988], we wish to note that a three-dimensional computer calculation of the barrier potential used in their calculations provides dramatic visualization of the anisotropy and inhomogeneity of the barrier. In particular the effects of the multiple-image interactions and their quantum corrections accentuate the anisotropy of the barrier in the region of the tip [see Figure 2 in Lucas, et al. 1988].

Since the tunnel barrier has axial symmetry, the problem is effectively reduced to two dimensions (2D). It can be shown that each axial angular momentum component, m , in the 2D cylindrically symmetric wave function contributes independently to the tunneling current. It is found that the tunneling current is dominated by the $m=0$ cylindrical wave. The total current carried by all the waves with $|m|>0$ is less than 10% of the $m=0$ wave. Therefore, the current is highly localized along the axis of the tip. A measure of this is that the current, at a radial distance from the tip axis equal to the tip radius, and measured on the sample surface is about 10% of its value on the axis. It can be concluded that this first-principles multidimensional tunneling calculation confirms that the lateral resolution of the STM has its origin in the sharp anisotropy of the tunneling phenomenon in the presence of a three-dimensional barrier.

The second approach to multidimensional tunneling theory is to generalize the one-dimensional WKB method. The method involves an approximation of the quantum mechanical Green function which, in turn, yields the wave function for the tunneling (i.e., scattered) wave function. G is a weighted average of all the particle "paths" leading from an initial state (\vec{r}_i, t_i) to the scattered (i.e., transmitted) state (\vec{r}_f, t_f) , including all possible paths through the barrier. The so-called semi-classical approximation is now invoked to exclude all paths except those which obey Newton's equations for the inverted potential $V(\vec{r}) \rightarrow -V(\vec{r})$ and $E \rightarrow -E$, when $V(\vec{r})$ is the barrier potential and $E < V(\vec{r})$. These trajectories are joined at the turning point of the barrier to those obtained from Newton's equation in the classically allowed regions. This procedure has been justified theoretically for the special case of particles incident normal to the barrier [Huang, et al., 1989c].

A simple example which illustrates this procedure [Huang, et al., 1989b] is the calculation of the current density of a model STM already described in the previous example.

We shall assume, for simplicity, a square barrier with $V(\rho, z) = V_m$, a constant, in the forbidden (barrier) region and $V = V_0$ inside the metal electrodes. In addition, only the case of current from tip to sample surface is treated, although this is not essential to the result. Then

$$j(\rho) = \frac{2e}{(2\pi)^3} \int d^3k D_k(\rho) \frac{\hbar k}{m} f(E) [1 - f(E+eV)]$$

where $D_k(\rho)$ is given by $D_{WKB}(\rho)$. In the WKB phase integral,

$\kappa(\rho, z) = \left\{ \frac{2m}{\hbar^2} [V(\rho, z) - E] \right\}^{1/2}$. For emission normal from the hemispherical tip, the current follows "semiclassical" radial trajectories. For this model

$$j(\rho, z) \propto D_{WKB} = \exp \left\{ -2\kappa \left[\sqrt{(d + R_t)^2 + \rho^2} - R \right] \right\}$$

where κ is now a constant, $\sqrt{\frac{2m}{\hbar^2} (V_m - E)}$, R is the radius of the tip, d is the smallest tip-sample separation distance and ρ is a radial coordinate in the sample surface with an origin on the tip axis. The resulting localized current distribution as a function of ρ on the sample surface agrees qualitatively with the results obtained by Lucas, et al. [1988].

These examples are intended to demonstrate the feasibility of calculating multidimensional transmission probabilities. These calculations are, in general, quite complex. The theories, as currently formulated, do not lend themselves, as yet, to the development of a sufficiently simple algorithm for practical use. There is, however, the special case of a tunneling electron which is incident normally on the barrier interface $V(\vec{r}) = E$, as described in the last example. Nevertheless, regardless of the present difficulty in implementing the calculation of multidimensional tunneling, we wish to stress the importance of this effect in realistically describing the operation of nanometer scale vacuum microelectronic devices. That is, in systems in which the deBroglie wavelength of the tunneling electron is comparable to the radius of curvature of constituent electrodes in the device.

V. SUMMARY

In this paper we have presented a concise review of tunneling theory beginning with the Fowler-Nordheim model of field-emission and extending through the more sophisticated formulations of tunneling in terms of scattering theory, and the transfer-Hamiltonian formalism. In this presentation, the focus was not so much on mathematical details, but rather on the physical content of the particular model for tunneling and on the limitations of its applicability. The role of the electron-surface interaction and the models for the resulting effective potential barrier was also considered. In particular, the importance of the classical multiple image interaction in contributing to the anisotropy of multidimensional barrier in close-spaced junction was emphasized. Quantum corrections to the image potential were also noted. For nanometer scale devices, a variety of shape and size effects manifest themselves requiring a more careful analysis of the inherently multidimensional tunneling barrier. Two recently developed approaches of multidimensional tunneling, a Green function method and a quasi-classical WKB formalism, were described in some detail and illustrated by presenting results of the current density in a model STM obtained with these methods. Since the STM is a prototype vacuum microelectronic device, these results have special significance to the full class of such devices.

References

- † This research was supported in part by the Office of Naval Research, Arlington, Virginia, Grant No. N00014-86K-0160.
- Banks, T., Bender, C. M. and Wu, T. T., Phys. Rev. D8, 3346 (1973); 3366 (1973).
- Banks, T., Nuclear Phys. B249, 332 (1985).
- Bardeen, J., Phys. Rev. Lett. 6, 51 (1961).
- Berry, V. and Mount, K. E., Rep. Prog. Physics 35, 315 (1972).
- Binnig, G., Garcia, N., Rohrer, H., Soler, J. M. and Flores, F., Phys. Rev. B30, 4816 (1984).
- Binnig, G., Frank, K. H., Fuchs, H., Garcia, N., Riehl, B., Rohrer, H., Salvan, F., and Williams, A. R., Phys. Rev. Lett. 55, 991 (1985).
- Binnig, T., Gerber, Ch., Stoll, E., Albrecht, T. R., and Quate, C. F., Europhys. Lett. 3, 1281 (1987).
- Bohm, D., Quantum Theory (Prentice-Hall, New York, 1955).
- Brout, R., Foundations of Physics 17, 603 (1987).
- Burstein, E. and Ludqvist, Tunneling Phenomena in Solids, (Plenum Press, New York, 1969).
- Caroli, C., Combescot, R., Noziere, P., and Saint James, D. C5, 21 (1972).
- Chung, M., Feuchtwang, T. E. and Cutler, P. H., Surf. Sci. 187, 559 (1987).
- Cutler, P. H. and Nagy, D., Surf. Sci. 3, 71 (1965).
- Dalvern, R., Introduction to Applied Solid State Physics (Plenum Press, New York, 1980).
- Duke, C. B., Tunneling in Solids, Suppl. 10 to Solid State Physics, ed. by F. Seitz, D. Turnbull and H. Ehrenreich (Academic Press, New York, 1969).
- Echenique, P. M., Gras-Marti, A., Manson, J. R., and Ritchie, R. H., Phys. Rev. B35, 7357 (1987).
- Feuchtwang, T. E., Phys. Rev. B13, 517 (1976).
- Feuchtwang, T. E. and Cutler, P. H., Physica Scripta 38, 252 (1988).
- Feuchtwang, T. E., Cutler, P. H., Miskovsky, N. M. and Lucas, A. A., in Quantum Metrology and Fundamental Physical Constants, P. H. Cutler and A. A. Lucas, eds. (Plenum Press, New York, 1983).
- Fowler, R. H. and Nordheim, L. W., Proc. Roy. Soc. (London) A19, 173 (1928).
- Gadzuk, J. W., Phys. Rev. 182, 416 (1969).
- Gadzuk, W. and Plummer, W., Rev. Mod. Phys. 45, 487 (1973).
- Garcia, M., Reihl, B., Frank, K. H., and Williams, A. R., Phys. Rev. Lett. 54, 591 (1985).
- Good, R. H., Jr. and Müller, E. W., Handbuch der Physik 2d Ed. (Springer, Berlin, 1956) 185.
- Hansma, P. K. and Tersoff, J., J. Appl. Phys. 61, R1 (1987).
- Huang, Z. H., Cutler, P. H., Feuchtwang, T. E. and Gray, H., 2nd International Vacuum Microelectronics Conf., Bath, England, July 24-26, 1989, and to be published. a.
- Huang, Z., Feuchtwang, T. E., Kazes, E., and Cutler, P. H., submitted to Phys. Rev. B. (1989) b.
- Huang, Z. H., Feuchtwang, T. E., Kazes E., and Cutler, P. H., submitted to Phys. Rev. D (1989) c.
- Jonson, M., Sol. State Comm. 33, 746 (1980).
- Keldysh, L. V., Soviet Physics, JETP 20, 1018 (1965).
- Lang, N. D., Phys. Rev. Lett. 55, 230 (1985); Phys. Rev. Lett. 56, 1164 (1986).
- Lang, N. D. and Kohn, W., Phys. Rev. B7, 3541 (1973).

- Lucas, A. A., Cutler, P. H., Feuchtwang, T. E., Tsong, T. T., Sullivan, T. E., Kuk, Y., Nguyen, H., and Silverman, P., *J. Vac. Sci. Technol.* **A6**(2), 461 (1988).
- Lucas, A. A., Morawitz, H., Henry, G. H., Vigneron, J. P., Lambin, Ph., Cutler, P. H., and Feuchtwang, T. E., *Phys. Rev.* **B37**, 10708 (1988).
- Lundquist, S. and March, N. H., *The Theory of the Inhomogeneous Electron Gas* (Plenum Press, New York, 1983).
- Miskovsky, N. M., Cutler, P. H., Feuchtwang, T. E. and Lucas, A. A., *Appl. Phys.* **A27**, 139 (1982).
- Modinos, Field, *Thermionic and Secondary Electron Emission Spectroscopy* (Plenum Press, New York, 1984).
- Müller, E. W. and Tsong, T. T., *Field Ion Microscopy. Principles and Applications* (Elsevier, Amsterdam, 1969).
- Oppenheimer, J. R., *Phys. Rev.* **31**, 67 (1928).
- Politzer, B. and Cutler, P. H., *Surf. Sci.* **22**, 277 (1970); *Phys. Rev. Lett.* **28**, 1330 (1972).
- Pollak, E. and Miller, W. H., *Phys. Rev. Lett.* **53**, 115 (1984);
- Pollak, E., *J. Chem. Phys.* **83**, 1111 (1985).
- Riehl, B., Frank, K. H. and Schlittler, *Phys. Rev.* **B30**, 7328 (1984).
- Seitz, F., *Modern Theory of Solids* (McGraw Hill, New York, 1940).
- Schrieffer, J. R., Scalapino, D. T., and Wilkins, J., *Phys. Rev. Lett.* **10**, 336 (1963); *ibid.*, *Phys. Rev.* **148**, 263 (1966).
- Simmons, J. G., *J. Appl. Phys.* **35**, 2472 (1964).
- Solymar, *Superconducting Tunneling and Application* (Chapman and Hall, London, 1972).
- Straub, D. and Himpel, H. J., *Phys. Rev.* **B33**, 2256 (1986).
- Tersoff, J. and Hamann, D., *Phys. Rev.* **B31**, 805 (1985).
- Tunneling Phenomena in Solids*, ed. by E. Burstein and S. Lundquist (Plenum Press, New York, 1969).
- Wolf, E. L., *Principles of Electron Tunneling Spectroscopy* (Oxford University Press, New York, 1985).

Monte Carlo calculation and vacuum emission experiments of hot and ballistic electrons from MIS-structures

H.-J. Fitting

Sektion Physik der Wilhelm-Pieck-Universität Rostock
 Universitätsplatz 3, DDR-2500 Rostock, German. Dem. Rep.

ABSTRACT: By means of MC-simulation of electron LO - phonon scattering we get transport parameters like electron mobility, saturation drift velocity, breakdown field strength, and the following "runaway" of the mean electron energy with field strength and drift distance in SiO_2 , Al_2O_3 , Ta_2O_5 , and ZnS-layers. Electron field emission measurements from MIS structures into vacuum maintain the MC-calculations and do not indicate an electron energy stabilization at few eV as has been predicted by strong acoustic phonon coupling but give evidence for high probability of intrinsic avalanching in SiO_2 below 10 kV/cm.

Hot electron transport and electronic breakdown processes play key role in MOS technology because they lead to threshold voltage shifts or even damage of field effect devices. On the other hand, these effects can be used for controlled charge injection and storage in memory devices like (E)EPROM's. We, Fitting and Friemann (1982) have started to calculate the energy balance of hot electrons in SiO_2 from the interaction with high energetic LO-phonons and the electric field. The corresponding Monte-Carlo simulations were performed on the Fröhlich-theory of electron-LO-phonon interaction taking into account the full energy and momentum balance under phonon creation and annihilation. In following years Fitting et al. (1982, 1983, 1984, 1986) have extended these calculations to electronic breakdown processes, electron attenuation and electron emission from insulating layers. Regarding electron transport in electric fields we find as expected below the runaway field strength F_0 steady state drift velocities v_D which can be expressed by an electron mobility μ according

$$v_D = \frac{\mu}{1 + \frac{\mu F}{v_{D0}}} F \quad (1)$$

with the well-known saturation behaviour $v_D(F \rightarrow F_0) = v_{D0}$, Fig. 1. In Tab. 1 material parameters, the resulting mobilities and runaway field strength values are presented for the different oxides and the II-VI compound semicond. ZnS.

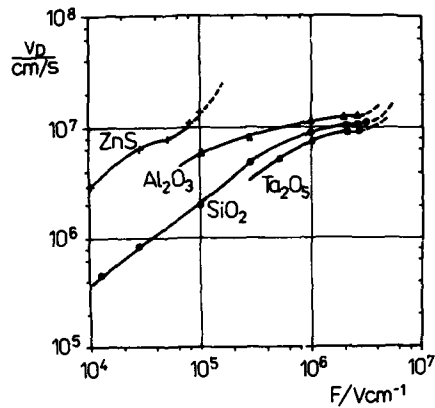


Fig. 1 MC-drift velocity v_D in dependence on field strength F

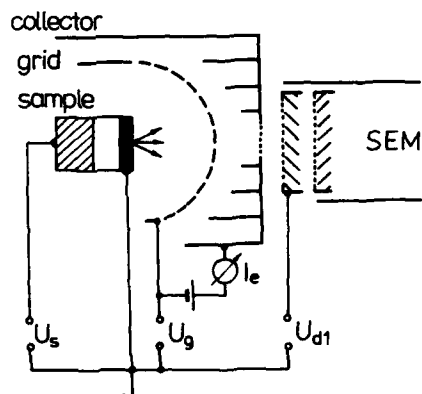


Fig. 2 Retarding field analyzer for vacuum emission experiments

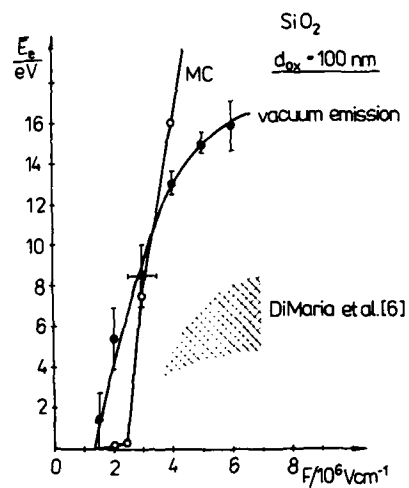


Fig. 3 Average energy \bar{E} from MC calculation and vacuum emission

Table 1

material	m^*/m_0	$\epsilon_{\text{stat.}}$	$\epsilon_{\text{opt.}}$	LO-phonons		$\mu/\text{cm}^2/\text{Vs}$	$F_0/\text{MV/cm}$
				$\hbar\omega_1$	$\hbar\omega_2$		
SiO_2	1	3,8	2,25	0,15	0,06	20	2,5
Al_2O_3	1	8,0	2,6	0,12	-	24	1,5
Ta_2O_5	1	25,0	4,4	0,108	0,062	16	2,2
ZnS	0,28	8,6	5,2	0,042	-	400	0,07

Above the critical field strength F_0 the energy distributions become unstable, i.e. electrons are being heated up with increasing drift path and field strength $F > F_0$ and finally approach to ballistic transport is observed for high fields $F \geq 10 \text{ MV/cm}$, Fitting and Czarnowski (1986). But here, when electron energy is exceeding the ionization threshold for the valence band $E > E_g \approx 9 \text{ eV}$ the question for the next relevant interaction mechanism arises. Fischetti (1984), Brorson and DiMaria et al. (1985), Porod and Ferry (1985) have taken into account additional acoustic phonon scattering, an almost elastic interaction but increasing the scattering path for LO-phonon energy losses. Thereby they get an energy stabilization with an average value $\bar{E} \approx (4-8) \text{ eV}$, still below the valence band ionization threshold E_g .

A direct prove can be performed by vacuum emission experiments from MOS samples, Fig. 2. Results for mean energy values \bar{E} of emitted electrons are presented in Fig. 3 and compared with MC values obtained for the same layer system. In both cases the mean energy values increase with electrical field above runaway field strength F_0 . Although the experimental vacuum emission curve becomes flatter for higher field strengths $F > 4 \text{ MV/cm}$ no stabilization of the mean energy at some eV is observed. Moreover this flattening seems to start with gradually transition to impact ionization of valence band electrons with electron energies $E > \frac{1}{2} E_g$ as known from secondary electron emission, Alig and Bloom (1978). This is maintained by appearance of positive holes in stressed MOS systems as well as by the wellknown decrease of breakdown field strength F_B and necessary breakdown charge Q_B leading to macroscopic damage of MOS capacitors, Fitting (1989), consistent with the conventional avalanching break down model of Di Stefano and Shatzkes (1976), Solomon (1977) and Klein (1978).

The correlation between the phonon-only scattering (MC - calculations) and the vacuum emission energy distribution are shown in Fig. 4. These results are presented along with a schematic valence band excitation model which is consistent with the observed properties of the MOS sample investigated. This model with hole migration and capture at the SiO_2/Si interface and electron trapping over the whole volume is able to account for the discrepancies between the MC calculations and the experimental results.

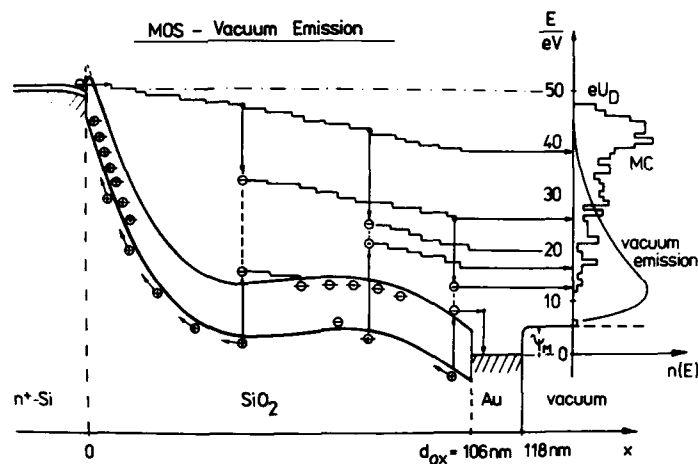


Fig. 4 Potential scheme, MC calculation and vacuum emission under valence band excitation of the MOS sample biased with $U_D = 50$ V

References:

- Alig R C and Bloom S 1978 J. appl. Phys. **49** 3476
 Brorson S D, DiMaria D J et al. 1985 J. appl. Phys. **58** 1302
 Di Stefano T H and Shatzkes M 1976 J. Vac. Sci. **13** 50
 Fischetti M V 1984 Phys. Rev. Letters **53** 1975
 Fitting H-J and Friemann J-U 1982 phys. stat. sol. (a) **69** 349
 Fitting H-J and Boyde J 1983 phys. stat. sol. (a) **75** 137
 Fitting H-J, Boyde J and Reinhardt J 1984 phys. stat. sol. (a) **81** 323
 Fitting H-J and von Czarnowski A 1986 phys. stat. sol. (a) **93** 385
 Fitting H-J 1989 Physik der Halbleiteroberfläche **20**
 ZIE of Acad Sci., Berlin, GDR
 Klein N 1978 Thin Solid Film **50** 223
 Porod W and Ferry D K 1985 Phys. Rev. Letters **54** 1189
 Solomon P 1977 J. Vac. Sci. Technol. **14** 1125

'Particle trajectory' tunnelling: a novel approach to quantum transport

K. L. Jensen* and F. A. Buot

Naval Research Laboratory Washington, D.C. 20375-5000

ABSTRACT: The nature of charge transport is being investigated using particle trajectory and effective quantum potential concepts through the Wigner distribution function analysis and the Schrodinger wave packet approach. The goal is to unite the particle trajectory description of quantum transport with particle Monte Carlo analysis so as to obtain simulations which will include scattering, self-consistency, multidimensionality, and tunneling phenomena. Statistics of "particle" trajectories can be used to calculate, for example, tunneling times in a substantially different manner than previous techniques, to calculate currents through devices, and to identify resonant tunneling behavior.

1. INTRODUCTION

The field of band-gap engineered electronic materials and devices may be considered to include vacuum microelectronic devices by considering vacuum as a "semiconductor material" of very large band gap, equal to twice the rest mass energy. Most formulations of quantum transport proceeded by assuming slow spatial and temporal variation in a system leading to the so-called quantum Boltzmann equation (QBE) (Mahan 1987, Jauho 1985, Khan, et al. 1987) and therefore essentially preclude full quantum tunneling and interference effects. On the other hand, for noninteracting particle quantum transport, the statistical Wigner distribution transport equation has been numerically applied to open-nonequilibrium systems to yield very useful results, demonstrating steady-state (Ravaioili, et al. 1985) and transient current-voltage characteristics of resonant-tunneling structures (Frensley 1987, Jensen, et al. 1989a). It has never been an easy task, nor has it been attempted, to include both full many-body effects and full quantum effects in the numerical simulation of quantum transport, particularly for open and multidimensional systems. Thus, it seems clear that some ingenuities are further required to attack quantum transport in realistic multidimensional devices.

The ensemble, self-consistent particle Monte Carlo (MC) technique (Hockney, et al. 1981) has proved to be a very powerful numerical technique for including all scattering mechanism, space nonuniformity, and all transient effects. Moreover, this "brute force" numerical technique remarkably allows for iterative and constant refinements of the transport physics model in the computer program. Since in most quantum-based devices,

*NRC/NRL Research Associate
Financial support provided by Office of Naval Research and Office of Naval Technology.

the "quantum region" is a small portion of the whole device, coupling of quantum transport technique with MC technique seems imperative. Thus far, the incorporation of quantum effects in the MC procedure to include space and time-dependent quantum processes has never been attempted, until very recently (Buot, et al. 1988), using the notion of traveling wavepacket/quantum potential particle trajectories, first proposed by Bohm for a causal interpretation of quantum mechanics (Bohm, et al. 1979, Dewdney, et al. 1982), to form an "impedance match" between MC and quantum transport. Scattering within the barrier can be handled in two ways, namely, (a) heuristically, by following the usual MC procedure for changing the momentum at each scattering event, after which the particle continue to "surf ride" the traveling wave packet representing the particle across the barrier, or (b) by incorporating built-in scattering in the quantum transport formulation across the "barrier region." One of the authors (Buot 1989), has generalized the Wigner distribution function transport equation to include all scattering and many-body effects, suitable for numerical simulation. Wigner trajectories also have been investigated (Jensen, et al., 1989b).

2. BOHM TRAJECTORY REPRESENTATION OF QUANTUM TRANSPORT

An interpretation of quantum transport in terms of elementary processes or particle trajectories has been achieved (Bohm, et al. 1979, Dewdney, et al.). To calculate particle trajectories, one integrates the velocity of the particle given by $v = \nabla S/m$ starting from an initial position in a traveling wave packet (Dewdney, et al. 1982), where $\psi = R \exp \frac{i}{\hbar} S$, and R and S are real. The quantum potential is $Q = -(\hbar^2/2mR) \nabla^2 R$, and arises in the imaginary part of Schrodinger's Eq.

2.1 Numerical Results

Single barrier trajectories have been discussed by Dewdney, et al., (1982). Examination of double barrier trajectories reveal that the rear trajectories exhibit behavior analogous to the single barrier. However, two difference features exist: first, as can be seen in Fig. 1, some of the trajectories are involved in filling up the well. Indeed, simulations at higher and lower momenta do not show this effect as strongly. Second, comparison of Fig. 1 to other simulations at slightly higher and lower momenta show that the number of tunneling trajectories is higher at the resonant energy level. These results strongly suggest that the trajectory approach is very useful for examining the resonant behavior of quantum well devices. Finally, an estimation of the tunneling times may be made on the basis of these trajectories: the fastest tunneling one does so on the order of 41 femtoseconds. Note that most of the interesting dynamics has occurred by about the 130 femtosecond mark, which should be compared to the 180 fs switching time from the current peak bias to the current valley bias for similar structures (Frensley 1987, Jensen, et al. 1989a).

3. WIGNER TRAJECTORY REPRESENTATION OF QUANTUM TRANSPORT

An alternative trajectory representation of nonequilibrium quantum processes which has been very useful in estimating scattering cross section in reactive molecular scattering processes is achieved by means of Wigner trajectories (Lee, et al. 1983). In general, the time evolution equation of the Wigner distribution equation can be obtained by application of Weyl transform (Buot 1986) to the time evolution equation of the density matrix operator of a nonequilibrium system. The numerical implementation of the resulting equation, with the boundary condition for resonant-tunneling diode (RTD), or double-barrier struc-

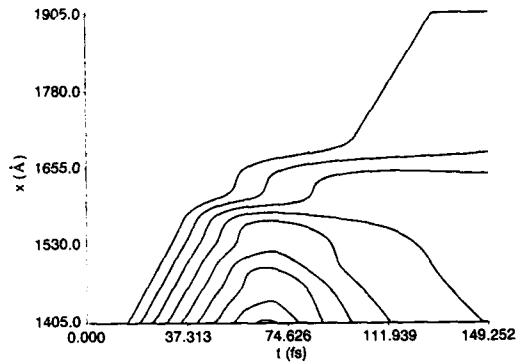


Fig. 1. Double barrier resonant tunneling trajectories for a Schrodinger Wave packet: potential height = 0.3 eV, potential well = 50 Å, barriers = 30 Å; wave packet spread $\sigma = 100$ Å; mass of particle = $0.0667 m_0$, kinetic energy = 0.087 eV. Dashed lines show location of barrier edges.

ture, has been described in detail by Frensky (1987). A more accurate numerical algorithm suitable for calculating Wigner trajectories has been found by Jensen and Buot (1989a, 1989b). Wigner trajectories can be easily determined as discussed in Jensen et al. (1989b). The equations of motion completely determine the dynamics of Wigner phase-space trajectories.

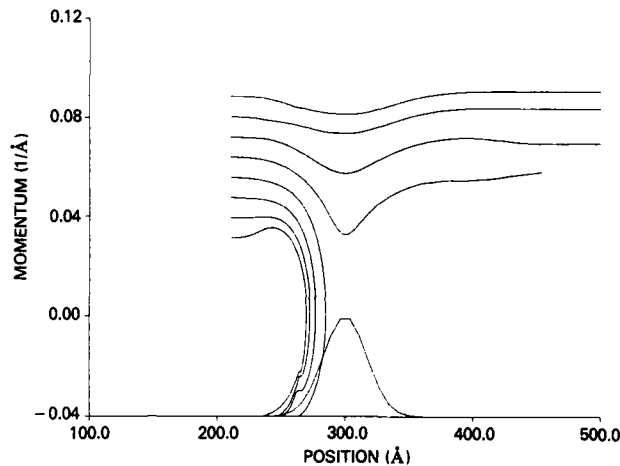
3.1 Numerical Results

Wigner trajectories are simulated for single barrier and double-barrier structures. For single barrier structures, and in order to show the relation between Bohm trajectories and Wigner trajectories, both the Bohm trajectories and Wigner trajectories are obtained from the same traveling Wigner distribution wave packet, obtained as a Weyl transform of Schrodinger wave packet. The double-barrier steady-state trajectories have been fully discussed in Jensen et al., (1989b). Most calculations of tunneling times (a particle trajectory concept) are based on an "arbitrary" use of traveling wave packet (Huang, et al. 1988) our calculations are unique in that it is based on "microscopically" examining the elementary and individual space-time dependent events in a tunneling process.

Although we can apply the method of Jensen et al., (1989b) for calculating the Wigner trajectories for a single-barrier structure at steady state, we have chosen to simulate a truly time-dependent problem, i.e., calculate Wigner trajectories from a traveling Wigner wave packet. In order to show the relation between Bohm trajectories and Wigner trajectories, we have also calculated the Bohm trajectories from the same Wigner wave packet. To calculate the Bohm trajectories from the traveling Wigner wave packet we calculate the velocity of the particle at each point in space as from the average momentum, which is numerically equal to $\nabla S/m$ from the Schrodinger wave packet. Notice that in the present case, the calculation of the particle trajectory representation of quantum transport involves a truly time-dependent problem since we are dealing with a traveling Wigner wave packet.

We have found that the Bohm trajectories obtained from both the Schrodinger wave packet and the corresponding Wigner wave packet show an exact resemblance, and clearly indicates that the particle velocity in the Bohm trajectories are averaged velocities calculated from the Wigner distribution function. The corresponding Wigner trajectories determined from the traveling Wigner wave packet, for a truly time-dependent transport problem, are shown for the first-time in Fig. 2.

Fig. 2. Wigner trajectories for a traveling Wigner wave packet. Center momentum of packet is 0.06 \AA^{-1} , and spread is $\sigma = 35 \text{ \AA}$. Gaussian potential is centered at 300 \AA , and is shown on the bottom of the graph. Initial positions of all trajectories are at $x_0 + 2\sigma$, where x_0 is the initial center of the packet.



4. CONCLUSION

In conclusion, the techniques of calculating phase space trajectories, their behavior and energetics, particle currents, and the tunneling times associated with them (Jensen, et al. 1989b), allows for the development of a physical intuition about the actual mechanism of quantum transport. That the trajectories calculated above support localized-particle transport ideas, tends to give physical meaning to Bohm and Wigner trajectories themselves, and their useful correspondence with the quantum trajectories of actual particles. Such a favorable relationship can be expected to impact on numerical simulations in which the dynamics of the actual particles are needed in "multidimensional" and realistic electronic device transport calculations.

REFERENCES

- Bohm D and Hiley B J 1979 *Nuovo Cim.* **52**, pp 246-265.
- Buot F A 1986 *Phys. Rev. A* **33**, pp 2544-2562. See Appendix A.
- Buot F A and Jensen K L 1988 "Self-Consistent Monte Carlo Particle Transport Including Space and Time-Dependent Quantum Tunneling," presented at the IEEE First International Vacuum Microelectronics Conference, Williamsburg, VA, June 13-15.
- Buot F A 1989 "Exact Integral Form of Wigner Distribution-Function Equation in Many-Body Quantum Transport Theory" NRL Preprint.
- Dewdney C and Hiley B J 1982 *Found. Phys.* **12**, pp 27-48.
- Frenley W 1987 *Phys. Rev.* **36**, pp 1570-1590.
- Hockney R W and Eastwood J W 1981 *Computer Simulation Using Particles*, (New York: McGraw Hill) pp 357-407.
- Huang Z, Cutler P H, Feuchtag F E, and Nguyen M 1988 "Computer Simulations of a Wave Packet Tunneling Through a Barrier," First International Vacuum Microelectronics Conference, Williamsburg, VA, June 13-15.
- Jauho A P 1985 *Phys. Rev.* **32**, pp 2248-2253.
- Jensen K L and Buot F A 1989a *J. Appl. Phys.* **65**, pp 5248-5250.
- Jensen K L and Buot F A 1989b *Appl. Phys. Letters* (August 14 issue).
- Khan F S, Davies J H, and Wilkins J W 1987, *Phys. Rev.* **36**, pp 2578-2599.
- Lee H W and Scully M O 1983 *Found. Phys.* **13**, pp 61-7.
- Mahan G D 1987 *Phys. Reports* **145**, pp 251-318.
- Ravaioili U, Osman M A, Potz W, Klusdahl N, and Ferry D K 1987 *Physica* **134B**, pp 36-56.

Silicon cold cathodes based on PIN diodes

P A M van der Heide, G G P van Gorkom, A M E Hoeberechts, A A van Gorkum
and G F A van de Walle

PHILIPS Research Laboratories, P.O. Box 80.000, 5600 JA Eindhoven, The Netherlands

ABSTRACT: Breakdown voltages and electron emission properties of PIN diodes at fields of $1-1.5 \cdot 10^6$ V/cm are presented and compared with model calculations. A possible explanation of the observed differences between theory and experiment would be, beside uncertainties in dopant concentrations, saturation of the avalanche breakdown at high fields. The present model for cold cathodes overestimates tunnelling. The measured electron temperatures qualitatively agree with the theory by Bartelink.

1. INTRODUCTION

In literature, data for the avalanche breakdown process in silicon have been published for electric fields around $4 \cdot 10^5$ V/cm. The silicon cold cathode, consisting of a reverse biased pn junction, offers an example of a device where field strengths of $1-2 \cdot 10^6$ V/cm are reached. These high fields will also be present in the next generation of MOS transistors. It is by no means certain that avalanche breakdown parameters valid at low fields are also correct at high fields. Also at these high fields a mixed breakdown occurs i.e. both impact ionization and tunnelling contribute to the current in the device.

Breakdown voltages of PIN diodes, which have a constant field inside the intrinsic layer, make a comparison with existing avalanche breakdown data sets possible. An analysis of the electron emission properties of PIN silicon cold cathodes allows for improvement of the existing model for silicon cold cathodes. The present model (van Gorkom and Hoeberechts 1986) is based on an abrupt junction where e.g. the field changes rapidly over distances short compared to the tunnelling lengths. In section 2 a theoretical background is given. In section 3 experimental details are described. In section 4 the experimental data are compared with model calculations. Finally in section 5 some conclusions are given.

2. THEORY

The basic mechanism in silicon cold cathodes is the impact ionization process occurring in avalanche breakdown, see e.g. Moll (1964).

The impact ionization process occurring in these cathodes can be characterized by the electron multiplication factors \bar{a}_n (electrons/cm) and \bar{a}_p (holes/cm), which depend on the field E in the depletion layer, where

$$(1) \quad \begin{aligned} \bar{a}_n &= A_n \cdot \exp(-B_n/E) \\ \bar{a}_p &= A_p \cdot \exp(-B_p/E) \end{aligned}$$

For the parameters A_n , A_p , B_n and B_p several data sets exist e.g. Lee (1964), Grant (1973), Decker-Dunn (1975) and van Overstraeten-de Man (1970).

In the case of an ideal PIN structure, i.e. where both p and n concentrations are infinitely high, the breakdown field can be calculated analytically (Moll 1964), using eq.(2):

$$(2) \quad 1 = \bar{a}_n / (\bar{a}_p - \bar{a}_n) \cdot (\exp((\bar{a}_p - \bar{a}_n)d) - 1),$$

where d is the i-layer thickness.

Thus given the parameters \bar{a}_n and \bar{a}_p one can calculate the electric field E at breakdown using eq. (1) and (2). The breakdown voltage V_B is then given by:

$$(3) \quad V_B = E \cdot d$$

In the case of the silicon cold cathodes with high electric fields a mixed breakdown occurs i.e. both avalanche breakdown and tunnelling occur, which can be modeled (van Gorkom and Hoeberechts 1986):

$$(4) \quad dj_n(x)/dx = (\bar{a}_n - \bar{a}_p)j_n + \bar{a}_p J_d + A_t \cdot E^2 \cdot \exp(-B_t/E)$$

where $j_n(x)$ is the electron current density and J_d the total current density (electrons and holes). The tunnelling is characterised by the parameters A_t and B_t , which are very uncertain as the field changes rapidly over distances shorter than the tunnelling mean free path. Van Gorkom and Hoeberechts (1986) assumed $A_t = 40 \text{ A/V}^2 \cdot \text{cm}$ and $B_t = 1.6 \cdot 10^7 \text{ V/cm}$.

The condition for breakdown is $j_n(W) = J_d$, where W is the depletion layer width. This equation can be numerically solved, resulting in a value of the breakdown voltage for given dopant distribution and i-layer width. A correction has to be applied for a "dead space" i.e. there is a minimum energy necessary for electron generation (1.1 eV) and hole generation (2.0 eV).

Experimentally it was found that the total number of electrons N emitted by silicon cold cathodes as a function of the workfunction ϕ of the surface can be described by:

$$(5) \quad N = A \cdot \exp(-\phi/kT_e)$$

where T_e is an effective electron temperature, which is equal to the electron temperature deduced from the Maxwellian electron energy distribution and A a constant. Bartelink et al (1963) predict a close to linear relation between electron temperature and the effective electric field in the diode. Thus the measured values of kT_e can be used to check this theory.

3. EXPERIMENTAL DETAILS.

The PIN emitters consisted of a p^+ layer defined by B implantation in an epi substrate, on top of which an i-layer was grown using silicon molecular beam epitaxy. The background concentration in the intrinsic layer was $2 \cdot 10^{15} \text{ atoms/cm}^3$. The n^{++} layer was defined by a 5 kV As implantation in the MBE grown layer, annealed at 700°C.

The breakdown voltages were measured by extrapolating the I-V curve at reverse bias currents between 0.5-1.0 mA towards zero current. The emission properties of the diodes according to eq.(5) as a function of work function were measured in a Vacuum Generators Escalab MKII.

The surface work function was varied by controlled barium deposition. The variations in work functions were obtained by measuring the change in the onset of secondary emission, as induced by X-ray irradiation. Surface barium coverages were measured using XPS and Auger. Before barium deposition about 0.4 monolayer (ML) of oxygen, about 0.1 ML of carbon and 0.2 ML of fluorine were present.

To be able to determine the influence of the actual dopant distribution on the model a program was written, which allows for numerical integration of equation (4). The model calculates the local electric field and the avalanche contribution at every point. A dead space correction and/or a tunnelling contribution, using the values described in the previous section can be applied.

4. RESULTS AND DISCUSSION

Cathodes were manufactured with 3 different nominal i-layer thicknesses: 40 nm-70 nm-100 nm. The nominal i-layer thicknesses were determined by subtraction of the width of the As implanted layer from the MBE deposited intrinsic layer. The diode characteristics in reverse bias are shown in figure 1, the breakdown voltages deduced from these graphs are given in table 1. The measured dependence of the emission current on workfunction, obtained by varying the barium coverage, could be fitted using (5). The resultant values of kT_e are also given in table 1, as well as the electric fields present calculated using (3).

Table 1

i-layer (nm)	V_B (V)	E (10^6 V/cm)	kT_e (eV)
40	6.1	1.5	0.36
70	7.1	1.0	0.25
100	8.6	0.9	0.23

To compare the actual breakdown voltages with theory the breakdown voltages as a function of i-layer width were also calculated using the data sets by Grant (1973), Lee (1964), Decker-Dunn (1975), and van Overstraeten-de Man (1970). From the calculated breakdown voltages, the built in potential (1.0 eV) has to be subtracted to get the plotted experimental breakdown voltages.

The experimental results and the calculated ones for the ideal pin diode are plotted in figure 2. It is seen that there are strong differences between the various data sets, especially for thin i-layers thus at high fields. The data by Grant and van Overstraeten-de Man give similar results at high fields. The experimental breakdown voltages are about 1-2 V higher than the model calculations predict. To explain this first the influence of the actual dopant distribution on the breakdown voltage was investigated. The actual As distribution (peak $4 \cdot 10^{19}$ at./cm³) has only little influence (0.1-0.2 V) on the breakdown voltage. The background concentration in the intrinsic layer has even less influence (0.1 V). The only parameter

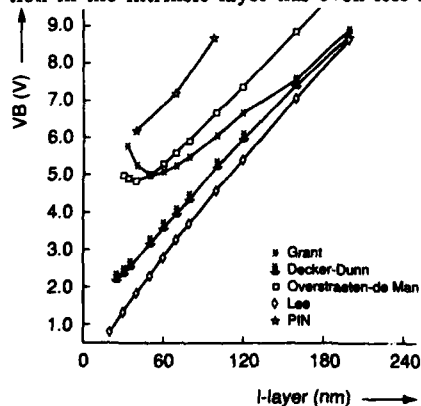


Figure 2: Breakdown voltage as a function of i-layer thickness for various impact ionization datasets as calculated and the experimental PIN results.

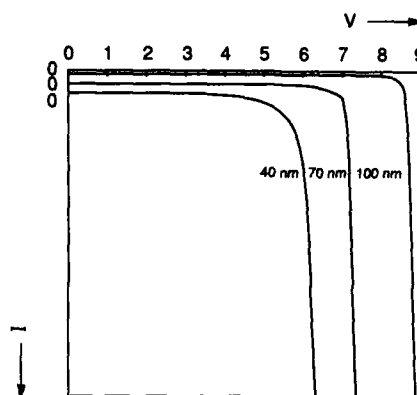


Figure 1: I-V characteristics in reverse bias of the PIN diodes.

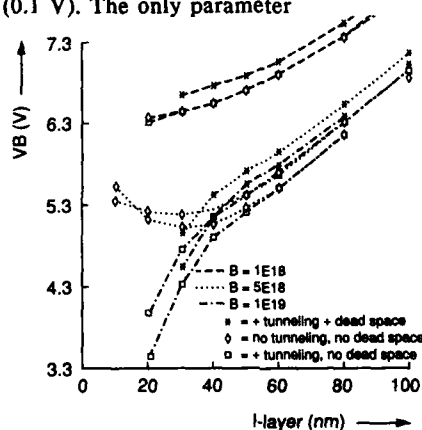


Figure 3: Calculated breakdown voltage as a function of i-layer thickness for various conditions using the Overstraeten-de Man parameters.

strongly influencing the field, and hence the breakdown voltage is the boron concentration. To see how the tunnelling contribution and or the dead space correction influence the results, the breakdown voltage was calculated as a function of i-layer thickness for various Boron concentrations in three cases (i) ideal case according to eq.(2) (ii) incorporating a dead space correction using eq.(4) (iii) incorporating a dead space correction and a tunnelling contribution using eq.(4). The results for the model by van Overstraten-de Man are given in figure 3. The results for the Grant parameters are similar. It is seen that below 40 nm layer thickness i.e. at fields larger than 1.10^6 V/cm tunnelling becomes important, decreasing the breakdown voltage strongly for B concentrations above 1.10^{18} atoms/cm³. As the deviation with experiment is strong it is expected that the present model overestimates the tunnelling contribution, in agreement with the results by Hurkx (1989), who measured much lower tunnel currents. The dead space correction only results in about 0.5 V shifts in the breakdown voltage. The experimentally observed breakdown voltages can be explained if the boron concentration is much lower than expected (1.10^{18} instead of 8.10^{18} atoms/cm³). Unfortunately it was not possible to check this in the present emitters using e.g. SIMS. Another explanation would be that the multiplication process saturates at field strengths near 1.10^6 V/cm.

The values of kT_e as a function of electric field are plotted in figure 4 to compare with the theory of Bartelink (1963) and previous results for pn cold cathodes. The theoretical curve was deduced for a constant electric field. The error bars in the experimental data for pn emitters and Bartelink et al. are due to uncertainties in taking a suitable mean electric field. For the PIN diodes the field is constant. These data points are qualitatively in agreement with the theory by Bartelink, although the values are lower.

5. CONCLUSIONS

The measured breakdown voltages of 3 different PIN diodes with electric fields of $1-1.5.10^6$ V/cm cannot be fully explained using the existing avalanche breakdown parameter sets. A possible explanation would be saturation of the avalanche process in thin i-layers (high fields). Further experiments are planned to clarify this point. For the dependence of the effective electron temperature kT_e on the electric field, there is qualitative agreement with the theory by Bartelink et al.

References

- D J Bartelink, J L Moll and N I Meyer, 1963, Phys. Rev. 130, 972.
- D R Decker and C N Dunn, 1975, J. of Elec. Mat., 4, 527.
- W N Grant, 1973, Sol. St. Electr. 16, 1189.
- G A M Hurkx, submitted for publication in Sol. St. Electr. 1989
- C A Lee, R A Logan, R L Batdorf, J J Kleimack and W Wiegmann, 1964, Phys. Rev. 134, 761.
- J L Moll, 1964, Physics of semiconductors, McGraw-Hill, New York.
- G G P van Gorkom and A M E Hoeberechts, 1986, Philips J. of Res. 41, 343.
- R van Overstraten and H de Man, 1970, Sol. St. Electr. 13, 583.

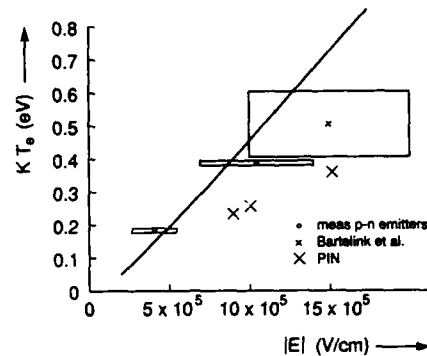


Figure 4: Electron temperature as a function of the electric field. Full curve: theory of Bartelink.

Theoretical study of the scanning tunnelling microscope

Th Laloyaux, A A Lucas, J-P Vigneron and Ph Lambin

Facultés universitaires ND de la paix, 61 rue de Bruxelles, B5000 Namur Belgium

H Morawitz

IBM Almaden Research Center, 650 Harry Road, San Jose California 95120

ABSTRACT: A model of scanning tunneling microscope (STM) composed of a planar metallic surface with a hemispherical protrusion in front of a planar metallic surface is studied using the numerical finite-element method to solve the Schrödinger equation and find the tunneling current and its spatial distribution. From the results for various values of the tip radius and the tip-sample distance, conclusions are drawn about the resolution of the STM and the behaviour of the tunneling current when the tip is moved away from the surface.

1. INTRODUCTION

The scanning tunneling microscope (STM), invented by Binnig et al (1982) is an instrument capable of investigating (semi)conducting surfaces down to the atomic scale. It is composed of a very thin tip mounted on a piezodrives and approached a few angstroms away from the sample surface. A potential difference applied between these two electrodes gives rise to a current carried by the conduction electrons of the tip and the sample, which tunnel across the vacuum gap. The transmission coefficient of a potential barrier is known to be strongly dependent on the barrier width. So, the tunneling current is very sensitive to the tip-sample distance. While the tip scans the surface along the two horizontal coordinates (X and Y), its vertical position (Z) is adjusted by a feed-back loop in such a way that the tunneling current (or its derivative with respect to Z) remains constant. The record of the 3D surface described by the tip in the (X,Y,Z) space is called an STM image and contains informations about the surface topography and electronic structure of the sample.

In order to gain a better understanding of the STM images, a theory of STM is needed, which is not an easy matter because the geometry of the tip-vacuum-sample junction is not planar and, since the tip radius is of the same order of magnitude as the wavelength of the electrons at the Fermi energy, a 1D approximation to the tunneling is not reliable. The most frequently used theory is Tersoff and Hamann's (1983, 1985) which relies on the transfer hamiltonian approximation of Bardeen (1961).

In this paper, we present exact numerical solutions of the Schrödinger equation for a simple model of STM. Our aim is to compute the current density in the STM junction, in order to estimate the resolution of the microscope and the behaviour of the tunneling current when the tip is moved away from the sample.

2. MODEL

The model we chose (Lucas et al 1988) is composed of a planar metal-vacuum-metal junction, with one electrode (the tip) surmounted by a hemispherical protrusion (Fig. 1). Both the tip and the sample are free-electron metals, i.e. the potential energy of an electron is constant

provided it stays inside the electrodes. In the vacuum, the electron interacts with its images in the electrodes. The image potential is exactly soluble in the plano-spherical geometry of our model as shown by Lucas et al (1984). The inner potential of the metals is taken to be -14 V with respect to the vacuum level, and the Fermi level is -4.5 eV. These values correspond to aluminium. We compute the current for a vanishing bias, so only the electrons at the Fermi level contribute to the current. The sign of the bias is chosen so that the electrons flow from the tip to the sample. We vary the tip radius and the tip-sample distance to study the influence of these parameters on the resolution of the microscope and on the tunneling current.

3. METHOD

A brief description of our method follows. More details can be found elsewhere (Laloyaux et al 1988). We solve the one-electron Schrödinger equation for each of the electrons impinging the potential barrier from the tip side.

$$\Delta\Psi + V\Psi = E_F\Psi \quad (1)$$

where Ψ is the wavefunction of the electron and V is its potential energy. Thanks to the rotational symmetry of the junction, the cylindrical coordinates ρ , z and ϕ can be used to separate ϕ from ρ and z :

$$\Psi_m(\rho, z, \phi) = e^{im\phi} \psi_m(\rho, z) \quad (2)$$

where m is the angular momentum. An equation in ρ and ϕ must be solved for every value of m . Only the states with the smallest values of $|m|$ contribute to the current: in practice, we consider $-2 \leq m \leq 2$. The 2-dimensionality of the problem reduces considerably the memory allocation and computer time needed for the numerical calculations.

Four regions must be considered for the resolution, according to the dependence of the potential V on the coordinates. The solutions have to obey usual matching conditions on the boundaries of the regions. Inside the tip, the potential is constant and the wavefunction is expressed analytically as a linear combination of incident and reflected waves, each of these being the product of a ρ -dependent part and a z -dependent part. Inside the sample, the potential is constant too, and ψ_m is a linear combination of transmitted waves of the same kind. In the vacuum, far enough from the tip, the potential depends on z only and ρ and z can still be separated. The z -dependent part of the wavefunction must be computed numerically: the 1-D finite-element method (FEM) developed by Laloyaux et al (1989) is used. In the region of the protrusion, where V depends on both ρ and z , ψ_m is computed fully numerically and we use the 2-D FEM. The FEM (see e.g. Mitchell and Wait 1985) consists essentially in approximating the unknown function by a polynomial in every cell of a discretization mesh. The FEM discretization reduces Schrödinger's equation to a finite linear system of equations,

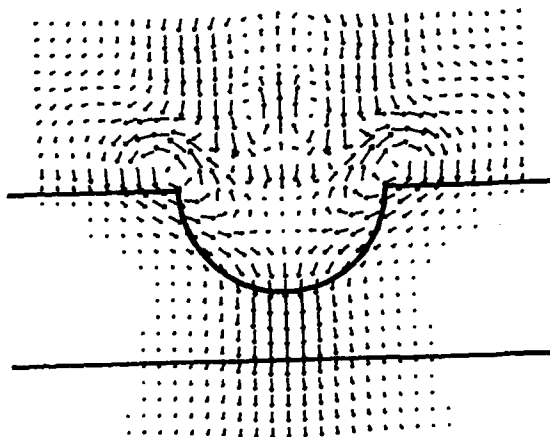


Fig. 1 Plano-spherical model of the STM with a tip radius = 3 Å and a tip-sample distance = 2 Å. The hemispherical protrusion is the apex of the tip. The lengths of the arrows are proportional to the local current densities.

that can be solved using standard numerical algorithms.

For every value of m , several electronic states must be computed, each of those being characterized by a different incident wave. From the calculated wavefunctions, we compute the current density associated with every electronic state using the well known formula for the current density j

$$j = \text{Im}(\Psi^* \nabla \Psi). \quad (3)$$

Adding up these individual current densities leads to the total current density carried by all the electrons.

4. RESULTS

Fig. 1 shows the current density between the STM tip and the sample, for a tip radius equal to 3 Å and a tip-sample distance equal to 2 Å. The current appears to be strongly localized near the protrusion, which is consistent with the high resolution obtained in STM experiments. The resolution of the STM is related to the width of the tunneling electron beam, which we define as the value of ρ at which the z -component of the current density at the sample surface is half its value at $\rho = 0$. The current channel width versus the tip radius is plotted on Fig. 2, for three different values of the tip-sample distance. The width of the current channel turns out to increase at a rate of 0.2 Å per Å increase in the tip radius and not to depend strongly on the tip-sample distance, at least in the range we explored. We represented on Fig. 3 the behaviour of the total tunneling current when the tip is moved away from the sample.

The logarithm of the total current is plotted versus the tip-sample distance, for various values of the tip radius. It can be seen that the current decreases exponentially as the barrier width increases, as predicted from the approximate 1-D formula for a square potential barrier

$$I \propto \exp(-1.025 \sqrt{\Phi} d) \quad (4)$$

where Φ is the work function expressed in electron-volts and d is the barrier width in angstroms. If we define an effective work function Φ_{eff} for our 3-D results from Eq (4), the slope of the curves in Fig. 3 gives

$$\Phi_{\text{eff}} = 4.6 \text{ eV} \quad (5)$$

This value is very similar to the value we put in our computations (Fermi level = -4.5 eV), but the image potential seems not to affect the logarithmic derivative of the current with respect to the distance. Binnig et al (1984) obtained a similar result. Nevertheless, the image potential does modify the barrier and has an effect on the value of the tunneling current, so it is worth considering it.

5. CONCLUSION AND OUTLOOK

We developed a method well-suited for the study of 3-D tunneling problems with a rotational symmetry. Our method consists in a resolution of the Schrödinger equation by a grid discretization technique, namely the finite-element method. An application was made to a model of STM consisting in a plano-spherical metal-vacuum-metal junction. The results show that the tunneling current flows across the vacuum in a narrow channel.

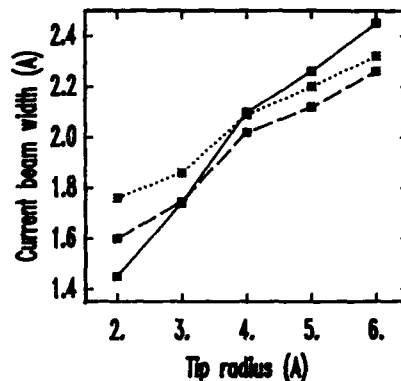


Fig. 2 Width of the tunneling current beam vs the tip radius for the tip-sample distance = 1 Å (solid line), 2 Å (dashed line) and 3 Å (dotted line).

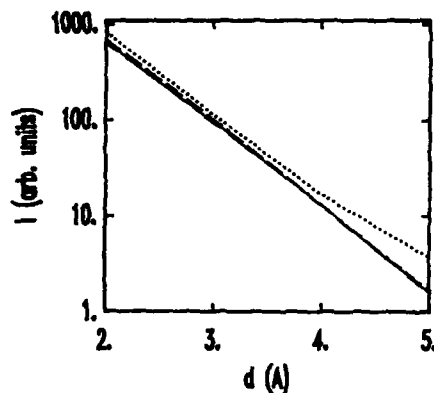


Fig. 3 Tunneling current (log scale) vs tip-sample distance for the tip radius = 3 Å (solid line), 4 Å (dashed line) and 5 Å (dotted line).

The width of this channel, to which the resolution of the microscope is most probably related, increases slowly with the tip radius and is not very sensitive to the tip-sample distance.

The intensity of the tunneling current decreases exponentially with the tip-sample distance; the rate of decrease appears not to be influenced by the image potential.

Since the FEM method works well for tunneling problems, we plan to apply it to other situations: more realistic STM models with a surface corrugation, tunnel junctions with spherical metallic inclusions, field emission tips.

ACKNOWLEDGEMENTS

This paper presents research results of the Belgian programme on interuniversity attraction poles initiated by the Belgian state-Prime Minister's Office-Science Policy Programming.

The scientific responsibility is assumed by its authors.

Two of us (Th L and Ph L) are grateful to the Belgian National Fund for Scientific Research for financial support.

REFERENCES

- Bardeen J 1961 *Phys. Rev. Lett.* 6 57
- Binnig G, Garcia N, Rohrer H, Soler J M and Flores F 1984 *Phys. Rev. B* 30 4816
- Binnig G, Rohrer H, Gerber Ch and Weibel E 1982 *Phys. Rev. Lett.* 49 57
- Laloyaux Th, Lambin Ph, Vigneron J-P and Lucas A A 1989 *J. Comput. Phys.* in press
- Laloyaux Th, Lucas A A, Vigneron J-P, Lambin Ph and Morawitz 1988 *J. Microscopy* 152 53
- Lucas A A, Morawitz H, Henry G R, Vigneron J-P, Lambin Ph, Cutler P H and Feuchtwang T E 1988 *Phys. Rev. B* 37 10708
- Lucas A A, Vigneron J-P, Bono J, Cutler P H, Feuchtwang T E, Good R H Jr and Huang Z 1984 *Journal de Physique* C9 125
- Mitchell A R and Wait R 1985 *The Finite Element Method in Partial Differential Equations* (New York: Wiley)
- Tersoff J and Hamann D R 1983 *Phys. Rev. Lett.* 50 1998
- Tersoff J and Hamann D R 1985 *Phys. Rev.* 31 805

Field-enhanced emission

P.T. Landsberg

Faculty of Mathematical Studies, University, Southampton, England.

ABSTRACT: The paper gives a digest of recent joint work by the author in conjunction with S.R. Dhariwal. In this field-enhanced emission from a Coulomb trap has been treated theoretically by including two effects which have been neglected in the past: (1) The emitted electron moves in the conduction band in a region in which the density of states depends on position. (2) The motion is terminated by a scattering event. These results are injected into a new type of approximated recombination theory ("truncated cascade recombination"), and some reasonable agreement with experiment is found.

1. BACKGROUND

I present here a digest of the main ideas involved in papers published in 1989 with Dr. S.R. Dhariwal.

Schottky (1923) used the image force in a classical discussion of field-enhanced emission:

$$V(x) = E_0 - eEx - e^2/4x \Rightarrow V(x_m) = E_0 - (e^3E)^{1/2}.$$

Here $V(x_m)$ is the height of the potential energy maximum and E is the electric field. Frenkel (1938) used the Coulomb potential of a trap in a semiconductor (dielectric constant ϵ) to discuss electron emission from the trap one-dimensionally:

$$V(x) = E_0 - eEx - e^2/\epsilon x \Rightarrow V(x_m) = E_0 - 2(e^3E/\epsilon)^{1/2}.$$

Jonscher (1967) and Hartke (1968) gave a three-dimensional discussion of this effect (θ is the angle the electron velocity makes with E):

$$V(x) = E_0 - eE\cos\theta x - e^2/\epsilon r \Rightarrow V(x_m) = E_0 - 2(e^3E\cos\theta/\epsilon)^{1/2}.$$

The electron emission rate was found to be changed by the ratio

$$\chi \equiv \frac{e_n(\beta)}{e_n(0)} = \begin{cases} \exp \beta & \text{(Schottky)} \\ \frac{1}{2} + \beta^{-2} [1 + (\beta-1)e^\beta] & \text{(Jonscher-Hartke)} \end{cases} \quad (1)$$

The first term in (2) arises from up-field the second term from down-field motion and

$$\beta \equiv (2/kT)(e^3 E/\epsilon)^{\frac{1}{2}}$$

The effect is often called Poole-Frenkel effect.

2. FIELD DEPENDENCE OF EMISSION FROM A TRAP

In our new theory (Dhariwal and Landsberg, 1989b) the electron of energy E ($< E_{co}$) can pass over the potential maximum and it enters the conduction band at

$$r_1 = (E_{co} - E)/eE \cos \theta$$

where E_{co} is the energy at $r = 0$ and also the band edge energy in the absence of a field. The density of states encountered by the electron thereafter increases with distance r from the trap since the horizontal line representing the electron energy departs more and more from the band edge which is downward sloping to the right (if E acts to the left). There is a probability

$$P(r)dr = \frac{1}{\lambda} \exp\left\{-\frac{r-r_1}{\lambda}\right\} dr$$

that the electron survives in the band in a region $(r, r+dr)$, λ being the mean free path. The density of states is

$$N(E, r, \theta) \propto [E - E_c(r, \theta)]^{\frac{1}{2}} = [E - (E_{co} - erE \cos \theta)]^{\frac{1}{2}}$$

and yields an averaged r -independent density of states

$$N(E, \theta) = \int_{r_1}^{\infty} N(E, r, \theta) P(r) dr.$$

The case $E > E_{co}$ has of course also to be considered: it leads to $r_1 = 0$. Thereafter one has to integrate the electron emission rate over θ to find a new and more accurate expression for χ . It results in a field dependence closer to (1) than to (2). In fact for Si at 80K and fields in excess of 10^4 V cm^{-1}

$$\chi \approx \left(\frac{ekT\lambda}{4e^2} \right)^{\frac{1}{2}} \exp \beta \quad (\sim 1.59 \exp \beta \text{ for Si}) .$$

is quite a good approximation.

3. TRUNCATED CASCADE RECOMBINATION (T.C.R.)

Take the trap to have only one (effective) excited state from which the electron emission rate is e_{ne} . Let t_n^{-1} be the relaxation rate from it to the ground state. Given the electron in the trap is in the excited state, the probability of the electron reaching the ground state (without being first emitted to the band) is

$$P_e \equiv \frac{t_n^{-1}}{t_n^{-1} + e_{ne}\chi} = \frac{1}{1 + e_{ne}t_n\chi}$$

which is Lax's "sticking probability" for this case, where it is uniquely simple. Note that χ is applied to emission rates only, not to capture coefficients c_{ng} , c_{ne} (into ground and excited states respectively), which are introduced below.

The effective capture coefficient is (Landsberg and Dhariwal, 1989)

$$c_{n \text{ eff}} = c_{ng} + P_e c_{ne} = c_{ng} + c_{ne} / (1 + e_{ne}t_n\chi) \quad (3)$$

Let v_g be the concentration of centres in the ground state, v_o the concentration of empty centres and n the electron concentration. Then the recombination rate per unit volume is

$$c_{n \text{ eff}} v_o n - e_{n \text{ eff}} v_g .$$

Hence the emission rate in the presence of an electric field is

$$e_{n \text{ eff}} \chi = c_{n \text{ eff}} \left(\frac{nv_o}{v_g} \right)_{\text{equ.}} \chi . \quad (4)$$

Thus as E is increased $c_{n \text{ eff}}$ decreases by (3) and $e_{n \text{ eff}}$ increases by (4) in semi-quantitative agreement with certain experiments (Rosier and Sah, 1971).

4. TRANSIENT EFFECTS

We have also considered the case when v_o , v_g , v_e (concentration of traps

with the electron in the excited state) depend on time. Model equations (specifying the possible transitions) and continuity equations yield equations of the type (Dhariwal and Landsberg, 1989a)

$$\ddot{v}_i + P\dot{v}_i + Qv_i + S_i = 0 \quad (i=0,g,e)$$

where P , Q , S_i are independent of time. The two lifetimes which are implied by this equation enable one to recover equations (3) and (4) as appropriate limiting cases.

5. CONCLUSION

A tractable and simplified cascade model has been developed into which new and more accurate Poole-Frenkel emission rates and capture coefficients can be inserted. This yields a description of steady state as well as transient recombination processes.

REFERENCES

- Dhariwal, S.R. and Landsberg, P.T. 1989a *J. Phys. Cond. Matt.* 1 569.
 Dhariwal, S.R. and Landsberg, P.T. 1989b *J. Phys. Chem. Sol.* 50 363.
 Frenkel, J. 1938 *Phys. Rev.* 54 647.
 Hartke, J.L. 1968 *J. App. Phys.* 39 4871.
 Jonscher, A.K. 1967 *Thin Solid Films* 1 213.
 Landsberg, P.T. and Dhariwal, S.R. 1989 *Phys. Rev.* B39 91.
 Rosier, L.L. and Sah, C.T. 1971 *Solid-State Electron.* 14 41.
 Schottky, W. 1923 *Physik Zeit.* 18 63.

Characterization of individual micro-emission centres distributed in planar arrays

R.V.Latham and A.D.Archer

Department of Electronic Engineering and Applied Physics
Aston University, Birmingham B4 7ET, U.K.

ABSTRACT: Three instrumental techniques are described that may be used for studying total arrays of field emission sites and the properties of the constituent micro-emission processes. The versatility and performance capability of these systems is illustrated by reference to previous investigations into a variety of metal-insulator field emission regimes. Also discussed is the potential application of these regimes to the production of practical broad-area cold-cathode electron sources, and arrays of discrete field emission centres.

1. INTRODUCTION

In the course of extended investigations into the physical origin of the prebreakdown currents that flow between vacuum-insulated high-voltage electrodes, it has been necessary to develop a range of sophisticated analytical techniques for studying isolated, micron-sized, field-induced electron emission processes (see reviews of Latham 1981,1988). The most important of these techniques are (i) an optical imaging facility for studying the spatial distribution and temporal stability of populations of emission "sites", (ii) a scanning micro-point anode in conjunction with a low-resolution SEM/Auger system for dynamically locating and subsequently identifying the topographical and chemical nature of individual emission sites, and (iii) a combined system for studying the electron emission images and associated electron spectra of individual processes. More recently, these same techniques have also been applied to the study of artificially created micro-emission structures that could form the basis of new types of cold-cathode electron source.

This paper will review the essential instrumental features of these novel analytical systems, and illustrate their performance capability with reference to selected data obtained from the experimental studies referred to above. Particular emphasis will be given to contrasting the differences between the characteristics of "metallic" and "non-metallic" emission processes, and discussing the technological significance of these findings in relation to the development of possible new cold-cathode electron sources. Finally, outline details will be given of new analytical approaches that are currently being developed to obtain higher resolution topographical information about individual emission processes.

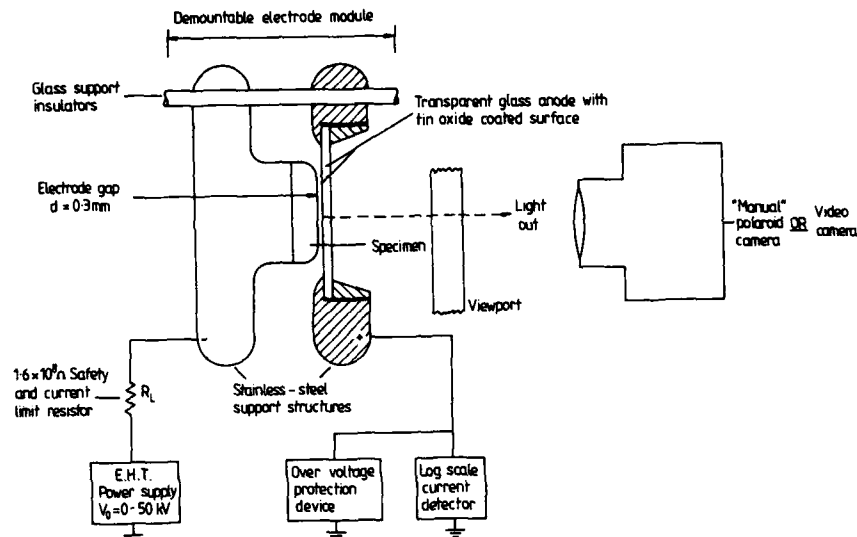


Fig. 1. A "transparent anode" analytical facility for studying planar distributions of point emission processes (Latham et al 1986).

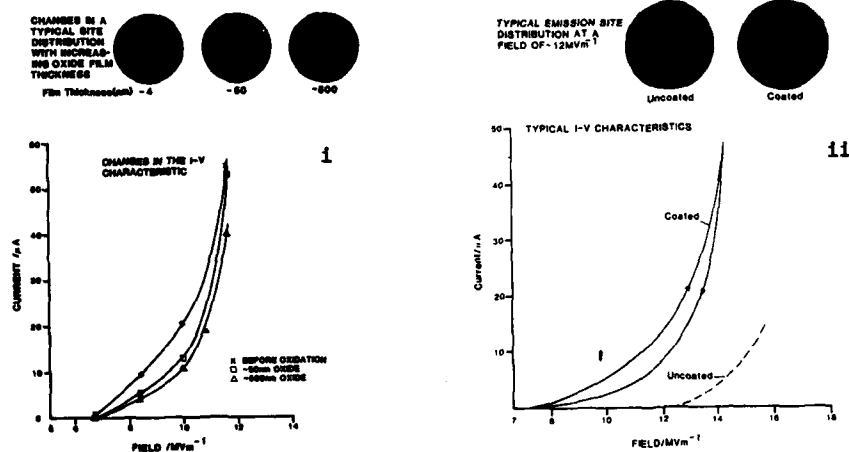


Fig. 3. "Before" and "after" site maps showing the effects of (i) in situ surface oxidation (Bajic et al 1989), and (ii) a thin dielectric coating (Cade et al 1988).

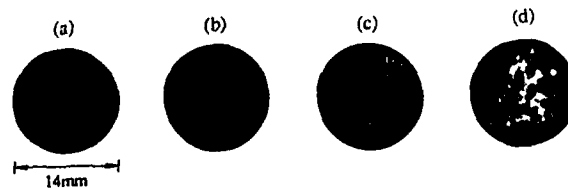


Fig. 4. A sequence of maps showing how the surface density of emission sites on a resin-composite cathode increases with applied field in the range 5-10 MV/m (Bajic 1989, Bajic and Latham 1989).

2. ANALYTICAL SYSTEMS

2.1 Spatial Imaging of Emission Site Populations

The "transparent anode" instrumental facility illustrated in Figure 1 was developed to provide a simple but powerful means of studying the spatial distribution of emission sites on planar cathodes, and also, in conjunction with video recording techniques, the temporal evolution of a population of such sites (Latham et al 1986). Typical examples of the type image obtained with this system are shown Figure 2, where each pin-point of light corresponds to the transition radiation generated in the conducting coating of the glass anode by the impact of a 1-10 microamp beam of high energy electrons emitted from a micron-sized feature on the cathode surface. (N.B. The three peripheral large bright spots appearing in these image correspond to the anode-cathode glass supporting rods; spurious reflected light has also highlighted the profiled edge of the electrode.) The analytical limitation of this planar electrode system is that all regions of the cathode surface are subjected to the same surface field, so that only those sites with similar I-V characteristics can be imaged simultaneously.

To illustrate the versatility of this imaging technique, Figures 2 to 4 present typical examples of data obtained from four diverse experimental studies that employed the system. Firstly, it provided an ideal tool for studying how the residual gas atmosphere influences the stability of emission processes: thus, Figure 2(a-c) shows how a population of emission sites on a planar OFHC Cu high voltage electrode are progressively extinguished in a residual atmosphere of He - the so-called "Gas Conditioning" effect (Bajic and Latham 1988a). Secondly, it has been used to investigate the effect of progressively oxidising an electrode surface and, as shown in Figure 3(i), surprisingly revealed that this procedure has little effect on the established emission processes (Latham et al 1989). Thirdly, Figure 3(ii) illustrates how the technique has been used to demonstrate that a thin dielectric coating on an electrode can typically increase the density of emission sites in a given field range by over an order of magnitude (Cade et al 1988; Bajic, Cade et al 1989). In the final application, Figure 4(a-d) dramatically illustrates how the density of emission sites on a resin-composite cathode increases with applied field (Bajic 1989, Bajic and Latham 1989). The practical significance of these latter two results will be discussed further in Section 3.

2.2 Individual Site Location - the Scanning Micropoint Anode

In order to study the properties of individual sites, it is necessary to employ some form of scanning probe technique to locate and position the chosen site for analysis. Two approaches may be considered. The first employs a planar anode with an axial probe hole; i.e. as was successfully used by Cox (1975) in his pioneering studies of the topographical nature of emission sites on HV electrodes. An alternative, and more convenient approach, is to use an electrolytically etched tungsten microtip anode in conjunction with the goniometer specimen stage of a SEM. Thus, by using the tip as a scanning current probe, it is possible to isolate an emission site on the axis of the SEM and hence image its topography. At the same time, an auxiliary X-ray or Auger facility will provide information about its material composition. It should also be noted that both probe techniques may be used to generate

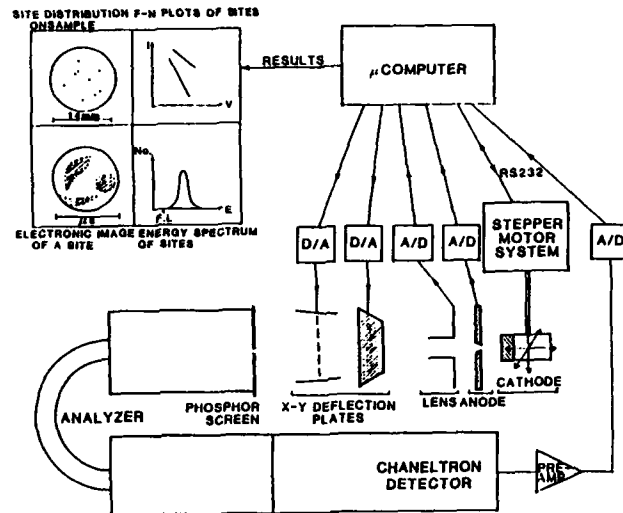


Fig. 6. A schematic illustration of an integrated, and fully automated, analysis facility for studying the electron spectral characteristics of micro-emission sites on planar electrodes.

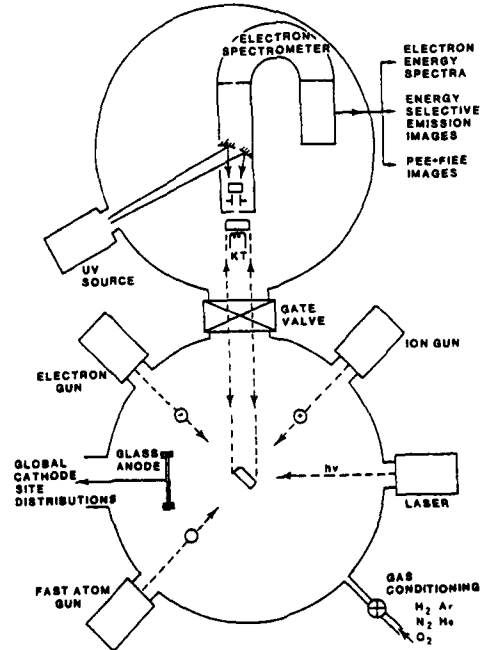


Fig. 7. A schematic illustration of the specimen chamber and pre-chamber facilities of the integrated analysis system depicted in Figure 6.

raster scan maps of emission sites by using the collected current to modulate either the z-input of a storage oscilloscope (Bayliss and Latham 1986), or the y-input of an x-y plotter (Niedermann 1986).

This latter micropoint anode technique was first demonstrated by Athwal and Latham (1981), and used routinely for recording the type of low-resolution image shown in Figure 5a. The important conclusion to emerge from this study was that emission sites on HV electrodes are invariably associated with the presence of particulate contamination; i.e. rather than metallic whiskers, as had traditionally been assumed. This investigation also revealed the technologically important fact that only about 1 in 10^6 of the micron-sized particles on an electrode surface actually give rise to emission in the field range 10-20MV/m. Subsequently, this type of analytical system was greatly improved by Niedermann and co-workers (Niedermann 1986, Niedermann et al 1986, Sankararaman et al 1986) to allow the possibility of a comprehensive Auger study of the material composition of a large sample of emitting structures under controlled UHV conditions. This investigation provided data of the type presented in Figure 5b, and revealed that "active" particles can have a wide range of elemental composition, with carbon being the most predominant and typically accounting for over 20% of emitters on Nb HV electrodes.

2.3 Individual Site Characteristics - Electron Spectrometry

To study the emission characteristics of individual sites, an advanced electron spectrometer facility has been progressively established by Latham and co-workers (Latham 1988). Recently, this has undergone a major up-grading to give an improved specimen handling capability, and enhanced data acquisition and analysis procedures. As illustrated schematically in Figure 6, this instrument is based upon a plane-parallel electrode gap with a 0.5mm diameter axial anode probe hole, and is interfaced with a hemispherical deflection spectrometer by means of a beam-forming electrostatic lens assembly. As illustrated schematically in Figure 8, the new up-graded facility is based upon a re-designed and more versatile experimental chamber and specimen handling module. In particular, the system now incorporates a turbo-pumped pre-chamber with load-lock, and a mechanically operated specimen transporter that uses Vacuum Generator's new bayonet-mounted integral specimen pod system. For the present application, the pod incorporates a heating element capable of raising the sample temperature to 800C; the latter being controlled by a Tactical 310 unit using a K-type monitoring thermocouple. With this facility, it is now possible to investigate the effects of a wide range of in situ surface treatments without the specimen ever being exposed to air. In order to make systematic, high-resolution spectral measurements of individual emission sites, the specimen is attached to a micro-manipulator that is controlled from the computer by stepper motors to provide a one-micron spatial resolution of the specimen position.

The computer control and measurement system is based upon an Acorn Archimedes 440 with Acorn I/O, Wild Vision ADC-1208, and Intelligent Interface IEEE-488 module attachments. The system is designed to provide a capability for rapid specimen analysis in terms of the following range of data acquisition and processing functions, all implemented directly from the keyboard.

a. The total gap I-V characteristic, with the additional option of a

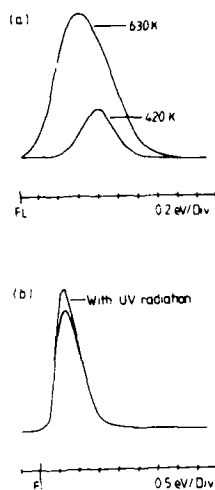


Fig. 9. Pairs of constant-field electron spectra, showing how the emission process is stimulated by both temperature and uv radiation (Xu and Latham 1986c).

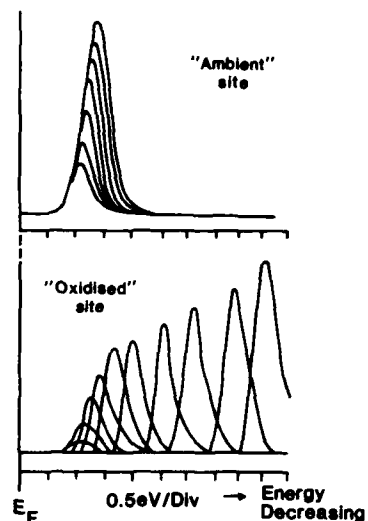


Fig. 10. "Before" and "after" sequences of electron spectra, recorded under incremental field conditions, showing the effect of surface oxidation (Latham et al 1989).

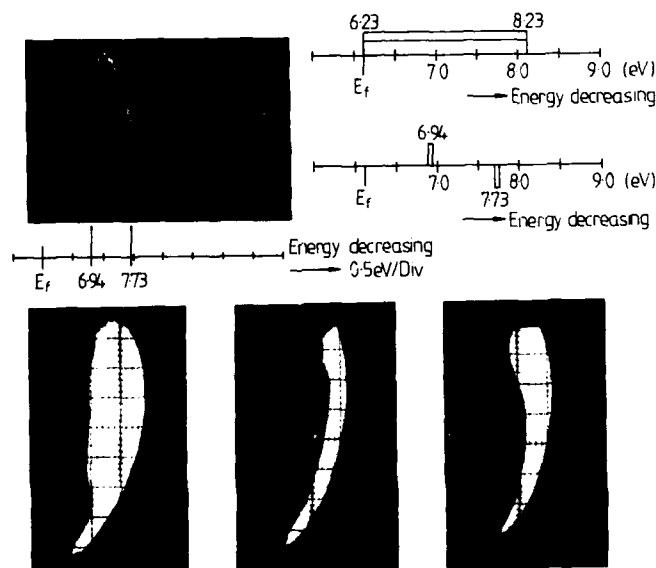


Fig. 11. The energy-selective recording of a single-segment emission image under (a) "total", (b) "high" and (c) "low" energy conditions (Xu and Latham 1986a).

Fowler-Nordheim (F-N) plot and a computed value for the associated beta-factor.

b. A low-resolution spatial "map" of all constituent emission sites, with their associated accessing coordinates.

c. A high-resolution scan of any localised emission centre.

d. A "total" or energy-selected emission image of any chosen site.

e. The electron spectrum of any chosen site at a resolution of 25meV, and referenced to the Fermi level (FL) of the cathode. Subsequently, the option is available for obtaining computed values of the half-width (FWHM), shift, F-N plot and beta-value of the site; the latter being computed from the spectral area, which is assumed to be proportional to the site current.

The performance of this integrated analytical facility is illustrated in Figures 8 to 11, which present typical data obtained from studies of the "non-metallic" micro-emission processes found on polished Cu electrodes. Firstly, Figure 8(a-c) shows three types of total-energy emission images that have been recorded directly from an intermediate phosphor screen (see Figure 6). The most commonly observed image is shown in Figure 8a, and is seen to consist of a random distribution of independent diffuse "spots" (Bayliss and Latham 1986). However, where sites are derived from a material having a layered structure, such as graphite, the emission image tends to have the multi-segment form shown in Figure 8b, and occasionally the single-segment structure of Figure 8c (Xu and Latham 1986b). From detailed spectral studies of these types of image, it has been established that each "spot" or "segment" has its own characteristic single-peak electron energy spectrum that has a unique low-current FWHM and shift from the Fermi level. Furthermore, if a series of spectra are successively recorded under gradually increasing field conditions, as illustrated in the sequence of Figure 8d, it is found that both the half-width and shift exhibit a strong field-dependence that is characteristic of a "non-metallic" emission mechanism (Bayliss and Latham 1986).

As further examples of the applications of this instrumental facility, Figure 9 illustrates how the emission mechanism is stimulated by both temperature and uv radiation (Xu and Latham 1986c), whilst Figure 10 illustrates how the spectral response is dramatically influenced by *in situ* surface oxidation (Latham et al 1989). As a final example, Figure 11 illustrates an application of the energy-selective imaging facility to record a single-segment emission image (c.f. Figure 8c) under "total", "high" and "low" energy" conditions (Xu and Latham 1986a). From this sequence, it is evident that the diffuse inner concave region of the image is formed predominantly from lower energy electrons; a result that is indicative of a scattering mechanism in the composite emitting structure.

3. DISCUSSION

In this section, consideration will firstly be given to the physical nature of the "non-metallic" emission mechanism responsible for the experimental data presented in the previous section. This will then be followed by a discussion of the technological implications of these findings, with particular emphasis being given to the potential of this mechanism to provide a basis for the development of a new range of practical cold-cathode electron sources.

3.1 The Electron Emission Mechanism

Two models have been considered, both involving an insulating medium. Thus, referring to Figure 12, the "ambient" M-I model represents a sub-micron thick insulating structure (I) in intimate contact with a metal electrode (M); i.e. corresponding to both the experimental situation shown in Figure 5 and the dielectric coating data of Figure 3(ii). This M-I regime is assumed to emit electrons as a result of a dielectric switching process, in which sub-micron conducting channels are electro-formed within the insulating medium. According to this model, electrons are "heated" through several eV and emitted quasi thermionically over the surface potential barrier (Latham 1982); i.e. as illustrated in the band diagram representation of Figure 13 (Latham and Bayliss 1986). A quantitative analysis of this system has shown that it provides a satisfactory explanation for the initial switch-on of sites, the linear and non-linear regions of the typical F-N plot of a gap (or site) characteristic, and the detailed field-dependent electron spectral data (i.e. shape, half-width and shift). An important prediction of this analysis, borne out by experiment (Bayliss and Latham 1986), is the existence of a sharp transition from a low-field contact-limited to a high-field bulk-limited conduction regime. In fact, it is this phenomenon that is thought to be responsible for the frequent high-field non-linearity of Fowler-Nordheim plots.

As discussed in detail elsewhere (Bajic 1989, Bajic et al 1989), the dielectric channel model of Figures 12 and 13, provides an "electronic" explanation for the Gas Conditioning effect illustrated in Figure 3. According to this interpretation, high-energy gas ions are assumed to be implanted into an emitting channel, and thereby create electron traps in the sensitive M-I interface region. Thus, different gas ions will penetrate to different depths for a given gap voltage, which explains the associated "Voltage" effect; conversely, the traps thus formed can be emptied through temperature-enhanced diffusion processes, and thus give rise to the associated "Temperature" effect.

The second emission model, also depicted in Figure 12, involves a M-I-M regime with built-in field enhancing "antenna" effect (Athwal et al 1985, Renner et al 1989). Here it is assumed that a particle or flake (e.g. of graphite), which is attached to an electrode surface by a blocking electrical contact, will probe the electric potential distribution at its highest point above the electrode, and hence establish a greatly enhanced electric field across the contact junction. Thus, the necessary conditions are created for the initiation of the dielectric switching process discussed above, with electrons being injected into the vacuum through the M-I-M contact junction (Xu and Latham 1986b). By assuming that the emitted electrons are coherently scattered at the flake edge, this model has also been able to provide a qualitative explanation of the segmented emission images shown in Figure 8. To confirm the validity of these and other future models, it will be necessary to employ new types of analytical techniques, such as scanning tunnelling microscopy (Niedermann and Fischer 1989), for studying the emission regime at nm resolution.

In terms of these two models, the surface oxidation data of Figure 10 can be qualitatively interpreted as illustrated in Figure 12 where, prior to emission in each case, electrons have to be transported through a lossy oxide layer in which multiple scattering events will occur. In

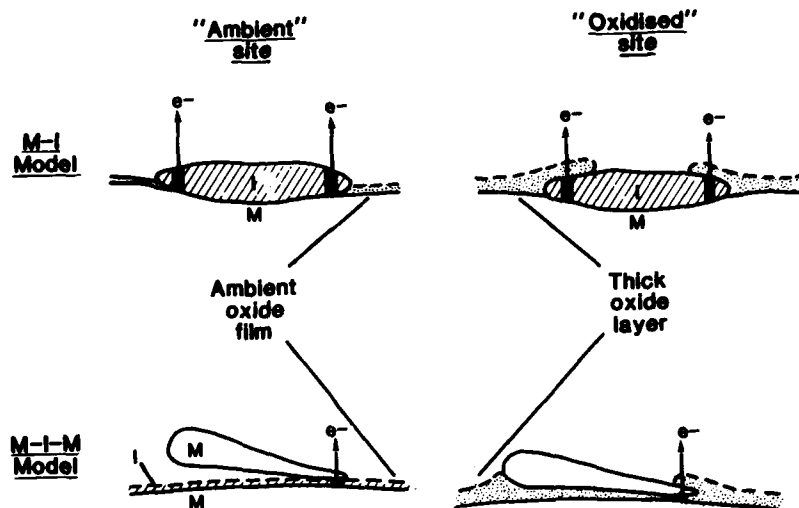
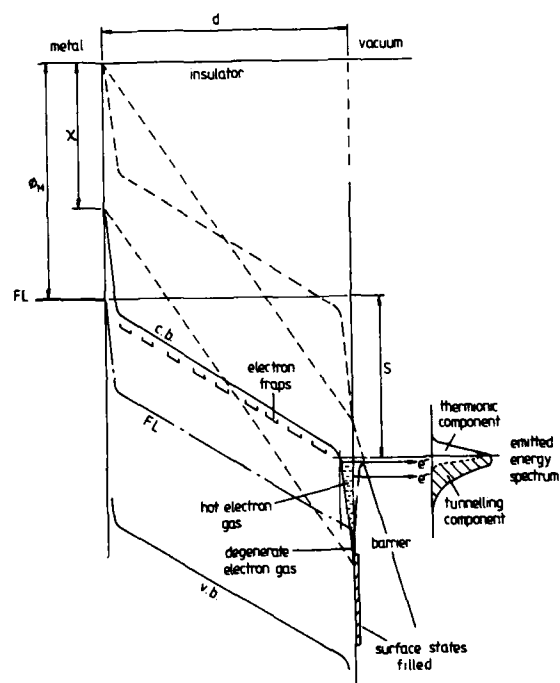


Fig. 12. Schematic illustrations of the metal-insulator (M-I) and M-I-M emission models, and how these could be influenced by surface oxidation (Latham, Bayliss et al 1989)

Fig. 13. A band diagram representation of the M-I model of Figure 12 (Bayliss and Latham 1986)



contrast, the composite cathodes, as represented by the data of Figure 4, are thought to emit by a hybrid two-stage mechanism involving features of both models. Thus, as explained elsewhere (Bajic and Latham 1988b), the "antenna" effect firstly gives rise to a sufficiently enhanced field across particle-electrode contact junction to precipitate a "primary" M-I-M switching event, which then triggers a "secondary" M-I switching event at the dielectric-vacuum interface.

3.2 Technological Implications

A dominant thrust of the work presented in this paper has been to gain a physical understanding, and hence a technological perspective, of how to control the localised field emission process that limits the performance of vacuum-insulated, high voltage electrodes (Latham 1988). Thus, the single most important technological conclusion to emerge from these programmes, is the over-riding need to eliminate particulate contamination from electrode assemblies. It is therefore crucially important to revise the standards relating to the purity of electrode materials, their manufacture and assembly procedures. In fact, by committing the necessary investment, and systematically following this more enlightened approach, the superconducting RF cavity community, for example, have been able to progressively, and reliably, raise the operating fields in their cavities by over an order of magnitude (Bloess 1984, Padamsee et al 1986), with every promise of further improvements. In particular, the beneficial influence of high-temperature processing of electrodes, revealed by the work of Niedermann and co-workers (Niedermann 1986, Sankarraman et al 1986), could well form the basis of further progress.

The other important aspect of this work is its relevance to the on-going search for alternative types of cold-cathode electron sources. Thus, the type of composite cathode illustrated in Figure 4 clearly has considerable potential for development as a broad-area source, where it could be realistically anticipated that current densities approaching 1A/sq.cm could be achieved at field levels of 10-20MV/m. Conversely, the M-I system of Figure 3(ii) offers a possible basis for producing arrays of microamp emission centres, if a suitable technique could be developed for "writing-in" emission sites at pre-determined locations. In this context, mention should also be made to an earlier study (Latham and Mousa 1986) where the concept of an M-I regime was applied to the conventional micro-tip structure, where a W tip was coated with a layer of epoxy resin. Apart from lowering the operating field, these coated tips also provided a brighter and more stable electron optical source.

A particularly desirable feature, shared by each of these M-I systems, is their relative immunity to the residual gas pressure. Thus, unlike clean metal emitters, it is possible to operate these structures under commercial vacuum conditions without serious degradation of the emission characteristics (Latham and Mousa 1986, Bajic 1989, Bajic, Mousa et al 1989); presumably because the insulator medium protects the sensitive M-I interface from the physical, chemical and mechanical effects of impinging gas ions and molecules. Conversely, it has to be said that these M-I systems also share the undesirable feature of sometimes being liable to exhibit a low-frequency switching instability (Bajic et al 1989); i.e. where an individual micro-emission process can randomly switch on and off with time under constant field and vacuum conditions. The physical reasons for this phenomenon are not well understood, but

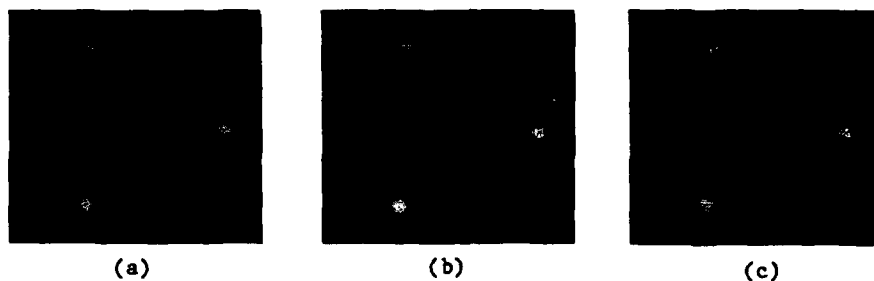


Fig. 2. A 20min. time-sequence of site maps illustrating the "Gas Conditioning" effect of He at a pressure of 10^{-4} mbar (Bajic and Latham 1988a).

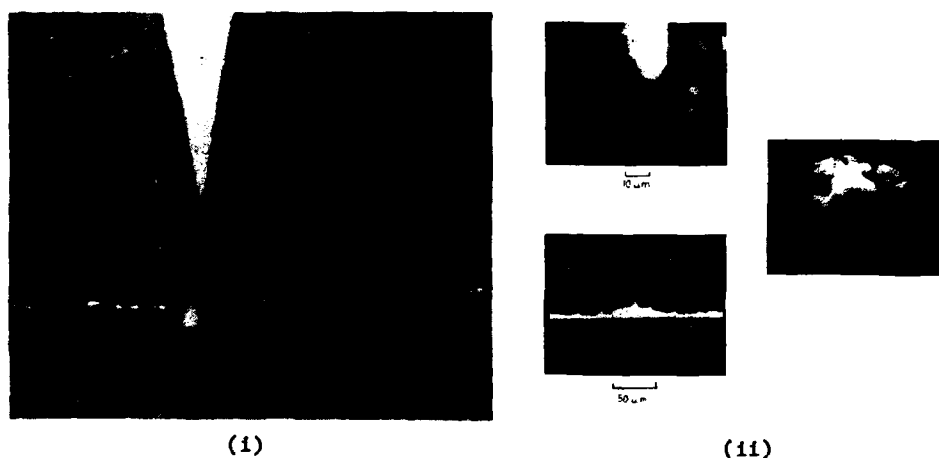


Fig. 5. (i) A low-magnification image of the micro-point anode technique identifying a contaminant particle as an emission site on a mechanically polished ofhc Cu electrode (Athwal and Latham 1981), and (ii) a high-magnification image of an Auger-identified S-particle emitter on a Nb electrode (Niedermann 1986).

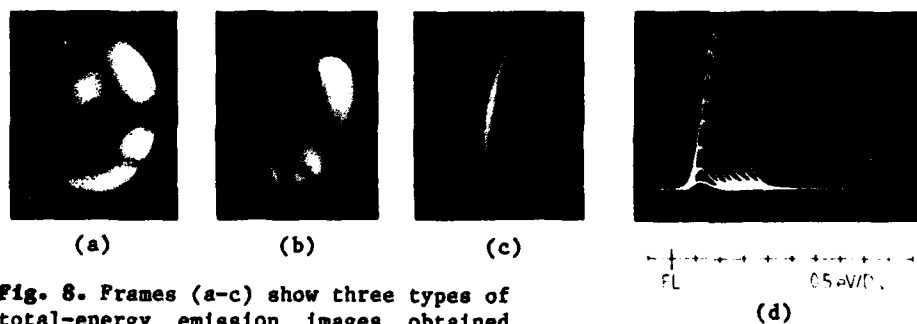


Fig. 8. Frames (a-c) show three types of total-energy emission images obtained from particulate emission sites on planar electrodes, whilst (d) is a typical sequence of electron spectra recorded at incremental field values from any given "spot" or "segment" (Xu and Latham 1986b)

are thought to be intimately associated with the properties of the sub-micron sized conducting channels that are believed to be responsible for the emission from these structures (Bayliss and Latham 1986). It follows therefore that an extended programme of fundamental research will be required before the M-I regime can be reliably used as a practical source.

ACKNOWLEDGEMENT

Some of the work reported in this paper was performed under a SDIO/IST sponsored programme managed by the Space Power Institute of Auburn University, Alabama, USA.

REFERENCES

- Athwal CS and Latham RV 1981 *Physica* **104C** 46
 Athwal CS, Bayliss KH, Calder R and Latham RV 1985 *IEEE Trans. Plasma Sci.* **13** 226
 Bajic S 1989 PhD Thesis, Aston Univ.
 Bajic S and Latham RV 1988a *J. Phys. D: Appl. Phys.* **21** 943
 Bajic S and Latham RV 1988b *J. Phys. D: Appl. Phys.* **21** 200
 Bajic S and Latham RV 1989 2nd Int. Conf. on Vac. Microelectronics (Bath, UK)
 Bajic S, Cade NA, Archer AD and Latham RV 1989 2nd Int. Conf. on Vac. Microelectronics (Bath, UK)
 Bajic S, Mousa MS and Latham RV 1989 36th Int. Field Emission Symp. (Oxford, UK)
 Bayliss KH and Latham RV 1985 *Vacuum* **35** 211
 Bayliss KH and Latham RV 1986 *Proc. Roy. Soc. A* **403** 285
 Bloess D 1984 Proc. 2nd Workshop on RF Supercond. (Geneva, Switzerland) pp 409-426
 Cade NA, Cross GH, Lee RA, Bajic S and Latham RV 1988 *J. Phys. D: Appl. Phys.* **21** 148
 Cox BM 1975 *J. Phys. D: Appl. Phys.* **8** 2065
 Niedermann Ph 1986 PhD Thesis, Univ. of Geneva
 Niedermann Ph, Sankarraman N, Noer RJ and Fischer O 1986 *J. Appl. Phys.* **59** 892
 Niedermann Ph and Fischer O 1989 *IEEE Trans. Elec. Insul.* (to be published)
 Latham RV 1981 "High Voltage Vacuum Insulation; The Physical Basis" Acad. Press Ldn/NY
 Latham RV 1982 *Vacuum* **32** 137
 Latham RV 1988 *IEEE Trans. Elec. Insul.* **23** 881
 Latham RV, Bayliss KH and Bajic S 1989 *IEEE Trans. Elec. Insul.* (to be published)
 Latham RV, Bayliss KH and Cox BM 1986 *J. Phys. D: Appl. Phys.* **19** 214
 Latham RV and Mousa MS 1986 *J. Phys. D: Appl. Phys.* **19** 699
 Renner Ch, Niedermann Ph and Fischer O 1989 *IEEE Trans. Elec. Insul.* (to be published)
 Sankarraman S, Niedermann Ph, Noer RJ and Fischer O 1986 *J. de Physique* **47** 133
 Xu NS and Latham RV 1986a *J. de Physique* **47** 95
 Xu NS and Latham RV 1986b *J. Phys. D: Appl. Phys.* **19** 477
 Xu NS and Latham RV *J. de Physique* **47** 73

An STM controlled field emission microlens electron source

M. A. McCord, T. H. P. Chang, D. P. Kern, and J. L. Speidell

IBM Research Division, T. J. Watson Research Center, Yorktown Heights, N. Y. 10598

SUMMARY ABSTRACT: By using a scanning tunneling microscope to position a field emission tip over a miniature aperture with dimensions on the order of one micrometer, a high performance electron source is obtained (Chang et al 1989, McCord et al 1989). While similar to a miniature field emission cold cathode that has been previously demonstrated by other researchers (Spindt et al 1976, Greene et al 1986), use of an STM gives several advantages over other designs. These include fine positioning of the tip both horizontally and vertically, active feedback stabilization of the emission current, and the ability to fabricate the tip separately from the aperture. This last point facilitates the manufacture of a microlens, where the simple aperture is replaced by a stacked structure of two or more electrodes separated by thin film insulating spacers, all made by standard integrated circuit processing techniques with micrometer dimensions. In addition, it allows use of a point source single atom tip developed by Fink (1988) which would provide tremendous improvements in the performance of the source.

Theoretical calculations of the operation and performance of the microlens have been performed using finite element numerical computation (Munro 1973). Lens aberrations are one of the primary limitations to the performance of electron beam systems. Because lens aberrations tend to scale with the lens dimensions, by reducing the size of the lens from millimeters to micrometers, commensurate improvement in the lens performance is expected. This is confirmed by the numeric calculations, which also show that a two electrode lens should be capable of forming a focussed spot outside the lens with an energy on the order of a kilovolt. Using the calculated aberrations, the performance of systems using various combinations of microlenses and conventional lenses has been simulated. The results indicate that the performance of systems using the microlens source should exceed that of conventional high performance systems by an order of magnitude in beam diameter or as much as three orders of magnitude in beam current. In particular, a system consisting of the microlens source with one additional microlens to further demagnify the beam should achieve a spot size of less than 0.1 nm with a current of 100 pA or greater.

Experimental demonstration of the STM electron source has so far been limited to use with a simple aperture. The apertures are fabricated on silicon nitride membranes using electron beam lithography and reactive ion etching. The tip is positioned over the aperture using the imaging capability of the STM, then the voltage between the tip and aperture is increased while monitoring the current passing through the aperture with a faraday cage electron collector. Using aperture diameters from 0.4 to 2 micrometers, extraction voltages have varied from 50 to 200 volts. The extraction voltage also depends critically on the tip radius. Currents as high as 80 μA have been obtained, while the source efficiency, or fraction of the total emission current transmitted through the aperture, has ranged from 80% to over 99%.

In conclusion, successful operation of an STM electron source has been demonstrated. This source has several advantages over standard miniature field emission cathodes in terms of flexibility, manufacturability, and control of emission current. Theoretical calculations of the performance of the source with a microlens have shown it to have a brightness an order of magnitude greater than conventional field emission sources due to the low aberrations of the microlens, and to give corresponding improvements in the performance of electron beam systems. Thus it has great potential for use in microscopy, microanalysis, electron beam testing and lithography. Future plans include demonstration of the STM source using the microlens.

REFERENCES

- Chang T H P, Kern D P and McCord M A 1989 to be published in *J. Vac. Sci. Technol. B*, Nov/Dec 1989
Fink 1988 *Physica Scripta* 38 260
Greene R, Gray H and Campisi G 1986 *Proceed. IEDM* 85 172
McCord M A, Chang T H P, Kern D P and Speidell J L 1989 to be published in *J. Vac. Sci. Technol. B*, Nov/Dec 1989
Munro E 1973 *Image Processing and Computer-Aided Design in Electron Optics*, edited by Hawkes P W (Academic New York) p 284
Spindt C A, Brodie I, Humphrey L and Westerberg E R 1976 *J. Appl. Phys.* 47 5248

The dynamics and stability of solid surfaces of nanostructures

Tien T. Tsong and Chonglin Chen

Physics Department, The Pennsylvania State University
University Park, Pennsylvania 16802 U.S.A.

ABSTRACT: Surfaces of solids and thin films are not static. Atoms and atomic clusters can move on the surface around room temperature for many materials. This can change the physical and chemical properties of these materials and the useful lifetimes of devices made of these materials. As the structures in microelectronic components gradually reduce in size, the dynamical behavior of the surfaces and interfaces play a more and more important role in their long term performance. Using high resolution microscopies, the dynamical behavior and stability of the surfaces and interfaces of materials of submicron sizes can be investigated in atomic details.

1. INTRODUCTION

The surfaces of solids and thin films are not static. Instead, atoms and atomic clusters can move on the surface continuously and structure changes on nanometer scale can occur even around room temperature for many materials. Such changes will of course modify the structures and chemistry of the surfaces and interfaces, and therefore the chemical and physical properties of these materials. They will affect the performance and the useful life times of devices containing structures of nanometer and submicron sizes. Using the field ion microscope (FIM), the atom-probe FIM and the scanning tunneling microscope (STM), the dynamical behavior of surfaces and interfaces of submicron size structures of materials can be studied.

There are two kinds of stability of the materials one must consider. These are the physical stability and the chemical stability. Physical stability refers to mechanical stability and thermal stability. The thermal stability arises from the atomic structure change and the material shape change produced by thermal effects such as the dissociation of atoms from lattice steps, surface diffusion of these atoms, stepping up and down the lattice steps of diffusing atoms, adatom-adatom interaction, and adatom-substrate interactions, etc. [Ehrlich and Stolt, 1980; Bassett, 1981; Tsong, 1988a, 1988b]. These effects can be investigated with the FIM, STM and atom-probe FIM. For the chemical stability, we refers to oxidation, corrosion, surface segregation and impurity segregation, etc. These phenomena can be investigated with the atom-probe FIM. Here I will summarize some of our recent investigations

of the dynamics and stabilities of solid surfaces using the FIM, STM and atom-probe FIM.

2. THE BEHAVIOR OF SINGLE ATOMS AND SMALL ATOMIC CLUSTERS ON SURFACES

Several aspects of the behavior of single atoms and small atomic clusters on solid surfaces have been studied with the field ion microscope. The advantage of using FIM for this type of studies is that an atomically perfect surface can be developed by low temperature field evaporation. While the atomic structure of the substrate may not be resolved in the field ion image, atoms in a small cluster can usually be resolved. The temperature of the surface can be changed without undue efforts. Some of the phenomena studied include surface diffusion of single atoms and small atomic clusters, adatom-adatom interactions, adsorption layer superstructure formation, structure transformation of small atomic clusters on the surface, atom-substrate interactions, and dissolution of surface layers at high temperature etc. In Fig. 1, data for surface diffusion of single Ir adatoms on the Ir (100) and (111) surfaces are shown. The activation energies of the very smooth (111) and the less smooth (100) surfaces differ by a factor greater than 4, 0.22 ± 0.04 eV vs. 0.93 ± 0.03 eV, but the pre-exponential factors have the same order of magnitude of $\sim 10^{-3}$ cm²/s [Chen and Tsong, 1989].

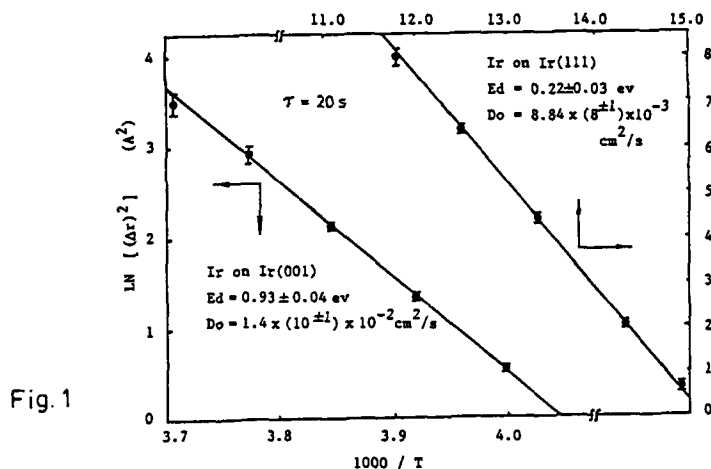


Fig. 1

When the temperature of a crystal is raised, surfaces of lower free surface energy will grow in size while those of larger free surface energy will reduce in size. This is achieved by a gradual dissociation of surface atoms from the edge of a plane, and then diffuse and be absorbed elsewhere. The dissociation energy of atoms from the edge of a surface layer can be derived from the slope of an Arrhenius plot where the logarithm of the inverse time of dissolving a surface layer is plotted against the inverse of the surface temperature [Chen and Tsong, 1989]. An example for the dissolution of the Ir (100) layer is shown in Fig. 2. From the slope it is found that the dissociation energy is about

1.4 eV. We have also studied the temperature dependence of the structure transformation of small Ir clusters on the Ir (100) surface. On this surface, clusters formed at low temperatures are usually linear. Upon heating to high temperatures, however, the cluster may transform into a two-dimensional structure if the number of atom in the cluster is larger than or equal to 6[Schoebel and Kellogg, 1988]. For 3-atom clusters, the $\ln(p_{1-D}/p_{2-D})$ vs. $1/T$ plot shows two linear sections, one with an activation energy of 0.347 eV, which we attribute to the difference in the total binding energies of the cluster in the 1-D and 2-D structures, and one with an activation energy as high as 3.89 eV. At the present moment, we have no interpretation of why there is this section, and why the activation energy is so high. FIM experiments consistently observe adatom-adatom interactions of strength on the order of 0.1 eV or less[Tsong, 1988a].

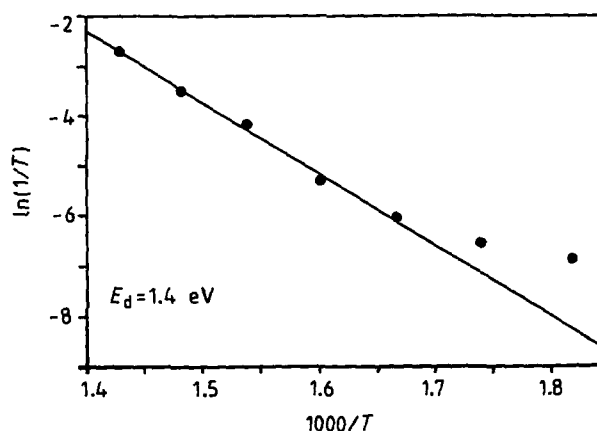


Fig. 2

III. Topographical Changes of Surfaces

To study the topographical changes of the surface of a solid or a thin film, the STM is most suitable. From the FIM studies of the behavior of atoms and clusters on the surface of various materials, it can be expected that for soft materials such as gold, atoms should be able to move at temperatures much lower than the room temperature. The FIM is, however, not suitable for studying topographical changes of surfaces of solids and thin films since FIM observations can be done only on 'smooth' emitter surfaces where the field distribution is fairly uniform. STM, on the other hand, is particularly powerful for such studies. The advantage of the STM is that the atomic structures as well as the topography of surfaces of solids and thin films can be obtained either in vacuum or in atmosphere. In Fig. 3, we show the formation of a new lattice step on the surface of a thin film of gold deposited on a thin carbon film[Tsong et. al., 1989a]. The two images were taken about 5 minutes apart in the atmosphere. Generation of a new atomic step on the gold surface is clearly visible as indicated by the arrows. At the present time, however, there is a serious difficulty of using the STM for studying quantitatively surface atomic processes as the sample temperature cannot be easily changed without also inducing a thermal drift of the STM.

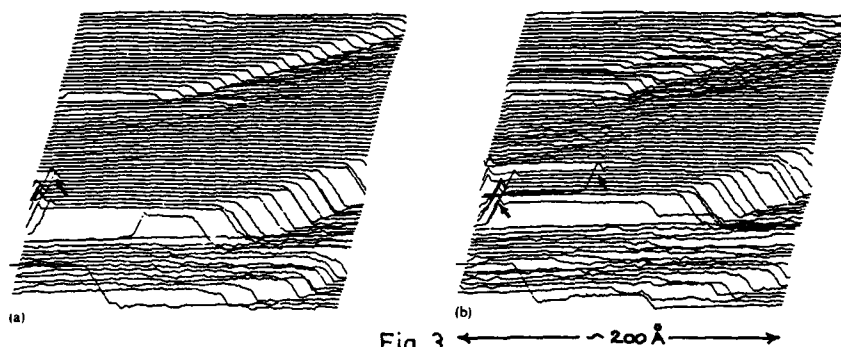


Fig. 3

IV. Binding Energy of Surface Atoms

The binding energy of surface atoms with the substrate can be derived from the critical energy deficit of low temperature field desorbed ions. In other words, the binding energy of surface atoms in their adsorption sites can be derived by measuring the ion energy distribution of low temperature field desorbed ions. It can be easily shown [Tsong et. al. 1989b] that the binding energy of kink site atoms is identical to the cohesive energy of the solid which is on the order of several eV for most solids. In order to be able to measure the binding energy of surface atoms to an accuracy of a few %, or to about 0.2 eV, the ion energy analysis has to have an accuracy of one to two parts in 100,000 as the kinetic energy of field desorbed ions is usually in the range of 10 to 20 keV. We have developed a high resolution pulsed-laser time-of flight atom-probe and a method for the accurate calibration of the system to achieved the desired accuracy in the ion energy distribution measurement. In Fig. 4, a diagram of the system is shown and in Fig. 5, a time of flight energy spectrum for tungsten in low temperature field evaporation is shown. The binding energies of kink site tungsten atoms in tungsten and of rhodium kink site atoms in rhodium from two separate measurements are listed in Table 1. Our result is in excellent agreement with the cohesive energies of W and Rh listed in a standard table [Kittel, 1986]. The advantage of this low temperature field evaporation method as compared to other thermodynamic methods is that the desorption is done at low temperature where the atoms remain in their original adsorption sites. In other thermal desorption methods, atoms may diffuse to other sites before they are desorbed. The desorption energy derived is not really the same as the binding energy. In any case, it is not site specific as in our method.

IV. Chemical Stability of Surfaces

Atom-probe FIM, with its ability to chemically analyze a solid surface one atom at a time and one atomic layer at a time, is ideally suited for studying the chemical stability of solid surfaces and interfaces such as oxidation, corrosion, surface segregation, and impurity segregation, etc. of submicron size materials. An example is the study of surface

Fig. 4

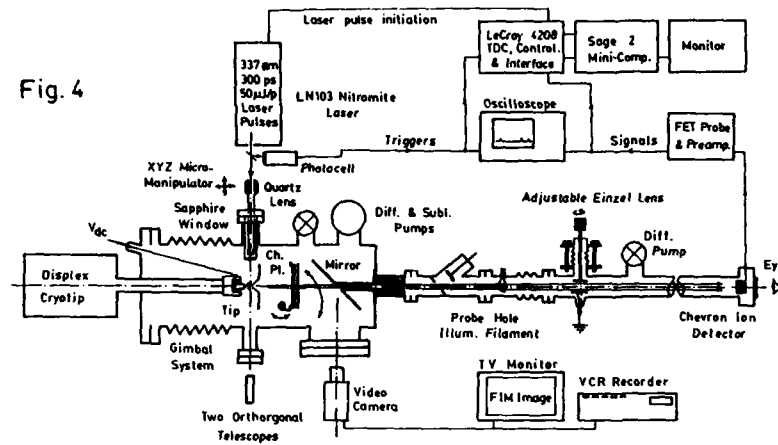
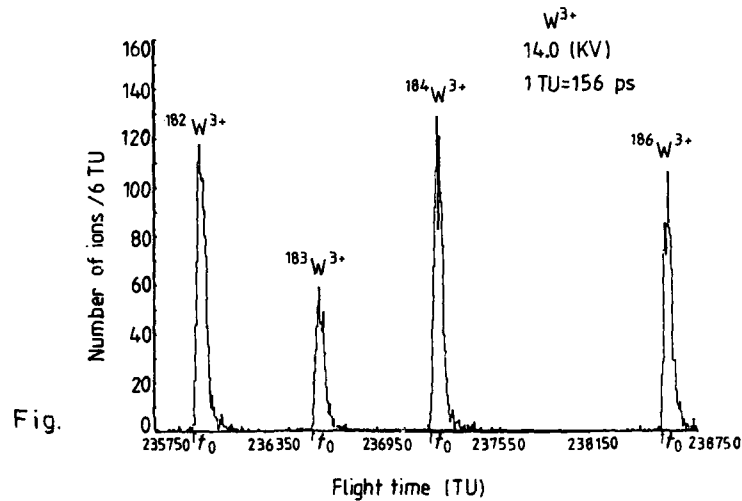


Table 1. Binding Energy of Kink Site Atoms

Element	Measured ΔE_c (eV)	Charge State	Measured E_k (eV)	E_c (eV)	Ref.
W	45.51 ± 0.47	3+	9.03 ± 0.47	8.90	(a)
	45.36 ± 0.51	3+	8.88 ± 0.51	"	(b)
Rh	22.44 ± 0.32	2+	5.90 ± 0.32	5.75	(a)
	22.46 ± 0.16	2+	5.92 ± 0.16	"	(b)

Ionization energies for W are: $I_1=7.98$ eV, $I_2=18$ eV, $I_3=24$ eV. For Rh, $I_1=7.46$ eV, $I_2=18.08$ eV.

(a) J. Liu and T. T. Tsong, to be published in J. de Phys. Coll. (b) Y. Liou and T. T. Tsong. See J. de Phys. Coll., 49, C6-105 (1988).



segregation and impurity cosegregation of Pt-Rh alloys [Ahmad and Tsong, 1986; Ren and Tsong, 1987]. As shown in Fig. 6, when a Pt-44.8at%Rh alloy is annealed to 700 °C and then quenched, the composition of the top (001) layer is found to be enriched with Pt and the second layer is depleted with Pt. However, when the sample contains about 50 ppm of sulfur, sulfur atoms segregate to the surface to form an over layer. In addition, the top surface layer of the alloy is now enriched with Rh, and the second layer is depleted with Rh. Such a reversal of segregation species of an alloy by the presence of sulfur impurity atoms is most interesting, and is definitely important in understanding the catalytic properties, such as the poisoning and promotion effects by impurity atoms, of the alloy.

V. SUMMARY

We have shown that by using the FIM, the STM and the Atom-Probe FIM, it is possible to investigate the various aspects of the dynamical behavior and the stability of solid surfaces on a subnanometer scale. These studies are important for our understanding of both the physical and mechanical stabilities and useful lifetimes of microelectronic components of submicron sizes.

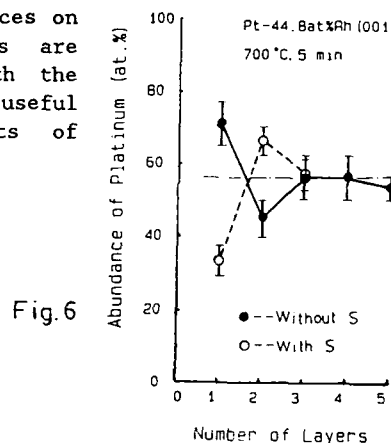


Fig.6

REFERENCES

- * Work supported by NSF.
- Ahmad, M. and T. T. Tsong, 1985, *J. Chem. Phys.* **83**, 338.
- Bassett, D. W., 1981, in *Surface Mobilities of Solid Materials*, V. T. Binh edit (Plenum, New York).
- Chen, C. L. and T. T. Tsong, 1989, submitted to *Phys. Rev. B*.
- Ehrlich, G. and K. Stolt, 1980, *Ann. Rev. Phys. Chem.* **31**, 603.
- Kittel, C., 1986, *Introduction to Solid State Physics*, Wiley, New York.
- Ren, D. M. and T. T. Tsong, 1987, *Surface Sci.* **184**, L439.
- Schwoebel, P. R. and G. L. Kellogg, 1988, *Phys. Rev. Lett.* **61**, 578.
- Tsong, T. T., 1988a, *Rept. Prog. Phys.* **51**, 759 (1988).
- Tsong, T. T., 1988b, *Surface Sci. Rept.* **8**, 127 (1988).
- Tsong, T. T., L. X. Li, S. D. Chi, Y. Liou and R. Messier, 1989a, *Thin Solid Films* **172**, L91.
- Tsong, T. T., Y. Liou and J. Liu, 1989b, *J. Vac. Sci. Technol.* **A7**, 1758.

Investigation of field emitting microstructures by scanning electron and scanning tunnelling microscopy

Ph.Niedermann, Ch.Renner, A.D.Kent and Ø.Fischer

Université de Genève, DPMC, 24 quai E.Ansermet, CH-1211 Genève, Switzerland.

ABSTRACT: A study of enhanced field emission on broad area niobium cathodes is presented. Emitting sites have been investigated by field emission scans, scanning electron microscopy and scanning tunneling microscopy. All except one of 14 studied emitters are of micron or submicron size. A trend is observed for the emitting structures to be smaller than predicted from the protrusion model as is also demonstrated with the aid of a specific example of a field emitting site.

1. INTRODUCTION

On macroscopic metal cathodes subjected to high electric fields electron field emission is observed at fields which are much below the value predicted by the Fowler-Nordheim law for flat, metallic surfaces. The characterization and understanding of this enhanced field emission (EFE) is important for high field vacuum applications (Latham, 1989). It is well established that EFE most typically originates from localized microparticles on a broad area cathode (Niedermann et al, 1986, Renner et al, 1989). However, the physical mechanism of EFE is not understood in detail.

In our earlier experiments, we had noticed a trend for the dominating EFE sites on chemically polished Nb to be of smaller size than the ones found on Nb that was heat-treated in addition. Submicron EFE sites appeared as an interesting starting point to explore the use of a scanning tunneling microscope (STM) in addition to our more standard characterization of EFE sites. The possibility to obtain both nanometer resolution topography and information on field emission properties makes the STM an attractive tool for such investigations.

2. EXPERIMENTAL

Field emission sites on two chemically polished niobium samples were characterized in a standard way with our field emission scanning microscope (FESM, Niedermann et al., 1986). This characterization includes local determination of field enhancement factor β and apparent emitting surface S from Fowler-Nordheim (F-N) plots as well as SEM images (*ex-situ*) of the emitting features. In addition, an STM which has recently been integrated (Emch et al., 1988) in our FESM has been used to investigate the previously identified EFE sites. An integrated SEM (0.5 μm resolution) allows us to observe the positions of the high-voltage anodes and of the STM tip so that features of interest can be localized without ambiguity.

3. RESULTS

Table 1 lists the measured values of β and S as well as the physical size of the

No.	β	S [cm ²]	$\beta\sqrt{S}$ [μ m]	size [μ m]	observation	composition
1/1	60	1×10^{-10}	6	~0.1	SEM+STM	
1/2	45	4×10^{-10}	9	0.25	SEM+STM	
1/3	75	1×10^{-12}	0.75	40x10	SEM	C,O,Al,Si,Ca,Fe
1/4	32	2×10^{-8}	45	1	SEM+STM	Cu
1/6	45	1×10^{-9}	14	0.1x0.3	SEM	
1/8	32	1×10^{-7}	900	0.4	SEM	Cu,Al
1/9	47	1×10^{-9}	15	0.2x0.6	SEM	
2/1	55	1×10^{-10}	5.5	1	SEM+STM	
2/2	70	4×10^{-10}	14	0.15x0.35	SEM+STM	
2/4	48	1×10^{-10}	4.8	1	SEM+STM	
2/5	60	4×10^{-10}	12	0.3x1	SEM+STM	W
2/6	52	1×10^{-9}	15	0.1x0.5	SEM+STM	
2/8	50	4×10^{-10}	10	≤ 0.1	SEM	
2/9	53	1×10^{-10}	5	0.7	SEM	Cu

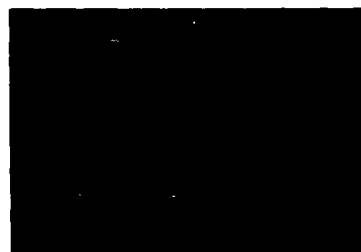
Table 1 Measured field enhancement factor β and apparent emitting surface S, predicted and observed physical size, methods of observation and elemental composition of the studied field emitting structures.

structures found at the emitting locations. In contrast to earlier detailed investigations on niobium (Niedermann et al., 1986) and Al cathodes (Renner et al., 1989), all but one (site 1/3) of the emitting structures on the present samples were of submicron or micron size. Table 1 also indicates where the EFE site has been successfully localized by STM in the sense that a strong emission site was identified and localized with respect to SEM. Structures smaller than 0.5 μ m identified by SEM alone are only *probable* candidates for EFE sites. At most of the sites (except site 1/1, which was too small to be studied in detail, and 2/5, which was associated with a crater due to a spark), a microscopic particle sitting on top of the niobium was found to be associated with EFE. The earlier qualitative observation that lightly fixed particles, often of 'flake-like' morphology, was again made for a majority of the present sites. Some of the structures were large enough for x-ray microanalysis (see Table 1). Since this method has poor sensitivity for carbon, the present findings on composition are not in contradiction with earlier results that EFE sites often consist of graphite.

In the model of purely electrostatic field enhancement due to a metallic cylinder of height h topped by a hemisphere of radius r , β is given by $h/r+2$ and S is of order r^2 . For large β , h is therefore of order $\beta r \sim \beta\sqrt{S}$. The latter quantity is listed in Table 1 and gives an independent estimate of the total size of the emitting structures. One has to keep in mind that S values are subject to relatively large experimental uncertainties. Also, if EFE originates from a metal, the image force has to be corrected for which would reduce the measured S values by a factor 10^2 (Niedermann, 1986) and thus the measured $\beta\sqrt{S}$ values by ten. But even including this correction, there remains a discrepancy between predicted and observed size of the emitting structures. Most of the particles found at the EFE sites seem too small to explain EFE by electrostatic field enhancement alone. Other models which could be able to explain EFE are described by Latham (1989).

We will now describe the specific example of site 1/1 which is an extreme case of a submicro. feature. Figure 1 shows the SEM image of this site where no feature is visible to 0.1 μ m resolution. Occasionally, emitting sites without detectable anomalous structure in the SEM (0.5 μ m resolution) had also been found earlier (Niedermann et

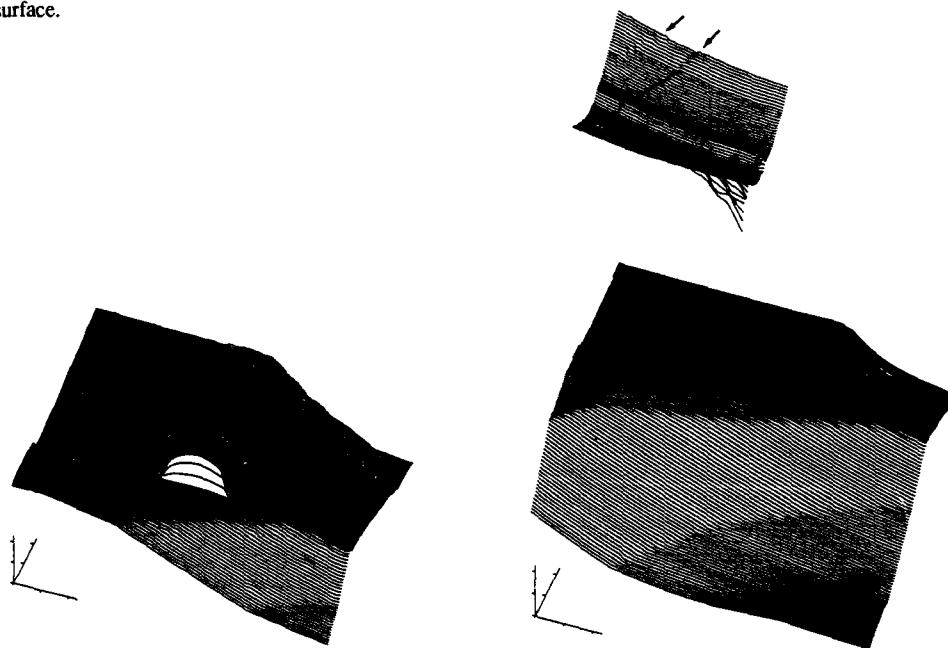
Figure 1 (right) SEM image of EFE site 1/1. Rectangle indicates scan area of Fig.2a.



10 μm

Figure 2a (bottom) STM scan in field emission mode ($U=+80\text{ V}$, $I=1\text{ nA}$) over $5.8\times 4.2\text{ }\mu\text{m}$. Scale divisions are $0.5\text{ }\mu\text{m}$.

Figure 2b (bottom right) STM scan in topographic mode ($U=-5\text{ V}$, $I=0.2\text{ nA}$) at the same scale. The arrow points to a feature of $0.1\text{ }\mu\text{m}$ size which we associate with the emission site. The flat part of the image is shown separately, blown up $10\times$ in z direction, with arrows pointing to $\sim 5\text{ nm}$ steps on the Nb surface.



al., 1986). Figure 2a shows an STM image obtained in field emission mode at the location of site 1/1 and Fig.2b shows an image obtained in topographic mode with a slight offset in position. The large bump in Fig.2a is significant for an EFE site; the strong emissivity of the site makes the tip move around it at a distance of the order of $0.5\text{ }\mu\text{m}$. At the corresponding location in the topographic image of Fig.2b, a feature of about $0.1\text{ }\mu\text{m}$ size is observed (arrow). In addition, somewhat enhanced emission (from the amplitude in the z deviation, we estimate $\beta\sim 4$) is observed along two lines visible on the left of Fig.2a which have been found to be associated with steps of $\sim 5\text{ nm}$ height (arrows in Fig.2b). This is a likely case of purely electrostatic field enhancement. After the image in Fig.2a was made, the STM was centered above the maximum of the emission due to the EFE site, and the tip to surface separation s was determined to be 610 nm by a U vs z plot (Fig.3a) taken at constant current. A F-N plot was then taken with the tip fixed at this distance, and under the approximation of parallel planes the F-N fit gave $\beta=34$ and $S=4\times 10^{-12}\text{ cm}^2$ (Fig.3b). Given the relatively strong non-

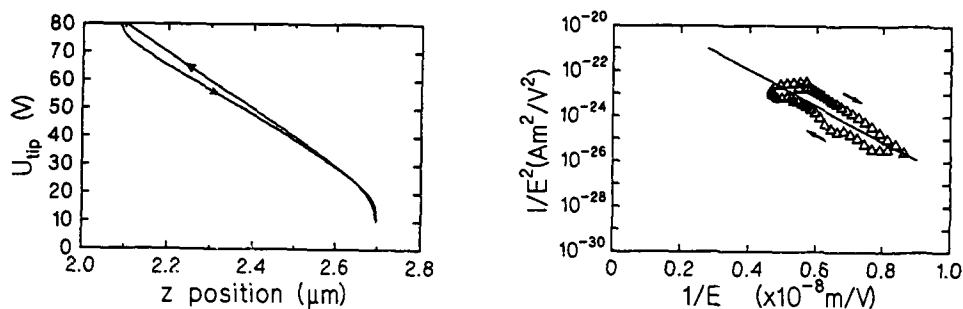


Figure 3a (left) Tip voltage versus tip z position at constant current (1 nA); **3b** (right) F-N plot taken with the tip locked in position 610 nm above the EFE site. Linear fit: see text.

linearity that this site displayed in the F-N plot, and the nature of the above approximation, these values can be considered in qualitative agreement with those listed in table 1. Unfortunately, after the topographic STM scan of Fig. 2b, the emission at this site was strongly reduced preventing further zooming on the site with the STM. Thus, the emitting site was modified by the proximity of the tip; its size cannot have been strongly reduced, however, since otherwise a feature should have been visible earlier in the SEM. The dimension of the active microstructure can therefore be estimated to $\sim 0.1 \mu\text{m}$. We would like to point out that the apparent emitting surface (see table 1) of this site is comparable to its physical size, which is in strong contrast to the assumption of purely electrostatic field enhancement.

We believe that the STM is a promising tool to study field emission phenomena associated with structures of submicron down to nanometer scale. The STM has completed our FESM with the possibility to relate topographic information and information on field emission strength with high spatial resolution. It is now possible to study EFE behaviour on broad area cathodes from low electric fields corresponding to high β values up to the theoretical Fowler-Nordheim limit of the order of 4 GV/m corresponding to $\beta = 1$. A method to directly compare information on topography and field emission strength by modulating s is presented elsewhere (Niedermann et al., 1989).

- Emch R, Niedermann Ph, Descouts P and Fischer Ø 1988 *J. Vac. Sci. Technol. A* **6** 379
 Latham R V 1988 *IEEE trans. Electr. Insul.* **23** 881
 Niedermann Ph, Sankararaman N, Noer R J and Fischer Ø 1986 *J. Appl. Phys.* **59** 892
 Niedermann Ph 1986 *Ph.D. thesis, University of Geneva*
 Niedermann Ph, Renner Ch, Kent A D and Fischer Ø 1989 submitted to *J. Vac. Sci. Technol.*
 Renner Ch, Niedermann Ph and Fischer Ø 1989 *IEEE trans. Electr. Insul.*, to be published

Lithography on Si by means of STM and SEM

JM Gómez-Rodríguez and AM Baró

Departamento de Física de la Materia Condensada C-III,
Universidad Autónoma de Madrid, 28049-Madrid (Spain).

ABSTRACT: By means of a scanning tunneling microscope (STM) integrated into a scanning electron microscope (SEM), we have been able to create nanometer-size metallic structures on a Si substrate from organometallic gases. A combined topographic/local barrier height study has been undertaken in order to achieve a better understanding of the lithographic process.

1. INTRODUCTION

In the last few years, Scanning Tunneling Microscopy (STM) (Binnig et al, 1982) has proven to be a powerful and versatile technique to investigate the topographic and electronic structure of metals and semiconductors with an unprecedented vertical (0.01nm) and lateral (0.2nm) resolution. The local character of the STM probe has also been used as a tool for nanolithography. Some advantages are connected with the high current density, which is obtained without use of any external focussing system, and the low beam energy, which reduces the radiation damage.

Many different approaches have been used with STM to produce microstructures. In this work, we have used the ability of STM to form deposits from organometallic compounds. The technique was first applied by Ehrichs et al (1988) and McCord et al (1989). We have used an STM integrated into a scanning electron microscope (SEM) to produce the deposits. This allows to observe the actual tip which operates during the lithographic process. We have also measured topographic and local barrier height images simultaneously, in order to achieve a more complete characterization of the deposits.

2. EXPERIMENTAL

Our STM/SEM combination has been described in detail earlier (Vázquez et al, 1988). In short, it consists of an STM placed on the sample stage of a commercial SEM allowing the simultaneous operation of both microscopes. In that way, we can combine the high resolution feature of the STM with the large scanning area of the SEM.

Metallic deposits were created on a p-doped Si substrate (resistivity = 0.01 Ohm.cm) from an organometallic gas ($W(CO)_6$) by applying short voltage pulses between tip and sample. The base pressure of the STM/SEM chamber was 10^{-6} torr. The entrance of the organometallic gas was

controlled with a leak valve. During lithographic processes, typical operating pressures ranged from 0.1×10^{-3} to 20×10^{-3} torr.

STM images were acquired and processed by means of a fully automated PC-AT workstation (Béjar et al, 1989). Typical scanning rate was 1 Hz. Barrier height images were acquired simultaneously with topographies by modulating the tip-to-sample distance at a frequency of 1 KHz and peak to peak amplitude of 0.25 nm and measuring the tunnel current with a lock-in amplifier, following a well-established technique (Binnig and Rohrer, 1986).

3. RESULTS AND DISCUSSION

Figure 1 shows a 3D view of one of our metallic deposits. It was fabricated by applying a short voltage pulse (10 msec) of -25 V (tip negative) at a 20 nA current. The STM image was then acquired with a tip-to-sample voltage of +2 V. at 1 nA. Figure 2 displays the local barrier height image (left) as well as the topographic contour map (right) of the same data as in Figure 1. As deduced from Figures 1 and 2, a small central deposit (about 100 nm in diameter), with higher barrier height than the substrate, was created.

Figure 3 is a SEM micrograph showing the STM probing tip as well as a larger metallic deposit (not the same as in Figure 1) after a lithographic process.

Several important features characterize the deposit imaged in Figures 1 and 2:

(i) In addition to the central hill which forms the main part of the deposit, there is a ring concentric with the hill with a positive corrugation (about 2 nm high). This particular fact was an exception with respect to many other deposits that we produced. Thus, we do not believe that this is a characteristic feature of the deposition process. We tentatively attribute this external ring to a tip shape effect. We have in fact observed that many electrochemically prepared W tips (as the one here used) show a concave surface which terminates quite abruptly into the lateral surface of the wire. This edge would produce a higher number of field-emitted electrons, due to the higher field at this point. The tip shape effect is supported by Figure 3: this SEM micrograph, taken on a different deposit, shows that the size of the fabricated structure is exactly the same as the size of the very end of the STM tip.

We would like to emphasize the interest of measuring in this case the local barrier height image (Figure 2 left). The fact that the surrounding ring has the same barrier height value as the central protrusion and higher than in the substrate favours the interpretation which attributes the whole structure to a metallic deposit. Other possible interpretation would attribute the structure to a contamination-like (instead of metallic) deposit. As Gómez-Rodríguez et al (1989), among others, have shown, a contaminated part would lead to a very small value (nearly zero) of the barrier height. The metallic character is then supported.

(ii) Between the hillock and the ring, there is an interface characterized by a valley of negative corrugation. This could be a real topographic effect which could be attributed in some way to an etching process. Nevertheless, this negative corrugation could be also an electronic effect

Figure 1. 3-dimensional STM shaded view of a metallic deposit created by applying -25 V at 20 nA for 10 mseconds.



Figure 2. (a) Contour map of the same data as in Fig.1. The gray-scale range is 32 nm. (b) Local barrier height image of the same data.

Figure 3. SEM micrograph showing a different metallic deposit as well as the STM probing tip after a lithographic process.



when imaging the structure with the STM. It could be produced by the change in the electronic properties in the metal-Si-metal surface. As a matter of fact, the Si-W Schottky barrier produces a 0.45 eV band bending in the p-semiconductor (Sze, 1981). Thus, the surface would be depleted of valence band electrons, inducing an apparent negative corrugation for positive tip voltages. We are actually studying this effect in a more systematic way.

Concerning the mechanism of the lithographic process, several possibilities have been advanced (Ehrichs et al, 1988; McCord et al). We believe that the process consists of breaking the adsorbed organometallic molecules on the Si surface by the bombardment with field-emitted electrons. We lean our belief in some numbers than come from our experimental data. The total charge during the deposition process in Figure 1 was $1 \text{ t} = 2 \times 10^{-9} \text{ C}$. Assuming a yield of 1 in the collisions of electrons and gas molecules, this would produce 1.2×10^9 metallic fragments. Taking the topographic data on Figures 1 and 2, we estimate between 10^7 and 10^8 metallic fragments on that deposit. Another interesting quantity is the actual number of gas molecules colliding within the area of the deposit on the Si substrate during the short voltage pulse. We obtain 2×10^6 , an order of magnitude too low. This would indicate that the existing multilayer of gas adsorbed on the surface is actually the responsible of the observed deposit. We think that these crude estimates give some figures reasonably close to the experimental situation.

In conclusion, we have been able to create nanometer-size deposits on a Si substrate from organometallic gases using an STM/SEM combined system. The metallic character of these deposits has been asserted from STM barrier height measurements.

REFERENCES

- Béjar M, Gómez-Rodríguez JM, Gómez-Herrero J and Baró AM 1989 J. Microsc. In press
 Binnig G, Rohrer H, Gerber Ch and Weibel E 1982 Appl. Phys. Lett. 40 178
 Binnig G and Rohrer H 1986 IBM J. Res. Develop. 30 355
 Ehrichs EE, Silver RM and de Lozanne AL 1988 J. Vac. Sci. Technol. A 6 540
 Gómez-Rodríguez JM, Gómez-Herrero J and Baró AM 1989 Surf. Sci. In press
 McCord M A, Kern D P and Chang T H P (1989) To be published
 Sze SM 1981 Physics of Semiconductor Devices (New York: Wiley) p 291
 Vázquez L, Bartolomé A, García R, Buendía A and Baró AM 1988 Rev. Sci. Instrum. 59 1286

Analysis of particle trajectories on an interactive desktop system

C J Edgcombe and D E Roberts

Department of Engineering, Trumpington Street, Cambridge CB2 1PZ, UK

ABSTRACT:

The software suite CIELAS2 provides rapid interactive calculation of trajectories and electron-optical properties for particle beams in systems of 2-D geometry. Behaviour near a thermionic cathode is modelled accurately even when the mesh spacing is too coarse to show the potential minimum. The displacement of trajectories by asymmetric or symmetric perturbations of electrodes can be displayed. The operation of PC-compatible computers has been enhanced to allow the program to be run on widely-available hardware.

1. INTRODUCTION

There is a continuing need to find details of the behaviour of beams of electrons and ions for many applications including electron-beam lithography, ion-beam milling, electron microscopy, X-ray analysis, electron-beam welding, imaging and microwave devices. For these purposes it is valuable to have a computational tool which can rapidly report a wide range of information about the system under analysis, with interactive facilities for changing the design parameters and enabling the effects of these changes to be shown quickly.

The software suite CIELAS2 has been developed to provide rapid definition of the geometry of electrodes, calculation of the particles' trajectories and analysis of the resulting particle beam, in systems of axial or translational symmetry. The geometry can be defined by use of a graphical editor, and mesh generation can be carried out automatically, with provision for varying the mesh density. Finite-element methods are then used to find the distribution of electric potential in the presence of space-charge, or the magnetic field of coil systems with (possibly non-linear) ironwork. When these potential distributions are known, the trajectories of particles of any charge/mass ratio can be traced, in a relativistically correct manner. The particles can be launched from a thermionic cathode, from a given file of data, or as if from a point source. More than one electron can be launched from each emitting point, over a range of angles. The current density over a thermionic emitter can be found by iteration, including correctly the effects of thermal velocities and the potential minimum near the cathode. When the trajectories are known, further processing can be carried out rapidly, by choice of command, to display stored trajectories, contours of variables, current density distribution across the beam or at the cathode, envelope of a given percentage of beam current, electron-optical emittance (phase-plane plot) and other electron-optical parameters. Trajectories can be saved at exit from one section and launched into an adjacent one, possibly of different scale. The program can show the effects on the beam of perturbation of electrodes, including tilts and transverse displacements, ellipticity, axial displacement and change of diameter. The effects of these perturbations on the beam in further sections of the system can also be shown.

In order to make possible the use of an inexpensive but powerful workstation, the capabilities of PC systems (from Amstrad to 80386) have been enhanced in many ways. As a result, a desktop computer using the 80386 processor and 80387 co-processor running at 20 MHz rate

can assemble coefficients and produce a first solution for voltage on a 57×119 mesh in 191 seconds. Subsequent solutions for the same geometry are obtained in 115 seconds.

2. GEOMETRIC DEFINITION AND DISPLAY FACILITIES

The geometry of the system to be analysed is defined by means of the associated program BSPEC. In this program, the lines forming the mesh are defined in two stages. First, 'major' lines are defined, to correspond to the surfaces of electrodes or other major subdivisions needed, e.g. for specifying the emitting area of a cathode. Then, between adjacent pairs of major lines, groups of 'minor' mesh lines are defined. The number of minors in each group can be chosen (subject to a maximum for the total), and their spacing can be varied in geometric progression by a simple command. The program can generate automatically a distribution of minor lines over the whole problem area, and this mesh can then be modified locally if required. Both major and minor lines, and individual mesh points, can be altered easily by using the graphical editing facilities provided. Regions of the mesh can be displayed, magnified, in windows of any dimensions, for increased accuracy where required. Areas of material defined in cross-section can be specified to be conductors or coil sections, to have given values of relative permittivity or permeability or non-linear magnetic properties, or to have given emission constants, as required.

3. FINITE-ELEMENT SOLUTION

In order to trace trajectories correctly in axisymmetric systems, it has been found essential to model accurately the distribution of variables near the axis. Some quantities, such as the phi-component of magnetic vector potential, vary linearly with radius as the radial coordinate tends to zero. Other quantities such as the electric scalar potential vary quadratically with radius, in the same limit. In this program, care has been taken that the interpolation schemes used, both for trajectory tracing and for display of contours, accurately reflect the type of variation near the axis of the variable concerned.

To achieve the maximum speed of solution for potential distributions, the 80387 numeric co-processor has been programmed in assembly language. This has allowed the internal registers to be used to their maximum accuracy of 80 bits, rather than the 64 bits normally available with double-precision Fortran. The resulting increase in accuracy of the potential solution has been found valuable in problems where the potential is nearly constant and the electric field is very small; then the increased accuracy reduces the fluctuations in calculated values of electric field and in the trajectories.

4. ESTIMATION OF CURRENT DENSITY AT A THERMIONIC CATHODE

When electrons leave a thermionic cathode, the distribution of their charge in space produces a potential minimum, separated typically by a few microns from the cathode surface. If this spacing is less than the distance from the cathode to the first mesh point in front of it, simple interpolation using only the potentials at mesh-points does not give accurate estimates of the potential gradient, the current density or the initial direction of trajectories.

In the program CIELAS2, the effects on the trajectories of the potential minimum due to space-charge are included correctly even when the mesh spacing is too coarse to show the minimum. At some distance s_1 from the cathode, further away than the potential minimum, the voltage V_1 is found. The potential is assumed to have a minimum value V_m (<0) at some distance s_m from the cathode. Then, according to 1-D thermal velocity theory, there are relations (1) between V_m , s_m , the cathode temperature T and the current density J at the

minimum; and (2) between $(V_1 - V_m)$, $(s_1 - s_m)$, T and J . Also, (3) the current density J beyond the minimum is related to J_0 , the maximum available at the cathode, by

$$J = J_0 \exp(e V_m / k T)$$

These relations allow V_m , s_m and J to be found when V_1 , s_1 , J_0 and T are known. Then, for trajectory tracing, the results of 1-D theory can be used to obtain more accurate values for the field components than would be found by interpolation between values at mesh-points.

Fig. 1 shows electrons diverging in many directions from points on the line of potential minima. The variation with radius of the spacing between the line of minima and the cathode surface can be clearly seen. This variation is related to the change of current density over the cathode surface, from possibly temperature-limited behaviour near the axis, to the very small space-charge-limited current density at the beam edge due to a negative grid aperture nearby.

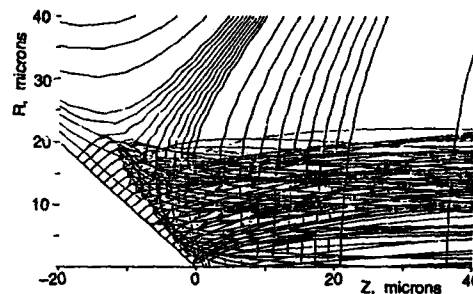


Fig. 1 Trajectories near a conical cathode

5. ELECTRON-OPTICAL CALCULATIONS

The program can display plots of trajectories (Figs 1,2) and also of beam emittance, or the distribution of electrons in a phase-plane (Fig. 3) whose coordinates are radius r and angle dr/dz , for a particular value of axial coordinate z . Diagrams of this type have been found particularly useful in the design of electron-beam instruments, where they aid comparison between the acceptance of the lens system and the distribution available from a given gun design. By this means it is possible to determine quickly the effect of changes of the gun geometry on the current delivered to the final spot.

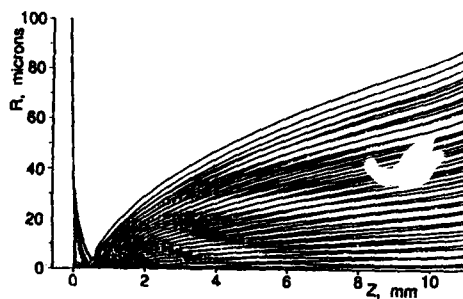


Fig. 2 Trajectories from a flat cathode

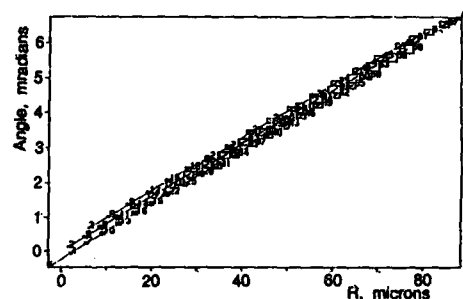


Fig. 3 Emittance plot at $z = 11$ mm

The parameters of rays in the beam, collected at one value of z -coordinate during the trajectory tracing, can be used as data for further processing. It appears straightforward to use this information to obtain a plot of current density as a function of radius. However, it has been found that the distribution so calculated may predict too small a spot with too high a current density. In fact, electrons which leave a single point on the cathode surface arrive at a cross-section later in the system with different values of radial coordinate, as a result of their initial variation of direction. To obtain an accurate estimate of the current distribution, it has been found desirable to trace electrons emitted from the cathode in more than one direction.

Other information which can be obtained from the coordinates of electrons at a particular cross-section includes the directional intensity – both the limiting value on the axis and the value averaged over chosen ranges of angle and radius. The particular calculations made, and the form of their presentation, may be developed to suit a particular application.

6. SOLUTION FOR PERTURBATION

Facilities have been provided in the program, at the request of users, to show the effects of changes in dimensions from the design values and of misalignment of electrodes or of sections of the system. The types of perturbation for which information can be obtained include:

- Axial movement of an electrode or change of its diameter (no variation round the axis);
- Tilt or transverse shift of an electrode, or of one section relative to another (one cycle);
- Ellipticity of an aperture (two cycles round the axis).

The method used is an extension of the standard method of finite-element solution, modified to allow for the cyclic variation of the perturbation potential round the axis. The potential so obtained is used in a modified form of the paraxial ray equation, where it adds a particular integral to the complementary function which describes the paraxial trajectory in the absence of perturbation. The resulting perturbed trajectory is then displayed, together with the unperturbed trajectory for comparison (Fig. 4). The effect of displacing an electrode in one defined section of a system may be carried through to show the perturbation produced in later sections, if required.

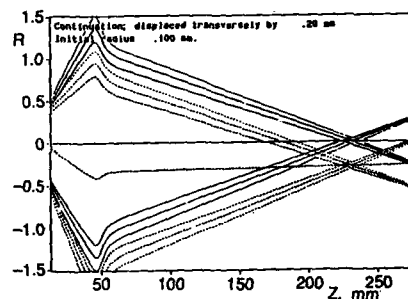


Fig. 4 Effect of a transverse displacement

7. CONCLUSION

The program CIELAS2 has been extensively developed in co-operation with users to offer a comprehensive range of interactive facilities which exploit many features of the PC environment. The capabilities of the program for accurate cathode modelling, electron-optical calculations and perturbation analysis are now being used to tackle a wide range of design problems, both in research establishments and in industry.

8. ACKNOWLEDGMENTS

The authors wish to thank Dr. K. C. A. Smith and Dr. J. Banbury for many stimulating discussions. This work was supported by contracts from the Science and Engineering Research Council and from the Royal Aircraft Establishment, Farnborough, and was carried out at the Department of Engineering, University of Cambridge.

An alternate cathode architecture

Edward J Daniszewski

Rome Air Development Center, Griffiss AFB, NY 13441-5700

ABSTRACT: Prototype cathodes have been developed in this research project. They are based on the principles responsible for thermionic emission from conventional impregnated dispenser cathodes (IDCs). However, the fabrication sequence has been altered in such a way that the optimal emissive centers, determined by Mossbauer analysis of the M-type IDC, are established and maintained by the activation schedule. This is accomplished by employing low weight loading and moderate decomposition temperature precursors. Hence, the active element, barium, achieves a surface site group configuration at much lower temperatures than conventionally produced cathodes. The high BET area of these cathodes, coupled with the strongly adsorbed electropositive monolayer, simulates the electronic and steric properties of the IDC, but effects comparable thermionic emission at lower temperatures because of the choice of a thermochemistry that establishes these optimal emissive centers before the onset the onset of monolayer evaporation.

1. INTRODUCTION

In the early 1960's, Zalm (1963) modified a tungsten dispenser cathode, a B-type, with a surface overcoat of select 5-d transition metals creating the M-type dispenser cathode. This device produced at least three times higher current density at a given temperature than the B-type. The reason for this emission enhancement remained unknown until Green (1981a) postulated a theory to explain this phenomenon. This report presents the experimental verification of Green's hypothesis and develops a more complete theory of thermionic emission from dispenser cathodes. The results of this study prompted further investigations to elucidate the impact of preparation procedures on their performance as thermionic emitters. To date, there has been no systematic study of cathode fabrication techniques. The affects of preparation variables have been systematically studied and two key areas were targeted for modification; optimized compounds for precursors of emission sites, and controlled impregnation procedures. By sequential construction, high surface area emitting structures have been produced which operate at lower temperatures than conventionally manufactured cathodes.

2. EXPERIMENTAL

Two commercially available cathodes, a B-type and an M-type, were obtained from Spectra-Mat and impurity doped with 10 Mci of Co 57. The rationale for this procedure was that the deposition of the Co 57 would be analogous to the transition metal over-coat used in fabricating the M

cathode. The incorporation of this Mossbauer probe would then yield valuable information on the geometric structure of the surface site group responsible for the observed difference in thermionic emission between a B-type and M-type dispenser cathode. These data were recorded in the emission mode using an Austin Science Associates Mossbauer Spectrometer, model S-600, against a single line stainless steel absorber, during the activation and operation of the respective cathodes in a vacuum environment.

Impregnant thermochemistry associated with the Philips-Emet manufacturing process of dispenser cathodes (Gupta et al 1977) was analyzed with a Perkin Elmer System 7/4 microprocessor controlled differential thermal analyzer. The DTA traces revealed an unwieldy number of component and preparation variables that could not be correlated with thermionic emission, but were, in fact, controlled by subtle changes in the fabrication sequence. Thus, a modified tungsten matrix was implemented in this stage of the research. It was fabricated using 8-12 micron tungsten powder mixed with an equal volume of ammonium metatungstate. Following ball milling for 1 hour, it was calcined at 573K until the cessation of ammonia vapor. The dry mixture was then isostatically pressed at 2.32 KPa in an argon atmosphere, and sintered at 2100K for 1 hour. Using the standard BET measurement technique of nitrogen physisorption at liquid nitrogen temperature, the surface area was found to be 2.3 square meters/gm; the pore volume was .15 cc/gm. Three discs, each approximately .61 cm in diameter and 1 cm thick, were cut from the modified tungsten matrix. The first was impregnated with barium nitrate, 136gms/L; the second disc was heated to 600K and placed in a saturated solution of titania, 100gms/L, and then dried at 400K in a 60 cc/min helium flow for 12 hours; and the third disc was immersed in 0.2 M chloroiridic acid for 24 hours, dried at 400K in a helium ambient, and then wet impregnated with barium nitrate at 600K. DTA traces were recorded during each sequence of preparation.

Emission studies from the prototype cathodes based on the Mossbauer results were conducted inside a standard four inch four-way stainless steel cross. The flanges supported the mounted cathode assembly with heater, an optical viewing port for pyrometry, a stainless steel anode, and a vac-ion pump. The important temperatures for activation were ascertained by reference to the DTA traces. Zero field emission curves were then taken.

3. RESULTS AND DISCUSSION

Following standard cathode activation and operation procedures, the Mossbauer isotopes resolved into a well defined Fe 2+ singlet for the B-type and a Fe III quadrupole doublet for the M-type. Once the oxidation state and the spin nature were identified, the isomer shift and the quadrupole splitting were cross referenced against existing data subject to the constraint that the structure must belong to one of the ten surface molecule or symmetry groups. This latter condition is necessary to insure that the surface monolayer has the proper dipole polarity necessary to lower the thermionic work function. The results showed that the B-cathode source was characteristic of Co 57 in pure tungsten (Schiffer et al 1964), while the M-cathode source coincided with Co 57 at the B atom site in ABO_3 compounds such as barium titanate (Bhide et al 1965). This low-spin state transition metal ion on the M-type cathode surface provides an experimental verification of Green's theory.

His theory divides the transition metals into three classes which are determined by d-orbital population and vacant metal surface orbitals. Class I, tungsten, has one vacant surface d-orbital; Class II, which included Ir, Os, and Re, has with two vacant surface orbitals; and Class III, such as Pt, has no vacant surface d-orbitals. He postulates that the Class II metals, with their two vacant surface d-orbitals, can accept the sp^2 electrons of the surface oxygen not involved in bonding to Ba, to form the most stable configuration. This transfer of negative charge elongates the surface dipole and provides increased barium surface coverage. These lower the thermionic work function causing increased emission at a given temperature. The Mossbauer results verify this theory if the empty surface d-orbitals are equated with low-spin state configurations. This is accomplished by crystal field theory. The only valid interpretation of the Mossbauer experiments is the existence of a surface site group that has symmetry which removes the degeneracy of the transition metal d-orbitals by crystal field splitting. A strong crystal field will energetically favor a low-spin state electron configuration, resulting in empty d-orbitals for d-4, d-5, d-6, and d-7 metals. From group theory, this is exactly the case at the titanium site in barium titanate. The B-type cathode, composed of pure tungsten, has cubic symmetry which results in a high-spin configuration consistent with the Class I metals; the M-type cathode, has tetragonal symmetry (Green et al 1981b) for the sigma phase W/Os and W/Re case, and orthorhombic symmetry for W/Ir. Assuming that the Fe ion represents the transition metal site on the M-cathode, these symmetries remove the degeneracy of the d-orbitals, creating the low-spin configurations of Class II metals; and Class III metals such as platinum, even in the strong field case, must spin pair the d-orbitals to accommodate all the electrons. Thus the M-cathode surface, composed of Class II metals, can offer empty d-orbitals for oxygen ligand stabilization of the barium monolayer because of the formation of a surface site group modeled by the barium titanates. This translates to increased barium coverage on the M-cathode and hence increased thermionic emission.

Whereas this proposal satisfactorily accounts for the performance of the M-type IDC, it does not address the problems encountered in cathode processing and production. The M-type cathode still suffers from poor reproducibility and barium evaporation from the cathode surface during operation. The former was well documented by the DTA data obtained from the analysis of the Philips-Emet procedure of the impregnant synthesis. These suggest incomplete dehydrations and carbonate calcinations, both CO_2 and H_2O readsorptions, polymorphic transitions, and incomplete and unknown chemical reactions. In addition, the DTA component traces showed activation temperatures above 1500K, which indicates that the optimal emissive site could be destroyed because of surface sintering, reconstruction, and creation of bulk oxides and aluminates, all contributing to barium evaporation.

It is interesting to note and significant to point out that barium titanate is also the prototype structure for strong metal-metal bond complexes (Tauster et al 1978). These comprise a large number of transition metal compounds in which direct chemical bonding, involving d-electrons and d-orbitals, takes place between neighboring metal atoms and cations. This structure appears well suited for thermionic emission. The strong metal-metal bond would be between barium and a transition metal, stabilized both electronically and structurally by the

oxygen ligands so that the barium would not evaporate, and therefore would not need to be dispensed. The structure of a binary oxide supported on a refractory surface of high BET area, which itself contains a strongly adsorbed oxide layer is proposed as the alternate cathode architecture. Thus prototype cathodes were constructed based on the assumption that the hexagonal barium titanate structure was the optimal thermionic cathode, and that this preferred structure could be fabricated at the very beginning of life.

Each of the three prototype cathodes exhibited decomposition and activation at less than 875K, and the latter two had strong exothermic reactions at 900K indicating possible formation of a strong surface metal-metal bond. The zero field emission from them is presented in Figure 1.

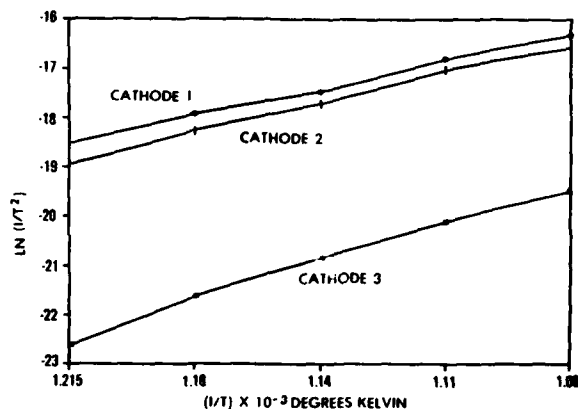


Figure 1
Zero Field Emission Data

SUMMARY

Mossbauer Emission Spectroscopy was used to probe both B-type and M-type cathode surfaces. Results indicated that enhanced thermionic emission was concomitant with the presence of a low-spin state transition metal ion. This low-spin Mossbauer probe identified a surface molecular configuration optimal for thermionic emission, hexagonal barium titanate. This structure also exhibits strong metal-metal surface bonds. Three cathodes prototypical of the strong metal-metal interaction were fabricated. Zero field emission from these data were in excellent agreement with the Richardson equation, and two of them exhibited emission densities comparable to state-of-the-art cathodes, but a much lower temperatures.

REFERENCES

- Bhide V G and Multani M S 1965 Phys. Rev. 139 6A A1983
- Green M C 1981a Dispenser Cathode Physics, RADC-TR-81-211
- Green M C, Skinner H B and Tuck R A 1981 App. of Surf. Science 8 p 13-35
- Gupta A and Young C O 1977 The Manufacture of M-type Impregnated Dispenser Cathodes, NASA-Lewis Research Center
- Schiffer J P, Parks P N and Haberle J 1964 Phys. Rev. 133 6A A1553
- Tauster S J, Fung S C and Garten S L Jour. A. Che. Soc. 1004, 170

Comparison of vacuum and semiconductor field effect transistor performance limits

Lester F. Eastman

School of Electrical Engineering and National Nanofabrication Facility,
Cornell University, Phillips Hall, Ithaca, NY 14853

ABSTRACT: The electron transport, space charge effects, impedance levels, power levels, and frequency limits of very small vacuum and semiconductor field effect transistors are compared. Parasitic capacitive elements are included. Limiting ballistic electron velocity, voltage and current are presented, along with device estimated equivalent circuit elements, current-gain and power gain cutoff frequencies, with size scaling. High frequency microwave performance of these microstructures allow efficient operation in the millimeter wave range for both, with considerably higher voltage and power for the vacuum microelectronic devices. The need for high current density in proportion to frequency, but with low resistance, is also presented.

There are several key differences between vacuum and solid state microelectronic amplifying devices. One such difference is the relative dielectric constant of the medium in which the electrical charge carriers are transported. Another is the effective mass of the charge carriers. Another is the limit of distance over which charge carriers are ballistic, to allow high carrier velocity. Still another is the degree of neutralization of charge carriers in the charge transport medium. The final, largest, difference is that of the limits of uniform current density at the negative electrode.

Usually a control electrode is used to control the amount of electron current flow between the cathode and the anode. There is a capacitance between this electrode and the cathode, and between this electrode and the anode. With a grounded cathode, the sum of these is the amplifier input capacitance, while the latter is the (negative) feedback capacitance. For high voltage gain, the sum must be much greater than the latter.

In order to have matched input impedance, the input capacitance can be resonated with an inductance for some specific high frequency performance. In order to have good performance at such a high frequency, a high conductive current density must be achieved from the charge carriers. Thus as one raises the operating frequency, raising the capacitive susceptance current, the carrier conductance current is raised to match this rise. This conductive current density is near 1×10^5 A/cm² in GaAs transistor channels for 100 GHz operation, and values as high as 5×10^5 A/cm² have been

achieved in a few laboratories. Because of the 13:1 lower dielectric constant, this value can be that much lower in a vacuum triode than in a GaAs transistor. Good operation at 100 GHz would then require only several thousand A/cm² in such a vacuum device.

The velocity that electrons have for a given kinetic energy depends on the reciprocal of the square root of the mass of the electron. In GaAs, this effective mass of electron is ~ 16:1 lower than that of free space electron. Thus ballistic electrons travel 4 times faster in short GaAs samples than they would in a vacuum, for the same kinetic energy. The effective mass is low for electrons in GaAs only over a limited range of kinetic energy; up to .25V, so this is a severe limitation on operating voltage.

The current density that ballistic electrons yield in GaAs short devices, compared with vacuum devices, is over 50 times higher for the same bias voltage and geometry. This is due to the fact that this current density depends directly on the relative dielectric constant and reciprocally on the square root of the effective mass of the carriers. As mentioned earlier, the required current density is 13:1 lower in vacuum, due to reduced dielectric constant. By raising the bias voltage, the current can be raised to this level, since electrons are ballistic to a much higher value of kinetic energy in vacuum.

In GaAs and related compounds, the electrons have ~ .2 μm mean free path, and hold some of their forward momentum even after collisions with the crystal lattice. Such collisions with the crystal lattice are reduced at low temperatures. Thus if electrons approach ballistic motion, their transport

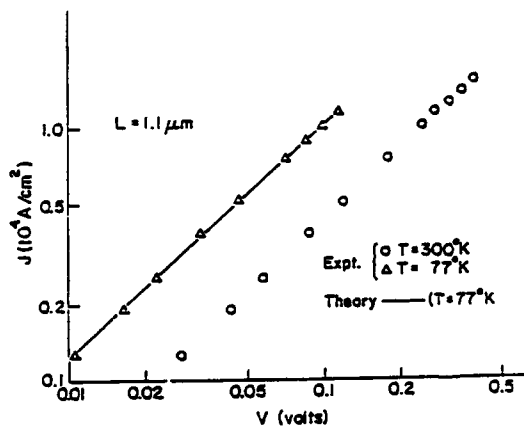
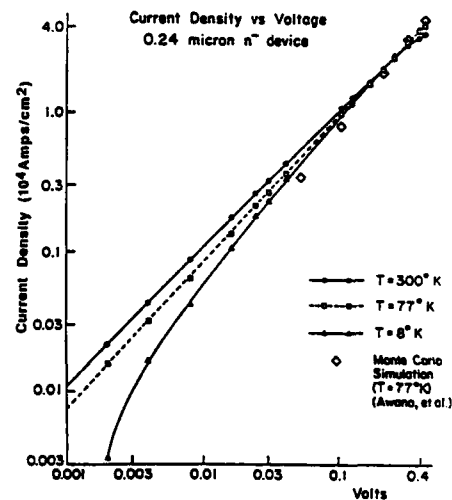


Figure 1(a) Electron current density vs voltage for 1.1 μm long GaAs, with $2 \times 10^{16}/\text{cm}^3$ donors at 300K and 77K.



1(b) Electron current density vs voltage for .24 μm long with $2 \times 10^{15}/\text{cm}^3$ donors, at 330K, 77K and 8K.

parameters become more independent of temperature. Figure 1a and 1b show current-voltage curves for 1.1 μm and .24 μm electrode separation parallel plate GaAs diodes. In the latter case the electrons have little change in properties with temperature and reach a velocity near 1×10^8 cm/s at the anode. 1×10^7 cm/s is the maximum velocity reached in GaAs long samples, due to collisions with the crystal lattice.

One strong benefit of semiconductor material is that positive ions can be placed in the material to neutralize the electron charge. Thus simple space-charge-limited current can be surpassed by orders of magnitude. For example, for .25 μm electrodes separation, only $2 \times 10^{15}/\text{cm}^3$ electrons will be present, for .20V bias, on the average, in undoped material. In contrast, $2 \times 10^{17}/\text{cm}^3$ and even $2 \times 10^{18}/\text{cm}^3$ electrons can be present in this material when their space charge is neutralized by positive doping ions. Even at 1×10^7 cm/s electron velocity, the $2 \times 10^{17}/\text{cm}^3$ doping, typical of GaAs MESFET devices, yields 3.2×10^5 A/cm² current density in the conduction region. In undoped quantum wells of GaAs, with charge-neutralization ions nearby, electrons can travel at 2×10^7 cm/s with up to $1 \times 10^{18}/\text{cm}^3$ density, yielding 3.2×10^6 A/cm² conduction current along this quantum well.

Another strong benefit of semiconductor structures is the capability of supplying high current density values from heavily doped negative electrodes. Normally this current density is kept below 5×10^5 A/cm². In order to get a high current density, the current in a thin channel is fet into that channel over a distance much ($> 10:1$) longer than the thickness of the channel. This "distance-source" allows lower values of source resistance, reducing the negative feedback term equal to the product of this source resistance times the mutual transconductance of the device.

Figure 2 shows the cross section of a "planar" heterojunction field effect transistor. The electrons travel horizontally from source to drain, along a quantum well, and their conductance current is modulated by the gate. Up to ~ 600 ma/mm current can flow, with $g_m = 600$ mS/mm, both normalized to the dimension perpendicular to the plane of the figure. The state of the art unity current gain frequency limit is 150 GHz, and the unity power gain frequency limit is 250 GHz [1]. There are a maximum of $\sim 2 \times 10^{12}/\text{cm}^2$ electrons in the ~ 100 Å thick quantum well, yielding $\sim 2 \times 10^{18}/\text{cm}^3$ average electron density. The electrons in this structure are not ballistic because the electric field, causing transport from source to drain, extends over a distance longer than .2 μm , even though the gate contacts the semiconductor for only .15 μm length of the electron path.

A GaAs device with only .13 μm distance between the electron source and drain has been constructed. The electrons flow in a vertical direction, in the

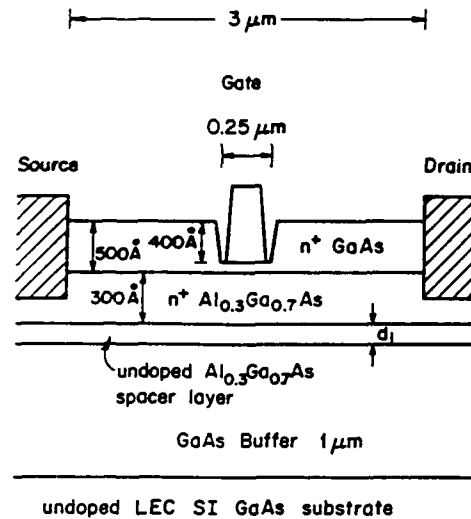


Figure 2. Cross section of a modulation-doped AlGaAs/GaAs field effect transistor. The electron flow in a potential well just below the space layer.

narrow ridges, and the metal gates are on the sides. This device had electron average transit velocity of $\sim 4 \times 10^7$ cm/s. If the electrons had been ballistic, accelerating from 0 to 1×10^8 cm/s, one would expect $\sim 5 \times 10^7$ cm/s. Here, they were injected with more than 5×10^7 cm/s, but lost some of their average velocity by collisions.

In comparing vacuum devices with these solid state devices, both configurations (planar/horizontal motion, and multi-channel/vertical motion) can be envisioned. The electrons in vacuum remain ballistic, following the Child-Langmuir law for conduction current versus voltage. Because there is no space charge neutralization from ions, close spacing and/or high bias voltage are required to obtain high enough conduction current for high frequency operation. With only 3 electrodes, the triode-like $I(V)$ characteristics have high output conductance, although this can be substantially alleviated using the beam-tetrode configuration.

Figure 3 shows the planar/horizontal motion structure that would be useful. The "distributed-source" would allow low source/cathode resistance. The dimensions shown could be realized using modern submicron fabrication techniques. Except for extra space-charge injected current, away from the gate, this structure could be modeled using triode theory applied to half of a period of a multi-gate vacuum structure.

Figure 4 shows the multi-channel vertical vacuum structure. Its performance follows the Child-Langmuir law [2]. For diodes with electrode separation s , in cm, the current density (in A/cm²) is:

$$I = \frac{2.336 \times 10^{-2}}{S^2} (V)^{3/2} \quad (1)$$

For the particular geometry shown, the amplification factor μ is 23. For 50 channels each 50 microns wide, this yields a mutual transconductance of:

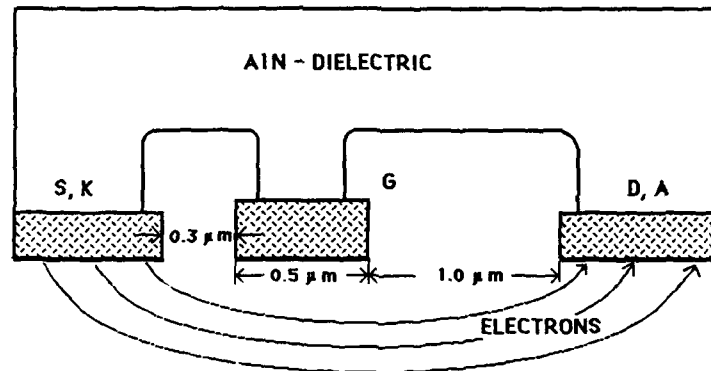


Figure 3. Submicrometer-gate vacuum triode in planar geometry cross section showing source, gate and drain electrodes supported by AlN dielectric.

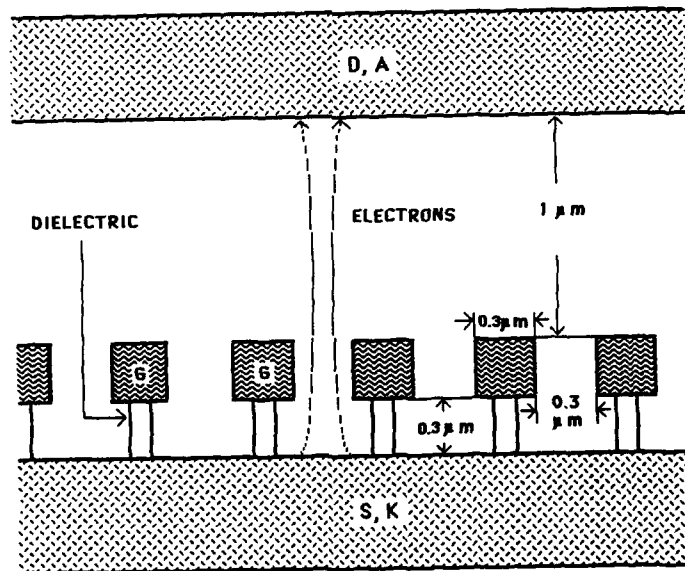


Figure 4. Submicrometer-gate vacuum triode cross section showing source, gate, and drain electrodes for multi-channel device.

$$g_m = 4.14 (V_a + \mu V_g)^{1/2} \text{ mS} \quad (2)$$

It also yields a shunt resistance at the anode of

$$r_a = 5,500 (V_a + \mu V_g)^{-1/2} \quad (3)$$

For this triode, the average current density is:

$$I = .12 (V_a + \mu V_g)^{3/2} \text{ mA} \quad (4)$$

The average transit time is:

$$\tau = 3S/u_a \quad (5)$$

where S is the separation of anode and cathode, and u_a is the electron velocity at the anode:

$$u_a = \left(\frac{2eV_a}{m} \right)^{1/2} \quad (6)$$

where V_a is the anode-cathode potential difference, m is the electron mass and e its charge.

In order to yield a velocity of 1×10^8 cm/s for ballistic electrons in GaAs, a voltage drop of ~ 25 V is required, while it would be ~ 4 V in vacuum, due to the higher electron mass. For a $1 \mu\text{m}$ separation of anode and cathode, a transit time of 3 picoseconds would occur for 1×10^8 cm/s in space-charge limited flow of ballistic electrons.

With this structure, the input capacitance at the gate would be about .057 pF. With $(V_a + \mu V_g) = 4$ V the g_m would be 8.28 mS, the V_a would be 2,750 Ω , and the current would be .96 ma (64 A/cm^2). This in turn yields a unity-current-gain frequency of 11.5 GHz, which would scale up in frequency in proportion to $(V_a + \mu V_g)^{1/2}$.

Conclusions

Comparisons between solid state and vacuum triode devices show that high current, low voltage and high frequency response are possible in the former, while low current, high voltage and high frequency response are possible in the latter. Obtaining current density values of 100's -1000's A/cm^2 over useful areas will be necessary in order to obtain high frequency response in the vacuum triodes.

This work is supported in part by ARO, ONR, RADC, G.E., Hughes, Boeing, and Martin Marietta.

Beck, A H W 1953 *Thermionic Valves* (Cambridge University Press) p 259.
 Nguyen L D, Tasker P J, Radulescu D C, and Eastman L F 1989 *IEEE Special Issue on Heterostructure Transistors* to be published.

Geometry optimization for a lateral triode

W. N. Carr, H. J. Wang, K. K. Chin
New Jersey Inst. of Technology
323 King Boulevard
Newark, New Jersey 07102
U. S. A.

R. B. Marcus
Bell Communications Research
331 Newman Springs Road
Red Bank, New Jersey 07701
U. S. A.

ABSTRACT: Geometry optimization is required for the fabrication of a successful family of lateral vacuum microelectronic active devices. Lateral triodes with deflector electrodes are modeled by tracing electron trajectories from cathode to anode. The field emission cathode wedge surface is spaced 0.9 to 1.1 μm from the grid field plate. Grid control voltages range from a few volts to 100 volts. Anode potentials range 30 to 100 volts. Cathode to anode average transit times for devices with maximum lateral trajectory lengths of approx. 10 μm are 3 to 4 $\times 10^{-12}$ sec. A transconductance of 1 μS per 100 μm cathode length at 80 V is calculated for triodes optimized with physical design constraints of 0.9 micron.

INTRODUCTION: This paper presents simulation of static characteristics for two lateral triode active devices based on a wedge-shaped field emission cathode. Deflecting electrodes are positioned near both the cathode and anode to eliminate space charge build up and to shorten the electron trajectory path. The lateral device geometries are of special interest since the potential exists for processing using technology compatible with VLSI production. Many device structures have been studied. The two structures described here are selected for simplicity of design and potential compatibility with existing wafer processing capability. A specific technology for the critical cathode structure is not assumed in this work. Cathode efficiency and a general discussion of applicability of different emitter tip technologies is the subject of a companion paper [Marcus et. al. 1989]. In the present paper we attempt to provide generic guide lines for fabrication of lateral triode devices with field emitter cathodes.

DEVICE MODEL: The device simulation is based on electron trajectory tracing within a calculated electric field region. The Laplace equation is solved in two dimensions for the potential field V ,

$$\nabla^2 V(r) = 0$$

The resulting electric field E together with the magnetic field B from nearby electron paths determines the trajectory of interest,

$$m \frac{d^2 \vec{r}}{dt^2} = q \left(\vec{E}(r) + \frac{d\vec{r}}{dt} \times \vec{B}(r) \right)$$

The Biot-Savart relationship is used to calculate local magnetic field effects

$$\vec{B}(r) = \frac{\mu_0}{4\pi} \int \vec{J}(r') \times \frac{\vec{r} - \vec{r}'}{|\vec{r} - \vec{r}'|^3} d^3r'$$

These relationships are solved in a two dimensional matrix with cylindrical symmetry using a modified form of SIMION [SIMION 1987]. The present simulator program is limited to 16000 grid points and does not permit the detail cathode geometric dimensioning that we would prefer.

The electric field at the cathode surface determines the electron flux tunneling into the vacuum. The cathode efficiency is described by the *F-N* relationship [Fowler-Nordheim 1928].

$$J = 6.2 \times 10^{-6} \left\{ \frac{\sqrt{E_F}}{(W + E_F)\sqrt{W}} \right\} E^2 \exp \left\{ \frac{-6.8 \times 10^{-7} W^{3/2}}{E} \right\}$$

TRIODE STRUCTURE: The basic triode device shown in cross-section in Fig. 1 has electron trajectories originating at the grounded cathode. The grid and anode are both maintained at +100 V potential in this example. In the upper location of Fig. 1 the electrons are not collected by the anode and contribute to an undesirable space-charge build up in the vicinity of the active device electrodes. Deflection electrodes biased at 0 and -100 V have been added to the lower location of Fig. 1. The importance of the deflecting electrodes is clearly shown as they cause all cathode electrons to be collected as they ballistically move to the anode electrode.

LATERAL ELECTRON INJECTOR: The basic triode structure uses the potential between the control grid and cathode to create the very high electric field required to launch electrons from the cathode surface. This cathode-grid structure functions as a specialized diode structure where electrons tunnel through the cathode surface into the vacuum and move toward the grid. In the structure cross-section of Fig. 2(a) a diode structure illustrates the electron extraction process. The position of the grid (collecting all of the electrons in this case) with respect to the cathode is specified by the parameter x_0 . The grid of Fig. 2(a) extends a sufficient distance to the right to collect all electrons from the cathode. A large negative value for x_0 corresponds to a vertical diode totally covered by the collecting grid. The small positive values of x_0 correspond to grid placement in a lateral triode structure. Figure 2(b) illustrates the dependence of cathode current in the Fig. 2(a) structure with +100 V potential on the grid electrode. [The very strong dependence of cathode current on relative grid location emphasizes the importance of minimizing the cathode-grid separation to obtain higher operating current levels.] Based on a cathode-grid separation of $x_0 = 0.9\mu\text{m}$, the cathode current is reduced by 100× compared to a device with a "vertical" trajectory: ($x_0 = -3$).

TYPE 1 LATERAL TRIODE: A triode structure with the deflector electrode 1 spaced to within $1\mu\text{m}$ (x -dimension) of the cathode tip is defined as "Type 1" in the Fig. 3 (a) device cross-section. The close proximity of deflector 1 to the cathode results in a stronger *E*-field focusing the electron beam onto the anode. The cathode tip is located $0.5\mu\text{m}$ above the conducting substrate—all maintained at 0 V potential. The anode extends over an area which will collect all deflected electrons within the selected range of grid and anode voltages. The anode extends $6\mu\text{m}$ toward the deflector 2 electrode and the grid spans $2\mu\text{m}$ as shown in Fig. 3. The dielectric thickness under the deflectors and grid-anode electrodes is 0.2 and $0.9\mu\text{m}$, respectively. In Fig. 3 (b), (c), (d) and (e) the selected electron trajectories, equal current tubes, equipotentials, and *E*-field contours are shown for the Type 1 device. In Fig. 4, 3-terminal characteristic curves for the Type 1 geometry indicate anode currents

in the nanoamp range for electrode voltages over 50 volts.

TYPE 2 LATERAL TRIODE: For higher current operation an improved ohmic contact to the cathode is shown in the Type 2 geometry of Fig. 5 (a)-(e). In Fig. 6 there is a reduced current density due to the increased deflector 1-cathode spacing compared with the Type 1 device of Fig. 4.

CONCLUSION: The lateral triode provides transconductance over a wide voltage range. The relative difficulty in obtaining sufficiently large E -fields at the cathode surface will probably continue to be a major factor limiting the power levels of lateral devices to the picowatt to microwatt level. The device appears best suited for micropower applications. This device has the potential of production compatibility with LSI integrated circuits equipment.

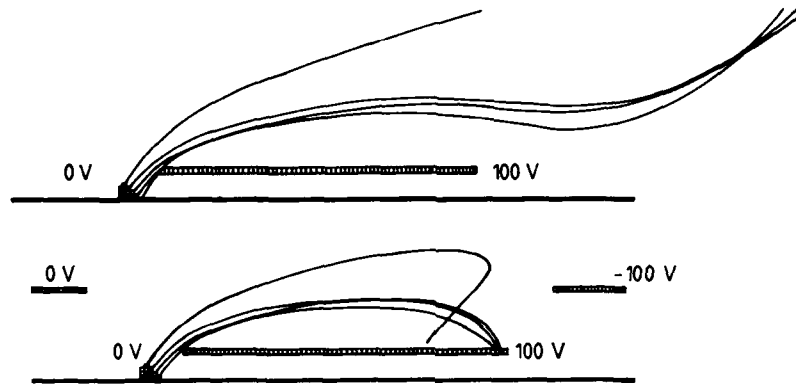


Fig 1 Electron trajectories for a diode (produced by connecting the grid and cathode of the triode in Fig 3(a)), with and without deflector electrodes.

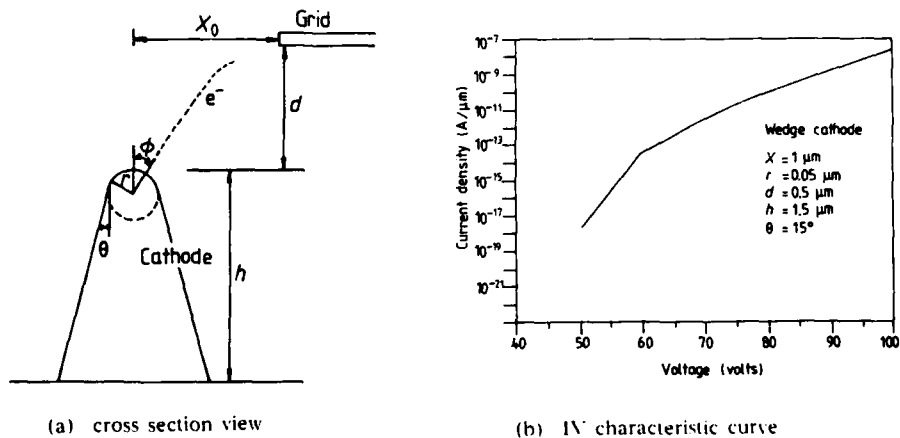


Fig. 2 Lateral diode with wedge cathode

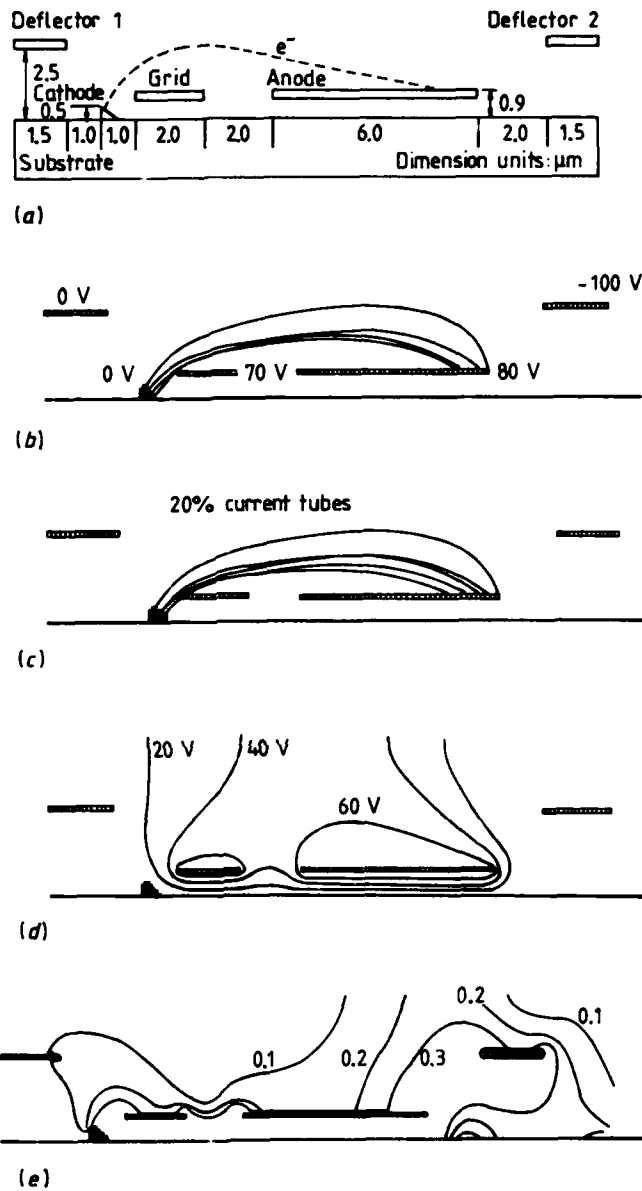
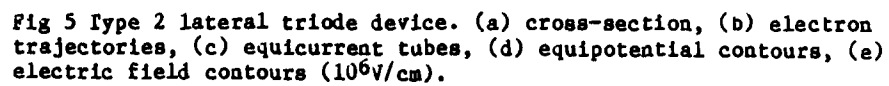


Fig 3 Type 1 lateral triode device. (a) cross-section, (b) electron trajectories, (c) equicurrent tubes, (d) equipotential contours, (e) electric field contours (10^6 V/cm).



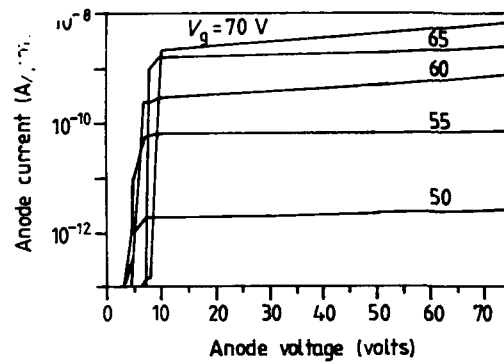


Fig 4 Type 1 lateral triode device

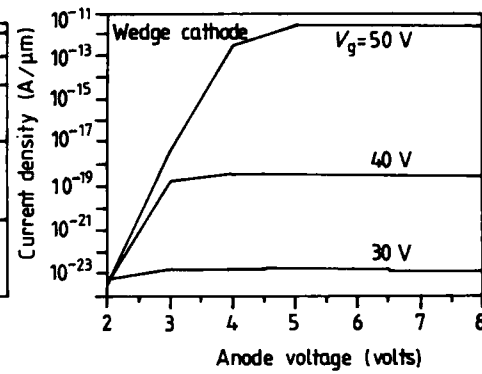


Fig 6 Type 2 lateral triode device

REFERENCES:

- (1) R. B. Marcus, K. K. Chin, Y. Yun, H. J. Wang, W. N. Carr, "Simulation and Design of Field Emitters", Int'l Conf. on Vacuum Microelectronics, 24-26 July 1989, Bath, England.
- (2) R. H. Fowler and L. Nordheim, "Electron Emission in Intense Fields", Proc. Royal Soc., A113, 173, 1928. See also Proc. Royal Soc., A114, 699, 1929.
- (3) SIMION Reference Manual, Idaho National Engineering Laboratory, 1988.

Miniaturization of electrovacuum microwave and radiofrequency low-power devices

N.D.Devyatkov(1), Yu.V.Gulyaev(1), A.M.Alexeenko(2), M.B.Golant(2),
J.L.Grigorishin(3), A.A.Negirev(2) and N.I.Sinit'syn(1)

- (1) Institute of Radio Eng.&El., Acad.Sci.USSR, Moscow 103907
(2) Electronic Industry's Ministry, USSR, Moscow 109240
(3) Institute of Electronics, Acad.Sci.BSSR, Minsk, USSR 220841

ABSTRACT: Results of investigation in the field of creation of miniaturized microwave reflex klystrons, low voltage resonance devices with a high electronic efficiency, BWOs with magnetic and electrostatic focusing and radiofrequency vacuum integral circuits are shown.

1. INTRODUCTION

Miniaturized electrovacuum microwave and radiofrequency devices coming near to semiconductor ones in a mass, dimensions and electrical characteristics maintain their obvious advantages opening new possibilities of their application including apparatus used in extreme conditions. Physical and chemical material properties and technological techniques used in fabrication of microvacuum devices allow to provide an unusually high parameters reproducibility and their stability.

In this paper the results of the investigations carried out in the Soviet Union in the field of miniaturized narrow-band reflex klystrons (minitrons), low voltage resonance devices with the high electronic efficiency (multigap monotrons), wide-band BWOs with the magnetic and electrostatic focusing and radiofrequency vacuum integral circuits are shown.

2. MINITRONS

In Fig.1 the view of two minitron types is demonstrated. There is shown (Golant et al 1983, Gulyaev et al 1988) that the main difference of the minitrons from the traditional reflex klystrons consists in using high permeanced electron beams (from 100 mA/V^{3/2} and higher). This quantitative, on the face of it, phenomenon leads to qualitative changes in device characteristics. Really:

- 1) a high electron beam conductivity is provided. This allows to extend considerably an electron tuning range in some cases up to 5 % and to increase the electronic efficiency by 2 or 3 compared with the common reflex klystrons;
- 2) using of the multiray electron beams with a small length provides a low probability of residual gas atoms ionization by electrons, promotes the higher durability and eliminates the

causes of relaxation processes appearing in an interaction space; 3) the device mass is brought to the fractions of a gramm and heat removal paths from an active device zone are minimized thereby sharply improving its parameters thermal stability; 4) work inputs for the minitrons fabrication are also lowered at a high precision, parameters reproducibility from one copy to another and possibility of the group technology using.

The minitron operates in the frequency range from 1.5 to 30 GHz. The actuation time is not more than 1s. The minitron oscillation

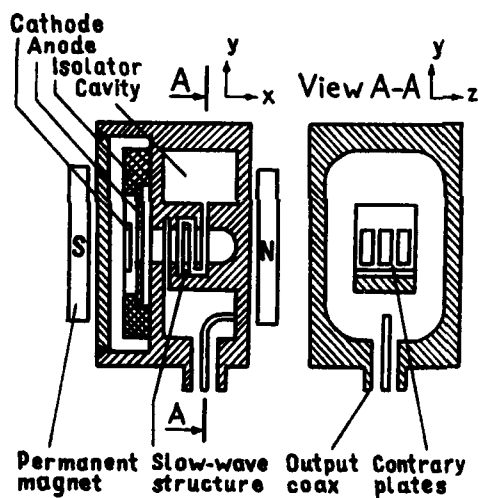


Fig.2. Schematic diagram of the multigap monotron



Fig.1. Two 3 cm band minitron types

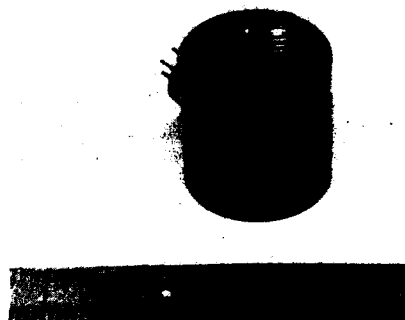


Fig.3. 3 cm band BWO with PEF



Fig.4. 3 cm band BWO with magnetic focusing

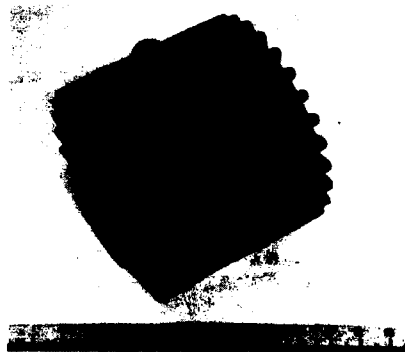


Fig.5. Mm band BWO

frequency is easy submitted to the pulling by the resonator with a high Q-factor due to the low loaded Q. This allows to low its frequency noise level considerably. Minित्रon durability is usually 10 000 hours. The parameters of the typical 3 centimeter band minित्रon are shown in the table 1.

Table 1 PARAMETERS OF THE MINITRON WITH $\lambda = 3$ CM

Output power	Electron tuning	Resonator voltage	Resonator current	Noise level at tuning away from carrier by 5 kHz
mW	%	V	mA	dB/Hz
50-80	1-5	25-85	40-90	-160(Ampl.) -85(FM)

3. MULTIGAP MONOTRON

The electronic efficiency of the discussed minित्रons does not exceed several percent. The possibility of the electronic efficiency increasing by more than one order for the miniaturized low voltage vacuum microwave devices is shown during the creation of the O-type resonance device in which the electron beam interacts with a field of the single cavity resonator having a concentrated capacity in a form of a slow-wave structure section of the type "contrary plates". This device was named "multigap monotron". Its schematic diagram is shown in Fig. 2. The multiray tape electron beam formed by an electron gun with a plane optics penetrates the cavity resonator through channels in the plates of the capacitive gap. The beam focusing is realized by the longitudinal magnetic field induced by a permanent magnet. The mass of Sa-Co magnet at the magnetic field strength of 5000-7000 Oe does not exceed 100 gr. A characteristic feature of the multigap monotron mechanism is its highest efficiency of several tens of volts at accelerating voltages. The centimeter band multigap monotrons provide the electron tuning in the frequency range of 50-150 MHz with the output power from ~100 mW to units of watts at the acceleration voltage of 40-80 V and electron efficiency up to 35-40%. A theoretical analysis gives evidence concerning the possibility of the multigap monotron's electronic efficiency increasing up to 70-80 %.

4. BACKWARD O-TYPE OSCILLATORS

A serious obstacle on the way of the miniaturization and BWOs supply voltage lowering is a space charge growth and a velocity electron spread connected with it. However, there was shown by Shevchik et al (1975) and Sinitsyn et al (1976) that these factors are not a principal restriction. This statement was assumed as a basis of the work on O-type BWT miniaturization.

The mechanism of electron interaction with the microwave field of the backward electromagnetic wave promotes the successful BWO miniaturization both in the decimeter band and at

the extremely high frequencies of the submillimeter band (up to $\lambda \sim 0.1$ mm). The chosen operating frequency defines the specific character of structural-technological device solutions and, as a consequence, its parameters complex.

5. BWO WITH ELECTROSTATIC FOCUSING

The first in the USSR miniaturized BWO with the periodic electrostatic focusing (PEF) operating in the 3 cm band was developed in the late fifties on the base of a multichannel slow-wave structure of the type "contrary plates" (Alexeenko 1968 a,b). In sixties a series of heterodyne BWOs with PEF was created covering the frequency range from 1 to 40 GHz with electric tuning from 40 % in the short wave part of this range to an octave in its long wave part, 3 cm band BWOs with the electrical tuning of the order of 5 %, the output power up to 1-1.5 W and the electronic efficiency of 4-5 %. The mass of the most developed BWOs was, as a rule, 200-300 gr and the maximum voltage did not exceed 1000-1500 V depending on the frequency range.

On the base of these results the accelerating voltages were lowered by one order (up to 150 V and lower) at the maintaining of the operating currents and thus the slow-wave structure length was sharply reduced thereby decreasing the mass (to the tens of gramm) and overall dimensions of devices. The view of 3 cm band BWO is shown in Fig.3.

6. BWO WITH MAGNETIC FOCUSING FOR CM AND DM BANDS

The works on BWO miniaturization with the magnetic focusing operating in cm and dm band and covering frequency range which substantially exceeds the octave have a principal character. During these works it was shown that the electron beams with the microperveance achieving two or three thousands onto 1 cm^2 and with the small electron velocity spread can be formed on the base of the multiray slow-wave structure and high enough power level can be maintained at the lowered accelerating voltage.

The set of BWOs with the magnetic focusing having the electrical tuning from the octave to 1.5-2 octaves which cover the frequency range from 1 to 18 GHz at the output power from several tens to hundreds of milliwatts was produced. The accelerating voltage values change from the units and tens volts to 120-150 V. The mass of the devices (in common with the magnetic system) lies in the ranges from tens to hundreds of gramms. The view of one such 3 cm band device is given in Fig.4.

7. BWO WITH MAGNETIC FOCUSING IN THE MILLIMETER BAND

The series of magnetically focused BWOs continuously covering the whole millimeter and submillimeter band was developed in the USSR to the middle of sixties (Golant et al 1969, Gershenzon et al 1985). However, great weights and overall dimensions of these devices (up to 10 kgr and more) and high supply

voltage (up to 5-6 kV) hampered and in some cases eliminated the possibility of their using.

A main direction of BWO miniaturization at the given magnetic field strength is connected with the magnetic gap decreasing and with BWO axial length reduction. This effect is achieved due to the application of the multiset slow-wave structure allowing to increase an interaction space, to lower the operating current density in the electron beam and to reduce electron pulsations induced by the space charge. The application of the compact electron gun with divergent optics providing small radial electron velocity components at the input into the interaction space also contributes to the lowering of the longitudinal length.

Naturally, the mm band BWO miniaturization required in the main new structural-technological solutions. Thus:

- construction and electrospark fabrication method of the multiset systems of the type "contrary pins", "comb" and others with a structure step up to 20 mkm was developed;
- high emission cathode-heated units with a small heating time and the current densities of tens and hundreds A/cm² in a continuous mode were created;
- miniaturized wide band constructions of the vacuum-tight energy outputs with small reflections and losses were developed.

As a result the set of the miniaturized BWOs with magnetic focusing was created which continuously cover the mm band from 36 to 260 GHz. The typical parameters of these devices are presented in the table 2. The view of device is shown in Fig.5.

Table 2 PARAMETERS OF MILLIMETER BAND BWO

	Operating frequency range	Minimal output power	Slow-wave struc- ture voltage
	GHz	mW	V
BWO-1	36- 55	40	400-1200
BWO-2	52- 79	30	400-1200
BWO-3	78-119	20	500-1500
BWO-4	118-178	15	500-1500
BWO-5	177-260	10	700-1800

Output power overfall in the operating range is not more than 6 dB, actuation time is 1-3 s, device mass is 1 kgr and 1.5 kgr for BWO-5, slow-wave structure current is 20 mA, the devices do not require a forced cooling.

For the present time the work on BWO minimization in the direction of the transition into the submillimeter wave length band is continued.

8. VACUUM INTEGRAL MICROCIRCUITS

The film vacuum integral circuits (VIC) performed after the

group technology are based on physic-technological methods of the growth of precision dielectric microstructures from aluminium-oxide ceramic. The VIC design principle is shown in Fig.6a. The microtriode is realized on two substrates on one of which a planar cathode-heating and on the other an anode-grid units are placed. The planar thermocathodes are performed in the form of the heater film on one substrate side and of the base with the active coating on the other one. The anode-grid unit substrate contains a formed space with cantilever sheds. The metal film on the cantilever forms a slotted control electrode ("grid").

The microdevices of the tetrode and pentode types are created by analogy with the triode (Fig.6b).

The shown diagrams of the microdevice construction on different levels allow to realize several variants of the specific integral volume circuits with a high integration level: triggers, multivibrators and also amplifiers and self-excited oscillators at the frequencies up to 150 MHz. These circuits are encapsulated in vacuum-dense metal-ceramic cases and maintain their efficiency at the ambient temperature of 770°K. Their durability exceeds 2000 hours.

9. CONCLUSION

Obtained results required creation of the corresponding technological base, new materials, special equipment and technological processes. Developed devices found wide practical application.

- Alexeenko A M 1968a Int.Conf.on MW and Opt.Generation and Amplification (Hamburg) Band 35
 Alexeenko A M et al 1968b UK Patent N 1227622, filed 8.04.68
 Gershenzon Ye M et al 1985 BWOs of mm and submm Wave Bands (Moscow: Radio i svyaz)
 Golant M B et al 1969 Pribori i tehnika experimenta (USSR) 3 231
 Golant M B, Bobrovsky Yu L 1983 Minitrans (Moscow: Radiosvyaz)
 Gulyaev Yu V, Sinitsyn N I 1988 Techn.Progr.1st Int.Vac.Microelectron.Conf. (Williamsburg) p 9-1
 Shevchik V N et al 1975 Electronics of BWOs (Saratov: Univ. Ed.) pp 102-134
 Sinitsyn N I, Popchenko Yu N 1976 Izv.VUZov, Radioelektronika (USSR) XIX 49

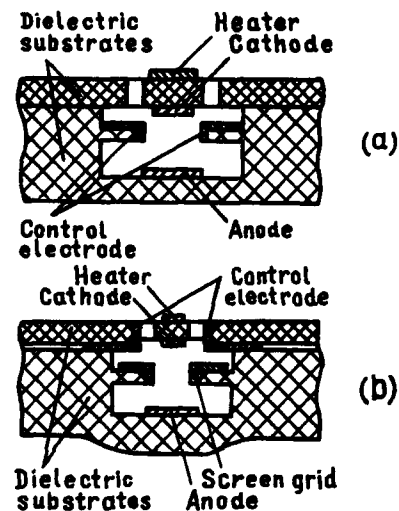


Fig.6. Schematic diagram of the microtriode (a) and microtetrode (b)

Micro-cavity integrable vacuum devices and triodes

William J. Orvis, Charles F. McConaghy, Dino R. Ciarlo, Jick H. Yee, Ed W. Hee

Lawrence Livermore National Laboratory, P.O. Box 5504, L-156, Livermore, CA, 94550, USA

Charles E. Hunt, Johann Trujillo

EECS Dept., University of California, Davis, CA 95616, USA

ABSTRACT: We are developing miniature, vacuum, field emission diodes, and triodes for use in electronics in hazardous environments. We have produced the structures for micrometer sized diodes and triodes. We are currently improving the emission rate of the field emission electron source, before inserting it into the diode and triode structures.

1. INTRODUCTION

Miniature vacuum diodes and triodes are micrometer sized, silicon, electronic switching and control devices with a vacuum as the active volume instead of silicon. They are fabricated on silicon wafers using much the same processing techniques as are used for solid-state integrated circuits, making them completely compatible with existing integrated circuit technology. This makes possible the eventual integration of miniature vacuum tubes with existing integrated circuit components. We use the sacrificial layer technique to produce the free standing structures (Orvis 1989).

2. FABRICATION OF A VACUUM TRIODE

First, coat the surface (100) of the silicon wafer with an isolation layer consisting of 0.5 μm of silicon dioxide and 0.4 μm of silicon nitride. Create the field emitters with an anisotropic etch behind a square mask of silicon nitride 800 Å thick. Fill the cavity containing the field emitter with low density glass and reflow the glass to planarize it. Pattern a layer of doped polysilicon to create the grid structure. Bury the grid structure in more low density glass. Pattern another layer of doped polysilicon to form the anode. Finally, remove the low density glass using hydrofluoric acid. The resulting structure, with the free standing anode and grid, is shown in Figures 1, and 2.

Figure 3 shows a vacuum diode with the anode structure broken loose and flipped over. The vacuum diode is a simple variation of the triode design, which leaves out the polysilicon grid.

3. TESTING AND PROBLEMS

Progress in this project has been delayed by seemingly minor processing problems that often required a complete rebuilding of the device to correct. Most of the processing problems are related to the sacrificial layer technique, and the long etch times associated with it. First, we had adhesion problems of the photoresist on the glass layers. The photoresist would come loose at the edges and allow etching to go on beneath it. We corrected this problem by using patterned chrome as a mask for the glass.

* This work was performed under the auspices of the U.S. Department of Energy by the Lawrence Livermore National Laboratory under contract No. W-7405-Eng-48.

Next, the silicon dioxide isolation layer under the bond pads was damaged by the long processing times for the sacrificial layer. When wires were attached to the pads, they tended to short to the substrate. We changed the isolation layer to silicon nitride, but Frenkel-Poole conduction in the silicon nitride obscured any field emission (Sze 1981). Frenkel-Poole conduction in silicon nitride is difficult to tell from field emission by the shape of the current versus voltage curve. However, it can be identified by the fact that it is bidirectional and temperature sensitive.

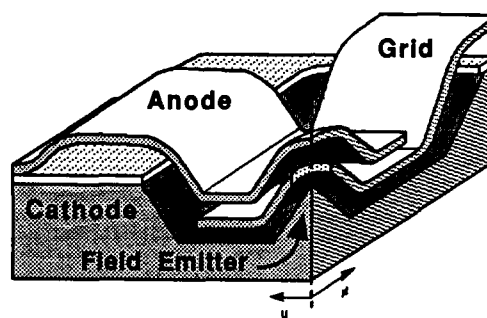


Figure 1 A cutaway section of the vacuum triode showing the field emitter, grid and anode.

We corrected this problem by first coating the wafer with silicon dioxide ($0.5\ \mu\text{m}$), and then with silicon nitride ($0.4\ \mu\text{m}$). Bond pads placed over this isolation layer can now withstand wirebonding without shorting and can hold off over 500 V without breaking down.

Our next problem involved shorting of the anode structure to the cathode due to electrostatic attraction. We applied 300 V across a vacuum diode and observed anomalous currents that would erratically turn on and off. It turns out that the electrostatic attraction between the anode and the substrate was sufficient to bend the anode down until it touched the substrate, causing a short and also collapsing the field. When the field collapsed, the anode would spring back and break the connection, creating the switching of the current.

There are two ways to correct this problem, the first is to stiffen the anode structure, and the second is to make the field emitters operate at a lower voltage. We are stiffening the anode by thickening it, and are currently working on the emission rate of our field emitters.

From discussions with other researchers, it appears that our field emission tips need to be sharper by a factor of about 2. Initially, we created our tips by anisotropic etching of silicon with ethylenediamine-pyrocatechol-water (EPW). EPW is hard to control, and resulted in tips with a radius of curvature on the order of $1000\ \text{\AA}$. We have changed to potassium hydroxide buffered

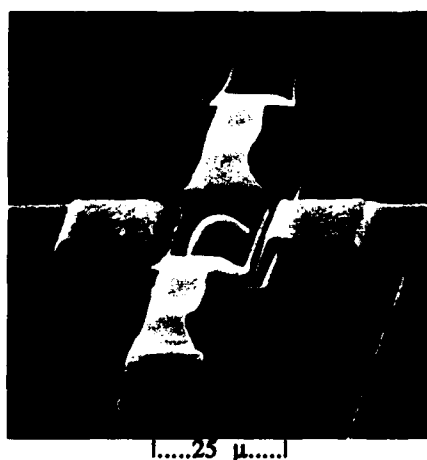


Figure 2. Electron-micrograph of the vacuum triode. the horizontal structure is the grid and the vertical structure is the anode. The field emitter is under the hemispherical section at the center of the anode.



Figure 3 Electron-micrograph of the vacuum diode with the anode broken off and flipped over to show its underside, and the field emitter.

with secondary butyl alcohol, which is slower, but much more controlled, resulting in tips with a curvature of less than 500 Å. Using a field of emitters created with this process, we achieved field emission with an applied voltage of 40 V across a 2 μm vacuum gap (Figure 4).

We are currently undertaking a systematic study of anisotropic etching of (001) silicon with various formulations of potassium hydroxide and water, mixed with alcohol, to obtain field emission points. The results show that uniform arrays of field tips, having eight {331} facets, can be obtained with solutions mixed with secondary or tertiary-butyl alcohols. These results are presented elsewhere (Hunt 1989).

We are applying these eight-sided field emission tips to the new dimpled diode structure, shown in Figure 5. The point is overcoated with a 1 μm sacrificial layer of spin-on glass. The glass is thinned, or dimpled over the tip and then the structure is overcoated with evaporated tungsten. After the tungsten is patterned to become the anode and the interconnect/pad layer, the glass layer is removed completely, leaving an air-bridge structure. Because the thinning of the glass can be controlled with precision, using reactive ion etching, the final cathode-anode spacing is uniform across the entire wafer and can be changed, if desired, without requiring a new mask.

4. MODELING

Using the combination of a two-dimensional static field modeling code, and the theoretical Fowler-Nordheim equation, we have estimated the operating characteristics of our vacuum triode (Figure 6). The curves were created by fitting the field at the tip of the field emitter, calculated with the static field modeling code, versus the voltage on the anode and grid. The resulting equation is inserted into the Fowler-Nordheim equation to calculate

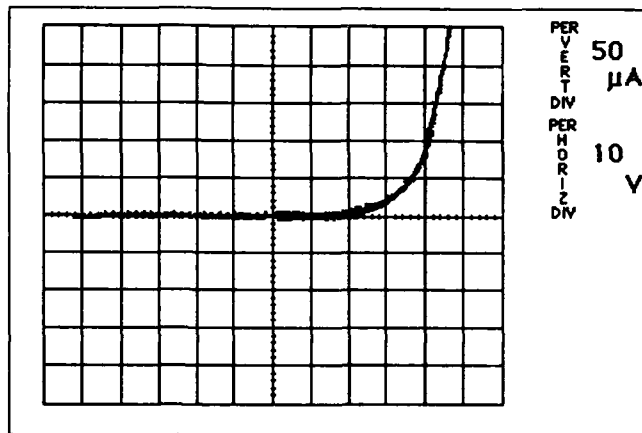


Figure 4 Current versus voltage curves for a field of 10,000 to 15,000 field emitters spaced two micrometers from an anode.

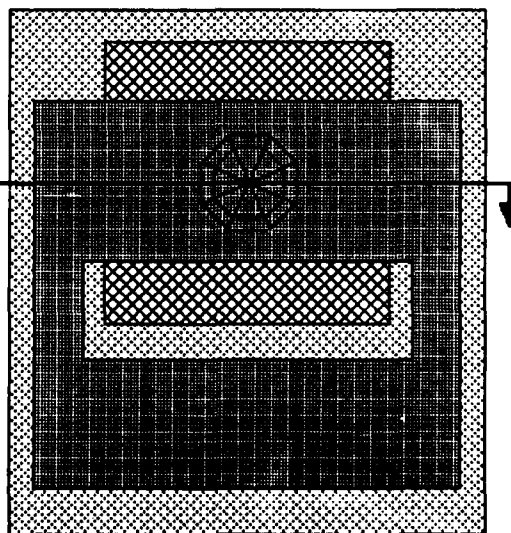
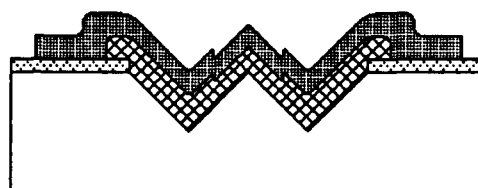


Figure 5: Cross section and top view of the dimpled diode structure.

the current-voltage characteristics. By taking the appropriate derivatives of the current-voltage curve (see Orvis 1989), we obtain the tube parameters. Note that these tube parameter values are not typical of those expected from more traditional vacuum tubes. The plate resistance is high, the transconductance is low, and the static gain is low. These differences must be taken into account when designing circuits for these devices.

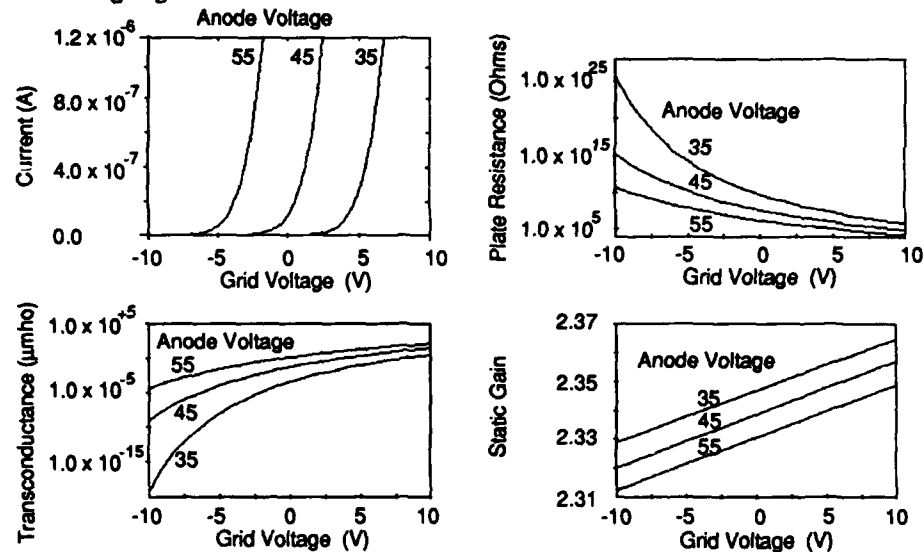


Figure 6 Theoretical current-voltage, plate resistance, transconductance and static gain curves for the miniature vacuum triode. These assume a 1.5 micrometer anode to cathode distance, the tip of the cathode is centered in a 1 micrometer radius hole, and even with the top of the grid, the emission area is 0.2 micrometers in diameter and the field at the tip has an additional enhancement factor of 20 due to microstructure on the tip.

5. CONCLUSION AND PLANS

We have completed the structures for a field emission diode, and triode, and are currently enhancing the field emission rate of our field emitters. When we are satisfied with the emission rate, we will insert the field emitters into our diode and triode structures, and evaluate the performance of the resulting devices. We are also considering a new anode structure that will allow more precise control of the anode to cathode spacing.

6. REFERENCES

- Hunt C. E., Trujillo J., Ciarlo D. R., Orvis W. J. 1989 "Silicon Field Emission Points for Vacuum Microelectronics Formed by Anisotropic Etching", submitted to *J. Electrochemical Soc.*
- Orvis W. J., McConaghy C. F., Ciarlo D. R., Yee J. H. and Hee E. W. 1989 "Modeling and Fabricating Micro-Cavity Integrated Vacuum Tubes", to be published in the *IEEE Transactions on Electron Devices part 2*
- Sze S.M. 1981, *Physics of Semiconductor Devices*, John Wiley & Sons, New York, pp. 402-7

Electromagnetic properties of a field emission distributed amplifier

Purobi M. Phillips*, Sidney T. Smith and Henry F. Gray.

Naval Research Laboratory, Washington D.C., U.S.A. * Science Applications International Corporation, Mclean, Va, U.S.A.

ABSTRACT: The basic idea and the design parameters of a fully Distributed Field Emitter Amplifier are described.

1. INTRODUCTION

The performance of many microwave and millimeter-wave devices can be improved significantly by using field-emitting arrays. The high-current density and low transit time of field emitter arrays make possible high-frequency, high-power triodes, better density-modulated klystrones, small and wide-band TWT's and wide-band, high-frequency, high-power, compact (magnet-less), radiation-hard distributed amplifiers. The idea of Distributed Amplification was first proposed by W. S. Percival in 1936¹ and the name "Distributed Amplifier" was due to Ginzton *et al.*² The present paper describes a continuously distributed amplifier using field emitters.

2. CONFIGURATION AND BASIC MECHANISM

The FEDA (Field Emission Distributed Amplifier) consists of two physically bonded, but electrically independent, parallel microstrip-like transmission lines, one lying parallel to and directly over, the other (figure 1).

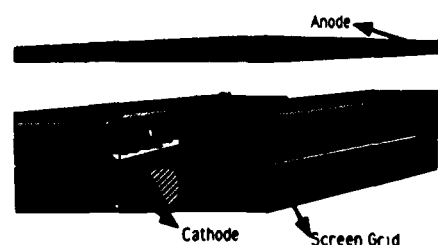


Figure 1. Field Emitter Distributed Amplifier

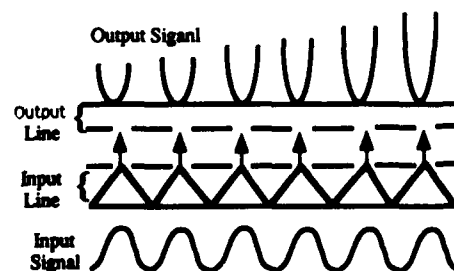


Figure 2. Basic Mechanism of a FEDA

The input line contains the wedge-like field emitters. A "grounded-grid" or "grounded-gate" triode distributed amplifier is not practical because the input signal must drive the cathode against the anode current, and this results in an excessive load ($1/g_m$) in the input circuit, where g_m is the transconductance. Therefore, a tetrode type of distributed amplifier design has been chosen. The screen-grid is AC grounded to shield the input from capacitively coupling to the output and thus avoid feedback oscillation. The width of the first grid is chosen to be smaller than the screen grid to minimize the capacitance between this and the cathode base.

The applied input signal produces a travelling-wave density-modulated signal that induces a similar amplified density-modulated signal on the output transmission line. Figure 2 demonstrates this mechanism in an exaggerated form. The input signal is applied at one end of the input transmission line, and the other end is terminated in a non-reflecting resistive load. The output transmission line serves as the electron collector and/or anode. This type of FEDA requires that the phase velocity in the input and the output transmission lines to be identical because the induced output travelling wave must be phase-matched with the input travelling wave. This phase-match is proposed to achieve by dielectrically loading the output line. Thus, the output line contains the anode, a layer of dielectric and a grounded heat sink. The output and input transmission lines were modelled macroscopically to determine the degree of match. The next section contains the results of these modellings as well as other design parameters.

3. CIRCUIT DESIGN

Four different output line structures were tested. Figure 3 shows the different dimensions of these structures. The dielectric used was styrcast with a dielectric constant of 9 to simulate BeO or Al_2O_3 .

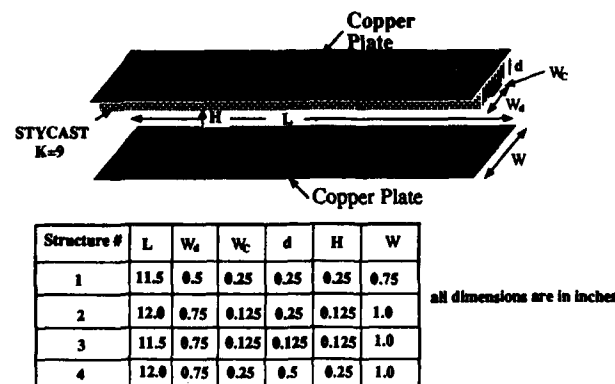


Figure 3. Modelling of Output Line.

Figure 4 (a, b, c, and d) shows the results of these preliminary tests along with theoretical values. The theoretical points were obtained from a 2-dimensional code for microstrip line that uses the full-wave analysis. It is to be noted that in a microstrip line the lowest order mode is the TM_0 which has a zero frequency cutoff. The next higher order mode is a TE mode with a divergence frequency f_c , below which it cannot exist (figure 5³). This divergence frequency f_{cTE} is calculated for all four structures tested and it can be seen that the agreement between the experimental points and the theory is quite good below this frequency as the theory does not include this TE mode. It is concluded from these tests that it is possible to slow the phase velocity in the output line sufficiently by dielectric loading to match the phase velocity of the dielectrically-loaded input line.

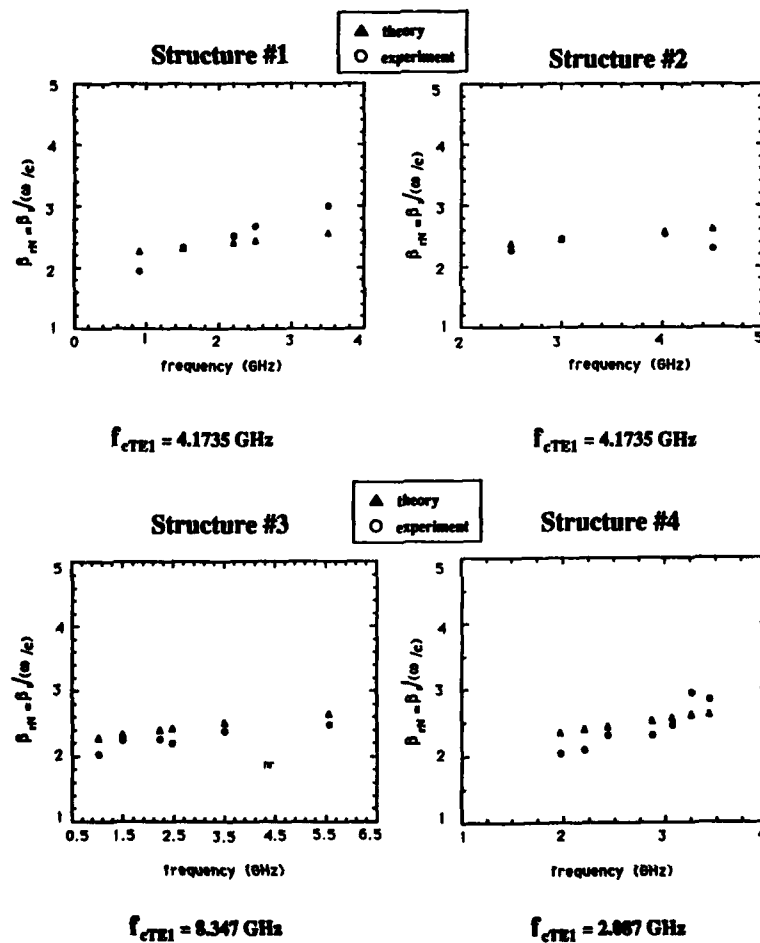


Figure 4. Dispersion in Output Line.

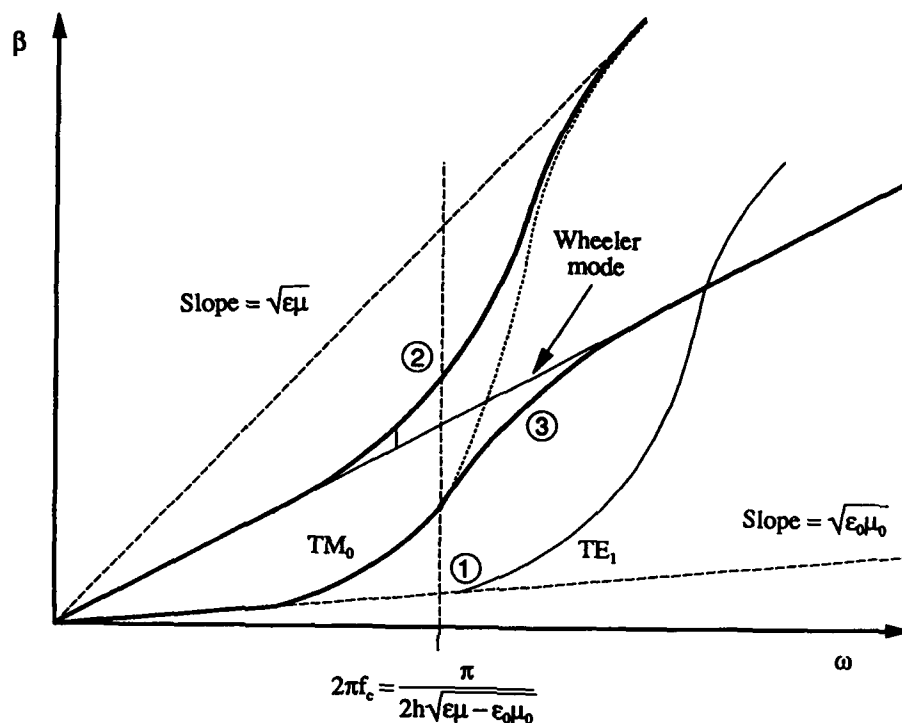


Figure 5. $\beta - \omega$ Diagram for Microstrip
and Surface Wave Modes.

To find the parametric dependence of output-line-impedance and the phase velocity, the simple, quasi-static microstrip line theory was used. Figure 6 shows the results. The critical parameter for the loss in the output line appears to be the air(vacuum) gap. The loss increases as the gap decreases, so the loss was calculated for a small value of this gap ($5\mu\text{m}$) as a function of frequency by again treating the output line as a microstrip line (Figure 7).

The input line was modelled (Figure 8a) to find the dispersion characteristics. Figure 8b shows the result. In order to find the loss in the input line it was treated as a covered stripline, and Figure 9 shows that for high frequency operation (50 GHz) and with all other parameters fixed, the cathode has to be tall ($8\mu\text{m}$).

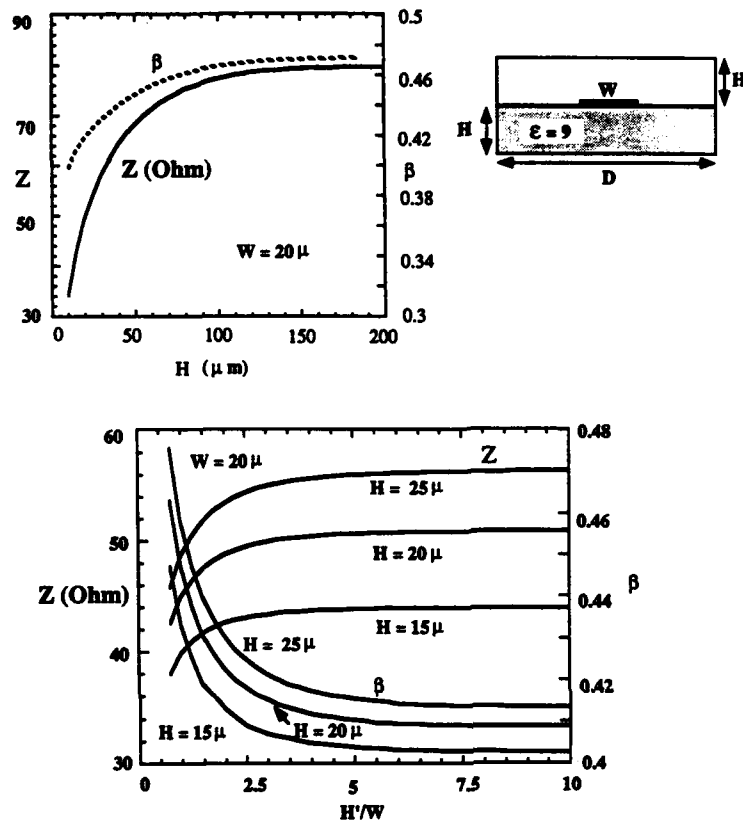


Figure 6. Scaling of Output Line.

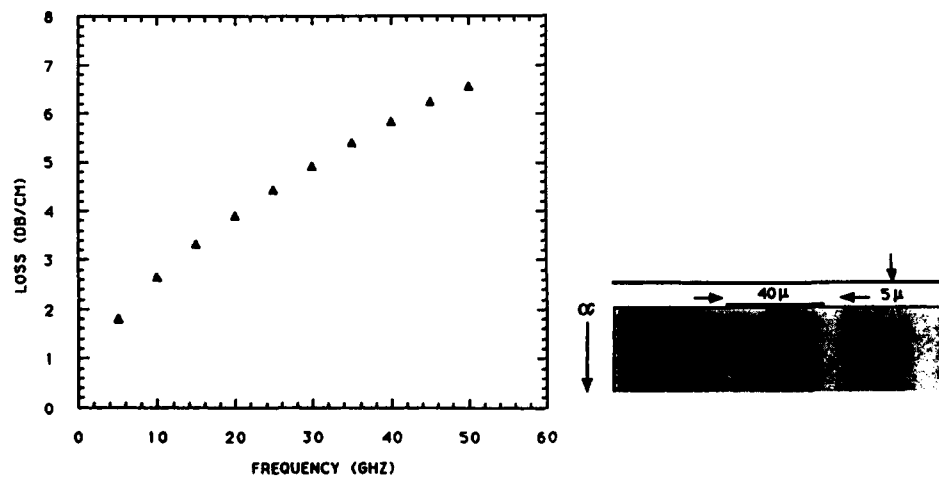


Figure 7. Output Line Loss.

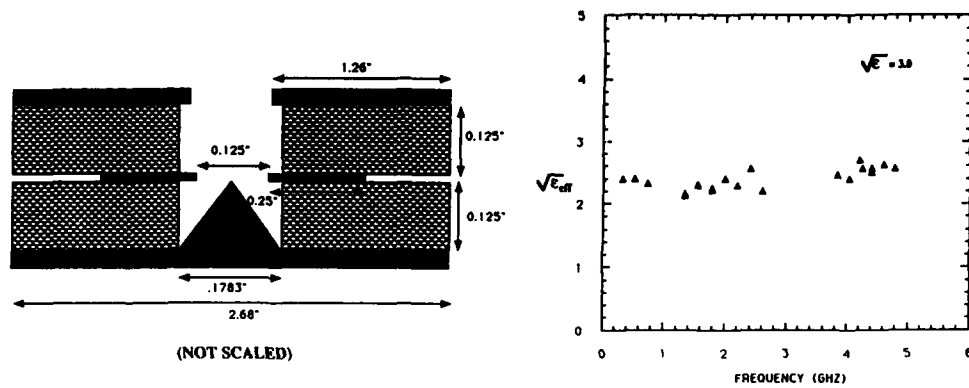


Figure 8. Modelling of Input Line.

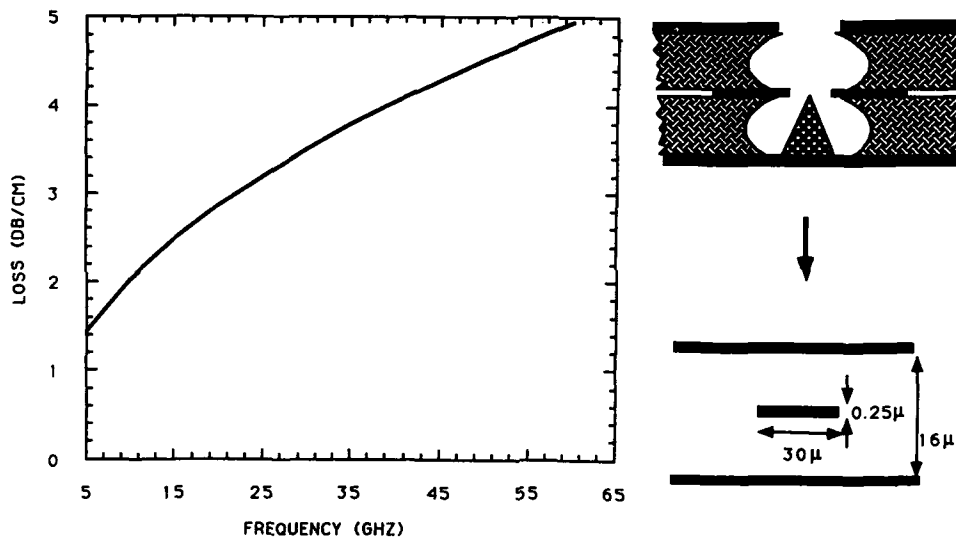


Figure 9. Input Line Loss.

4. ACKNOWLEDGEMENT

The authors gratefully acknowledge constant helpful discussions and stimulating interactions with their co-workers Robert E. Neidert and Achintya K. Ganguly.

5. REFERENCES

1. W. S. Percival, *British Patent Specification* No. 460, 562, July, 1936.
2. E. L. Ginzton *et al.* *Proceedings of the I. R. E.*, pp. 956-969, August, 1948.
3. C P. Hartwig *et al.* *G-MTT Int. Microwave Symp. Digest, Detroit, Michigan*, pp. 110-116, 1968.

Frequency limits of electronic tubes with field emission cathodes

Weston A. Anderson

Varian Associates, 611 Hansen Way, Palo Alto, CA 94303 U.S.A.

ABSTRACT: The gain-bandwidth product of vacuum microelectronic triodes with field-emission cathodes is analyzed. The Fowler-Nordheim field emission equations permit calculation of the transconductance, g_m , of a triode; capacitance can be estimated from the geometry. Using reasonable geometry for the field emitter tip yields cutoff frequencies in the GHz region, which is less than that achieved from III-V semiconductor devices. Using literature values for the current-voltage relationship of typical field emitters yields cutoff frequencies in the MHz region. The gain-bandwidth and cutoff frequencies, f_T , of both vacuum and solid state devices reach an asymptote as the dimensions are reduced with solid state devices having the higher f_T .

1. INTRODUCTION

High speed is an advantage often cited (Gray et al, 1986) for electron tubes with field emission cathodes because the electron velocity in vacuum is only limited by the velocity of light whereas the saturation drift velocity in solid state devices is limited to less than 5×10^7 cm/s. To overcome this limit solid state devices have continued to be scaled down in size with device dimensions now in the sub-micrometer range. With feature sizes in this range current solid state devices are achieving amplification at frequencies in the 100 GHz region. (Y-K. Chen et al, 1989; Wang et al 1989a,b,c). The gain-bandwidth for both field emission devices and solid state devices is not only limited by transit times but by the electrode capacitance and other factors. Electrical breakdown due to the high electric fields near the field emitter tip and Joule heating of the tip limit the maximum voltage and current and thus the transconductance, g_m , of a vacuum microelectronic tube. Another limiting factor can be the heat loading on the anode produced by the stopping of the electron beam by the anode.

2. FIELD EMISSION EQUATIONS

The Fowler-Nordheim theory (Dyke & Dolan, 1956) relates the field emission current density, J in amps/cm², to the electric field, F in volts/cm, at the surface of the field emitter tip.

$$J = 1.54 \times 10^{-6} \{ F^2 / \phi r^2(y) \} \exp \{ -6.83 \times 10^7 \phi^{3/2} v(y) / F \}$$

where ϕ is the work function in eV. Spindt et al (1976) have shown that to a good approximation $r^2(y) = 1.1$ and for $y^2 < 0.95$, $v(y) = 0.95 - y^2$, else $v(y) = 0$, where $y = 3.79 \times 10^{-4} F^{1/2} / \phi$.

The total current, I in amps, emitted by the field emitter tip is proportional to the effective tip area, α in cm², and the electric field, F , is proportional to the voltage difference, V in volts, between the tip and surrounding electrodes, i.e. $I = \alpha J$ and $F = \beta V$. With these substitutions one can put the Fowler-Nordheim equation into the following form:

$$\log_{10}(I / V^2) = -5.85 + 4.26 / \phi^{1/2} + \log_{10}(\alpha \beta^2 / \phi) - 2.82 \times 10^7 \phi^{3/2} / (\beta V)$$

By plotting $\log_{10}(I/V^2)$ vs $1/V$ one obtains a straight line as observed by Spindt et al (1976). From the slope of this line one can determine β , and from the intercept one obtains $\alpha\beta^2$.

3. THE GAIN-BANDWIDTH PRODUCT

The gain-bandwidth product is just g_m/C , where the transconductance, g_m , is measured in siemens, and C is measured in farads. The cutoff frequency, f_T measured in Hz, is just $f_T = g_m / (2\pi C)$. Actual measurements of f_T or the gain-bandwidth product of a field emitter vacuum microelectronic tube have not appeared in the literature. One can estimate g_m from the I-V relationship given by the Fowler-Nordheim equation. It is assumed that the field at the emitter tip is essentially controlled by the grid, and that the anode is well screened from the field emitter tip. In this case the transconductance of a triode is given by $g_m = dI/dV$.

Under normal "low temperature" conditions with $\phi > \phi_i$

$$g_m = 1.4 \times 10^{-6} \alpha \beta (F/\phi) [2 + 6.49 \times 10^7 \phi^{3/2} / F] \exp\{-6.49 \times 10^7 \phi^{3/2} / F + 9.81 / \phi^{1/2}\}$$

Under sufficiently strong electric fields, the surface potential barrier is depressed below the Fermi level causing a strong increase in current from the field emitter. Under this condition, small changes of the potential are less effective in controlling the current with the result the g_m shows a sharp drop. This condition occurs when $\phi < \phi_i$ where $\phi_i^2 = 1.51 \times 10^{-7} F$, with $g_m = 2.8 \times 10^{-6} \alpha \beta F / \phi$.

The output current must drive the output capacitance of that stage and the input capacitance of the next stage. The capacitance is estimated for a single device, length L on a side, with the grid separated from the cathode plane by height H , and the anode plane a distance H above the grid plane. The capacitances are estimated by assuming 20% of the space between the grid and anode is filled with dielectric, and 50% of the space between the cathode plane and the grid plane. The anode capacitance, $C_a = (0.2k + 0.8)\epsilon_s L^2 / H$, and the grid capacitance C_g is given by $C_g = (0.5k + 0.5)\epsilon_s L^2 / H$. Here the dimensions are given in cm and the constant $\epsilon_s = 8.86 \times 10^{-14}$ farads/cm. The dielectric constant $k = 3.9$ for silicon dioxide, the usual insulating material. The total capacity driven by the anode is just $C = C_a + 2C_g$. The cutoff frequency $f_T = g_m / (2\pi C)$.

The total power density, P_d in watts/cm², dissipated by the anode is $P_d = IV / L^2$. Temperature rise in the cathode tip and stem is proportional to the product I^2 and the resistivity of the material. Under the conditions reported the temperature rise at the tip never exceeded 200°C.

A simple program was used to numerically calculate I , V , g_m , f_T and P_d for various values of α , β , and the electric field, F , at the tip. In this analysis $v(y)$ was determined from the tables of Burgess & Kromer (1953). For an initial estimate, the values of α and β were related directly to the radius of curvature, R_0 , of field emitter tip. Choosing $\alpha = R_0^2$ corresponds to limiting the effective emitting region of the tip to a polar angle of about 32°. Choosing $\beta = 1/R_0$ assumes the field gradient is the same as would be obtained from a section of a small isolated sphere of radius R_0 . With the parameters $R_0 = 4 \times 10^{-6}$ cm, $H = 0.75 \mu\text{m}$, and $L = 2.6 \mu\text{m}$ the values of V , I , g_m , and f_T were calculated, Table I. The work function $\phi = 4.35$ for molybdenum and a work function $\phi = 3.0$ corresponds to the case yielding a local maximum of g_m for an electric field strength $F = 6 \times 10^7$ volts/cm.

4. EXPERIMENTALLY DETERMINED PARAMETERS

As described above one can obtain α and β from graphical plots of I/V^2 vs $1/V$ or directly from numerical data assuming that it obeys the Fowler-Nordheim equation. With two data pairs $I_1 V_1$ and $I_2 V_2$, one can find β and α as follows:

$$\beta = 6.49 \times 10^7 \phi^{3/2} \{1/V_2 - 1/V_1\} / \{\ln(I_1/V_1) - \ln(I_2/V_2)\}$$

$$\alpha = 7.14 \times 10^5 (\phi/\beta^2) (I_1/V_1^2) \exp\{(6.49 \times 10^7) \phi^{3/2} / (\beta V_1) - 9.81 / \phi^{1/2}\}$$

Data from Fig. 4 of Spindt et al (1986) was used to determine α and β of two field emitter arrays. Although the spacing of the emitter arrays corresponded to $9.1 \mu\text{m}$, Spindt, et al (1986) indicated with their advanced technology a spacing of $2.6 \mu\text{m}$ could be achieved. Using $H=0.75 \mu\text{m}$ and $L=2.6 \mu\text{m}$, Table II was generated. The two devices had a tip radius $R_t = 4 \times 10^{-6} \text{ cm}$ leading one to expect that the effective areas of the emitting tips would be about $1.6 \times 10^{-11} \text{ sq. cm}$. The effective areas, α , are factors of 340 and 82 times smaller than this. Spindt et al (1976) postulate that the small effective area must be due to protuberances on the tip of the field emitter. Insulating microstructures on the field emitting area as described by Latham (1988) and Bayliss and Latham (1986) may also play a role in producing small emitting areas. It is this very small effective area that causes the discouraging low values of the cutoff frequencies.

5. CONCLUSIONS

The maximum g_m from a field emitter triode is obtained with the maximum electric field strength at the tip, generally in the range of 4×10^7 to $6 \times 10^7 \text{ v/cm}$. Alpert et al (1964) have surveyed the literature in electrical breakdown phenomena in high vacuum systems. They have shown that breakdown occurs when the electric field strength on the cathode reaches approximately $6.5 \times 10^7 \text{ v/cm}$. The field strength may vary greatly over the surface of the cathode due to conditions such as insulating microstructures and local protuberances such as whiskers. The slope of the Fowler-Nordheim curves yield the field strength at the cathode where the electron emission is taking place. Thus the g_m values in Tables I and II for the field strength of $8 \times 10^7 \text{ v/cm}$ is certainly an upper limit.

Paralleling a large number of devices in an array increases the g_m and the capacitances so that f_T remains unchanged. Reducing the effective radius of the field emitting tip will proportionately reduce the g_m and f_T . Reducing the lateral spacings and the lateral dimensions of the tip will correspondingly increase f_T . This cannot be carried very far, however, as it will make the structures more unstable and also increase the tip inductance which will ultimately hurt the high frequency response. Reducing all dimensions, including the tip size, will leave f_T unchanged, however it may be beneficial because the effective tip emitting areas are much smaller than the actual tip areas. To increase the g_m one should try to eliminate insulating microstructures, whiskers and protuberances so that electron emission would take place over the maximum tip area. One should also look for materials and tip treatments that will yield a work function slightly greater than ϕ_1 as defined above.

Current FETs made with III-V semiconductor have submicrometer dimensions and have cutoff frequencies, f_T , near 100 GHz. Wang et al (1989b) have reported that the saturation velocity v_s for GaAs MESFET is $1.5 \times 10^7 \text{ cm/s}$ for a gate length, L_g , of $0.3 \mu\text{m}$, leading to an upper frequency limit of $v_s / (2\pi L_g) = 80 \text{ GHz}$. With $L_g = 0.1 \mu\text{m}$, operation at 240 GHz is projected. Mishra et al (1988) have reported $f_T = 170 \text{ GHz}$ in a HEMT device with a gate length $L_g = 0.1 \mu\text{m}$. With an upper limit of saturation velocity $v_s = 5 \times 10^7 \text{ cm/sec}$ and $L_g = 0.1 \mu\text{m}$ yields an upper frequency limit of 800 GHz. For a fixed gate length of an FET, the g_m is proportional to its width and the gate capacitance is also proportional to the width. Scaling in the length direction will have a much smaller effect on either the g_m or the gate capacitance. Since the gate capacitance predominates we have neglected the drain-gate and the drain-source capacitances. Thus to the extent that the upper frequency depends upon capacity, and not transit time, the cutoff frequency becomes nearly independent of the transverse dimensions. To the extent the voltage scales with thickness and the gate capacitance inversely with the thickness, the g_m and the f_T will be approximately independent of size.

Within the approximations made in this analysis the limits that set the upper frequency capabilities of the of current solid state devices far exceeds those of vacuum microelectronic triodes, and it appears that in the limit of small dimensions the solid state devices will maintain their lead in high frequency capabilities. In both cases sufficiently small structures must be used to avoid electron transit effects, and in both cases distributed amplifier techniques may be used to increase the capabilities of amplifiers made with these devices.

Schematic of a Field Emission Microtriode Array Model

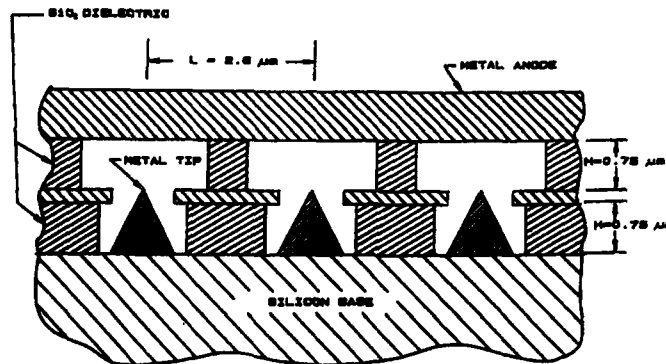
used in the Analysis of g_m , C and f_T .

TABLE I.

ϕ eV	F V/cm	V volts	I amps	g_m siemens	f_T MHz	Pd W/cm ²
4.35	4E+7	160	4.5E-7	4.7E-8	1.8E+1	1.1E+3
	6E+7	240	1.3E-4	6.1E-6	2.4E+3	4.5E+5
	8E+7	320	2.3E-3	6.6E-5	2.6E+4	1.1E+7
3.0	4E+7	160	7.4E-4	4.6E-5	1.8E+4	1.8E+6
	6E+7	240	2.2E-2	6.3E-4	2.5E+5	7.8E+7
	8E+7	320	4.8E-2	3.0E-4	1.2E+5	2.3E+8

Calculated values for the parameters of a field emission triode with $R_c = 4 \times 10^{-6}$ cm, $H = 0.75 \mu\text{m}$ and $L = 2.6 \mu\text{m}$. It is assumed $\alpha = R_c^2$ and $\beta = R_c^{-1}$. The work function $\phi = 4.35$ eV for molybdenum, and $\phi = 3.0$ eV corresponds to a local maximum g_m for $F = 6 \times 10^7$ volts/cm.

TABLE II

Sample Ref. No.	F V/cm	V volts	I amps	g_m siemens	f_T MHz	Pd W/cm ²
28C-189-8B	4E+7	54	1.3E-9	4.2E-10	1.6E-1	1.1
	6E+7	82	3.7E-7	5.3E-8	2.1E+1	4.5E+2
	8E+7	109	6.9E-6	5.7E-7	2.2E+2	1.1E+4
28C-189-8N	4E+7	20	5.5E-9	4.6E-9	1.8E+0	1.6
	6E+7	30	1.5E-6	5.9E-7	2.3E+2	6.9E+2
	8E+7	40	2.9E-5	6.4E-6	2.5E+3	1.7E+4

Calculated values for the parameters of a field emission triode using α and β values determined from Spindt et al (1986) and using $\phi = 4.35$ eV, $R_c = 4 \text{E-}6 \text{cm}$, $H = 0.75 \mu\text{m}$, and $L = 2.6 \mu\text{m}$. All values have been normalised to refer to a single device. It has been assumed that all devices of the array provide approximately the same contribution. Sample 28C-189-8B ($\alpha = 4.7 \text{E-}14 \text{cm}^2$, $\beta = 7.3 \text{E+}5 \text{cm}^{-1}$). Sample 28C-189-8N ($\alpha = 1.96 \text{E-}13 \text{cm}^2$, $\beta = 2.0 \text{E+}6 \text{cm}^{-1}$).

6. REFERENCES

- D. Alpert, D. A. Lee, E. M. Lyman, & H. E. Tomaschke, *J. Vac. Sci. Tech.*, 1, 35, 1964.
K.H. Bayliss & R.V. Latham, *Proc. Roy. Soc. Lond. A*403, 285, 1986.
R.E. Burgess & H. Kromer, *Phys. Rev.* 90(4), 515, May 15, 1953.
Y-K. Chen, R. N. Nottenburg, M. B. Panish, R. A. Hamm & D. A. Humphrey, *IEEE Electron Device Letters*, 10(6), 267, 1989.
H. F. Gray, G. J. Campisi, & R. F. Green, *IEDM Technical Digest*, p. 776, 1986.
R.V. Latham, *IEEE Trans. Elect. Insulation* 23(1), 9, 1988.
U.K. Mishra, A.R. Brown, S.E. Rosenbaum, C.E. Hooper, M.W. Pierce, M.J. Delancy, S. Vaugn, & K. White, *IEEE Electron Device Letters* 9(12), 647, Dec. 1988.
C. A. Spindt, I. Brodie, L. Humphrey, & E. R. Westerberg, *J. Appl. Phys.* 47(12), 1976.
C. A. Spindt, C. Holland, & R. D. Stowell, 33rd Intl. Field Emission Symp., Fritz-Halber Institut, Berlin, May 1986.
G. W. Wang, M. Feng, C. L. Lau, C. Ito, & T. R. Lepkowski, *IEEE Electron Device Letters*, 10(5), 186, May 1989a.
Ibid, Vol. 10, No. 5, p. 206, 1989b.
G. W. Wang, M. Feng, Y. P. Liaw, R. Kaliske, C. L. Lau, & C. Ito, *IEEE Electron Device Letters*, 10(6), 264, June 1989c.

Theoretical study of a vacuum field effect transistor

Z. H. Huang, P. H. Cutler, T. E. Feuchtwang, and H. F. Gray[†]
Pennsylvania State University, 104 Davey Lab, University Park, PA 16802, USA
[†] Naval Research Laboratory, Washington, DC 20375, USA

The field emitter arrays field effect transistor (FEAFET), a typical vacuum micro-electronic device, is investigated theoretically. The multi-dimensional character of the device is modeled as a cone representing the emitter and two concentric disks each with a hole in the middle for the gate and drain. The potential and electric field are evaluated approximately throughout the space and exactly in the region very close to the tip. The trajectories and the transit time of the electrons from the emitter to the drain are calculated using Newton's equations of motion. The results show that the transit times are of the order of picoseconds, which compare favorably with values predicted by others.

1. INTRODUCTION

Vacuum microelectronics has attracted much attention recently because it has the potential of increasing the operational speed of microelectronic devices and improving their reliability against temperature extremes and radiations. Recently, a vacuum field effect transistor based on Field Emitter Arrays (Spindt 1968) has been fabricated (Gray et al 1987, Campisi et al 1987). The carrier transit time for the device is predicted to be about 1 ps (Gray et al 1987).

The Field Emitter Arrays Field Effect Transistor (FEAFET) has a set of emitter (tip), gate, and drain electrodes separated by distances in the order of μm . Under proper applied voltages, the electrons in the emitter tunnel through the potential barrier into the vacuum and travel to the drain. The purpose of this paper is to study how electrons travel in such a vacuum microelectronic device, specifically, the electron trajectories and the traversal time from the emitter to the drain. In Section 2, we introduce a model which is a reasonable first approximation to the actual device and is tractable either numerically and analytically. The global potential field is then calculated approximately, but the field near the emitter tip is evaluated exactly. The results of the calculations for the trajectories and the transit time show that the model device is capable of operating in the picosecond range. Discussions of the results and the conclusions are presented in Section 3.

2. MODEL, CALCULATIONS, AND THE RESULTS

The vacuum field effect transistor is modeled by three closed-spaced electrodes as is shown in Fig. 1. The emitter is represented by a cone, while the gate and drain are the two concentric circular disks each with a hole in the middle. The electrodes are kept at different voltages, V_e , V_g , and V_d for emitter, gate and drain respectively. The silicon substrate and silicon oxide layer are ignored in this model.

Since the model is cylindrically symmetric, the cylindrical coordinate system (r, z, ϕ) is used with the origin located at the apex of the cone. The inner radii for the gate and drain are denoted as R_g and R_d respectively. The widths of the electrodes are w_e for the emitter,

w_g for the gate, and w_d for the drain.

An analytical solution of the potential field, $V(r)$, for this model geometry is not available. We have used the following scheme to evaluate $V(r)$: The charge density distributions on the electrodes are assumed to be

$$\rho_c(r, z) = \frac{C_1}{(r^2 + z^2)^{0.3}} + \frac{C_2}{(r^2 + z^2)^{0.35}} + C_3 + C_4 \sqrt{(r^2 + z^2)} + C_5(r^2 + z^2), \quad (2.1)$$

for the emitter,

$$\rho_g(r) = \frac{C_6}{\sqrt{r^2 - R_g^2}} + \frac{C_7}{\sqrt{(R_g + w_g)^2 - r^2}} + C_8 + C_9 r + C_{10} r^2, \quad (2.2)$$

for the gate, and

$$\rho_d(r) = \frac{C_{11}}{\sqrt{r^2 - R_d^2}} + \frac{C_{12}}{\sqrt{(R_d + w_d)^2 - r^2}} + C_{13} + C_{14} r + C_{15} r^2, \quad (2.3)$$

for the drain. The coefficients C_1, \dots, C_{15} are to be determined by the boundary conditions, i.e., the applied voltages at the electrodes and the field at infinity, which we have assumed to be zero. The exponents 0.3 and 0.35 are chosen in Eq. (2.1) for the following reasons. For an isolated cone, the charge density diverges as $(r^2 + z^2)$ approaches zero. The exponent v in the diverging term $(r^2 + z^2)^{-v}$ is a function of cone angle θ . It is found numerically that when $\theta = 70^\circ$, $v = 0.32$; therefore, the two values 0.3 and 0.35 are chosen to ensure the required divergence in the charge density and to allow for the possible modification of the divergence due to the other electrodes. For the gate, ρ_g diverges as r approaches R_g or $R_g + w_g$. Again, the diverging terms are chosen so that ρ_g has the correct form when it is an isolated electrode. For similar reasons, the expression for the drain has the form given by Eq. (2.3).

The potential and electric field for a uniformly charged ring can be calculated exactly. Treating the cone and the disk electrodes as superpositions of charged rings, we can evaluate the potential and electric field for the model device if the charge density distributions are known. Hence, the C_i 's in Eqs. (2.1) to (2.3) have to be evaluated first. To determine these coefficients, we choose 20 points on each electrode.

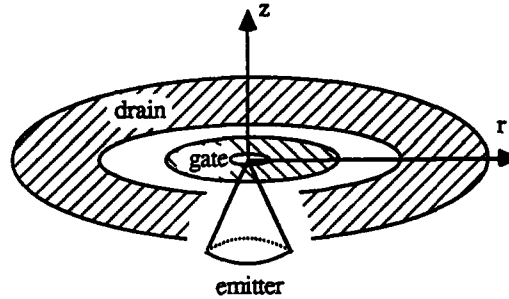


Fig. 1. The model device consists of an emitter, a gate, and a drain.

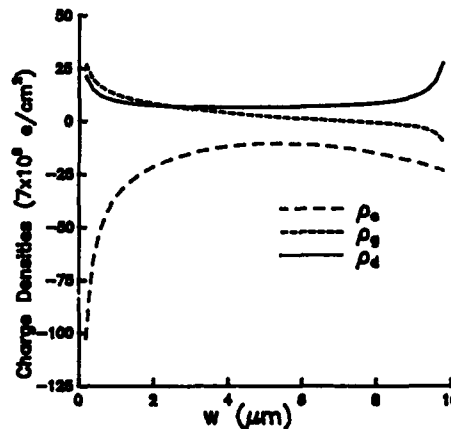


Fig. 2. The charge density distributions on different electrodes.

Since the C_i 's only appear as multiplicative constants, the integrals for $V(r)$ can still be calculated. Hence we obtain a matrix equation

$$AC = V, \quad (2.4)$$

where A is a 60×15 matrix consisting of the integrals of the separate terms in Eqs. (2.1-2.3), C is a 15×1 column matrix consisting of the coefficients, and V is a 60×1 column matrix consisting of the applied voltages on the electrodes. Equation (2.4) was solved to obtain the coefficients for the charge density distributions, which are plotted in Fig. 2.

Once ρ_e , ρ_g , and ρ_c are known, the global potential and the electric field can be determined. As is shown in Fig. 3, the potential changes very rapidly near the tip of the emitter, indicating that the largest fields exist near the apex of the emitter. Since the tunneling and the trajectories are strongly dependent on the field in this region, a detailed analysis is needed to determine the field in the space surrounding the tip.

An exactly solvable model that was used to represent the emitter tip is the sphere-on-orthogonal cone (Hall 1949, Dyke et al 1953). The potential distribution for this model is

$$V_i(R, \theta) = V_{\text{cone}} + (V_g/R_g)(R/a)^{2v+1} R^{-v-1} P_v(\cos \theta), \quad (2.5)$$

where R and θ are spherical coordinates, a is the radius of the sphere, and v is chosen so that the Legendre function $P_v(\cos \theta)$ vanishes on the cone surface. That is, $P_v(\cos \theta_0) = 0$, where θ_0 describes the cone surface. For this problem, we have assigned $V_{\text{cone}} = V_e$, $V_g = V_g - V_e$, and R_g is used as a parameter to match the local field $V_i(r)$ to the global field $V(r)$. Equation (2.5) has the following properties:

$$V_i(a, \theta) = V_i(R, \theta_0) = V_{\text{cone}}, \quad (2.6)$$

and

$$V_i(R_g, \theta) = V_{\text{cone}} + V_g P_v(\cos \theta). \quad (2.7)$$

It is expected that $V_i(R, \theta)$ to be a good representation of the potential near the tip.

With the known fields, Newton's equations of motion can be solved to

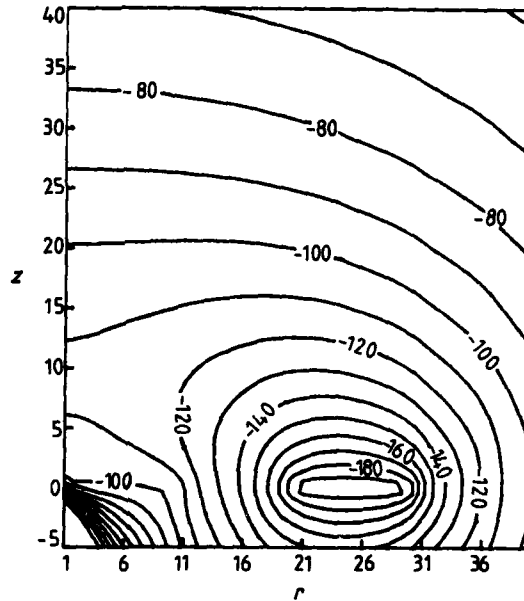


Fig. 3. A cross section of the global potential distribution.

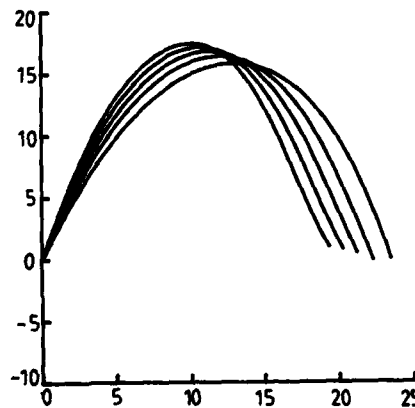


Fig. 4. The electron trajectories from the emitter to the drain for different angles of emission.

obtain the trajectories and transit times for the electrons to travel from the emitter to the drain. When the applied voltages are $V_e=0V$, $V_g=100V$, and $V_d=200V$, it is found that the electrons travel a distance of $\sim 1000 \mu m$ from the emitter to the drain. The corresponding traversal times are of the order of 1 ns. However, if the applied voltages are $V_e=200V$, $V_g=300V$, and $V_d=400V$, the electrons travel a much shorter distance ($\sim 10 \mu m$) to the drain. The trajectories are plotted in Fig. 4 for different angles of emission. The transit time is now about 10 ps. This difference is examined in the following section.

3. DISCUSSIONS AND CONCLUSIONS

As is expected, it is found that the electric field is strong only in the neighborhood of the tip. Far from the tip, the potential varies slowly and approaches $1/r$ as r goes to infinity. When electrons leave the strong field region, they have near maximum velocity in the radial direction. To reach the drain electrode, an electron has to change its initial upward directed velocity to a downward one. If the emitter is grounded, then the potential energy at the emitter has the same value as at infinity (i.e., zero). A moving electron experiences a weak field along that trajectory (excluding the near tip region), which does not significantly change the direction of motion until the velocity of the electron is small enough so that the weak field influences its trajectory. The trajectory resembles half of a long oval with a length of about $1000 \mu m$, and the traversal time of the electron from the emitter to the drain is estimated to be a few nanoseconds. However, when the emitter, the gate, and the drain are biased several hundred volts relative to the ground, the trajectory has a much shorter path. The traversal time is now found to be about 10 ps. That is, the trajectories and hence the transit times are sensitive to the absolute values of the applied voltages.

In the real device (FEAFET), the geometry is much more complicated than our model presented above. The long range Coulomb force may alter the global field and hence the electron trajectories, but the potential field near the tip should not be affected much. Consequently, the conclusion that the electron gains much of its kinetic energy in the near tip region with velocity in the radial direction and that the trajectories and the transit times are sensitively dependent on the absolute values of the applied voltages should still be valid for the real device.

Not included in the analysis is the effect of high electron density or space charge in the vacuum near the tip region. The effect of the repulsive Coulomb interaction in the field emission, or the so-called Boersch effect (Ward et al 1981), on the trajectories and transit times has not been analyzed for this device. A qualitative picture is that the Coulomb repulsion among the electrons repels them away from the symmetry (z -) axis. The transit time should be shorter due to this effect.

* This research was supported in part by the Office of Naval Research, Arlington, Virginia, Contract No. N00014-86K-0160

References:

- Campisi, G. J., and Gray, H. F. (1987) *Mat. Res. Soc. Symp. Proc.* Vol. 76, 67
- Dyke, W. P., Trolan, J. K., Dolan, W. W., and Barnes, G. (1953) *J. Appl. Phys.* 24, 570
- Gray, H. F., and Campisi, G. J. (1987) *Mat. Res. Soc. Symp. Proc.* Vol. 76, 25
- Hall, R. N. (1949) *J. Appl. Phys.* 20, 925
- Spindt, C. A. (1968) *J. Appl. Phys.* 39, 3505
- Ward, J. R., and Seliger, R. L. (1981) *J. Vac. Sci. Technol.* 19, 1082

Appendix

In principle all the charge densities can be represented by power series expansions. However, the series can be truncated after the quadratic term because the densities are not expected to exhibit very pronounced oscillations. The divergent terms, which occur near the edges of the electrodes, are chosen to have the same analytic form as those of the isolated electrodes.

Scaling laws for temporal and spatial dispersions of a short pulse of electrons in a diode in the space-charge regime

C. Girardeau-Montaut*, J.P. Girardeau-Montaut*, H. Leboutet**

* Université Lyon I, 43, bd du 11 novembre 1918, 69622 Villeurbanne, France

** C.E.A., S.P.T.N., B.P. n° 12, 91680 Bruyères-le-Châtel, France

ABSTRACT : The space-charge phenomenon in the diode of a photo-injector induces simultaneously temporal and spatial dispersions of the electrons burst, in pulsed regime. Here we present results for spatial and temporal dispersions obtained by computer simulation. We give simple scaling laws accounting for them.

1. INTRODUCTION

Many previous workers have extensively studied spatial and temporal evolutions of current in a vacuum diode, considering both quasi-stationary and transient regimes. Most such theories are based upon the assumption that a steady space-charge distribution has been established in the vacuum tube and that the high-frequency signal is merely a small disturbance compared to the steady component. But recent electron accelerator applications such as free-electron lasers, synchrotron sources, and powerful microwave tubes require bursts of very short pulses, high repetition rates and very high peak brightness. As few experimental data are available today, we study numerically the behaviour of photo-injectors in space-charge and very short pulses regime.

2. SIMULATION OF THE BEHAVIOUR OF AN ELECTRON PULSE IN A DIODE

We consider a plane diode with axial symmetry and inter-electrodes distance d . The applied voltage is V . The departure of electrons from the injector is made possible by a central hole of radius R_h opened in the anode. We suppose that the radius R_k of the emissive part of the cathode is small compared with d and R_h , so that the radial effects of the fields can be considered only as a correction of axial effects. In such conditions, we may neglect the magnetic fields.

We use for the electron pulse a description which was often used in more elaborated codes, cutting up the beam in a sequence of disks of small thickness, emitted at regular time spacings, as a train of micro-pulses. The distribution of elementary charge in the micropulses can be adapted to various shapes. The disks are divided in concentric rings in the radial direction. We suppose that in each element, all the electrons are submitted to the same forces, and have the same energy. We consider the mean values of the forces, and we take in account that the electrons can be relativistic. Each electron in an element is submitted to three kinds of electric fields : the first due to the applied voltage, the second due to the coulombian

interaction with electrons of the others elements, and the last induced by the image charges appearing when electrons leave the cathode.

The KIVI code is written for an I.B.M. PS/2 computer. The results are in good agreement with the accepted values.

We analyze temporal and spatial evolutions of electron beams with various conditions for charge distributions, pulse durations, dimensions of the diode and applied electric fields. In the following, R is the radius of the beam, τ the pulse duration, indexes K and A correspond to the values at the cathode and at the anode respectively.

3. TEMPORAL DISPERSION

The scaling law concerning the variation of τ uses normalized variables previously defined (Girardeau-Montaut 1989) :

$$\bar{\tau} = \tau \cdot v^{1/2} / d \quad (1)$$

This allows us to generalize the results to any operating conditions. Then $\bar{\tau}_g = 38 \text{ ns} \cdot \text{cm}^{-1} \cdot v^{1/2}$ is the characteristic time separating pulsed from quasi-continuous regimes.

The first set of operating conditions is labelled [G] : the electron pulse is gaussian, divided into 27 micro-pulses, across a diode in which $d = 5 \text{ mm}$, $R_h = 3 \text{ mm}$, and the emissive area of the cathode $= 1 \text{ mm}^2$. The applied field is $E = 18 \text{ MV} \cdot \text{m}^{-1}$. The total extracted density of charge is $\sigma = 15.9 \text{ nC} \cdot \text{cm}^{-2}$, very close to the space charge limit. In such conditions, the travelling time of the electrons across the diode is about 60 ps. Calculations were done with 8 different values of τ_k between 0.25 and 32 ps, e.g. $\bar{\tau}_k$ varying between 0.15 and $19.2 \text{ ns} \cdot v^{1/2} \cdot \text{cm}^{-1}$.

Figure 1 represents an initial pulse with a duration $\tau_k = 4 \text{ ps}$, and the same impulsion after the diode crossing. Values of $\bar{\tau}_A$ versus $\bar{\tau}_k$ are reported on Figure 2. The values of τ_A for the values of τ_k given above vary from 2 to 34 ps, and are more high as τ_k is smaller.

Another set of results was obtained in very different conditions : uniform distribution of the charge, cut up in 20 disks, in a diode in which $d = 5 \text{ cm}$, $R_h = 2 \text{ cm}$, and for $E = 20 \text{ MV} \cdot \text{m}^{-1}$. The radius of the beam at the cathode is successively 0.5 and 0.25 cm, corresponding to 2 sets $[U_1]$ and $[U_2]$ of operating conditions. The charge density is $17.64 \text{ nC} \cdot \text{cm}^{-2}$; pulse durations at the cathode are 75, 50 and 37.5 ps, corresponding to $\bar{\tau}_k = 15, 10, \text{ and } 7.5 \text{ ns} \cdot v^{1/2} \cdot \text{cm}^{-1}$. Results are reported also on Figure 2.

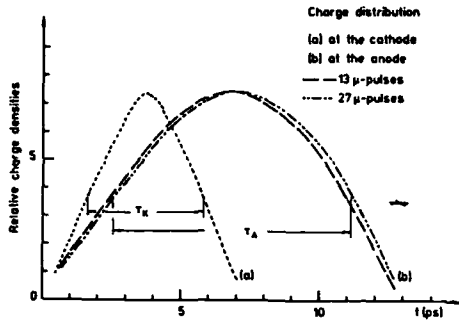


Fig. 1 - Temporal variations of the charge of an electron pulse between the cathode and the anode

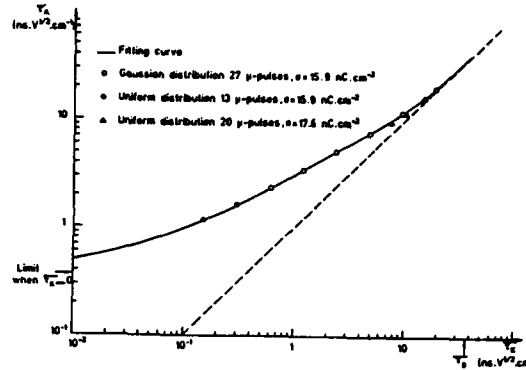


Fig. 2 - Normalized electron pulse duration at the anode versus initial duration at the cathode

Searching for an analytical expression of variation of $\bar{\tau}_A$ versus $\bar{\tau}_K$, we introduced an extra point corresponding to $\bar{\tau}_K = \bar{\tau}_g = 38 \text{ ns} \cdot \text{V}^{1/2} \cdot \text{cm}^{-1}$, as we expect that there is no more temporal distortion of the beam during the crossing of the diode above this value. Then the expression giving the best fitting for the curve on Figure 2 is a polynomial of successive powers of $[\tau_K/\tau_g]^{2/3}$:

$$\bar{\tau}_A = \sum_i a_i [\tau_K/\tau_g]^{2n_i/3} \quad (2)$$

where a_i is in the same units as $\bar{\tau}_A$. For i varying from 0 to 4, the values of n_i are respectively 0, 1, 2, 4 and 5 and the corresponding values of a_i are 0.366, 33.4, -18.6, 66.7 and -44.8. Equation (2) shows that, even if the emission time of the electrons at the cathode is very small, the pulse duration will always have a lower limit $\bar{\tau}_A$ of approximatively one percent of $\bar{\tau}_g$.

4. SPATIAL DISPERSION

Some results for spatial evolution are reported on Figure 3, for $[U_1]$ and $[U_2]$: the dispersion varies inversely to R_K and τ_K . The beam is widened mainly in its middle part, except when charges concentration is so high that the end of the pulse is even more broadened. To characterize this deformation, we consider the value of $r = R_A/R_K$. On Figure 4 are reported results for the 3 sets $[G]$ (curve a), $[U_1]$ (curve b) and $[U_2]$ (curve c), each curve corresponding to the same value of $F/\bar{\tau}_g$: the parameter F is proportional to the volumic density of electrostatic energy stored in the diode, $E\sigma$, and to $(R_K/R_h)^{1/2}$, accounting for the electric field distortions in the injector. Then r is proportional to the inverse values of F and of τ_K/τ_g respectively. It varies with decreasing values of $F \cdot \tau_K/\tau_g$ from 1 to some limit depending on F . Computations on limits of the curves give the values 2.4 for $[G]$ and $[U_1]$, as they

have the same value of $F = 12.5$ in arbitrary units, and 3.6 for $[U_2]$, $F = 17.65$ in the same units. F/τ_0 is the maximum power density available in the diode, modulated by the geometry of the diode; as expected, the distortion is greater as time of extraction is shortened.

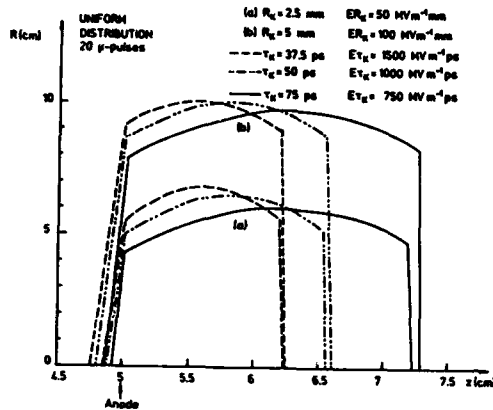


Fig. 3 - Geometry of an electron beam of initial uniform distribution after crossing the diode

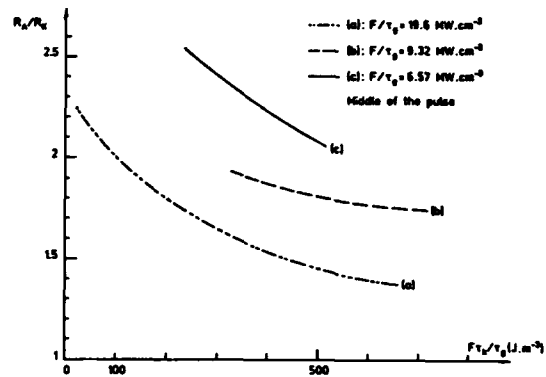


Fig. 4 - Spatial dispersion of a uniform electron distribution in a plane diode, for different operating conditions

5. CONCLUSION

This simplified analytical study gives the order of variations that have to be expected when parameters of the diode or operating conditions vary. It shows that in each case, limiting values exist and have to be taken in account.

Girardeau-Montaut JP, Girardeau-Montaut C 1989 *J. Appl. Phys.* 65 (8) 2889

Fabrication and theoretical study of micron-size vertical vacuum triodes

J Itoh and H Hiroshima

Electrotechnical Laboratory, 1-1-4 Umezono, Tsukuba-shi, Ibaraki-ken 305, Japan

We have fabricated vertical triode arrays with pyramidal Si field emitters. The fabrication method is based on a simple self-aligned process. The triode fabricated has a column-shape cavity of $8\text{-}\mu\text{m}$ diameter above the emitter, through which electron passes in a linear orbit. The thicknesses of the substrate-gate and the gate-anode insulating films are $2\text{ }\mu\text{m}$ and $1\text{ }\mu\text{m}$, respectively. The electric field at the emitter apex and the emission current were theoretically calculated. With calculation results, the device structure was optimized and the device characteristics were estimated.

1. INTRODUCTION

There has been an increasing interest in miniature vacuum tubes fabricated with microfabrication technologies used for integrated circuit. They are expected to be ultra-high speed and radiation-hard devices. The vacuum triode having a planer structure has already been proposed (Gray, Campisi and Greene 1986, Campisi and Gray 1987).

We have fabricated a vertical triode with pyramidal Si field emitter. In the present structure, the gate and the anode electrode are deposited on a Si substrate with intermediate insulating layers. Electrons emitted from the emitter move to the anode in a linear orbit through the column-shape cavity formed above the emitter.

The electric field at the emitter apex and the field-emission current density were calculated. With the results, we optimized the device structure and derived the current-voltage characteristics.

2. FABRICATION OF VERTICAL TRIODE

The schematic diagram of fabrication process is shown in Fig.1. At first, $4\text{-}\mu\text{m}$ -thick SiN and $0.1\text{-}\mu\text{m}$ -thick W films are deposited on n-Si(100) substrate by rf-sputtering ((1) in the diagram). Then $5\text{-}\mu\text{m}$ -diameter SiN disks are formed by reactive ion etching (RIE) with SF_6 gas and wet etching with HF solution (2). By using these disks as etching masks, pyramidal field emitters are made by orientation-dependent etching (ODE) technique (3), which is similar to

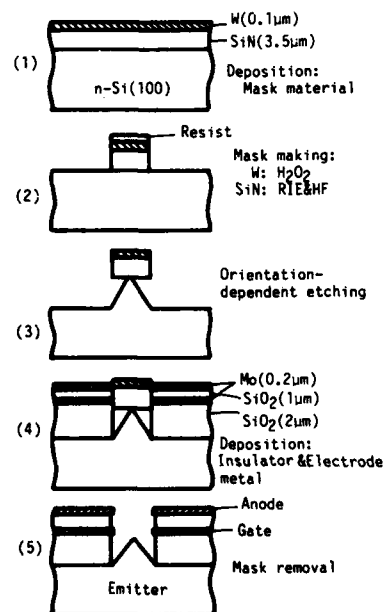


Fig.1. Schematic diagram of fabrication process.

that of Campisi and Gray (1987). The etchant used is a mixture of KOH, H₂O and isopropanol (IPA) in ratios of 40:400:100. The etch rate in depth is about 26 nm/min at $30 \pm 0.5^\circ\text{C}$, which is almost the same as that of undercut. By changing the mixture ratios, one can control the etch rates in these directions; the rate in depth is enhanced by increasing the KOH ratio.

After making the emitters, 0.2- μm -thick molybdenum layers for the gate and the anode electrodes are deposited in series with intermediate insulating films by electron-beam evaporation (4). A compound of SiO₂ and Al₂O₃ is used for evaporation source to deposit the insulating films (Vanfleteren and Calster 1986). The thicknesses of substrate-gate and gate-anode insulating films are 2 μm and 1 μm , respectively.

Finally, the SiN masks are removed by ultrasonic agitation leaving column-shape cavities. Then, the emitters are again etched with the ODE etchant to sharpen their apexes (5). In this fabrication process, the gate and the anode are self-aligned to the emitter because they are made with the same mask used for definition of the emitter.

Figure 2 shows a scanning electron micrograph of the emitter formed with the ODE technique; in this micrograph, the SiN mask is just removed to observe the apex. It is found from the figure that the apex can be as small as 0.3- μm diameter without removing the mask.

An 11x11 array of triodes fabricated is shown in Fig. 3. The diameter of the cavity is about 8 μm , which is larger than that of the SiN mask used. As shown in the figure, the diameter of the emitter apex is less than 0.1 μm .

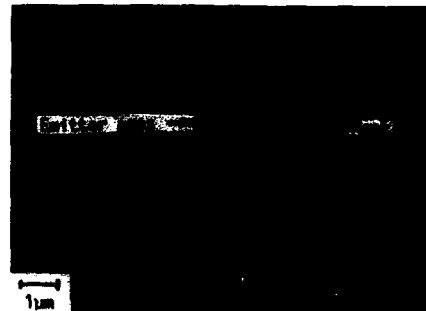


Fig. 2. Scanning electron micrograph of the emitter apex formed with orientation dependent etching described in text.

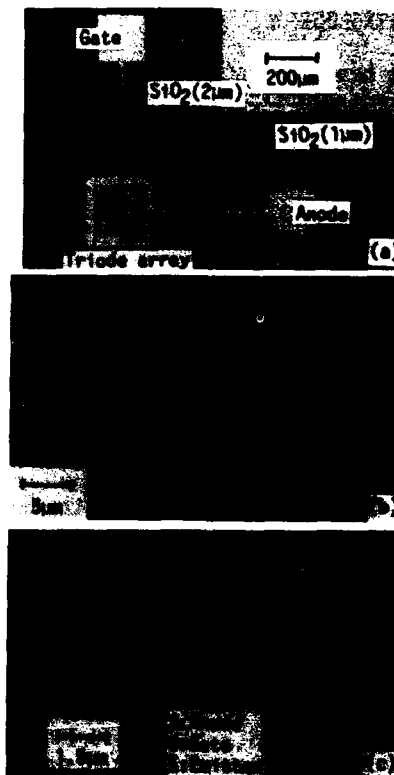


Fig. 3. An array of 121 (11x11) vertical triodes. (a) is a photograph and (b), (c) are scanning electron micrographs.

3. CALCULATION OF THE DEVICE CHARACTERISTICS

We have calculated the electric field at the emitter apex by the charge simulation method (Hoch, Kasper and Kern 1978). Figure 4 shows an example of two-dimensional equipotential diagram calculated for the triode having a $1\text{-}\mu\text{m}$ -diameter cavity and the emitter apex with $0.025\text{-}\mu\text{m}$ radius of curvature. In the calculation, the gate bias voltage, V_g , is fixed as a half of the anode voltage, V_a . One can see from the figure that the electric field is mainly influenced by the gate voltage. In order to increase the emission current, therefore, we need to increase the gate bias voltage or put the gate electrode close to the emitter apex.

The emission current density I_0 (A/cm^2) was calculated with a field emission theory from semiconductor proposed by Stratton (1962, 1964). According to the theory, the emission current from the conduction band is small compared with that from the valence band because of the band bending effect due to the surface states. Furthermore, I_0 is almost independent on the donor concentration. Figure 5 shows the current density at $T=300\text{ K}$ emitted from n-type Si calculated as a function of the electric field.

In order to optimize the device structure, we considered three typical cases as shown in Fig. 6. For each structure, we calculated the electric field, the emission current density and the transconductance. The results are shown in Fig. 7 as a function of V_a . In the calculation, the following conditions are assumed; radius of the emitter apex is $r=0.025\text{ }\mu\text{m}$, $V_g=3/4V_a$ and diameter of the cavity is $1\text{ }\mu\text{m}$.

As shown in Fig. 7, the structure of (b) in Fig. 6 is better than the

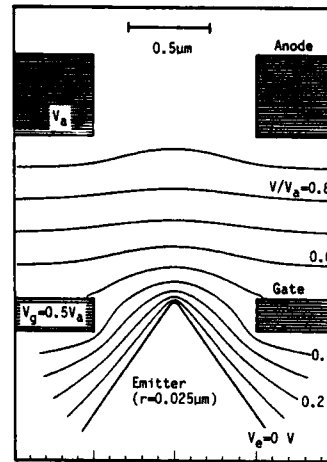


Fig. 4. Two dimensional equipotential diagram calculated by charge simulation method. In this case, bias voltage of the gate, V_g , is $0.5V_a$, where V_a is anode voltage. The radius of the emitter apex is $r=0.025\text{ }\mu\text{m}$.

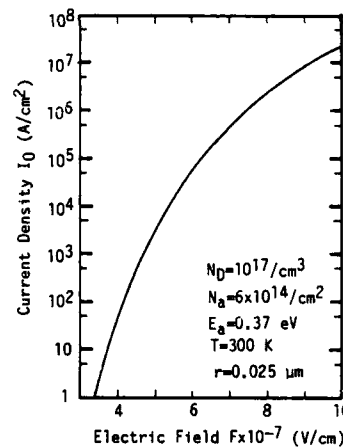


Fig. 5 Field emission current density calculated as a function of the electric field. N_D is the donor concentration, N_A is the acceptor-type surface state density with a single energy level, E_a is activation energy of the surface state measured from the top of the valence band.

others. In this case, the current density of $I_0 = 4 \times 10^4 \text{ A/cm}^2$ and the trans-conductance ($= \Delta I / \Delta V_g$, $I = \pi r^2 I_0$) of $g_m = 0.4 \mu\text{S}$ are obtained for $V_a = 400 \text{ V}$. This value of g_m , however, is not sufficient to use the present triode in an ultra-high speed circuit; for such use, g_m should be improved by at least one order or the gate capacity should be less than 10^{-17} F . Reduction of the dimensions, especially diameter of the cavity and radius of the emitter apex, is most effective to improve the device characteristics.

4. CONCLUSION

We have fabricated micron-size vertical vacuum triodes with a simple self-align process. The device characteristics are estimated theoretically and the device structure is optimized. It becomes clear from the calculations that reduction of the device dimensions is essentially important to use the present triode as an ultra-high speed electron device.

The authors are grateful to Drs. T. Tsurushima, K. Shimizu, K. Hoh, N. Atoda and M. Komuro for helpful advice and continuous encouragement. They also thank Drs. T. Kanayama and S. Kanemaru for helpful discussions on the fabrication process and theoretical calculations.

Campisi G J and Gray H F 1987 *Proc. Mat. Res. Soc. Symp.* 76 67
 Gray H F, Campisi G J and Greene R F 1986 *IEDM Tech. Digest* 776
 Hoch H, Kasper E and Kern D 1978 *Optik* 50 413
 Stratton R 1962 *Phys. Rev.* 125 67
 Stratton R 1964 *Phys. Rev.* 135 A784
 Vanfleteren J and Calster A V 1986 *Thin Solid Films* 139 89

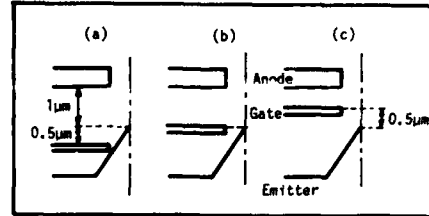


Fig.6. Three typical structures of vertical triode used for optimization of the device structure.

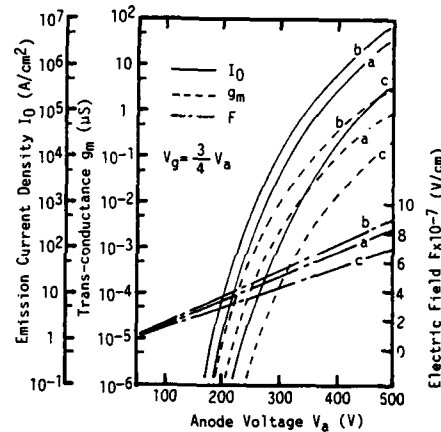


Fig.7. Electric field at the emitter apex, emission current density and trans-conductance at room temperature calculated as a function of the anode voltage for the three structures shown in Fig.6. In the calculation, $V_g = 3/4 V_a$ and $r = 0.025 \mu\text{m}$.

Ballistic field emission devices

V.I. Makhov

Moscow Physical Technical Institute, Dolgoprudny, USSR

ABSTRACT: The current-voltage characteristics of the microelectronic diodes with a silicon field emission cathode (FEC) in the wide range of pressure values have been studied. The operating voltages were up to 12V. The C-V characteristics of the microdevices remained stable at pressures ranging from 10^{-5} to 10^5 Pa. At the atmospheric pressure the microdiodes operate in a ballistic mode without the change of emissive properties.

1. INTRODUCTION

A number of authors acknowledge [Dyke, 1956] the reasons accounting for FEC failures in the vacuum with the pressure 10^5 Pa and analyse various factors affecting the field emission current instability. The first reason is a change of the size and the pattern of the emitting surface due to ion bombardment from the ambient gas medium. The second reason is the change of the work function while adsorbing residual gas molecules. And the third factor is the rearrangement of the emitting surface and even its destruction under the action of ponderomotive loads due to strong electric fields with the intensity more than 10^4 V/cm.

2. ELIMINATION OF ION BOMBARDMENT OF THE FEC

To provide the stability of the FEC in the wide pressure range it is necessary to eliminate ion sputtering of the cathode surface. The presence of ions in the field emission device is caused by a collision ionization of the residual gases molecules by the emitting electrons in the interelectrode space. The maximum energy that an electron can obtain from the field in the interelectrode space depends on the anode voltage. Consequently, ion bombardment would not appear until the operating voltages of the field emission device do not exceed the minimum value of the gas ionization potential in a working volume. In the atmospheric air the ion bombardment won't take place at $U_p < 12,5$ V.

If the work function of the field emission cathode doesn't depend on the pressure of the gases present, the maximum value of the admissible pressure in the working volume of

the field emission device will be related to the electron ballistic movement in the interelectrode space. This movement allows insignificant dissipation of the emitted electrons at the gas molecules. An observable electron dissipation will be observed when the characteristic size of the device exceeds the free electron path travelling in the given gas (quasi-ballistic operation mode). At room temperature and the pressure of 1 atm. the length of the free electron path in the air makes $\leq 0,4 \mu\text{m}$ and in He $\leq 1 \mu\text{m}$. Consequently, the electron dissipation in the field emission devices having characteristic size of the working space $0,4 \mu\text{m}$ will be considerable at the pressure of 1 atm and at He pressure 2,5 atm. It means that the reduction of the operating voltages of the field emission devices below the value of the gas molecules ionization potential allows to considerably extend the admissible range of the gas pressure up to atmospheric and higher for several types of devices.

3. STABILIZATION OF THE WORK FUNCTION AND THE GEOMETRY OF THE EMITTING SURFACE OF THE FEC

The problems of the change of the work function and rearrangement of the surface under the influence of adsorption and ponderomotive loads still remain unsolved. The change of the work function of the FEC surface can be prevented by depositing a tunnel-thick dielectric layer onto its surface ($d \sim 20 \text{\AA}$) [Makhov, 1984]

In such a structure of the FEC the adsorbed gases, which are located in the dielectric interface do not affect the stoichiometry of the emitting area - tunnel layer at the dielectric interface.

The dielectric layer deposited onto the cathode surface eliminates one more factor causing the change of the cathode current, that is - sharpening of the working end due to the surface particle migration in the electric field. Reliability of the FEC with such layers depend on the stability of layers to the bulk electromechanical forces [Makhov, 1987a]

When the electrons tunnel directly into a vacuum, the emission current density exponentially depends on the dielectric film thickness. Consequently in this emission mode the fluctuations of the emission current may be caused by the processes of desorption and adsorption and also by the chemical interaction with the active gases that particularly increases in poor vacuum. So to provide stability of the FEC in the wide pressure range we must use such emission mode when the electrons emit into the dielectric conductance area [Makhov, 1987b]. In this case the cathode current does not depend on the thickness of the dielectric film. Meanwhile we can neglect the nonelastic electron dissipation in the dielectric. Evaluations show that when the intensity of the field is $E \sim 4 \cdot 10^7 \text{ V/cm}$ and $\varphi \leq 3,2 \text{ eV}$, the part of nonelastically dissipated electrons will be small at $d \leq 26 \text{\AA}$. The silicon oxide film thickness is 15 to 20 \AA which satisfies this condition.

Exponential relationship between the emission current and the geometry and the work function puts strong limitations on the tolerances and reproducibility of parameters. We manage to observe these limitations by applying a well-developed grouping technique of the microelectronic technology. It is based on a rapid drop of the etching rate of Si in anisotropic etchant with excessive B concentrations. The thickness of the FEC made on film and the geometry of the top of the cathode were determined by the character of B diffusion into Si. After formation of the cathode geometry a dielectric layer was deposited onto the surface of the cathode, having the tunnel thickness near 20 Å. For this purpose a method of thermal oxidation was used. Figure 1 shows the structure of the diode with the film FEC.

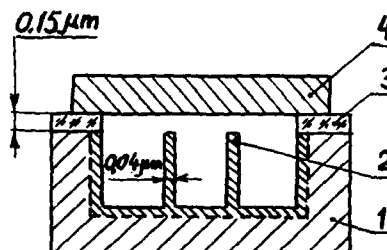


Fig.1. The structure of the diode with the film FEC.

- 1- the substrate
- 2- the film FEC
- 3- the dielectric film
- 4- the anode

4. EXPERIMENTAL STUDY OF THE EMISSION STABILITY OF THE SILICON FEC

The diodes were studied in a disassembling vacuum chamber at the pressure ranging from $3 \cdot 10^5$ to 10 Pa. Figure 2 shows a typical C-V characteristics of the diode. The diode current of the order of microampere had appeared after the operating voltage was greater than 5 V. The pressure rise up to 10^5 Pa did not cause obvious changes in the diode currents. The stability of C-V characteristics of the diodes had been tested in the various operating modes.

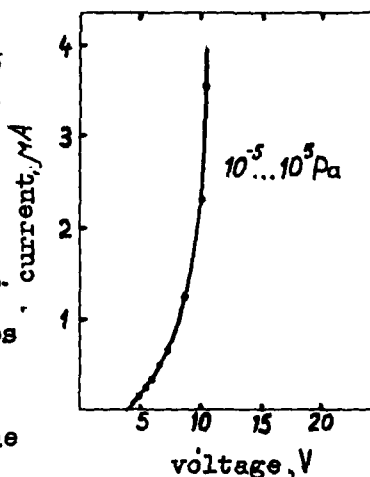


Fig.2. Typical C-V characteristics of the diode

The short-period stability of the field emission current can be most adequately described by the relation between the average value of the current $\Delta J/J$.

Figure 3 shows the relationship

$\Delta J/J = f(U)$, obtained for the cathode separated by the distance of $0.3 \mu\text{m}$ from the top of the film silicon FEC of P type at the atmospheric pressure at $P = 5 \cdot 10^{-3}$ mm Hg. As it follows from the curves presented, at $U \sim 15$ V the value $\Delta J/J$ does not depend on the air pressure and makes less than 0.01. If we continue to increase U value when $P = 5 \cdot 10^{-3}$ mm Hg the value $\Delta J/J$ remain practically unchanged. But at $P = 1$ atm. the value $\Delta J/J$ abruptly rise and at $U = 17$ V it

reaches the value 0,1. A slight difference of the voltage value, at which $\Delta J/J$ starts rising from the definite value of a threshold quartz sputtering $U_s = 16$ V can be caused by the difference in stoichiometry of the tunnel-thick dielectric and the silicon oxide. The time testing of the diodes was performed at a constant operating voltage $U = 7$ V and the pressure 10^5 Pa. Emission parameters of FEC + tunnel-thick dielectric were stable for more than 10000 hours and slight fluctuations ($\sim 5\%$) of the emission current were of a random character.

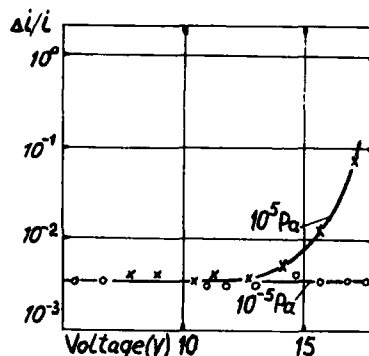


Fig.3. Relationship $\Delta J/J = f(U)$

5. CONCLUSION

The study of C-V characteristics of the microelectronic diode with the FEC which has a tunnel-thick dielectric layer deposited over the cathode surface was carried out.

We have demonstrated stable functioning of the diodes at pressures ranging from 10^{-5} to 10^5 Pa, including atmospheric pressure at operating voltages not exceeding the value of the ionization gas potential (12,5 V).

At the pressure of 10^5 Pa the diodes can operate in a ballistic mode, since the distance between the anode and the cathode was smaller than the free electron path in atmosphere.

REFERENCES

- Dyke W.P., Dolan W.W., Field emission In *Advances in Electronics*, New York, Academic Press, 1956, v.8, p.88-115.
- Elinson M.I., Vasilyev G.F. *Field emission*, M., Physmatizdat, 1958.
- Makhov V.I., Duzshev N.A., Pinaev I. The effect of the tunnel-thick dielectric layer on the emissive properties of FEC. Abstr. to the XIX All-Union Conference on Emissive Electronics, FAN Publishing House, Tashkent, 1984.
- Makhov V.I., Duzshev N.A., Eremchenko D.V. Stability conditions for the field emission cathode with a dielectric layer. Abstr. to the XX All-Union Conf. of Emission Electronics, Kiev, 1987a vol.1, p. 231.
- Makhov V.I. Low-voltage emission structures based on silicon FEC of submicron size. Abstr. to the I All-Union Conference "Physical and Chemical Problems of Microelectronics", Vilnius, 1987b

Papers and posters presented but not included in the proceedings

A proposed superconducting photoemission source of high brightness

H Piel et al, Universität Wuppertal, FRG

**(Published in the Proceedings of the European Particle Accelerator Conference
Rome, June 1988)**

Field emission arrays

C A Spindt, SRI International, Menlo Park, USA

Field emitter array structures for vacuum microelectronics

H F Gray, Naval Research Laboratory, Washington, DC, USA

Serial addressing for field emission tips flat panel TV

J P Biberian, Faculté des Sciences de Luminy, Marseille, France

Author Index

- Alexeenko A M, 201
Allen P C, 17
Anderson W A, 217
Archer A D, 57, 153
Arney S C, 1
- Bajic S, 57, 101
Baptist R, 85
Barengolzs Yu, 73
Baró A M, 177
Brodie I, 89
Buot F A, 137
Busta H H, 29
- Cade N A, 5, 57, 109
Carr W N, 77, 195
Chang T H P, 165
Chapman A T, 117
Chen C, 167
Cheng C C, 1
Chin K K, 77, 195
Ciario D R, 207
Cochran J K, 117
Crombeen J E, 25
Cutler P H, 121, 223
- Daniszewski E J, 185
Devyatkov N D, 201
- Eastman L F, 189
Edgcombe C J, 181
Eibl J, 9
Enze Luo, 95
- Feeney R K, 117
Feuchtwang T E, 121, 223
Filippov S L, 53
Fischer Ø, 173
Fitting H-J, 133
- Gärtner G, 25
Ghis A, 85
Girardeau-Montaut C, 227
Girardeau-Montaut J P, 227
Golant M B, 201
Gómez-Rodríguez J M, 177
Gray H F, 211, 223
Grigorishin L, 201
Groves R D, 81
Gulyaev Yu V, 201
- Harvey R J, 113
Hashimoto Y, 13
Hasker J, 25
Hee E W, 207
Hill D N, 117
Hiroshima H, 231
Hockley P J, 69
Hoeberechts A M E, 41, 141
Hoshinouchi S, 13
Howell D F, 81
Huang Z, 121, 223
- Itoh J, 231
- Jacobsen S E, 5
Janiel P, 25
Jensen K L, 137
- Katzschner W, 33
Kent A D, 173
Kern D P, 165
Kessler I, 33
Khaskelberg M, 73
Kobayashi M, 13
Korotkikh V L, 53
Kretschmer K-H, 33
- Laloyaux Th, 145
Lambin Ph, 145
Landsberg P T, 149
Latham R V, 57, 101, 153
Leboutet H, 227
Lee R A, 5, 81, 105, 113
Lucas A A, 145
- MacDonald N C, 1
Makhov V I, 235
Marcus R B, 77, 195
Matl K, 33
McConaghy C F, 207
McCord M A, 165
Meyer R, 85
Miller A J, 105, 113
Mitterauer J, 61
Morita N, 13
Musatov A L, 53
- Nakamura R, 21
Nakanishi H, 13
Negirev A A, 201

242 *Author Index*

Niedermann Ph, 173

Ogishi T, 21

Okunuki M, 65

Ono S, 21

Orvis W J, 207

Patel C, 81, 105

Phillips P M, 211

Renner Ch, 173

Roberts D E, 181

Sano K, 13

Sinitsyn N I, 201

Smith S T, 211

Spallas J P, 1

Speidell J L, 165

Stephani D, 9

Sullivan T, 121

Thomas H, 69

Tsong T T, 167

Tsukamoto T, 65

Uchimi A, 21

Usami K, 21

van de Walle G F A, 141

van der Heide P A M, 141

van Gorkom A A, 141

van Gorkom G G P, 41, 141

Vigneron J-P, 145

Wang H J, 77, 195

Warren J B, 37

Watanabe N, 65

Wenhu Huang, 95

Wigmore J K, 113

Williams H A, 81, 105

Yankelevitch Yu, 73

Yee J H, 207

Yokoo K, 21

Yuan Y, 77

Yunpeng Liu, 95

Subject Index

- Adhesion, 13
- Adsorption, 113
- Amplifier, 211
- Array, 1
- Atomic clusters, 167
- Avalanche breakdown, 41, 65, 141
- Average curvature, 95

- Binding energies, 167
- Boundary element numerical method, 95
- Burst noise, 89

- Capture, 149
- Cathodes, 105, 117, 165
- Cold cathodes, 17, 41, 57, 65, 69, 101, 141, 153
 - triodes, 29
- Composite, 117
- Cones, 77
- Cut-off frequency, 217

- Diodes, 207, 235
- Dissolution of surface layers, 167

- Eight-inch ECR source, 33
- Electron, 117
 - beams, 181
 - emission, 41, 69
 - gun, 85, 181
 - optics, 181
 - pulse, 227
 - spectroscopy, 153
 - transport, 189
- Electronic breakdown, 133
- Electrostatics, 109
- Emission, 105, 149
- Energy distribution, 81
- Energy spread, 85
- Enhanced field emission, 173
- Etchings, 5

- Fabrication, 5
- FIB implantation, 65
- Field distribution, 223
- Field effects, 149
- Field emission, 1, 5, 17, 29, 61, 77, 85, 109, 117, 165, 173, 207, 211
 - arrays, 37, 113, 231
 - cathodes, 89
- Field emitter, 37, 217

- Field enhancement, 109
- Field ionization, 61
- Forming, 73
- Frequency limits, 217
- Finite-element method, 145

- GaAs Schottky diode, 65
- Gain bandwidth, 217
- Green's equation, 95
- Gridded arrays, 81

- Heating element, 13
- Hot electron scattering, 133
- Hot electrons, 53

- I - V characteristics, 81
- Indium phosphide, 53
- Ion beam etching, 9
- Ion milling, 5

- Langmuir-Blodgett multilayers, 57
- Laplace's equation, 109
- Lateral micromachined triodes, 29
- Liquid metal-ion sources, 61
- Lithography, 177
- Low-temperature oxidation, 9

- Magnetic and electrostatic focusing, 201
- Microfabrication, 37, 231
- Microlens, 165
- Microlithographic process, 113
- Microscope, 145
- Microwave backward-wave oscillator, 201
- Microwave reflex klystron, 201
- MIM cathode, 73
- Miniature valve, 17
- Miniaturization, 61, 201
- MIS diode, 21
- MIS vacuum emission, 133
- Molybdenum tips, 89
- Mossbauer spectroscopy, 185
- Multidimensional tunnelling, 121

- NEA, 69
- Non-heated, 73
- Numerical simulation of quantum transport, 137

- Optimized static characteristics, 195

244 *Subject Index*

- Particle beams, 181
- Particle trajectories, 137
- Performance limits, 189
- Perturbation analysis, 181
- Photoemission, 53
- Picosecond, 1
- Plasma-activated CVD, 25
- Processing, 105

- Quantum well devices, 137

- Radiofrequency vacuum integral circuit, 201
- Reactive ion etching, 9
- Recombination, 149
- Resin-particle composite, 101

- Sapphire, 13
- Scanning electron microscopy, 173, 177
- Scanning tunnelling microscopy, 121, 165, 173, 177
- Scandate cathode, 25
- Schottky diodes, 53
- Self-aligned gate, 1
- Silicon, 81, 105, 113
- Silicon dioxide, 21
- Silicon field emitters, 9, 235
- Silicon micro-engineering, 17
- Silicon strips, 1
- Spindt's device, 95
- STM/SEM combination, 177
- Surface diffusion, 167

- Surface segregations, 167

- Temperature variation, 113
- Testing, 105
- Theory, 145
- Thermionic cathodes, 185
- Thermionic emission, 25
- Thin-film, 73
- Titanium, 13
- Trajectories, 223
- Transit line, 223
- Transmission line, 211
- Triode, 195, 207, 217
- Tungsten, 13
- Tunnelling, 77, 137, 141, 145
- Tunnelling emitter, 21

- Sacrificial layer, 207
- Short-time region in a diode, 227
- Solid state triodes, 189
- Strong metal-metal interactions, 185

- Vacuum, 207
 - microelectronics, 29, 89, 121, 195, 223
 - transistor, 29
 - triodes, 189, 231
 - tube, 231
 - tunnelling, 121

- Wedges, 77
- Wigner distribution function, 137

Vacuum Microelectronics 1989

STEERING COMMITTEE

Professor Lester F Eastman, Cornell University, Ithaca, USA
Dr Gerard G van Gorkom, Philips Research Laboratories, Eindhoven, Netherlands
Dr Henry F Gray, Naval Research Laboratory, Washington, DC, USA
Dr Rosemary A Lee, GEC Hirst Research Centre, Wembley, UK
Dr Johannes Mitterauer, Technische Universität, Wien, Austria
Mr Charles A Spindt, SRI International, Menlo Park, USA
Dr Takao Utsumi, Canon Inc., Kanagawa, Japan

ORGANIZING COMMITTEE

R A Lee *Chairman*, GEC Hirst Research Centre, Wembley, UK
J Mitterauer *Vice-Chairman*, Technische Universität, Wien, Austria
J K Wigmore *Secretary*, Physics Department, University of Lancaster, UK
C Hilsum *Sponsorship*, GEC plc, Wembley, UK
R V Latham *Publicity*, University of Aston, UK
D G Scotter *Treasurer*, GEC Hirst Research Centre, Wembley, UK
R E Turner *Publications*, Thorn EMI Central Research Laboratory, Hayes, UK
P D Wilson *Local Arrangements*, Fulmer Research Institute Ltd, Stoke Poges, UK

PROGRAMME COMMITTEE

R A Lee *Chairman*, GEC Hirst Research Centre, Wembley, UK
D C Young *Secretary*, Thorn EMI Central Research Laboratory, Hayes, UK
N A Cade, GEC Hirst Research Centre, Wembley, UK
I Gallimberti, University of Padova, Italy
H F Gray, Naval Research Laboratory, Washington, DC, USA
G G van Gorkom, Philips Research Laboratories, Eindhoven, Netherlands
I Green, Thorn EMI Central Research Laboratory, Hayes, UK
Y V Gulyaev, Institute of Radio Engineering and Electronics, Moscow, USSR
C Hilsum, GEC plc, Wembley, UK
G P Labrunie, LETI, Grenoble, France
R V Latham, University of Aston, UK
J Mitterauer, Technische Universität, Wien, Austria
P Niederman, University of Geneva, Switzerland
H Schindler, Siemens AG, Erlangen, FRG
C A Spindt, SRI International, Menlo Park, USA
T Utsumi, Canon Inc., Kanagawa, Japan
R H Williams, University College, Cardiff, UK